FERMILAB-THESIS-2024-03

UNIVERSITÀ DI PISA

Università degli Studi di Pisa

Dipartimento di Fisica E. Fermi
Corso di Dottorato di Ricerca in Fisica - XXXVI Ciclo

Measurement of the muon anomalous precession frequency with the Run-2/3 data in the Muon $g-2$ experiment at Fermilab

Candidato:
Lorenzo Cotrozzi
Matricola 624521

Supervisore:
Prof. Graziano Venanzoni
Supervisore interno:
Prof. Giovanni Batignani

Anno Accademico 2022-2023

My thoughts go to the students of my city who,
on the morning of February 23rd, 2024,
were peacefully marching in favour of Peace.
My soul will be forever wounded by the horrifying
scenes of repression of that same morning.
My heart belongs to the beautiful people in Pisa
who, on the evening of that day, gathered in
Piazza dei Cavalieri to give a powerful demonstration
of what values like "Freedom of Speech", "Democracy"
and "Anti-Fascism" really mean.

Forever I will say "Peace!", forever I will say
"Freedom!", without fear. Thank you Mum, Dad and
Auntie, for raising me this way.

Il mio pensiero va agli studenti della mia città,
che la mattina del 23 Febbraio 2024 stavano
pacificamente marciando in nome della Pace.
La mia anima sarà per sempre ferita
dalle orrende immagini di repressione
di quella stessa mattinata.
Il mio cuore appartiene alle bellissime persone
di Pisa, che si sono riunite la sera stessa
in Piazza dei Cavalieri, per dare una forte
dimostrazione di cosa vogliano davvero dire valori come
"Libertà di Espressione", "Democrazia" e
"Antifascismo".

Per sempre dirò, a testa alta: "Viva la Pace!",
"Viva la Libertà!". Grazie a Mamma, Papà e Zia,
per avermi cresciuto così.

Contents

Introduction

The measurement of the muon magnetic anomaly $a_\mu = (g_\mu - 2)/2$, where g_μ is the g-factor of the muon, is one of the most accurate tests of the Standard Model (SM) theory of elementary particles. Its theoretical value is dominated by the QED Schwinger term $\frac{\alpha}{2\pi} \approx 0.00116$, but all sectors of the SM contribute to the interaction of muons with a magnetic field through virtual particles in quantum loops, and the calculation has reached the high precision of ~ 0.37 parts per million (ppm).

On the experimental side, the anomaly can be measured very precisely, with a well-established technique. Indeed, when muons are injected into a magnetic field $\vec{B}$, both their spin and their momentum vectors precess, and the precession frequency of the spin with respect to the momentum, the so-called "anomalous precession frequency", can be obtained as $\omega_a \equiv a_\mu \frac{e}{m} B$. This means that a_μ can be extracted by accurately measuring ω_a and B. In the Muon $g-2$ experiment at Fermilab (E989), a 3.1-GeV spin-polarized beam of positive muons is injected into a storage ring of 14 m of diameter, in the presence of a 1.45 T magnetic field. Due to parity violation in the weak process of muon decay, high-energy positrons are emitted preferably towards the muon's spin direction and can be detected by 24 electromagnetic calorimeters placed around the inner circumference of the storage ring. Each calorimeter can measure the energy and the arrival time of emitted positrons and is made up of 6×9 crystals of lead-fluoride (PbF_2). If we count all emitted positrons with an energy above 1.7 GeV as a function of time, the counting rate oscillates with ω_a frequency and its maximum occurs when the muon spin and momentum vectors are aligned. ω_a can therefore be extracted by fitting the histogram of the oscillating number of counted positrons as a function of time, also called "wiggle plot", with a 28-parameter function that takes into account, amongst others, many beam dynamics effects. The magnetic field is constantly monitored by nuclear magnetic resonance (NMR) probes: 378 fixed probes are distributed in many azimuthal positions of the storage ring and placed on the walls of the vacuum chambers, to continuously track field drifts; a set of 17 probes are part of a moving device, the so-called "field trolley", that is pulled through the ring every $3-5$ days without the muon beam, to measure the spatial field distribution in the storage region. The NMR probes are calibrated twice a year with a retractable cylindrical high-purity water sample probe.

The Fermilab E989 collaboration, of which I am part since 2020, published the first result of the positive muon anomaly a_μ in 2021 with a precision of 0.46 ppm [1], 20 years after the previous result at Brookhaven National Laboratory (BNL) [2]. At the time of BNL, the experimental measurement was in a $3.7\,\sigma$ disagreement with the theoretical prediction, and the 2021 result at Fermilab confirmed the long standing discrepancy, bringing its significance to $4.2\,\sigma$. In August 2023, the experiment published a new measurement bringing the precision down to 0.20 ppm [3], a more than two-fold improvement with respect to the first measurement. The new result is based on the 2019 and 2020 data (namely Run-2/3), and it is in very good agreement with the previous experimental results. From the combination, the new experimental world average is $a_\mu(\text{Exp}) = 116592059(22) \times 10^{-11}$ (0.19 ppm). As reported in the Technical Design Report (TDR) [4], the final goal of the experiment is to measure a_μ with a precision of 0.14 ppm, by achieving statistical and systematic errors of comparable size (~ 0.1 ppm). With the 2023 re-

sult, the goal has been surpassed for the systematic uncertainties. When we will have analyzed our final data, collected from 2021 to 2023, we also expect to surpass the goal for statistical uncertainties.
On the theory side, there are tensions in the calculation of the hadronic vacuum polarization (HVP) contribution to a_μ. The consensus prediction of the Muon $g-2$ Theory Initiative White Paper [5], published in 2020, is based on the dispersive approach, for which experimental measurements of low-energy e^+e^- to hadrons cross sections serve as input. The current discrepancy between this calculation and the new experimental value is $a_\mu^{exp} - a_\mu^{SM} = (249 \pm 48) \cdot 10^{-11}$, with a significance of $5.1\,\sigma$. In 2021, the BMW collaboration published the first complete lattice QCD prediction of HVP with subpercent precision, that was closer to the experimental value and in $2.1\,\sigma$ tension with the prediction from the dispersive approach [6]. In 2023, the CMD-3 collaboration released results on the $e^+e^- \to \pi^+\pi^-$ cross section that disagree with all previous measurements used in the 2020 White Paper, and that, when taken individually as an input to the HVP, are less in tension with the experimental value [7]. Many efforts are ongoing in order to clarify the origin of all the discrepancies in the theoretical calculation.
In this Thesis, I will present my contribution to the analysis of the anomalous precession frequency ω_a, which is a main ingredient for the a_μ measurement together with the magnetic field, for the Run-2/3 result published in 2023. I will describe my work on the reconstruction, analysis, and fitting of the data to measure ω_a, and on the assessment of systematic effects such as detector gain changes, pileup events and beam dynamics. This work was performed within one of the analysis group of ω_a (the so-called "ω_aEuropa") whose result was included in the final evaluation of ω_a.
Chapters 1, 2 and 3 introduce the concept of the magnetic anomaly, provide details about the current status of the SM prediction and the history of the muon $g-2$ experiments. Chapter 4 describes the Muon $g-2$ experiment at Fermilab, and Chapters 5 and 6 describe the measurement of ω_a. Finally, in Chapter 7 we present the experimental results published in 2021 and 2023, with an outlook in Chapter 8 on the remaining data to be analyzed. The original work of this Thesis is presented in Chapters from 5 to 8: in particular, the "Ratio-Asymmetry" method, which was new with respect to Run-1, to analyze the anomalous ω_a frequency with the 2019 and 2020 data. This method greatly reduces the sensitivity of ω_a to all slowly varying systematic effects (e.g., gain changes that occur while the muons are stored in the ring), and it also achieves the maximum statistical power on ω_a by applying appropriate weights to the data. My results for ω_a were averaged with those from 5 other independent groups, to produce the final ω_a values and uncertainties that were published in 2023.

Chapter 1

The anomalous magnetic moment

1.1 Magnetic moment of elementary particles

The intrinsic magnetic moment of a charged particle with spin is equal to:

$$\vec{\mu} = g\frac{e}{2m}\vec{S} \tag{1.1.1}$$

where e is the particle charge, m its mass, $\vec{S}$ its spin vector and g the dimensionless *gyromagnetic ratio*, also called *g-factor* or *Landé factor*.
The relationship between the magnetic moment $\vec{\mu}$ and the angular momentum $\vec{L}$ can be easily derived from a classical perspective: if we consider the motion of a charged particle around a closed loop with radius r with uniform speed v, the electric current carried by the particle is $I = e\frac{v}{2\pi r}$. In the general formula, where $\vec{J}(\vec{r})$ is the current density distribution, the expression of the magnetic moment is:

$$\vec{\mu} \equiv \frac{1}{2}\int \vec{r} \wedge \vec{J}(\vec{r}) d^3\vec{r} \tag{1.1.2}$$

so, for a uniform current I in a closed loop, we have $\vec{\mu} = \frac{I}{2}\oint \vec{r} \wedge d\vec{l}$ where dl can be rewritten as $rd\theta$. Choosing the coordinate system such that the particle rotates around the z-axis, and using the fact that $\vec{r}$ is orthogonal to $d\vec{l}$ (see Figure 1.1.1), the resulting magnetic moment is:

$$\vec{\mu} = \frac{I}{2}\oint \vec{r} \wedge d\vec{l} = \hat{z}\frac{I}{2}\int_0^{2\pi} r^2 d\theta = \hat{z} I\pi r^2 \equiv IA\hat{z} \tag{1.1.3}$$

where A is the area of the loop.

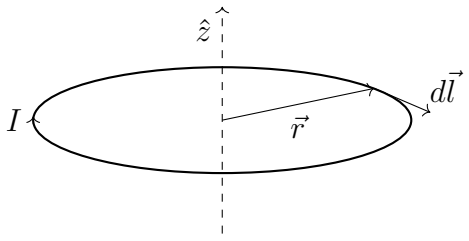

Figure 1.1.1: Representation of a charged particle moving at uniform speed in a closed loop around the z-axis.

We can replace $I = e\frac{v}{2\pi r}$ and $A = \pi r^2$ in Equation (1.1.3), and notice that $mvr\hat{z}$ is the angular momentum $\vec{L}$:

$$\vec{\mu} = \hat{z}\frac{ev\pi r^2}{2\pi r} = \hat{z}\frac{emvr}{2m} = \frac{e}{2m}\vec{L} \tag{1.1.4}$$

Equation (1.1.4) shows that, for a classical description of a rotating particle, $g = 1$.

The magnetic moment $\vec{\mu}$ gives us a measure of the torque and the energy that a charged particle feels when it is placed in a magnetic field:

$$\vec{\tau} = \vec{\mu} \wedge \vec{B}; \qquad U = -\vec{\mu} \cdot \vec{B} \tag{1.1.5}$$

In order to move forward from the classical description of magnetic moment to the quantum one, the concept of spin has to be introduced. One of the milestone experiments of quantum physics at the beginning of the 20$^{\text{th}}$ century was carried out by Stern and Gerlach in 1922 [8]: it was observed that, when a beam of neutral silver atoms passed through a magnetic field, the beam was clearly split into two bands along the axis of the magnetic field, meaning that two separate components experienced torques with opposite signs; from the expression of the torque in Equation (1.1.5), it can be inferred that silver atoms have two possible magnetic moments. Furthermore, if the magnetic moment were due to the electric charge of the nucleus, then a scaling of $\frac{1}{m_N}$ where m_N is the mass of the nucleus would be expected; however, such scaling was not observed neither in silver nor in hydrogen experiments [9], suggesting that the orbiting electrons were the source of the magnetic moment, instead of the nucleus. The idea of a fourth quantum number - the first three being n, m and l - arose from spectroscopy experiments, since it was the only way to fully remove all the degeneracies in the experimental data in accordance with Pauli's exclusion principle, which states that two electrons in an atom cannot have the same quantum numbers.
In 1925, two young physicists, the experimentalist Samuel Goudsmit and the theorist George Uhlenbeck, elaborated on the idea of this new quantum number: the concept of *spin* was born, together with the convention that its eigenvalues were $\pm\frac{1}{2}$. The classical Equation (1.1.4) underestimated the magnetic moment measured in the experimental results (such as the ones from Stern-Gerlach) by a factor of 2: this discrepancy was accounted for by the insertion of the Landé g-factor, as in Equation (1.1.1), so that experimental results were reproduced by requiring that g was equal to 2 in the case of electrons.

1.2 Magnetic anomaly

Paul Dirac's equation, presented in 1928 in Dirac's *The Quantum Theory of the Electron*, described the dynamics of electrons in the presence of electromagnetic fields [10], extending Schrödinger's wave equation to the relativistic case while preserving linearity with respect to time:

$$(i\gamma^{\mu}_{\alpha\beta}\partial_{\mu} - m\delta_{\alpha\beta})\psi_{\beta}(x) = 0 \tag{1.2.1}$$

where γ^{μ} are hermitian 4×4 matrices, δ is the identity, $\psi(x)$ is a 4-component spinor field, α and β are spinor indices that, for readability, will be omitted from now on. The Gamma matrices γ^{μ} have to be chosen such that $\{\gamma^{\mu}, \gamma^{\nu}\} = 2\eta^{\mu\nu}$ ($\eta^{\mu\nu}$ being the Minkowski metric), to make sure that Dirac's equation is Lorentz covariant and that Klein-Gordon's equation can still be obtained. As a result of Equation (1.2.1), the existence of spin and of anti-particles was predicted, as well as the value $g = 2$ for any elementary charged particle with spin-$\frac{1}{2}$: the steps leading to this result will be presented in Section 1.2.1.

1.2.1 $g = 2$ from Dirac's equation

As already mentioned, Dirac's equation preserves linearity with respect to time, which means:

$$i\ \frac{\partial\psi}{\partial t} = \mathcal{H}\psi \tag{1.2.2}$$

where $\mathcal{H}$ is the Dirac Hamiltonian operator, which we can write as:

$$\mathcal{H} = \vec{\alpha}\cdot\vec{p}c + \beta mc^2 \tag{1.2.3}$$

In Equation (1.2.3), α^k (with $k = 1,\ 2,\ 3$) and β are 4×4 traceless hermitian matrices whose square is equal to the identity. Recalling that the operator $\vec{p}$ is equal to $-i\ \vec{\nabla}$, and comparing Equations (1.2.3) and (1.2.1), we have that $\gamma^0 = \beta$ and $\gamma^k = \beta\alpha^k$, which means:

$$\gamma^0 = \begin{bmatrix} \mathbb{1} & 0 \\ 0 & -\mathbb{1} \end{bmatrix} \qquad\qquad \gamma^k = \begin{bmatrix} 0 & \sigma^k \\ -\sigma^k & 0 \end{bmatrix} \tag{1.2.4}$$

where σ^k are the Pauli 2×2 matrices. When looking for static solutions of Dirac's equation, we have:

$$i\ \frac{\partial\psi}{\partial t} = \beta mc^2\psi \tag{1.2.5}$$

which has a very simple solution: $\psi(t) = \begin{bmatrix} \psi_1(0)\exp\left(-imc^2t/\ \right) \\ \psi_2(0)\exp\left(-imc^2t/\ \right) \\ \psi_3(0)\exp\left(+imc^2t/\ \right) \\ \psi_4(0)\exp\left(+imc^2t/\ \right) \end{bmatrix}$.

The first two components, with the minus sign in the exponential, are called "large", whereas the ones with the plus sign are called "small" components (this nomenclature will be clarified below). If we let an electron interact with an electromagnetic field, the Hamiltonian changes since the electromagnetic four-potential A^μ is included and simple derivatives need to be replaced with covariant derivatives:

$$\vec{p}\to\vec{p} - \frac{e}{c}\vec{A} \qquad\qquad \text{and} \qquad\qquad \partial_\mu = \frac{\partial}{\partial x^\mu} \to \partial_\mu + \frac{ie}{c}A_\mu \tag{1.2.6}$$

We can now look for solutions of this type: $\psi(t) \propto \exp\left(-imc^2t/\ \right)\begin{bmatrix}\phi(t)\\ \chi(t)\end{bmatrix}$ where ϕ and χ are large and small components, respectively. Putting this type of solution into Equation (1.2.2), we obtain:

$$\begin{aligned} i\ \frac{\partial\phi}{\partial t} &= -i\ \ c(\vec{\sigma}\cdot\vec{\pi})\chi + eA_0\phi \\ i\ \frac{\partial\chi}{\partial t} &= -i\ \ c(\vec{\sigma}\cdot\vec{\pi})\phi + eA_0\chi - 2mc^2\chi \end{aligned} \tag{1.2.7}$$

where we have defined $\vec{\pi} = \vec{\nabla} - \frac{ie}{c}\vec{A}$. In the semiclassical approximation, we can assume that the electromagnetic field is not too strong ($eA_0 << mc^2$) and that χ is slowly varying in time (i.e., the kinetic term $i\ \frac{\partial\chi}{\partial t}$ is negligible with respect to the rest mass): then, $\chi(t) \approx -\frac{i}{2mc}(\vec{\sigma}\cdot\vec{\pi})\phi(t)$, where it is evident that $\chi(t)\to 0$ in the non-relativistic limit (allowing c to infinity), from which comes the attribute "small" to this component. By combining the two equations in (1.2.7) within this approximation, using some basic properties of the Pauli matrices algebra and recalling that the magnetic field is $\vec{B} = \vec{\nabla}\wedge\vec{A}$, we obtain:

$$i\ \frac{\partial\phi}{\partial t} = \left[\frac{(\vec{p} - \frac{e}{c}\vec{A})^2}{2m} + eA^0 - \frac{e}{2mc}(\vec{\sigma}\cdot\vec{B})\right]\phi \tag{1.2.8}$$

From the last term $-\frac{e}{2mc}(\vec{\sigma}\cdot\vec{B})$ we can point out the spin operator $\vec{S}=\frac{}{2}\vec{\sigma}$ and recognize the scalar product between the magnetic moment and the magnetic field in Equation (1.1.5): we therefore have $\vec{\mu}=g\frac{e}{2m}\vec{S}=2\frac{e}{2m}\vec{S}$, from which $g=2$ predicted from Dirac's equation for electrons (or, in general, for any elementary charged particle with spin-$\frac{1}{2}$, such as the muon).

1.2.2 The Zeeman effect

In 1897, Pieter Zeeman discovered that, in the presence of a magnetic field $\vec{B}=B\hat{z}$, the degeneration on J_z (the projection of $\vec{J}=\vec{L}+\vec{S}$ along the z-axis) is broken [11]. This can be explained in the following way: the Hamiltonian of an atomic electron contains an additional term due to $\vec{L}$, so the last term in Equation (1.2.8) becomes $\frac{e}{2mc}B(l_z+gs_z)$, which splits a state $|j,j_z\rangle$ in $2j+1$ components. Therefore, spectral lines due to the transition from a level a to a level b disintegrate in a multiplet of spectral lines, giving rise to the so-called *Zeeman effect*. Assuming that the magnetic field is weak, we can estimate the energy shift for fixed j in perturbation theory, starting from the eigenstates $|n,l,s;j,j_z\rangle$, each with $(2j_z+1)$ degeneration. The first order in the energy shift is proportional to $\langle j,j_z|\,(l_z+gs_z)\,|j,j_z\rangle$, so the operator (l_z+gs_z) has to be rewritten in terms of j_z only. Having fixed j, we can say that $\vec{s}=\alpha_S\vec{j}$, and starting from $\alpha_S\vec{j}^2=\vec{j}\cdot\vec{s}$ we obtain:

$$\alpha_S=\frac{j(j+1)+s(s+1)-l(l+1)}{2j(j+1)} \tag{1.2.9}$$

Finally, we can say the energy shifts for each of the $2j+1$ levels are proportional to g_Jm, where m is the eigenvalue of j_z, and g_J is defined as:

$$g_J=1+(g-1)\alpha_S \tag{1.2.10}$$

Since $g\neq 1$ for the electron, the Zeeman shifts depend on j and in general there are more than 3 spectral lines due to the Zeeman effect.

The coupling between the electron spin and the magnetic field also gives rise to fine structure (discovered by Michelson and Morley in 1887 [12]) and hyperfine structure in atoms, allowing atomic models to go beyond Bohr's description.

1.2.3 Deviation from $g=2$

In the previous sections, many merits of Dirac's equation were pointed out. However, two experiments in 1947 showed that Dirac's theory still had some limitations and that, in particular, its prediction for the g-factor of the electron differed from the real value.

The first experiment, carried out by Lamb and Retherford [13], measured the splitting between the $2S_{\frac{1}{2}}$ and $2P_{\frac{1}{2}}$ levels in the hydrogen atom (in spectroscopic notation nL_j): according to Dirac's theory, those two states would be degenerate because they have the same n and j quantum numbers, so no difference of energy should be observed; experimentally, instead, the $2P_{\frac{1}{2}}$ state has a lower energy than $2S_{\frac{1}{2}}$; the shift is approximately 1.058 GHz which is equivalent to 4.375 µeV. The discovery of the so-called "Lamb shift" was therefore an important step towards the modern development of Quantum Electrodynamics (QED).
The second experiment that was in disagreement with Dirac's prediction was carried out by Kusch and Foley [14], who studied the spectral lines due to Zeeman effect on Gallium inside a 380-gauss magnetic field, and measured the ratio between the g_J factors of the ${}^2P_{3/2}$ and ${}^2P_{1/2}$ states (in spectroscopic notation ${}^{2s+1}L_j$). According to Equation (1.2.10), the ratio between the

two g_J factors should be equal to 2 if, for electrons, $g = 2$. Instead, Foley and Kusch measured a slightly greater ratio between the two factors, which provided an indirect measurement of the electron g-factor: $g = 2.00229 \pm 0.00008$. Previous studies on hydrogen and deuterium had suggested that a value of $g_e \neq 2$ could explain a 0.26% anomaly in the hyperfine splitting (see References [15, 16, 17]).

The results of all these experiments could not be explained by Dirac's theory, since Equation (1.2.1) is only valid for the dynamics of a single free particle, moving in the presence of a weak electromagnetic field. Instead, deviations from $g = 2$ are possible in the framework of Quantum Field Theories (QFT) such as QED, a theory in which the interaction between charged particles and electromagnetic fields can be studied perturbatively using diagrams, namely Feynman diagrams, where virtual particles (such as virtual photons) are exchanged. Virtual particles cannot be detected in experiments, but in perturbation theory they significantly contribute to the measurable rate and properties of physical processes and modify the values of electron charge and mass (the so-called *radiative* corrections). Thanks to the development of renormalization techniques, theorists were able to establish, for the first time, a prediction of the electron g-factor which differed from $g = 2$ and was in agreement with Kusch and Foley's results. Thanks to Tomonaga, Schwinger and Feynman who, around 1948, independently elaborated different methods of renormalization, and for which they were awarded the Nobel Prize in 1965, QED became one of the most accurate theories that have ever been developed and tested.
Defining the magnetic anomaly of the electron as:

$$a_e = \frac{g_e - 2}{2} \tag{1.2.11}$$

the first-order value found by Schwinger [18] was $a_e = \frac{\alpha}{2\pi} \approx 0.00116$, where α is the fine structure constant $\alpha^{-1} = 137.035999084(21)$ [19]. The most important details of this calculation are covered in the Appendix A. This first term comes from a 1-loop contribution that accounts for $\sim 99\%$ of the anomaly and it is universal to all leptons (electron, muon, tau): its Feynman diagram is shown in Figure 1.2.1(c), along with the general and the tree-order diagrams, in Figures 1.2.1(a) and 1.2.1(b) respectively.

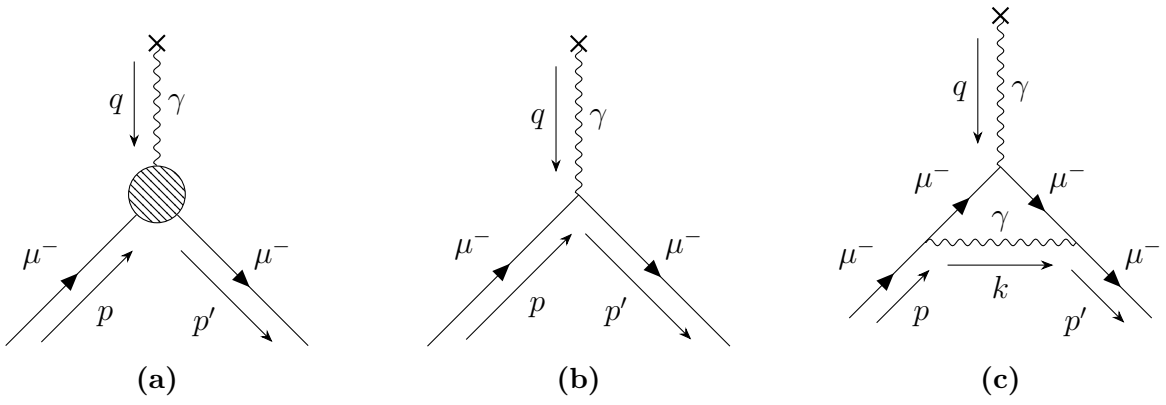

Figure 1.2.1: QED prediction for the muon magnetic anomaly: (a) is the general form of diagrams that contribute to the anomaly, (b) is the tree-order contribution which yields $g = 2$ and (c) is the 1-loop Feynman diagram that leads to the first radiative correction, $a = \alpha/2\pi$.

1.3 Measurement principle of a_μ

1.3.1 Why $a_\mu = (g_\mu - 2)/2$ is a good probe for new physics

There are three massive particles in the charged lepton family: electron, muon and tau. Their main properties, compiled by the Particle Data Group [19], are displayed in Table 1.3.1.

	e^-	μ^-	τ^-	
Charge	-1	-1	-1	
Spin	1/2	1/2	1/2	
Mass [MeV/c^2]	0.511	105.7	1776.9	
Mean life [s]	$> 2.0 \cdot 10^{36}$	$2.2 \cdot 10^{-6}$	$290.3 \cdot 10^{-15}$	
Main decay mode(s)	-	$e^-\bar{\nu}_e\nu_\mu$	$\mu^-\bar{\nu}_\mu\nu_\tau$	$e^-\bar{\nu}_e\nu_\tau$
Branching ratio [%]	-	≈ 100	17.39	17.82

Table 1.3.1: Charged lepton properties.

In principle, the anomalous magnetic moment could be observed for all leptons, but from an experimental point of view there are some critical differences: measuring a_e is easier than a_μ or a_τ, since the electron is a stable particle, whereas the short lifetime of muons and tau particles is a limitation for experiments. The current best measurement of a_e [20], which uses a one-electron quantum cyclotron, is ~ 1700 more precise than the current best measurement of a_μ. However, quantum fluctuations due to heavy particles or contributions at high energy scales are proportional to $\delta a_l \propto m_l^2/\Lambda^2$ where m_l is the lepton mass and Λ is the mass of a hypothetical heavy particle beyond SM. So, while the measurement of a_e is an ideal test for QED (see Section 2.1.1), it is not as sensitive to possible new physics as the muon is: the relative mass ratio $m_\mu^2/m_e^2 \approx 43000$ enhances the muon sensitivity. Clearly, experiments with tau particles would have an even greater sensitivity to new physics, but they would have to face two problems: firstly, tau particles have a very short lifetime, so a significant Lorentz boost would be needed; secondly, contrarily to muons, tau particles do not have a single, dominant decay mode, but instead they decay into hadronic states which would need to be identified. Recently, two proposals were made to measure the magnetic anomaly a_τ at the LHC and improve the current limits by the DELPHI collaboration [21]: one is based on selecting polarized τ^+ from D_s^+ decays, and determine the rotation of the spin-polarization vector induced by electromagnetic fields [22]; the other is based on ultra-peripheral collisions of heavy ions, where hadronic interactions are strongly suppressed and long-distance electromagnetic processes dominate [23].

1.3.2 The anomalous precession frequency

Let us recall that, if we can write, for a vector $\vec{v}$, a differential equation of the type in Equation (1.3.1) :

$$\frac{d\vec{v}}{dt} = \vec{\Omega} \wedge \vec{v}, \qquad \vec{\Omega} = \Omega\hat{z} \tag{1.3.1}$$

then $\vec{v}$ precesses along the z-axis with frequency Ω.

In the Fermilab Muon $g-2$ experiment, polarized muons are produced from pion decay (see Section 1.3.3) and injected into a storage ring with a magnetic field orthogonal to the ring plane. In the muon rest frame, the interaction term in the Hamiltonian is of the type $\mathcal{H} = -\vec{\mu} \cdot \vec{B}$, so from Heisenberg equation it is possible to obtain:

$$\frac{d\vec{s}}{dt} = -g\frac{e}{2m}\vec{B} \wedge \vec{s} \tag{1.3.2}$$

Comparing Equations (1.3.1) and (1.3.2), we derive that, for a muon at rest, the rate at which the spin turns is given by the so-called Larmor frequency:

$$\omega_S \equiv g\left(\frac{e}{2m}\right)B \tag{1.3.3}$$

In the lab frame, due to Lorentz force $\frac{d\vec{p}}{dt} = e\vec{v} \wedge \vec{B} = -\frac{e}{m\gamma}\vec{B} \wedge \vec{p}$, the relativistic muons orbit in the storage ring with a frequency called "cyclotron frequency":

$$\omega_C \equiv \left(\frac{e}{m\gamma}\right)B \tag{1.3.4}$$

Moreover, the muons in the storage ring experience a centripetal force that leads to the Thomas precession term $\vec{\omega}_T = \gamma^2/(\gamma+1)\cdot(\vec{a} \wedge \vec{v})/c^2$, where $\vec{a}$ and $\vec{v}$ are the particles' acceleration and velocity, respectively [24]. This effect is connected to the fact that two successive non-collinear Lorentz transformations are equivalent to a Lorentz transformation plus a three dimensional rotation. As a result, an additional term contributes to the spin frequency:

$$\omega_T \equiv (1-\gamma)\left(\frac{e}{m\gamma}\right)B \tag{1.3.5}$$

So, in the presence of a magnetic field which is such that $\vec{B}\cdot\vec{\beta} = 0$, we have that:

$$\omega_S = g\left(\frac{e}{2m}\right)B + (1-\gamma)\left(\frac{e}{m\gamma}\right)B; \qquad \omega_C = \left(\frac{e}{m\gamma}\right)B \tag{1.3.6}$$

In the lab frame, the rate at which the muon spin rotates with respect to the momentum is therefore $\omega_a \equiv \omega_S - \omega_C$ and it is called the "anomalous precession frequency":

$$\omega_a \equiv \omega_S - \omega_C = a_\mu\left(\frac{e}{m}\right)B \tag{1.3.7}$$

There are three important features of ω_a from Equation (1.3.7): (i) it does not depend on γ; (ii) it only depends on a_μ, rather than the full magnetic moment; (iii) it depends linearly on the applied magnetic field. In the general case where an electric field is also present, and where $\vec{B}\cdot\vec{\beta}$ is not cancelled out, the above formulas can be expanded [25]:

$$\begin{aligned}
\vec{\omega}_S &= \frac{e}{m}\left[\left(\frac{g}{2}-1+\frac{1}{\gamma}\right)\vec{B} - \left(\frac{g}{2}-1\right)\frac{\gamma}{\gamma+1}(\vec{\beta}\cdot\vec{B})\vec{\beta} - \left(\frac{g}{2}-\frac{\gamma}{\gamma+1}\right)\frac{\vec{\beta}\wedge\vec{E}}{c}\right] \\
\vec{\omega}_C &= \frac{e}{m}\left[\frac{1}{\gamma}\vec{B} - \frac{\gamma}{\gamma^2-1}\cdot\frac{\vec{\beta}\wedge\vec{E}}{c}\right]
\end{aligned} \tag{1.3.8}$$

So that ω_a becomes, in the general case:

$$\vec{\omega}_a = \vec{\omega}_S - \vec{\omega}_C = \frac{e}{m}\left[a_\mu\vec{B} - a_\mu\frac{\gamma}{\gamma+1}(\vec{\beta}\cdot\vec{B})\vec{\beta} - \left(a_\mu - \frac{1}{\gamma^2-1}\right)\frac{\vec{\beta}\wedge\vec{E}}{c}\right] \tag{1.3.9}$$

Again, we can assume that the motion of the muons is purely longitudinal so that $\vec{\beta}\cdot\vec{B} = 0$ and the second term in the square brackets vanishes. The expression can be further simplified to cancel out the effect of the E-field, by choosing a specific value of the Lorentz boost:

$\gamma = \sqrt{1 + 1/a_\mu} \approx 29.3$. This corresponds to $p_\mu \simeq 3.09\,\text{GeV}/c$, which is the so-called "magic" momentum: the experiments since CERN III (see Section 3.2.3) used the magic momentum to minimize the influence of the E-field on muons orbiting around the storage ring. In this configuration, the expression for the anomalous precession frequency becomes the same as Equation (1.3.7): this is the reason why, in order to extract a_μ from the experiment, the two main quantities to measure are ω_a and B, as a_μ will be proportional to their ratio. Given that the muon beam is not ideal but, for instance, there is a momentum distribution peaked at the magic value, the above cancellations are only to first order, and there are corrections that take into account the effects of the E-field and of the $(\vec{\beta} \cdot \vec{B})\vec{\beta}$ terms.

The diagrams in Figure 1.3.1 show how the muon spin and momentum vectors precess inside the storage ring during a complete turn in the ring. The two vectors are assumed to be aligned at the beginning of the precession: according to Equation (1.3.7), if g_μ were equal to exactly 2, the spin would remain parallel to the momentum at all times. Since $g_\mu > 2$, the spin precesses relatively to the momentum, with the frequency ω_a that is proportional to the muon anomaly and to the magnetic field. After one complete turn, the angle between the muon spin and momentum changes proportionally to the ratio $T_C/T_a = \omega_a/\omega_C = a_\mu\gamma$. For muons at the magic momentum, this means that the anomalous precession frequency ω_a is $\sim$12.3°/turn.

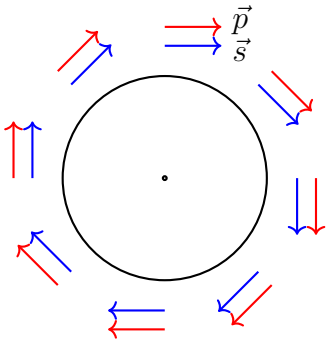

(a) Precession of muon spin and momentum if $g = 2$.

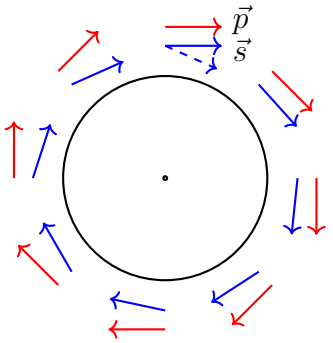

(b) Precession of muon spin and momentum if $g > 2$.

Figure 1.3.1: Motion of the spin (blue) relative to the momentum (red) vector. Figure (a) shows the case when $a_\mu = 0$, so the spin does not rotate relatively to the muon momentum; Figure (b) shows what happens when $g > 2$. In this example, the precession frequency is 24°/turn, i.e. about twice the actual value in the E989 experiment, for better visibility. The dashed blue arrow is the muon spin vector after one complete turn.

1.3.3 Muon decay chain

An important role in the E989 experiment is played by charged pions $\pi^\pm$, which are produced copiously when an energetic proton beam impacts a target (see Chapter 4). After neutral pions π^0, the charged $\pi^\pm$ are the lightest hadrons, with a mass of about $139.6\,\text{MeV}/c^2$. The main decay mode for charged pions is $\pi^\pm \to l^\pm \overset{(-)}{\nu}_l$ where l stands for lepton: the only possibilities are electrons and muons, but not tau particles due to their mass. The parity violation in the weak decay makes sure that muons in the forward decay of the π are longitudinally polarized, which is a key feature when measuring ω_a.

Pion decay

The most probable final state in positively charged pion decay is $\mu^+\nu_\mu$ with a branching ratio of 99.98770(4)%. Since muons have a much greater mass than electrons, one would expect that the phase space favored the $e^+\nu_e$ final state: this is not the case, and the ratio between the two processes is [19]:

$$R_\pi = \frac{\Gamma(\pi \to \mu + \nu_\mu)}{\Gamma(\pi \to e + \nu_e)} \approx 8.13 \cdot 10^3 \tag{1.3.10}$$

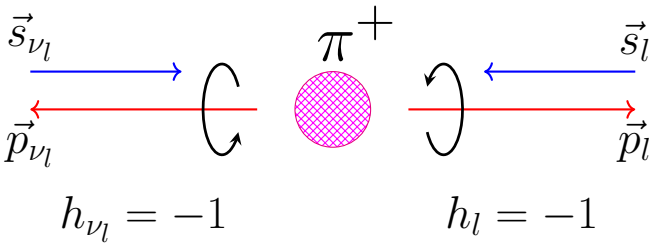

Figure 1.3.2: Diagram of a positively charged pion decaying into a positive lepton and a neutrino. The value of the helicity $h \propto \vec{p} \cdot \vec{s}$ is shown for both the emitted particles. $h = -1$ means left-handed.

Figure 1.3.2 helps to understand this experimental value for R_π: in the π^+ rest frame, the lepton and neutrino are emitted back-to-back and, in the limit of massless neutrinos, the neutrino is always emitted with a left-handed helicity. In the weak decay, the positively charged leptons would be preferentially emitted with right-handed helicity, but this is vetoed by the massless neutrino and by the conservation of angular momentum (the pion has zero spin). Thus, the more massive the emitted lepton is, the more favored the decay mode becomes. Equation (1.3.11) shows the computation of R_π at tree order in the massless neutrino limit:

$$R_\pi \propto \underbrace{\left[\frac{m_\pi^2 - m_\mu^2}{m_\pi^2 - m_e^2}\right]^2}_{\text{Phase space}} \underbrace{\frac{m_\mu^2}{m_e^2}}_{\text{Helicity}} \approx 7.79 \cdot 10^3 \tag{1.3.11}$$

Muon decay

The muon decay process is represented in the following diagram in Figure 1.3.3(a).

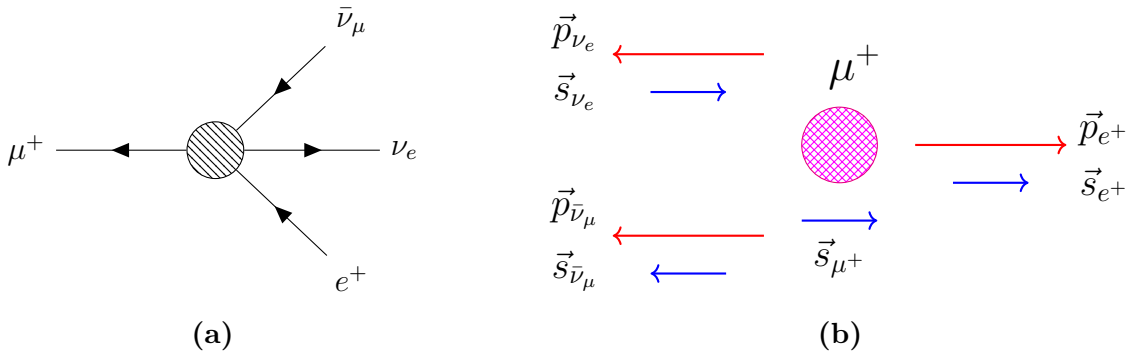

Figure 1.3.3: Diagrams of a positively charged muon decaying into a positron, a muon antineutrino and an electron neutrino: (a) represents the current-current Fermi-like interaction, from which we can derive the effective Lagrangian in Equation (1.3.12); (b) shows the helicity constraints when neutrinos are emitted in the same direction.

Assuming a current-current Fermi-like interaction, one can start from an effective lepton Lagrangian of the form:

$$L_f = \frac{G_F}{\sqrt{2}} J_\mu J^{\mu\dagger}, \qquad J_\mu^{(lep.)} = \sum_{l=e,\mu,\tau} \bar{\psi}_{\nu_l} \gamma_\mu (1-\gamma_5) \psi_l \tag{1.3.12}$$

then calculate the complex amplitude for the tree-order process where the "blob" in the above diagram is replaced by a 4-point interaction; take its square module and, at last, sum on the polarization of all the emitted particles. The integration on phase space for a polarized muon yields the differential decay width in Equation (1.3.13):

$$\frac{d^2\Gamma_{(\mu\to e\nu\nu)}}{dy^* d\cos\theta^*} \propto n^*(y^*)[1 + a^*(y^*)\cos(\theta^*)] \tag{1.3.13}$$

where the star (*) refers to the muon rest frame (center-of-mass frame). Equation (1.3.13) introduces two kinematic parameters: y^*, which is the ratio between the energy of the emitted positron and the maximum energy the positron can take (approximately half of the muon mass); and θ^*, the angle of the positron momentum with respect to the muon spin vector. Two functions are introduced, $n^*(y^*)$ and $a^*(y^*)$: the latter is called "asymmetry" in the center of mass. The Equations in (1.3.14) show the explicit expressions of these coefficients, whereas Figure 1.3.4 shows the behaviour of these functions.

$$n^*(y^*) = y^{*2}(3 - 2y^*); \qquad a^*(y^*) = \frac{2y^* - 1}{3 - 2y^*} \tag{1.3.14}$$

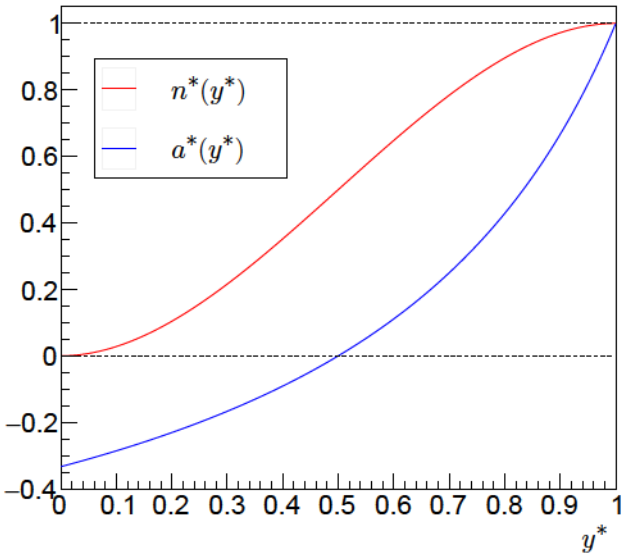

Figure 1.3.4: In the center-of-mass frame, the functions $n^*(y^*)$ and $a^*(y^*)$ from Equation (1.3.14) are plotted.

There are values of y^* for which the asymmetry takes negative values. We shall see that this also happens in the lab frame, where a different asymmetry coefficient will be introduced. The differential decay width takes its maximum value for the highest energy positron whose momentum is parallel to the muon polarization: once again, this is a result of the parity violation of the V-A nature of weak decay, which prefers to couple to a right-handed positron. Figure 1.3.3(b) illustrates the decay of the highest energy positrons in the muon rest frame: the positron's energy is approximately half of the muon mass, while the other half is shared by the two neutrinos that are emitted in the same direction; the neutrino and anti-neutrino spins

cancel, so the decay positron is forced to carry the spin of the parent muon.

With a Lorentz boost, it is possible to derive the differential decay width in the laboratory frame. Since the gamma-factor γ_{Boost} of the Lorentz transformation is approximately 30, much greater than 1, and since the positron mass is much smaller than the muon mass m_μ, the maximum positron energy in the lab frame is $\gamma_{\text{Boost}} m_\mu \approx 3.1\,\text{GeV}$. In this frame, there is a new kinematic variable which greatly influences the positron energy spectrum: it is the angle α formed between the muon spin and the muon momentum. It is possible to show that the differential decay width in the lab frame is given by Equation (1.3.15).

$$\frac{dN_{e^+}}{dy}(y,\alpha) = \frac{(y-1)[4y^2-5y-5-(8y^2-y-1)\cos(\alpha)]}{3} \equiv \frac{N(y)[1+A(y)\cos(\alpha)]}{3} \tag{1.3.15}$$

where y is the ratio between the positron lab energy and $\gamma_{\text{Boost}} m_\mu$, while $N(y)$ and $A(y)$ are defined by the relations in (1.3.16) and plotted in Figure 1.3.5:

$$N(y) = (y-1)(4y^2-5y-5); \qquad A(y) = \frac{-8y^2+y+1}{4y^2-5y-5} \tag{1.3.16}$$

The factor 3 in the denominator ensures that the integral of $\frac{d}{dy}N_{e^+}$ from $y=0$ to $y=1$ is equal to 1, so that Equation (1.3.15) is actually a probability density function.

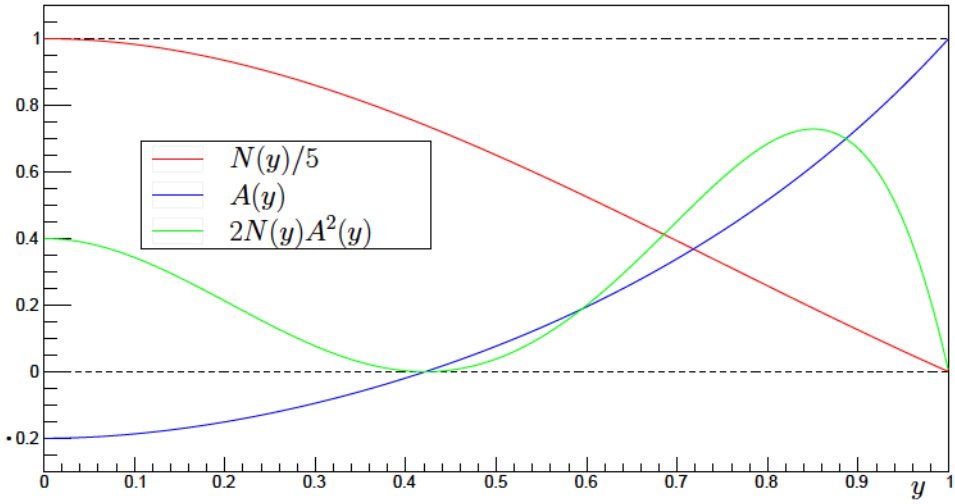

Figure 1.3.5: In the lab frame, the functions $N(y)$ (rescaled by 1/5 so that it fits the range $[0,1]$ on y-axis) and $A(y)$ from Equation (1.3.16) are plotted, as well as $N(y)A^2(y)$, rescaled by a factor of 2 for better visibility. The importance of the latter function will be clarified at the end of this Section.

Equation (1.3.15) can be obtained from the following steps. In the muon rest frame, we can define:

- $\hat{k}$ the direction of the muon beam;
- $\hat{p}_e = \cos(\theta_e)\hat{k} + \sin(\theta_e)\cos(\phi_e)\hat{\imath} + \sin(\theta_e)\sin(\phi_e)\hat{\jmath}$ the direction of the emitted positron;
- $\hat{s} = \cos(\alpha)\hat{k} + \sin(\alpha)\hat{\imath}$ the direction of the muon polarization, which rotates with frequency ω_a around the y-axis;
- $\xi = \cos(\theta_e)$.

Then, $\cos(\theta^*) = \hat{p}_e \cdot \hat{s} = \cos(\theta_e)\cos(\alpha) + \sin(\theta_e)\cos(\phi_e)\sin(\alpha)$ is the angle that appears in Equation (1.3.13), which can therefore be integrated over ϕ from 0 to 2π, yielding:

$$\frac{d^2\Gamma_{(\mu\to e\nu\nu)}}{dy^* d\xi} \propto n^*(y^*)[1 + a^*(y^*)\cos(\alpha)\xi] \tag{1.3.17}$$

Again, neglecting the positron mass, we can say that the positron lab energy E is approximately equal to $y^*\gamma_{\text{Boost}} m_\mu(1+\xi)/2$, so the y parameter in the lab frame is $y = y^*(1+\xi)/2$. Calling $P(a,b)$ the differential decay width as function of a and b, we can use that:

$$\begin{aligned} P(y^*, y)dy^*dy &= P(y^*, \xi)dy^*d\xi \\ \xi = \cos(\theta_e) = \frac{2y}{y^*} - 1 &\Rightarrow \frac{d\xi}{dy} = \frac{2}{y^*} \\ P(y^*, y) &= P(y^*, \xi)\frac{d\xi}{dy} = P(y^*, \xi)\frac{2}{y^*} \end{aligned} \tag{1.3.18}$$

Since $\xi = \cos(\theta_e) = \frac{2y}{y^*} - 1$, we have that $\frac{2y}{y^*} - 1 \leq 1$, therefore $y^* \geq y$, and of course, by definition, $y^* \leq 1$. The right-hand side of Equation (1.3.17) is our $P(y^*, \xi)$, so we can obtain $P(y^*, y)$ using the last equation in (1.3.18), and integrate it over y^* that goes from y to 1, obtaining Equation (1.3.15). It is essential to notice that the energy spectrum depends on α, which is not constant over time, because it oscillates from 0 to 2π with frequency ω_a: thanks to the V-A nature of weak decay, there is a strong correlation between the anomalous precession frequency and the positron energies, that allows us to accurately measure ω_a from fits of the so-called "wiggle plots".

If we are counting all positrons above a certain energy threshold, Equation (1.3.15) can be integrated over y going from y_{th} to 1: this gives us the probability that a positron is emitted with an energy of, at least, $y_{th}\gamma_{\text{Boost}} m_\mu$ in the lab frame. The integration yields:

$$N(y_{th}) = N_0(y_{th})[1 + A_0(y_{th})\cos(\alpha)] \tag{1.3.19}$$

where Equation (1.3.20) defines two new coefficients, whose behaviour is shown in Figure 1.3.6:

$$N_0(y) = (y-1)^2(-y^2 + y + 3); \qquad A_0(y) = \frac{y(2y+1)}{-y^2 + y + 3} \tag{1.3.20}$$

Again, it should be stressed that α precesses with frequency ω_a, so that the Equation (1.3.19) implicitly contains a time dependency. In the storage rings, muons decay over time, with a lifetime dilated due to Lorentz boost: $\gamma_{\text{Boost}}\tau \approx 64.4\,\mu\text{s}$. So, in the lab frame, the distribution of emitted positrons will be:

$$N(t) = N_0(y_{th})e^{-t/\gamma\tau}\left[1 + A_0(y_{th})\cos(\omega_a t + \phi_a)\right] \tag{1.3.21}$$

where ϕ_a is the initial phase of the muons' spin relative to the momentum, at the time of injection. From Figure 1.3.7, it is evident that, for higher thresholds, the count rate of positrons have a larger oscillation, but the number of events per bin is lower.
In previous studies [26] on wiggle plot fitting techniques, it was shown that the sensitivity of the anomalous precession frequency to the energy threshold is given by:

$$\frac{\delta\omega_a}{\omega_a} = \frac{\sqrt{2}}{\omega_a \mathcal{P}\sqrt{N_0^{TOT} A_0^2(y_{th})}} \tag{1.3.22}$$

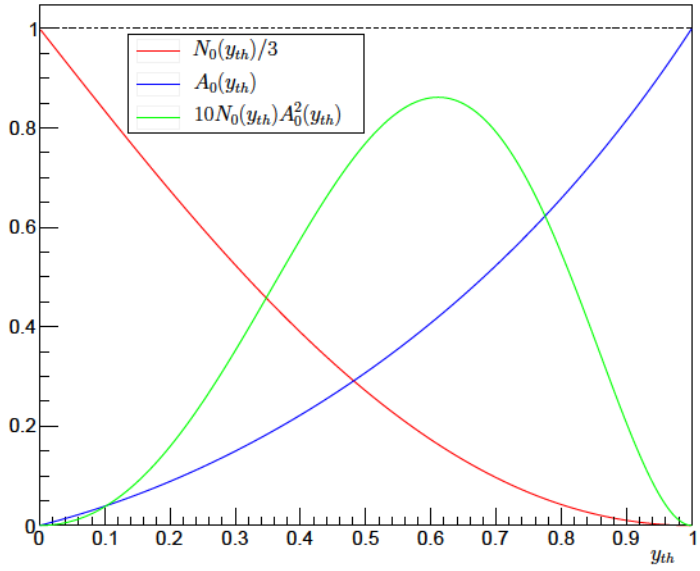

Figure 1.3.6: In the lab frame, the functions $N_0(y_{th})$ (rescaled by $1/3$ so that it fits the range $[0, 1]$ on y-axis) and $A_0(y_{th})$ from Equation (1.3.20) are plotted, as well as $N_0(y_{th})A_0^2(y_{th})$, rescaled by a factor 10 for better visibility.

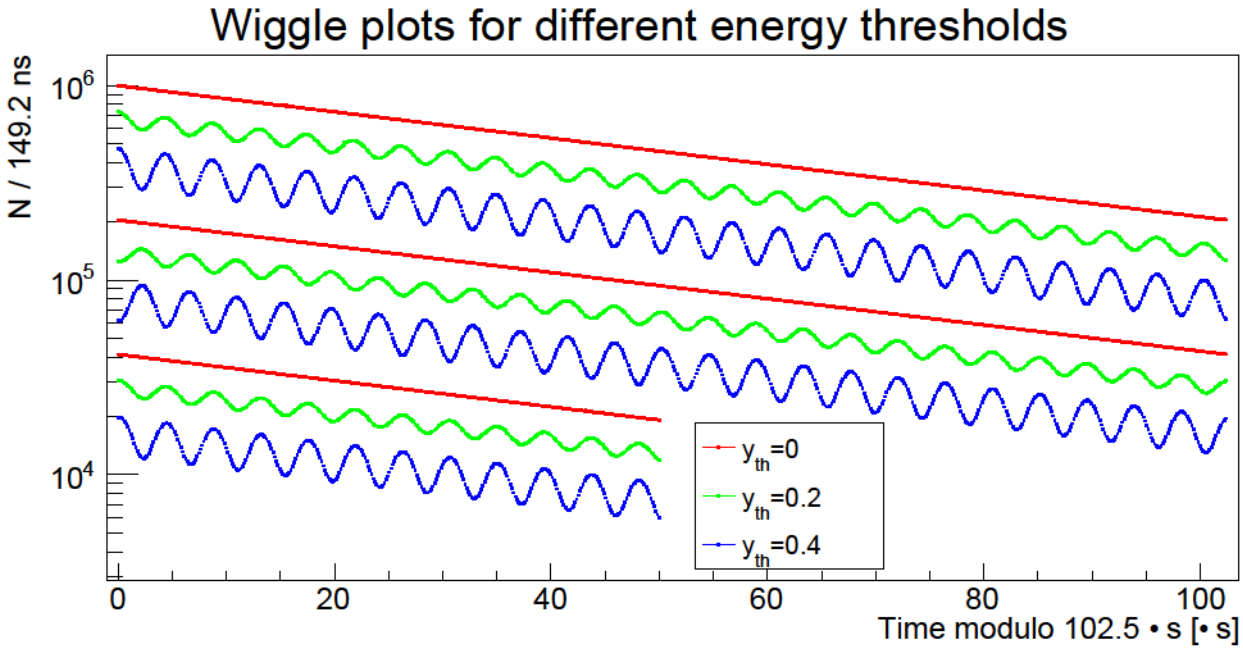

Figure 1.3.7: Number of positrons produced in the storage ring, as a function of time, for three different values of the energy threshold, according to Equation (1.3.21).

where $\mathcal{P}$ represents the average polarization of the muons, and N_0^{TOT} the total number of positrons with y above y_{th}. Since $N_0^{TOT} \propto N_0$, Equation (1.3.22) tells us that the Figure of Merit (FOM) to be maximized for better statistical results is $N_0 A_0^2$, plotted in Figure 1.3.6, where it can be seen that $y_{th} \approx 0.6$ - approximately 1.86 GeV - would be the optimal threshold. For real data, the limited detector acceptance and the energy resolution also play a role, moving the optimal energy threshold to a slightly lower value, around 1.7 GeV.

Chapter 2

Theoretical calculation of a_μ

Since Schwinger computed the first, leading order, 1-loop QED radiative correction to the magnetic anomaly in 1948, a large community of physicist has been continuously working with the aim of reaching a new level of precision on the theoretical prediction of a_μ. Recently, after the Brookhaven results exhibited tensions with the theoretical prediction, and especially in view of the results at Fermilab, the efforts on the theory side were particularly revived. A few years ago, the "Muon $g-2$ Theory Initiative" was formed, with the goal of bringing together experimental and theoretical physicists, in order to produce a single consensus on the theoretical value of a_μ.
This Chapter will summarize the latest results from the Standard Model (SM), focusing in particular on the current issues in the calculation of the hadronic contributions. Some example of models for new physics Beyond the Standard Model (BSM) will be mentioned, which could affect the muon's g-factor.

2.1 Summary of the main SM contributions

The value of the muon g-factor different from 2 is theoretically explained by Feynman diagrams where virtual particles are exchanged. These diagrams can come from three different sectors of the SM: Quantum Electrodynamics (QED), Electroweak Theory (EW) and Quantum Chromodynamics (QCD). Therefore, a_μ^{SM} is written as a sum of different terms [5]:

$$a_\mu^{SM} = a_\mu^{QED} + a_\mu^{EW} + \underbrace{a_\mu^{HVP-LO} + a_\mu^{HVP-HO} + a_\mu^{HLBL}}_{\text{QCD}} \tag{2.1.1}$$

where QCD carries the highest uncertainty and is divided in three parts:

- HVP-LO is the leading order of the hadronic vacuum polarization (HVP), where a loop of quark-antiquark is inserted in the virtual photon line of Figure 1.2.1(c).
- HVP-HO embraces all the higher order contributions to HVP (we will refer to the currently evaluated next-to-leading order and next-to-next-to-leading order with NLO and NNLO, respectively), where additional loops, either leptonic or hadronic, are inserted.
- HLBL is the hadronic light-by-light scattering, a diagram where photon propagators interact with hadrons as in Figure 2.1.2(b).

Table 2.1.1 shows a comparison between the recent measurements of a_μ and the recommendation from White Paper 2020 (WP2020 [5]) for the SM prediction.

SM terms [5]	Magnetic anomaly $a_\mu^{SM} \times 10^{11}$
QED	116584718.931 ± 0.104
EW	153.6 ± 1.0
HVP-LO	6931 ± 40
HVP-NLO	−98.3 ± 0.7
HVP-NNLO	12.4 ± 0.1
HLBL	92 ± 18
Total a_μ^{SM}	116591810 ± 43 (WP2020 [5])
Lattice HVP-LO from BMWc [6]	7075 ± 55

Experimental values	Magnetic anomaly $a_\mu^{Experimental} \times 10^{11}$
a_μ^{E821} (2006) [2]	116592089 ± 63
a_μ^{E989} (Run-1, 2021) [1]	116592040 ± 54
a_μ^{E989} (Run-2/3, 2023) [3]	116592057 ± 25
a_μ^{exp} average	116592059 ± 22

Table 2.1.1: Values of the SM terms that define the a_μ^{SM} prediction (White Paper 2020 recommendation [5]) compared with the experimental results in E821 at BNL [2] and E989 at FNAL [1, 3], and with the experimental average. The lattice calculation from the BMW collaboration [6] is also reported (see Section 2.1.3).

2.1.1 QED term

The QED correction to the magnetic anomaly is the largest one, but also the most precise. QED contributions come from diagrams where only leptons (e, μ, τ) and photons (γ) are present. It is possible to write the QED term as a sum of terms which only depend on the ratio between the lepton masses [27]:

$$a_\mu^{QED} = A_1 + A_2(m_\mu/m_e) + A_2(m_\mu/m_\tau) + A_3(m_\mu/m_e, m_\mu/m_\tau) \tag{2.1.2}$$

where A_1 is universal for all leptons, just like the Schwinger term derived in Appendix A, and contains diagrams where the closed lepton loops have the same mass as the external lepton; A_2 contains loops where the internal leptons have a different mass, so it starts at 2-loops order; A_3 accounts for diagrams in which all three leptons are present. Since QED is a renormalizable theory, each of the A_i terms can be expanded in series of powers of α:

$$A_i = \sum_{n=1}^{+\infty} A_i^{(2n)} \left(\frac{\alpha}{\pi}\right)^n \tag{2.1.3}$$

For instance, at 1-loop order, $A_1^{(2)}$ comes from the Schwinger term and is equal to 0.5, whereas $A_2^{(2)} = A_3^{(2)} = 0$. At 2-loop order, there are 9 diagrams in total: 7 diagrams contribute to $A_1^{(4)}$, 1 contributes to $A_2^{(4)}(m_\mu/m_e)$ and the last one to $A_2^{(4)}(m_\mu/m_\tau)$; $A_3^{(2)}$ is still equal to 0. At 3-loop order, the analytical computation was carried out by Remiddi and collaborators and completed in 1996 [28]: it was the last one to be computed analytically, with 72 diagrams contributing to $A_1^{(6)}$ and $A_2^{(6)}$ divided into two sets - a "heavy" one, due to e and τ vacuum polarization loops, and a "light" one, due to light-by-light scattering with e and τ loops. From the fourth order on, only a few diagrams have been computed analytically so far; numerical calculations were carried out by Kinoshita and collaborators [29]. In the final value of the QED prediction based on SM (Table 2.1.1), the uncertainty of ~ 1.2 parts per billion (ppb) comes from the lepton mass ratios, from the 4-loop and 5-loop contributions, and from a precision of ~ 0.15 ppb on

the fine structure constant α [19]. In the last 5 years, two independent determinations of α were performed, with rubidium (Rb) [30] and cesium Cs [31] atomic interferometry. These measurements disagree with each other by $5.5\,\sigma$: when this discrepancy will be resolved, the new measurement of g_e with an uncertainty of 0.13 ppt will be available for precise tests for BSM physics. The values of a_e^{SM} based on Rb and Cs determinations of α imply, respectively, a positive $(+2\,\sigma)$ and negative $(-4\,\sigma)$ tension with a_e^{exp}. These results have invoked much theoretical work into explaining the deviations in the electron sector. As stated in Ref. [32], 'a negative Δa_e could require BSM models that break lepton flavor universality'.

2.1.2 EW term

The electroweak contribution comes from the coupling with gauge bosons, Z, $W^\pm$ and H, and it is mass-suppressed by a factor $\sim m_\mu^2/M_W^2$ with respect to the QED contribution. Figure 2.1.1 shows the three diagrams that affect a_μ at 1-loop order.

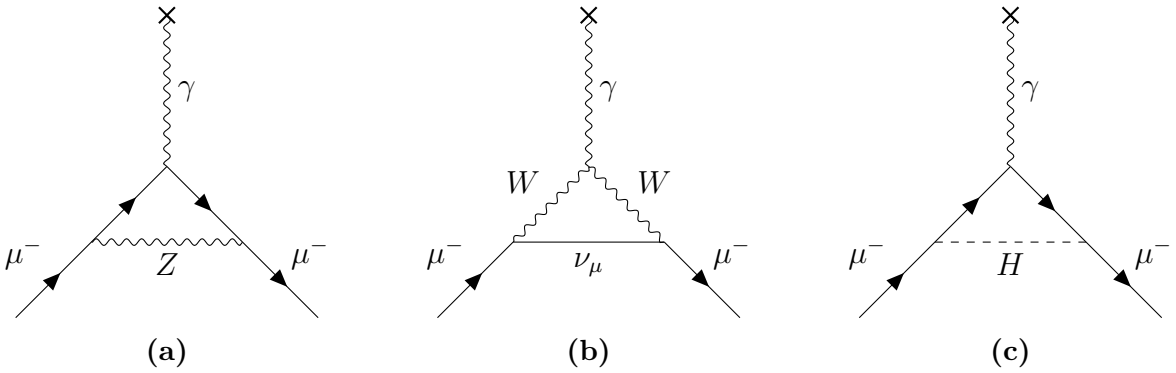

Figure 2.1.1: 1-loop EW contributions to a_μ.

In the SM:

- The Fermi Constant is $G_F = 1.1663788(6) \cdot 10^{-5}\,\text{GeV}^{-2}$ in units of $(\ \ c)^3$;
- θ_W is the Weinberg angle of weak interaction mixing: $\sin^2(\theta_W) = 1 - M_W^2/M_Z^2 \simeq 0.231$;
- $M_{Z,W,H}^2 >> m_\mu^2$.

Thus, the total EW contribution at 1-loop can be written as:

$$a_\mu^{EW} = \frac{G_F m_\mu^2}{8\sqrt{2}\pi^2}\left[\frac{5}{3} + \frac{1}{3}\left(1 - 4\sin^2(\theta_W)\right)^2 + \mathcal{O}\left(\frac{m_\mu^2}{M_W^2}\right) + \mathcal{O}\left(\frac{m_\mu^2}{M_H^2}\right)\right] \tag{2.1.4}$$

whereas the single contributions from gauge bosons are:

$$a_\mu^{EW}(Z) = \frac{\sqrt{2}G_F m_\mu^2}{16\pi^2}\frac{(-1 + 4\sin^2(\theta_W))^2 - 5}{3} = (-193.89 \pm 0.02)\cdot 10^{-11} \tag{2.1.5}$$

$$a_\mu^{EW}(W) = \frac{\sqrt{2}G_F m_\mu^2}{16\pi^2}\frac{10}{3} = (+388.70 \pm 0.10)\cdot 10^{-11} \tag{2.1.6}$$

$$\begin{aligned} a_\mu^{EW}(H) = \frac{\sqrt{2}G_F m_\mu^2}{4\pi^2}\int_0^1 dy \frac{(2-y)y^2}{y^2 + (1-y)(M_H/m_\mu)^2} \simeq \\ \simeq \frac{\sqrt{2}G_F m_\mu^2}{4\pi^2}\frac{m_\mu^2}{M_H^2}\ln\left(\frac{M_H^2}{m_\mu^2}\right) \quad 5\cdot 10^{-14} \end{aligned} \tag{2.1.7}$$

More details about the EW calculation are present in the papers in Ref. [33]. The contribution of the diagram in Figure 2.1.1(c) is relatively small, due to the mass of the Higgs boson measured at LHC. The total contribution of the $(1 + 2)$ loop order was recently evaluated numerically, taking into account the Higgs mass and appropriate light quark masses [34], and is shown in Table 2.1.1. Contributions from the 3-loop leading logarithms were found to be negligible [19].

2.1.3 QCD term

The hadronic contribution to a_μ amounts to $\sim$ 60 parts per million (ppm) and carries an uncertainty of $\sim$ 0.40 ppm, which dominates the uncertainty on the theoretical prediction of the magnetic anomaly: efforts to improve the QCD prediction are therefore crucial, as the experimental precision improves. The largest hadronic term comes from the leading order hadronic vacuum polarization diagrams (HVP-LO), such as the one in Figure 2.1.2(a) where the internal photon propagator line contains a hadronic loop. The problem with this type of diagram is that the energy scale is of order of the muon mass, well below the region where QCD can be studied perturbatively, so the approach to evaluate the contribution is different from the QED and EW case. The dispersive approach and the lattice calculations will be presented in the rest of this Section. The higher order contributions HVP-NLO and HVP-NNLO, which involve the addition of further vacuum polarization loops, have similar difficulties in calculating a_μ^{HVP-LO}, but they do not affect significantly the overall error because they are suppressed by further powers of α [35] (as shown in Table 2.1.1). The second largest source of uncertainty in the hadronic sector comes from the hadronic light-by-light (HLBL) term: as shown in Figure 2.1.2(b), its amplitude is given by a four-point correlation function instead of the two-point of HVP, which makes the computation even harder. Nevertheless, requirements on the accuracy of a_μ^{HLBL} are less demanding, since this term is suppressed by an extra power of α, and its contribution has a similar size as the NLO term of HVP: a relative accuracy of $\sim$ 10% is sufficient to meet the precision goal of the E989 experiment at Fermilab [5]. Currently, the HLBL is calculated up to the next-to-leading order: the lattice and the data-driven dispersive approaches yield compatible results with uncertainties at the 20% level, so the current estimate combines them. In the upcoming years, we can expect that the efforts on both approaches will reduce uncertainties down to the 10% level.

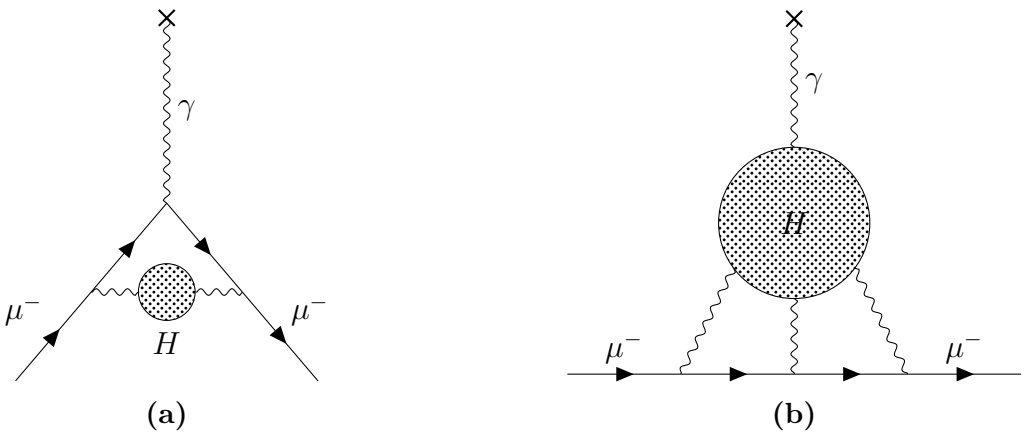

Figure 2.1.2: Examples of hadronic contributions to a_μ: diagram in figure (a) shows the leading order HVP, while the one in figure (b) shows the general case of the light-by-light scattering. The letter H denotes a generic hadronic blob.

The ongoing efforts on the theoretical prediction of the hadronic components of a_μ are currently summarized by the Muon $g - 2$ Theory Initiative at https://muon-gm2-theory.illinois.edu.

Dispersive approach calculation of a_μ^{HVP-LO}

The leading order HVP term has traditionally been obtained through a dispersion integral, whose derivation is based on the general principles of causality and unitarity, which imply respectively analyticity of quantum field theory and validity of the optical theorem [35]. The obtained dispersion integral is [36, 35]:

$$a_\mu^{HVP-LO} = \frac{\alpha}{\pi} \int_0^\infty \frac{ds}{\pi} \mathrm{Im}\Pi_{had}(s) \frac{K(s)}{s} \tag{2.1.8}$$

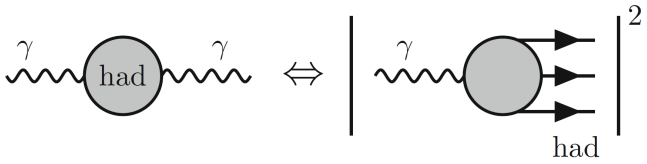

Figure 2.1.3: From Ref. [35]. Schematic representation of the optical theorem.

In this relation, $\Pi_{had}(s)$ is the hadronic part of the photon vacuum polarization as a function of the time-like squared momentum transfer $s = q^2 > 0$, while the kernel function $K(s)$ is a kinematic factor that behaves like $1/s$, ranging from ~ 0.03 when $s = 4m_\pi^2$ (threshold of $\pi^+\pi^-$ pair) to 0 when $s \to \infty$, as defined by Equation (2.1.9).

$$K(s > 4m_\mu^2) \equiv \int_0^1 dx \frac{x^2(1-x)}{x^2 + (1-x)s/m_\mu^2} \tag{2.1.9}$$

The shape of $K(s)$ for $\sqrt{s}$ below $2m_\mu$ is reported in Ref. [37], where it was found to give a negligible contribution to the integral. Taking advantage of the optical theorem, diagrammatically represented in Figure 2.1.3, the imaginary part of the hadronic vacuum polarization function is related to the annihilation cross section of e^+e^- to hadrons, or rather to the hadronic ratio $R(s)$:

$$\mathrm{Im}\Pi_{had}(s) = \frac{\sigma(e^+e^- \to \text{hadrons})}{4\pi\alpha/s} = \frac{\alpha}{3} R(s), \qquad R(s) = \frac{\sigma(e^+e^- \to \text{hadrons})}{\sigma_0(e^+e^- \to \mu^+\mu^-)} \tag{2.1.10}$$

The leading hadronic contribution to the muon anomaly is thus given by:

$$a_\mu^{HVP-LO} = \frac{\alpha^2}{3\pi^2} \int_{m_\pi^2}^\infty ds \frac{K(s)}{s} R(s) \tag{2.1.11}$$

The integral goes from the pion π^0 production threshold (the lowest hadronic state) to infinity. This method is known as the time-like dispersive approach, and relies on the cross sections measured at e^+e^- colliders to determine $R(s)$.
Figure 2.1.4(a) shows the behaviour of $R(s)$ up to $\sim 10\,\mathrm{GeV}$, the region where it is computed using experimental data. Above that energy, which corresponds to the open $b\bar{b}$ threshold, the general consensus is that we can trust perturbative QCD due to its asymptotic freedom. The shape of $R(s)$ is highly fluctuating because of hadronic resonances and flavour threshold effects. The main contribution to the final value of a_μ^{HVP-LO} comes from the energy region 2 GeV, since the hadronic ratio is weighted by the factor $K(s)/s \sim 1/s^2$ in Equation (2.1.11): here, the total hadronic cross section is obtained by summing more than 35 exclusive channels, the dominant one being the $\pi^+\pi^-$ final state. This channel accounts for approximately 75% of the whole value of a_μ^{HVP-LO}, but it also represents the largest source of uncertainty because

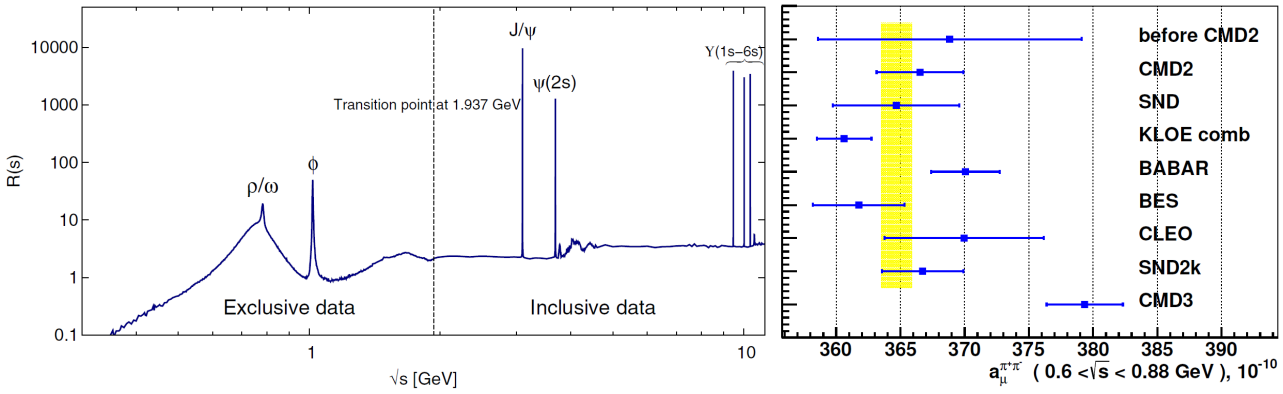

(a) From Ref. [38] **(b)** From Ref. [7]

Figure 2.1.4: (a): the $R(s)$ ratio in the range $m_\pi \leq \sqrt{s} \leq 11.1985\,\text{GeV}$, with labels on the prominent resonances. (b): the $\pi^+\pi^-(\gamma)$ contribution in the range $0.6\,\text{GeV} \leq \sqrt{s} \leq 0.88\,\text{GeV}$.

of a long standing discrepancy between KLOE and BaBar measurements (see Figure 2.1.4(b)), which must be properly dealt with when combining data [5].
The current reference value for a_μ^{HVP-LO} [5] is based on merging the evaluations carried out by DHMZ and KNT groups: the former implements an approach based on an accurate data interpolation with polynomial functions for each experiment, which are then combined together through a weighted average [39]; the latter combines different datasets for a given channel using a clustering procedure, to determine the optimal bin width for each channel starting from datasets with different binnings [40]. Both groups include systematic uncertainties to properly treat the tension between KLOE and BaBar results from $\pi^+\pi^-$ final state (Figure 2.1.4(b)). The merging procedure described in the White Paper of the Muon $g-2$ Theory Initiative [5] was aimed at determining a conservative estimate of a_μ^{HVP-LO} from the dispersive approach: this was motivated by the tension in the e^+e^- experimental data pointed out before, as well as by different approaches to combine the same input data by different groups. As it can be seen in Figure 2.1.4(b), a recent measurement of the $e^+e^- \to \pi^+\pi^-$ cross section with the CMD-3 detector was significantly larger than the value obtained from previous measurements [7], hence the theoretical prediction that uses it as an input to HVP is in closer agreement with the experimental measurement of a_μ.

Lattice QCD calculation of a_μ^{HVP-LO}

A different approach can be used to determine the HVP-LO contribution to a_μ instead of the dispersive relation in Equation (2.1.11), which is lattice QCD, based on computing observables over a discrete number of points in space-time, and extrapolating the continuum limit when the spacing becomes infinitesimal. The following description of this method is taken from Ref. [41] and follows Ref. [5], which reviews it in detail.

Lattice QCD evaluations of a_μ^{HVP-LO} are based on the determination of the two-point correlator of the electromagnetic current $j_\mu(x)$:

$$C_{\mu\nu}(x) = \langle\, j_\mu(x)\; j_\nu(0)\,\rangle, \qquad j_\mu(x) = \sum_{f=1}^{N_f} Q_f \bar{\psi}_f(x)\gamma_\mu\psi_f(x) \tag{2.1.12}$$

where the subscript f labels the quark flavours, N_f and Q_f being the number of flavours and the flavour electric charge in units of the electron charge respectively.

Traditionally, the vacuum polarization tensor is introduced by means of a Fourier transform on the two-point correlator:

$$\Pi_{\mu\nu}(Q) = \int d^4x e^{iQ\cdot x} C_{\mu\nu}(x) \tag{2.1.13}$$

where Q is the four-momentum transfer. This allows to compute a_μ^{HVP-LO} through an integration over Q^2 [42, 43]:

$$a_\mu^{HVP-LO} = \left(\frac{\alpha}{\pi}\right)^2 \int_0^\infty dQ^2 f(Q^2)\hat{\Pi}(Q^2) \tag{2.1.14}$$

where $\hat{\Pi}(Q^2) \equiv 4\pi^2[\Pi(0) - \Pi(Q^2)]$ and

$$f(Q^2) = \frac{m_\mu^2 Q^2 Z^3(1 - Q^2 Z)}{1 + m_\mu^2 Q^2 Z^2}, \qquad Z = -\frac{Q^2 - \sqrt{Q^4 + 4m_\mu^2 Q^2}}{2m_\mu^2 Q^2} \tag{2.1.15}$$

Latest lattice evaluations are based on the so-called time-momentum representation [44], which modifies Equation (2.1.14) by introducing an alternative expression of the vacuum polarization:

$$\hat{\Pi}(Q^2) = 4\pi^2 \int_0^\infty dx_0 C(x_0) \left[x_0^2 - \frac{4}{Q^2}\sin^2\left(\frac{Qx_0}{2}\right)\right] \tag{2.1.16}$$

Here, the integration on the spatial indices is already performed, hence the correlator only depends on the Euclidean time x_0:

$$C(x_0) = -\frac{1}{3}\sum_{k=1}^{3} \int d^3x C_{kk}(x) \tag{2.1.17}$$

This leads to a new formulation of a_μ^{HVP-LO}:

$$a_\mu^{HVP-LO} = \left(\frac{\alpha}{\pi}\right)^2 \int_0^\infty dx_0 C(x_0)\tilde{f}(x_0) \tag{2.1.18}$$

where the new kernel function $\tilde{f}(x_0)$ is the expression in Equation (2.1.19), and can be both evaluated numerically or expressed in terms of a modified Bessel function of the second kind and Meijer's G function [45].

$$\tilde{f}(x_0) = 8\pi^2 \int_0^\infty \frac{d\omega}{\omega} f(\omega^2) \left[\omega^2 x_0^2 - 4\sin^2\left(\frac{\omega x_0}{2}\right)\right] \tag{2.1.19}$$

Lattice calculations are performed by replacing integrals over the full phase space with sums over finite lattice volumes. Extrapolation to continuum, namely to lattice spacings $a \to 0$, and to infinite volumes are therefore required to obtain the desired quantities. Systematic errors due to the extrapolation are a major source of uncertainty, and must be managed carefully.

White Paper 2020 (WP2020) prediction

Before the Fermilab Run-1 result, the Theory Initiative recommended a value for the theoretical prediction for a_μ in the 2020 White Paper [5]. Figure 2.1.5 shows a recent comparison of the theoretical evaluations of a_μ^{HVP-LO} obtained with dispersive (grey band) and lattice (blue band) approaches: in both cases, all results below the horizontal dashed line were taken into account for the White Paper; the black square shows the recommended value, which is also reported in Table 2.1.1.

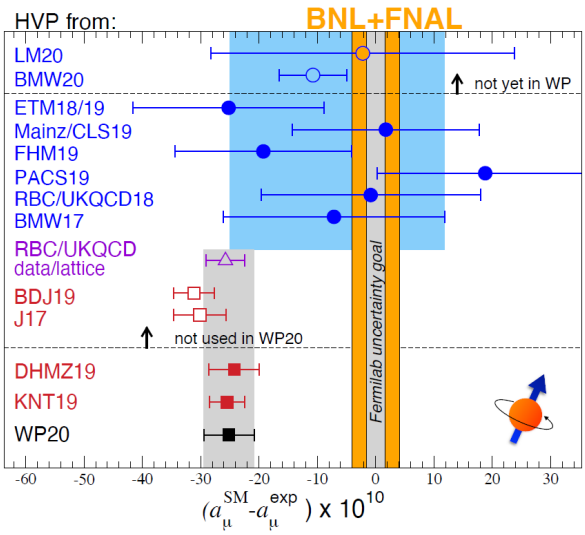

Figure 2.1.5: From Ref. [47]. Comparison of theoretical predictions of a_μ with the experimental value of 2022 (combination of BNL and first results from FNAL) [1]. Each data point represents a different evaluation of leading order HVP, to which the remaining SM contributions, as given in Ref. [5], have been added. Red squares show data-driven results; filled blue circles indicate lattice QCD calculations that were taken into account in the WP20 lattice average, while the open ones show results published after the deadline for inclusion in that average; the purple triangle gives a hybrid of the two approaches. The SM prediction of Ref. [5] is shown as the black square and grey band.

Updates to HVP-LO since the WP2020 recommendation

In 2021, using the lattice QCD approach, the BMW collaboration presented the first evaluation of a_μ^{HVP-LO} with a sub-percent uncertainty, which was in a $2.2\,\sigma$ tension with the prediction from the dispersive approach [6].
In 2018, the RBC/UKQCD collaboration had proposed [46] to separate the integral in Equation (2.1.18) into three different time regions, in order to facilitate the comparison of new results between different lattice groups:

$$
\begin{aligned}
a_\mu^{HVP-LO,\ SD} &= \left(\frac{\alpha}{\pi}\right)^2 \int_0^\infty dx_0 C(x_0)\tilde{f}(x_0)\left[1-\Theta(x_0,t_0,\Delta)\right] \\
a_\mu^{HVP-LO,\ W} &= \left(\frac{\alpha}{\pi}\right)^2 \int_0^\infty dx_0 C(x_0)\tilde{f}(x_0)\left[\Theta(x_0,t_0,\Delta)-\Theta(x_0,t_1,\Delta)\right] \\
a_\mu^{HVP-LO,\ LD} &= \left(\frac{\alpha}{\pi}\right)^2 \int_0^\infty dx_0 C(x_0)\tilde{f}(x_0)\Theta(x_0,t_1,\Delta) \\
\Theta(t,t',\Delta) &= \frac{1+\tanh[(t-t')/\Delta]}{2}
\end{aligned}
\tag{2.1.20}
$$

The function $\Theta(t,t',\Delta)$ allows to define smooth windows in the Euclidean time with width Δ, while the parameters t_0 and t_1 are chosen to separate short and long distance effects. A convenient choice of these parameters is $\Delta = 0.15\,\text{fm}$, $t_0 = 0.4\,\text{fm}$, and $t_1 = 1\,\text{fm}$ [5]. Corrections due to systematic effects and extrapolation to the continuum and infinite-volume can be applied separately to each window. The windows are designed such that the intermediate one $a_\mu^{HVP-LO,\ W}$ is less sensitive to discretization errors than the short distance one $a_\mu^{HVP-LO,\ SD}$, as well as less sensitive to statistical fluctuations and other long distance effects than $a_\mu^{HVP-LO,\ LD}$. It follows that $a_\mu^{HVP-LO,\ W}$ can be computed with good precision and reduced systematics, thus being

an effective intermediate quantity for cross-checks between different calculations. Furthermore, the two-point correlator can be expressed as a function of the hadronic ratio $R(s)$, enabling a direct comparison between lattice QCD and dispersive method [46]. The intermediate window corresponds to energies $\sqrt{s}$ $1 \div 2\,\text{GeV}$ in the time-like approach, as shown in Figure 2.1.6(a).

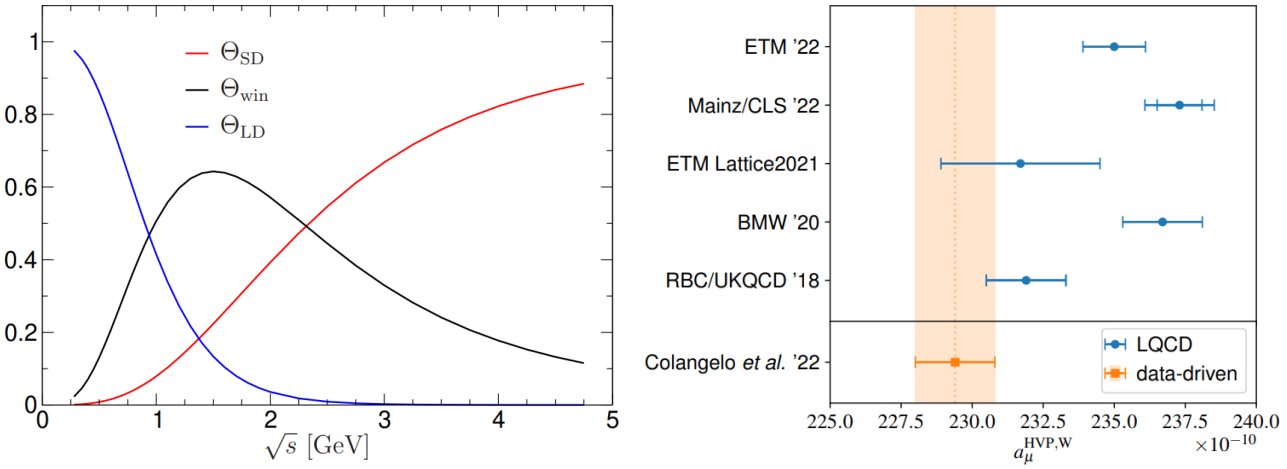

(a) From Ref. [48] **(b)** From Ref. [49]

Figure 2.1.6: (a): weight functions for the three windows, defined by Equation (2.1.20), in the $\sqrt{s}$ space. (b): recent comparison of $a_\mu^{HVP-LO,\,W}$ results from lattice QCD calculations, and estimate based on the dispersive approach in the orange band.

Figure 2.1.6(b) shows recent evaluations of the intermediate window along with a calculation based on the dispersive approach. Latest lattice results reached a precision comparable with BMW evaluation, and are in good agreement with each other.

As already mentioned, in early 2023 the CMD-3 collaboration released results on the $e^+e^- \to \pi^+\pi^-$ cross section that disagree with all previous measurements used in the 2020 White Paper, and that, when taken individually as an input to the HVP, are less in tension with the experimental value [7]. Many efforts are ongoing in order to clarify the origin of all the discrepancies in the theoretical calculation.

This was the situation in the a_μ theoretical scenario at the time of the Run-2/3 publication in August 2023. In this context, the future MUonE experiment, described in Section 2.3.1, will provide a third independent method to evaluate a_μ^{HVP-LO}, and could contribute in solving the tensions and consolidate the theoretical prediction of a_μ^{HVP-LO}.

2.2 Examples of possible Beyond the SM contributions

As it can be seen from Table 2.1.1, the difference between the latest experimental value for a_μ [3] and the recommendation for the theoretical prediction from the Theory Initiative (WP2020 [5]) is equal to:

$$a_\mu^{exp} - a_\mu^{SM} = (249 \pm 48) \cdot 10^{-11} \tag{2.2.1}$$

corresponding to a $\sim 5.1\,\sigma$ discrepancy; since the previous experiment at BNL, the deviation between experiment and theory has been studied extensively in the literature and many models Beyond the Standard Model (BSM) that can contribute to a_μ have been considered. The

constant search for BSM is motivated by the failure of the SM to explain some fundamental facts: e.g., the asymmetry between matter and antimatter in the Universe, the presence of dark matter and dark energy, or the non-zero mass of neutrinos; it also cannot provide a complete theory that includes the force of gravity. Measuring the muon magnetic anomaly at high precision is a good way to probe for new physics, and at the same time it can strengthen constraints on otherwise plausible SM extensions: the a_μ observable is CP-conserving, flavour conserving, loop induced and chirality flipping [50], and these properties can highly constrain BSM models, together with precision observables and results from collider and dark matter searches. The current discrepancy between theory and experiment could support several scenarios, for instance: muon compositeness, supersymmetric particles, coupling to axion-like particles, or rare decays that do not conserve the lepton family number, such as $\mu^- \to \gamma\, e^-$. A thorough compilation of models is found in Ref. [50]: they are grouped into minimal 1-, 2- and 3-field extensions of the SM, and in the Minimal Supersymmetric Standard Model. The latter is a well-motivated and promising extension of the SM, which could explain EW naturalness and dark matter as the lighest supersymmetric particle, but which is also highly constrained by LHC and dark matter searches. Possible 1-field extensions are dark photons and dark Z, or two-Higgs doublet models, or scalar leptoquarks. Leptoquarks would be colour-triplet bosons that carry both baryon and lepton numbers: their capability to address several anomalies simultaneously make them good candidates for new physics BSM. For instance, the CDF collaboration has recently published the world's most precise direct measurement of the W mass, which presents a $\sim 7\,\sigma$ tension with the SM prediction [51]. One could explore the possibility that the W mass and the muon $g-2$ anomalies actually stem from uncertainties in the common hadronic contributions. By performing EW fits in which hadronic contributions are allowed to float, Ref. [52] shows that adjustments that alleviate the CDF tension would worsen the $g-2$ discrepancy, and vice versa. Instead, a leptoquark extension of the SM could explain both at the same time.
Although the main goal of the E989 experiment at Fermilab is to measure the magnetic anomaly of the muon at a precision of 0.14 ppm, there are a few BSM possibilities that we are pursuing in our data: CPT- and Lorentz-Violation [53], direct dark matter search [54], and muon Electric Dipole Moment (which will be explained in more detail in Section 2.2.2). For these searches, we expect to have results in the near future.

2.2.1 Dark photon

A possible BSM scenario involves a hypothetical particle called "dark photon", which would be a relatively light vector boson from an extra $U(1)$ gauge group in the dark matter sector. The assumptions are that it interacts with ordinary matter through a mixing with the ordinary photon, where the strength of the interaction is governed by a kinetic mixing parameter ε. The contribution to the muon magnetic anomaly would be $\Delta a_\mu^{A'}$ [55]:

$$\Delta a_\mu^{A'} = \frac{\alpha}{2\pi}\varepsilon^2 F(m_{A'}/m_\mu), \qquad F(x) = \int_0^1 dz \frac{2z(1-z)^2}{(1-z)^2 + x^2 z} \tag{2.2.2}$$

$m_{A'}$ being the dark photon mass and $F(x)$ a function that monotonously decreases from 1, when $m_{A'} << m_\mu$, to 0, when $m_{A'} \to +\infty$, with a $2m_\mu^2/3m_{A'}^2$ dependence. Searches for a dark photon were originally motivated by cosmology, and recently the Atomki pair spectrometer has observed an anomaly in $^8\mathrm{Be}^*$ decay [56] which could be explained by the presence of dark photons of mass $17\,\mathrm{MeV}/c^2$ [57].
However, many experimental results have excluded the ε and $m_{A'}$ parameters that can explain the muon $g-2$ discrepancy, in the assumption that the dark photon exhibits exclusively visible or invisible decays [58, 59]. Figure 2.2.1 shows the exclusion plots with the dark photon mass on the x-axis and the kinetic mixing parameter on the y-axis, from different experiments or

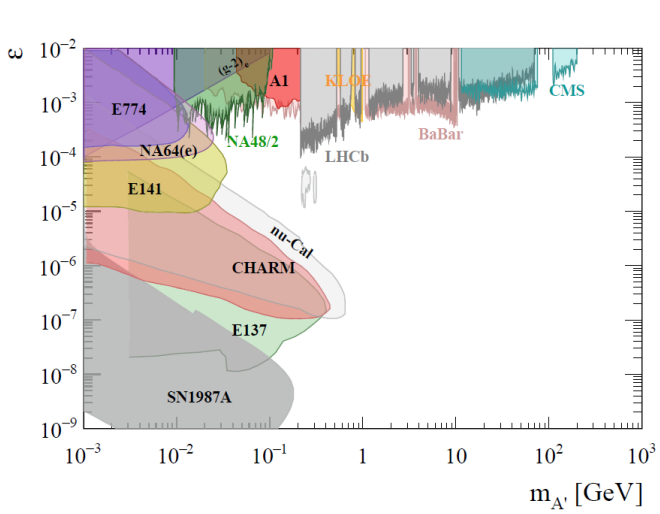

(a) Limits reported in Ref. [58] for dark photon decays to visible final states, from collider and beam-dump experiments, energy losses in supernovae and electron $g-2$.

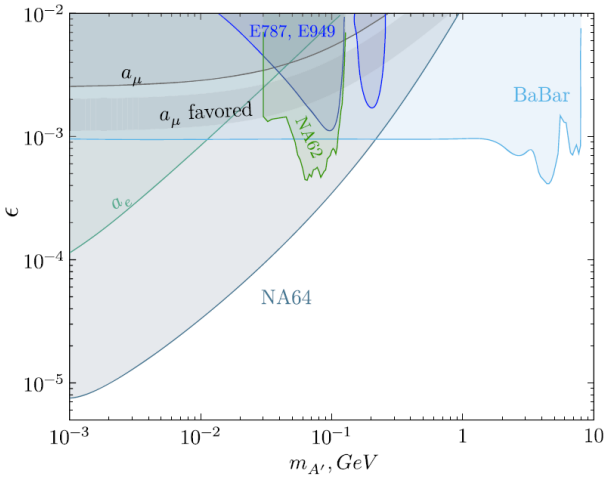

(b) Indirect dark photon searches: NA64 90% C.L. exclusion region, constraints from the E787 and E949, BaBar and NA62 experiments, and favored area for a_μ (from Ref. [59]).

Figure 2.2.1: Existing limits on dark photon searches in the $(m_{A'}, \varepsilon)$ plane.

from indirect limits such as the electron $g-2$. The experimental results have excluded the possibility that the dark photon could explain the discrepancy in the a_μ anomaly, assuming its decays are exclusively visible (SM leptons) or invisible (e.g. dark matter). Recently, the proposal for dark photon as a solution has been revisited, in the hypothesis that its decays are semivisible [60]. It was shown that, in some cases, this scenario no longer excludes large kinetic mixing parameters that could explain the discrepancy in the muon anomaly, and it reopens a window in parameter space for dark photon with exciting discovery prospects.

2.2.2 Muon Electric Dipole Moment (EDM)

For fundamental, point-like particles, an electric dipole moment d has never been measured: the current experimental limit for muons is $d_\mu \quad 1.8 \cdot 10^{-19}\,\mathrm{e\,cm}$ with 95% C.L. from the analysis at the BNL $g-2$ experiment [61]. The SM predicts values for EDMs that are far below foreseeable experimental sensitivities. A non-zero EDM for a particle in a non-degenerate state would violate both parity (P) and time reversal (T) symmetries; by invoking the CPT-theorem, T violation implies CP violation, which has never been observed in the leptonic sector of the SM but only in the hadronic sector related to the complex phase of the CKM mixing matrix. If a small d_μ were present, the anomalous spin precession frequency of muons in a magnetic field would be modified, and the variation would be equal to [62]:

$$\Delta\vec{\omega}_a = -2d_\mu \frac{c}{}\vec{\beta} \wedge \vec{B} - 2d_\mu \frac{\vec{E}}{} \tag{2.2.3}$$

which in general has a different direction than $\vec{\omega}_a$ in Equation (1.3.9), so it also tilts the spin precession plane. Typically, the E-field effect is negligible compared to the B-field, so only the radial component of the muon's spin precesses due to EDM. The EDM term of the ω_a precession will thus be perpendicular to the a_μ term, and, since we measure $|\vec{\omega}_a|$, Equation (1.3.7) will become:

$$\omega_a = B\sqrt{\left(\frac{e}{m}a_\mu\right)^2 + \left(2\frac{c}{}d_\mu\right)^2} \tag{2.2.4}$$

If the discrepancy in a_μ could be explained by an increase in ω_a due to the muon electric dipole moment, this would require (using the Run-2/3 result for a_μ and for the discrepancy with respect to the White Paper prediction) a value of $d_\mu \sim 2.3 \cdot 10^{-19}$ e cm, which is already excluded by the BNL upper bound. In Ref. [63] it is shown how the lepton family violation process $\mu^- \to e^-\gamma$ could explain both the discrepancy on a_μ and the muon EDM, related respectively to the real and imaginary parts of an effective Lagrangian coupling. A model-independent upper bound on the muon's electric dipole moment is $d_\mu \quad 3 \cdot 10^{-22}$ e cm, which is still below the current bound from the BNL experiment.

The Muon $g-2$ experiments E989 at FNAL and E821 at BNL are not the ideal ones to probe for muon EDM, since the effect of the B-field dominates on $\vec{\omega}_a$ and reduces the sensitivity on d_μ. A non-zero EDM causes a tilt in the precession plane (Equation (2.2.3)) and therefore an oscillation in the vertical angle of decay positrons, which is measured at Fermilab by tracker detectors. The first result based on the dataset collected in 2018 is expected to be published soon. With the full statistics collected by the E989 experiment, the goal sensitivity for muon EDM will be 10^{-21} e cm, two order of magnitude lower than in BNL [64].

A proposal was made for an experiment [65] that uses the Muon $g-2$ superconducting ring, where the effect of the magnetic anomaly on spin precession is removed, therefore maximizing the sensitivity on EDM up to $\sim 10^{-24}$ e cm. This is the so-called "frozen-spin" technique. Two other experiments, under construction, will aim to measure the muon EDM with improved sensitivities. The first one is the J-PARC muon $g-2$/EDM experiment at KEK, Japan (see Section 3.5). It will use a 300 MeV/c low-emittance muon beam, prepared by reaccelerating thermal-energy muons created from laser-resonant ionization of muonium atoms, instead of the 3 GeV/c muon beam of the E989 experiment: this will allow for the use of a compact magnetic storage ring with very weak magnetic focusing. The experiment at J-PARC aims to measure the muon magnetic anomaly with a statistical uncertainty of 450 ppb (and negligible systematics), and at the same time the muon EDM with a sensitivity of $\sim 1.5 \cdot 10^{-21}$ e cm [66]. The second experiment is in construction at PSI and aims to measure the electric dipole moment of the muon based on the frozen-spin technique. Muons with a momentum of 125 MeV/c will pass through a large magnetic field of 3 T and experience, in their rest frame, the high electric field of $E = 1$GV/m. With the current muon fluxes at the μE1 beamline, the search for muon EDM will have a sensitivity $\quad 6 \cdot 10^{-23}$ e cm. In the future, thanks to improvements of the PSI beamline, a cold muon source, and a reacceleration scheme, the muon beam will have an even larger intensity allowing for a greater sensitivity of the muon EDM search. More details about the experimental procedure and future plans are reported in the letter of intent in Ref. [67].

2.3 Prospects for the theoretical prediction

The current status of the theoretical prediction of a_μ and the future efforts on understanding both the "old" $g-2$ puzzle (the discrepancy between the White Paper prediction and the experimental measurement) and the "new" $g-2$ puzzle [68] (which includes the discrepancy between most data-driven evaluations of and lattice calculations) are summarized in https://muon-gm2-theory.illinois.edu. New analyses of the hadronic cross section of e^+e^- are ongoing for several experiments: BaBar, SND, BESIII, KLOE and Belle II. There is an ongoing effort in the lattice community to consolidate the HVP prediction with a precision comparable with the one from BMW and from the data-driven approach. Radiative corrections and Monte Carlo generators are being scrutinized, in particular from the dominant channel $e^+e^- \to \pi^+\pi^-(\gamma)$. All this effort should help to clarify the situation in the next years.

2.3.1 The MUonE experiment

The MUonE experiment at CERN proposes a novel approach to measure a_μ^{HVP-LO}, competitive and independent of the existing ones [69]. It will be based on the high-precision measurement of the running of the electromagnetic coupling constant in the space-like region, via $\mu - e$ elastic scattering. The measurement will be performed by scattering a 160 GeV positively charged muon beam, currently available at CERN M2 beamline, on the atomic electrons of a low-Z fixed target such as beryllium or carbon.
The new MUonE method is based on the direct measurement of the hadronic contribution to the running of the electromagnetic coupling constant ($\Delta\alpha_{\text{had}}$) in the space-like region [70]. The following relation will be used to extract a_μ^{HVP-LO} from the running $\Delta\alpha_{\text{had}}$:

$$a_\mu^{HVP-LO} = \frac{\alpha}{\pi}\int_0^1 (1-x)\Delta\alpha_{\text{had}}\left[t(x)\right]dx, \qquad t(x) \equiv \frac{x^2 m_\mu^2}{x-1} < 0 \tag{2.3.1}$$

where $t(x)$ is the space-like squared four-momentum transfer [42]. The experimental apparatus consists of a repetition of 40 identical stations, each one composed of a 15 mm thick target, followed by a tracking system that measures the scattering angles with very high precision. A CAD drawing of a single MUonE station is shown in Figure 2.3.1: the tracking system is composed of three pairs of silicon strip sensors that measure the transverse coordinates on both the x-axis and the y-axis. The tilt and orientation of the three pairs are chosen to maximize the sensors' resolution [41, 71].

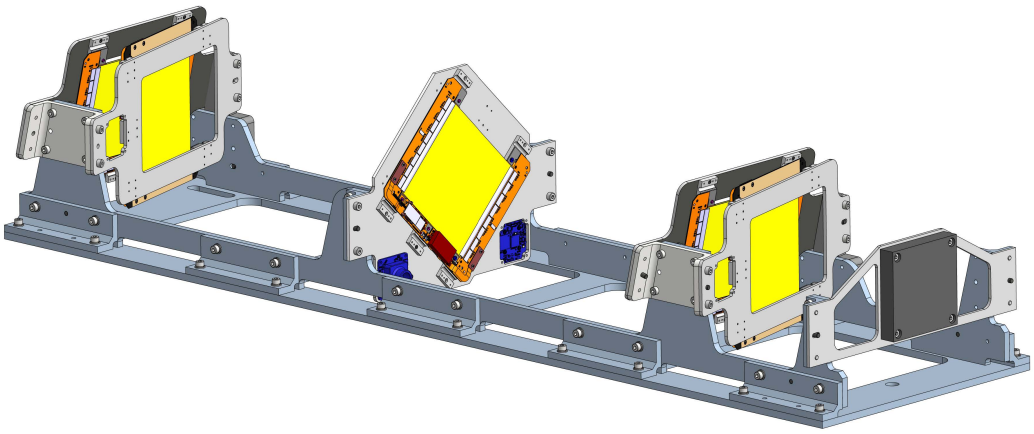

Figure 2.3.1: CAD drawing of a MUonE station, which consists of three pairs of silicon strip sensors and a fixed beryllium target [41, 71].

A test run was conducted at the CERN M2 beamline in August-September 2023, on a prototype detector composed of two tracking stations and a calorimeter. This test showed for the first time the ability of the detector to sustain 160 GeV muons with a beam intensity of $4 \cdot 10^7$ muons/s. Results of the test run will be included in an experiment proposal which will be submitted to CERN in 2024, with the prospect of performing a first measurement of a_μ^{HVP-LO} in 2025 instrumenting more tracking stations with respect to the test run. The full detector construction is expected to take place during the CERN Long Shutdown 3 of 2026-2028. The final run with the complete detector is foreseen for the following years, and it will measure a_μ^{HVP-LO} with a comparable uncertainty to the data-driven approach: $\sim 0.3\%$ of statistical uncertainty, and a systematic uncertainty of similar size [41, 71].

Chapter 3

The history of muon $g-2$ experiments

3.1 Early muon experiments

In 1956, Lee and Yang suggested several experiments that could provide evidence for parity (P) violation in weak interactions [72], as well as charge conjugation (C) and time reversal (T) violations: in the same year, Madame Wu measured P violation studying the β decay of ^{60}Co atoms [73]. As explained in Section 1.3.3, P violation allows to produce polarized muons from pion decay, and this feature was exploited since the very first experiments that measured the muon g-factor.

In 1957, Garwin, Lederman and Weinrich carried out the first experiment to measure the muon g-factor [74]: they used a positively charged pion beam of 85 MeV/c from the Nevis cyclotron (Columbia University) stopped in a carbon absorber, and a carbon target to stop the polarized muons emitted from pion decay. A scintillator telescope was used to count the positrons emitted from muon decay in the carbon target, which was immersed in a magnetic field that made the muon spin vector precess over time at the Larmor precession frequency. Increasing the intensity of the magnetic field would cause higher spin precession frequency for the muon stopped in the carbon target, before it decayed.

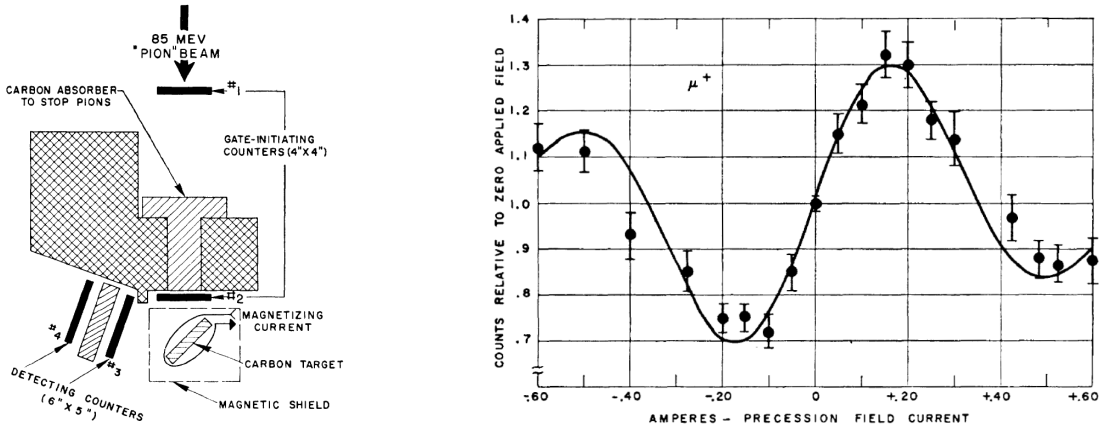

(a) **(b)**

Figure 3.1.1: From Ref. [74]. (a) Experimental setup at Nevis. (b) Number of positron counts, normalized relatively to $B = 0$, as a function of the magnetizing current.

Figure 3.1.1 shows the experimental arrangement at Nevis and the resulting plot of counts as a function of the magnetic field applied: the number of detected positrons changes according to the precession angle θ, so the points are fitted assuming a positron angular distribution of

$1 + a\cos\theta$, with detector resolutions folded in. This experiment showed the failure of P and C conservation in muon decay ($a = -0.33 \pm 0.03$, whereas parity conservation would have implied $a = 0$), and it also provided the first measurement of the muon g-factor with a 10% precision, which wasn't enough to observe the magnetic anomaly.

Over the course of the following five years, several other groups improved the experimental result on the muon g-factor performing "Larmor precession" type experiments on stopped muons, starting from Cassels and collaborators at the University of Liverpool cyclotron [75], who lowered down the experimental precision to $\sim 1\%$. The experiment consisted in stopping polarized muons in Cu or C targets, placed inside of an external magnetic field, and counting decay positrons with a technique which was the beginning of what we call, today, a "time to digital" converter [76]. In 1960, Garwin and collaborators were able to measure, for the first time, a value of a_μ different from 0 [77]: the lower limit on g_μ was set to $2(1.00122 \pm 0.00008)$, in agreement with Schwinger's prediction (see Appendix A). In 1963, the most precise experiment with Garwin's technique was carried out by Hutchinson and collaborators [78]. In this experiment, the homogeneous magnetic field in which muons were stopped was measured via nuclear magnetic resonance (NMR) in terms of the Larmor precession frequency of protons in a polarized water sample (ω_p), and Hutchinson had the foresight to express his result as the ratio λ with a 10 ppm precision:

$$\lambda = \frac{\omega_\mu}{\omega_p} = \frac{\mu_\mu}{\mu_p} = 3.18338(4) \tag{3.1.1}$$

The indirect measurement of g_μ from λ was limited by the 100 ppm precision on the muon mass from x rays experiments. Hutchinson combined the measurement of λ with the 1961's measurement of g_μ from the CERN I experiment (see Section 3.2.1) and with the most recent measurement of g_e of the time [79], in order to lower down the precision on the muon mass to 13 ppm. From Equations (1.1.1) and (1.3.3), one obtains:

$$\frac{m_\mu}{m_e} = \frac{g_\mu}{g_e}\frac{(\omega_e/\omega_p)}{(\omega_\mu/\omega_p)} \tag{3.1.2}$$

which yielded $(m_\mu/m_e) = 206.765 \pm 0.003$.

3.2 The CERN experiments

Starting from 1961, a series of experiments at CERN improved the precision on the muon magnetic anomaly a_μ with the aim to search for a breakdown of QED: in some cases some differences arose between the theoretical prediction and the experimental results, and were later explained. The underlying idea of these experiments was similar to the early ones: a beam of polarized muons was produced by pion decay and immersed in an external magnetic dipole; the time distribution of the muon decay products (electrons or positrons) were measured in order to extract a_μ. In the following Sections, we will highlight the improvements that each new experiment brought to this technique.

3.2.1 CERN I

CERN I was the first experiment carried out in the Swiss laboratory of CERN: protons were accelerated in the 600-MeV synchro-cyclotron, scattered against a beryllium target and produced pions; a positively charged muon beam was thus produced from pion decays. The main goal was to reach an experimental precision of 1% on a_μ, because, at the time, the theoretical prediction had reached the QED second order [80]:

$$a_\mu = \frac{g_\mu - 2}{2} = \frac{1}{2}\left(\frac{\alpha}{\pi}\right) + 0.75\left(\frac{\alpha}{\pi}\right)^2 + \cdots = 0.001165 \tag{3.2.1}$$

In this experiment, a forward polarized muon beam was injected into a 6 m long magnet with a magnetic field of 1.5 T: as we have shown in Section 1.3.2, in this condition the muon spin precesses $(1 + \gamma a_\mu)$ times as fast as the muon momentum, thus increasing the angle between spin and momentum linearly with time and proportionally to the magnetic anomaly and to the magnetic field.

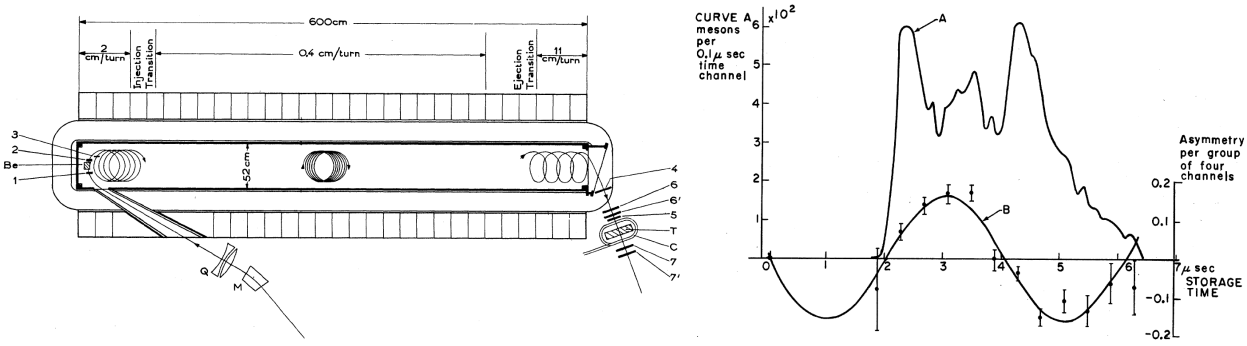

(a) **(b)**

Figure 3.2.1: From Ref. [80]. (a) Overview of the CERN I experimental setup: a μ^+ beam was injected in the dipole magnet and the coincidence of 1, 2 and 3 counters defined the injection signal; ejected muons stopped in target T, where the stop signal was a coincidence of counters 4, 5, 6, 6′ and a veto on counter 7; after the stop signal, the coincidence of $6-6'$ or $7-7'$ defined forward and backward emitted positrons. (b) Measured distributions as a function of storage time: curve A is the number of muons that stopped and decayed; curve B is the forward-backward positron asymmetry, with the best fit according to Equation (3.2.2).

Figure 3.2.1(a) shows the muon path in the magnet: the magnetic field had a small gradient that caused the muon circular orbits to drift slowly towards the end of the magnet; the gradient could be adjusted in order to vary the step size of the orbital advancement; a coincidence of three scintillation counters was used to define the incident muon signal. At the end of the magnet, a large magnetic gradient ejected the muons from the target, which were then stopped in a methylene-iodide target and the emitted positrons in the backward and forward directions were counted by telescopes. The muon spin direction was flipped by $\pm 90°$ in successive runs, by means of a pulsed vertical magnetic field produced in the first microsecond after the muon arrival on target: this way, forward (c_n^+) and backward (c_n^+) emitted positrons were counted by the same pair of telescope counters, instead of using two different telescopes with different efficiencies. Several storage times were measured in the range $[2.0, 6.5]$ µs, and each one corresponded to a different channel in the electronics: for the first 50 channels the telescope $6-6'$ was used, for the second 50 channels the telescope $7-7'$ was used instead. Given the forward and backward counts c_n^+ and c_n^-, the asymmetry at storage time t_n was defined as:

$$A_n = \frac{c_n^+ - c_n^-}{c_n^+ + c_n^-} = A\sin\left(a_\mu B \omega_C t_n\right) \tag{3.2.2}$$

with ω_C the cyclotron frequency of the muon beam. Figure 3.2.1(b) shows the best fit on CERN I data, which yielded $a_\mu = 0.001145(22)$, thus a $\sim 2\%$ precision on a_μ. This preliminary result was refined with new data collected in the following year, where the same basic technique was employed but many improvements were incorporated to reach a new level of accuracy [81].

The final CERN I result was:

$$a_\mu^{\text{exp}}(\text{CERN I}) = 0.001162(5) \rightarrow \pm 4300\,\text{ppm} \tag{3.2.3}$$

in agreement with the theoretical prediction. One of the limitations of this experiment was that the muons decayed at rest, so their lifetime was $\sim 2.2\,\mu\text{s}$, which limited the measuring period (equal to a few lifetimes), resulting in a small number of measured muon decays.

3.2.2 CERN II

The CERN II experiment brought many improvements from the first one: a storage ring with 5 m of diameter and a C-shape cross section was built; in the late 1950s, a brand new accelerator, the PS (proton synchrotron), was implemented at CERN, which injected a 10.5 GeV proton beam into the storage ring, and made it collide against a target placed inside. Muons emitted from pion decay had a momentum of $1.27\,\text{GeV}/c$ (so a γ factor of ~ 12 that boosted the muon lifetime in the lab frame) and were captured by a magnetic field of 1.7 T generated by a series of 40 independent bending magnets. This experiment was limited by the inefficient injection method: protons that did not hit the target and pions that had not decayed created a large background (namely, the hadronic flash) and did not allow for an optimal initial muon polarization; however, this limitation was made up for by the high luminosity of the PS and the relativistic gamma-factor of ~ 12 which dilated the muon lifetime and allowed the muon beam to precess in the ring for about ~ 50 cycles (around 4.4 µs), instead of only ~ 2 cycles at CERN I.

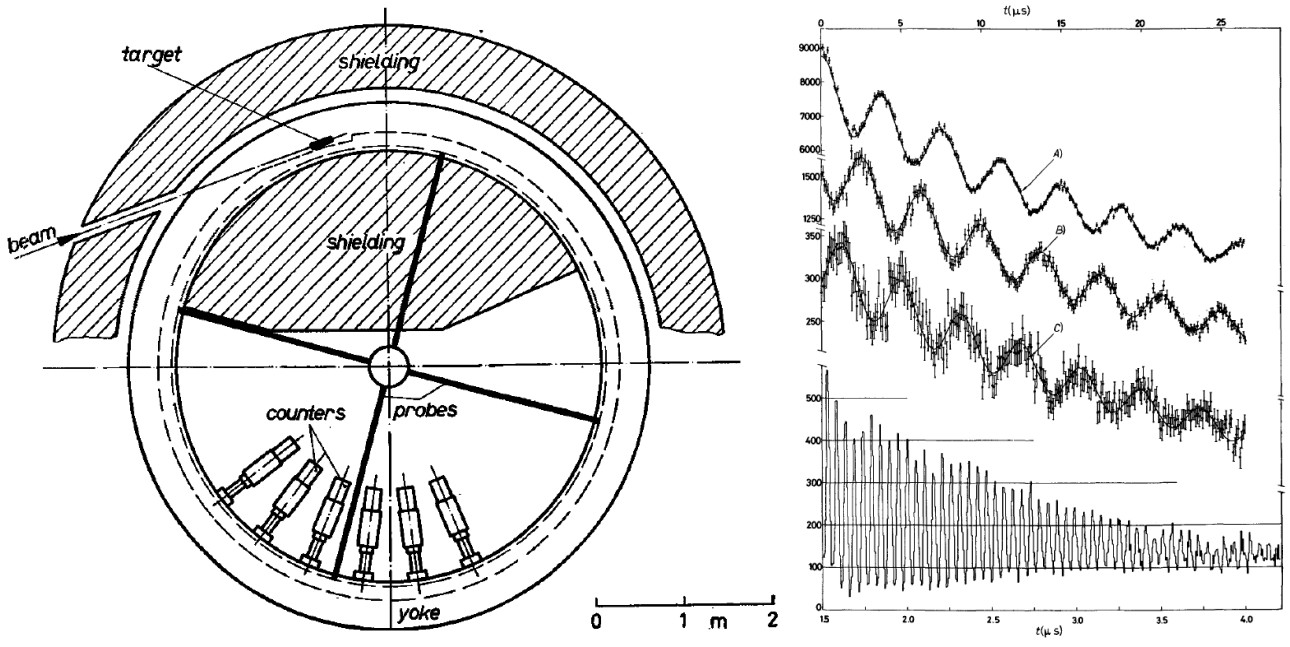

(a) **(b)**

Figure 3.2.2: From Ref. [82]. (a) Plan of 5-m diameter ring magnet: the proton beam enters the yoke and hits a target inside a magnetic field. (b) Distribution of decay positrons/electrons as a function of time. Upper scale of time: curve A) goes from 20 µs to 45 µs, curve B) from 65 µs to 90 µs, curve C) from 105 µs to 130 µs. Lower scale of time: the rotation frequency of the muon at early times.

Figure 3.2.2(a) shows an overview of the CERN II experimental setup [82]: the data acquisition was made by 6 lead-scintillator counters placed in a quarter of the ring in the inner radius, which

counted the decay positrons that had a lower momentum than stored muons, and therefore bent radially inwards. The detectors recorded the times of arrival of high-energy decay positrons, which were the ones that carried the muon spin information at the time of decay (as explained in Section 1.3.3). Equation (14) in Ref. [82] was used to perform a maximum-likelihood fit on the arrival time spectrum:

$$N(t) = N_0 e^{-t/\tau}\left(1 + E e^{-t/\tau_e}\right)\left[1 - A\cos\left(\omega_a t + \varphi\right)\right] + B_g \tag{3.2.4}$$

where the N_0, τ, A, ω_a and φ parameters have similar meanings to the ones in Equation (1.3.21); E and τ_e were introduced to take into account the extra-counts at early times, possibly due to perturbations of the electronics by the hadronic flash, or due to extra particles that entered the ring and scattered away over time; B_g was added to include a possible source of background. The optimal energy threshold to minimize the statistical uncertainty on a_μ was found to be around 780 MeV, which corresponds to a value of $y_{th} \approx 0.6$ as in Equation (1.3.22). The positron counts, fitted with Equation (3.2.4) in a time range from 20 µs to 189 µs, are shown in Figure 3.2.2(b). Four NMR probes, not shown in Figure 3.2.2(a), were periodically inserted into the storage region to measure the magnetic field. By taking the ratio of ω_a and B-field, according to Equation (1.3.7), the final result for the muon anomaly from CERN II was [82]:

$$a_\mu^{\text{exp}}(\text{CERN II}) = 0.00116616(31) \rightarrow \pm 270\,\text{ppm} \tag{3.2.5}$$

which differed of almost 2 standard deviations from the theoretical value known in 1968, the year when the preliminary report was published [83]. This level of discrepancy was resolved by Aldins and collaborators [84], who examined the sixth-order QED contributions (proportional to $\left(\frac{\alpha}{\pi}\right)^3$) from light-by-light scattering, which was initially thought to be negligible but turned out to be a ~ 200 ppm contribution instead. The theoretical value determined in 1969 was:

$$a_\mu^{\text{th}}(1969) = 0.00116587(3) \rightarrow \pm 25\,\text{ppm} \tag{3.2.6}$$

essentially eliminating the discrepancy between theory and experiment mentioned above.

3.2.3 CERN III

CERN III was the third and last experiment of the CERN series, completed in 1976; it brought a series of important improvements, both from the engineering and the physics point of view.

Figure 3.2.3(a) shows the experimental apparatus: a storage ring with a diameter of 14 m was built and immersed in a 1.5 T dipole magnet field; rather than injecting the protons into the ring, the beam target was moved outside of the ring so that the hadronic flash could be greatly reduced. This meant that pions were transported to the ring through a beamline, which selected a narrow range of pion momenta and therefore increased the initial polarization of muons from pion decay; an inflector was used to cancel the storage ring magnetic field so that the beam deflection entering the ring was minimal. Electric quadrupoles focused the muon beam in the vertical direction, whereas the dipole magnet provided a weak focusing along the horizontal axis (in atomic physics, this is known as a "Penning trap"). 24 lead-scintillator shower counters were placed symmetrically around the inside of the ring to measure the arrival time and the energy of the positrons. The so-called "magic" momentum, $p_\mu = 3.094\,\text{GeV}/c$, was chosen in order to cancel the effect of the electric field in the anomalous precession frequency (as discussed in Section 1.3.2): muons boosted with $\gamma = 29.3$ have a dilated lifetime of 64.4 µs, which meant that the storage time in CERN III could be extended to 655.35 µs, allowing for more muons and thus increasing the statistical precision with respect to CERN II. The maximum-likelihood fit on data, shown in Figure 3.2.3(b), was performed with the function in Equation (3.2.4), the

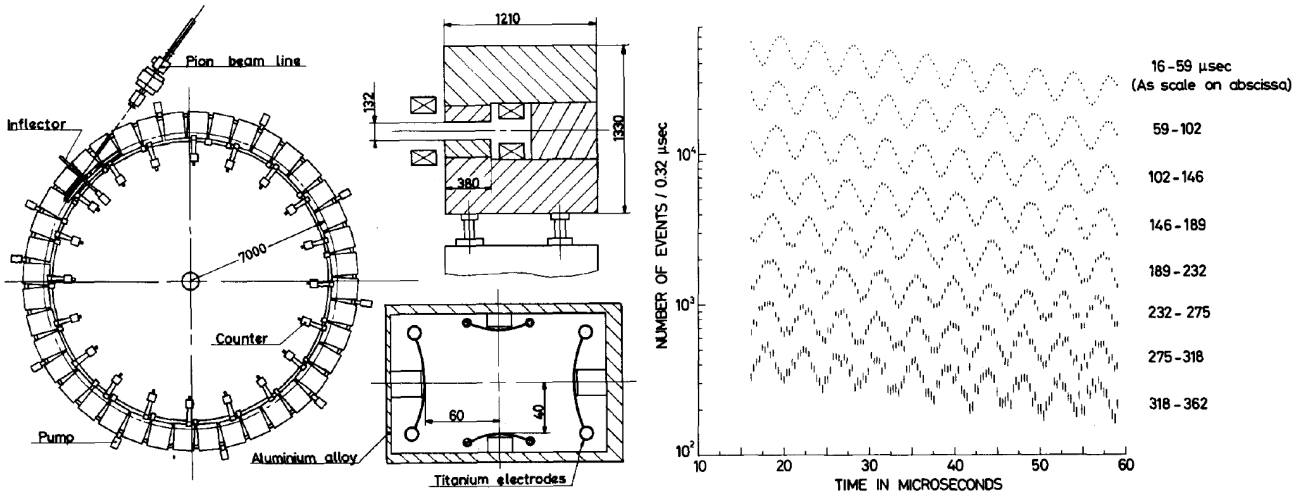

(a) **(b)**

Figure 3.2.3: From Ref. [85]. (a) Overview on CERN III 14-m diameter 40-magnet ring. On the top right the C-shaped yoke is shown, the open side faced the center of the ring; on the bottom right the cross section of the vacuum chamber and the electric quadrupoles are shown. (b) Time distribution of decay electrons from a portion of CERN III data (the first 80 $g-2$ cycles are shown).

same as CERN II.

All the improvements of CERN III allowed to obtain an unprecedented experimental precision on a_μ. Both CERN II and CERN III measured the magnetic anomaly for positive and negative muons, which required to reverse the polarities of all magnetic and electric fields of the experiment. With a precision of the order of $\mathcal{O}(10)$ ppm, the final results at CERN III were [85]:

$$\begin{aligned} a_{\mu^+}^{\text{exp}}(\text{CERN III}) &= 0.001165911(11) \rightarrow \pm 9\,\text{ppm} \\ a_{\mu^-}^{\text{exp}}(\text{CERN III}) &= 0.001165937(12) \rightarrow \pm 10\,\text{ppm} \\ a_{\mu}^{\text{exp}}(\text{CERN III}) &= 0.001165924(8.5) \rightarrow \pm 7.3\,\text{ppm} \end{aligned} \tag{3.2.7}$$

where the error was completely dominated by statistics. Having measured the anomaly for positive and negative muons with such precision, CERN III could perform a verification of the CPT theorem, which is assumed valid in the Standard Model and implies that $a_{\mu^+} = a_{\mu^-}$. This equality was verified within the 95% confidence limits:

$$\frac{a_{\mu^+} - a_{\mu^-}}{a_\mu} \in [-50, 6] \times 10^{-6} \qquad \text{at } 95\%\text{ CL} \tag{3.2.8}$$

The precision obtained at CERN III was enough to be sensitive to 3-loop order QED and, most importantly, to the hadronic contribution (the HVP term of the anomaly, explained in Section 2.1.3). The theoretical prediction at the time was:

$$a_\mu^{\text{th}}(1977) = 0.001165921(13) \rightarrow \pm 11\,\text{ppm} \tag{3.2.9}$$

in agreement with the experimental value, with a similar level of precision.

3.3 The E821 experiment at BNL

The next experiment after CERN III was E821 at Brookhaven National Laboratory (BNL): one of the goals was to reach enough sensitivity to observe contributions from the electroweak sector, or search for New Physics such as supersymmetry. In 1984, Kinoshita and collaborators [29] presented the results of complete QED calculations up to the fourth power of (α/π); furthermore, they reduced the error on the hadronic sector by improvements on the $R(s)$ function defined in Section 2.1.3, for the data-driven approach that uses the experimental results from $e^+\,e^-$ colliders. In response to the tremendous improvement in the theoretical prediction, Yale Professor Vernon Hughes, and a group of physicists that included many of the original CERN collaborators, initiated a new project for a Muon $g-2$ experiment to be performed at the Alternating Gradient Synchrotron (AGS) at BNL, and established the design goal to measure a_μ at 0.35 ppm [86]. Figure 3.3.1 shows a top view of the E821 muon storage ring.

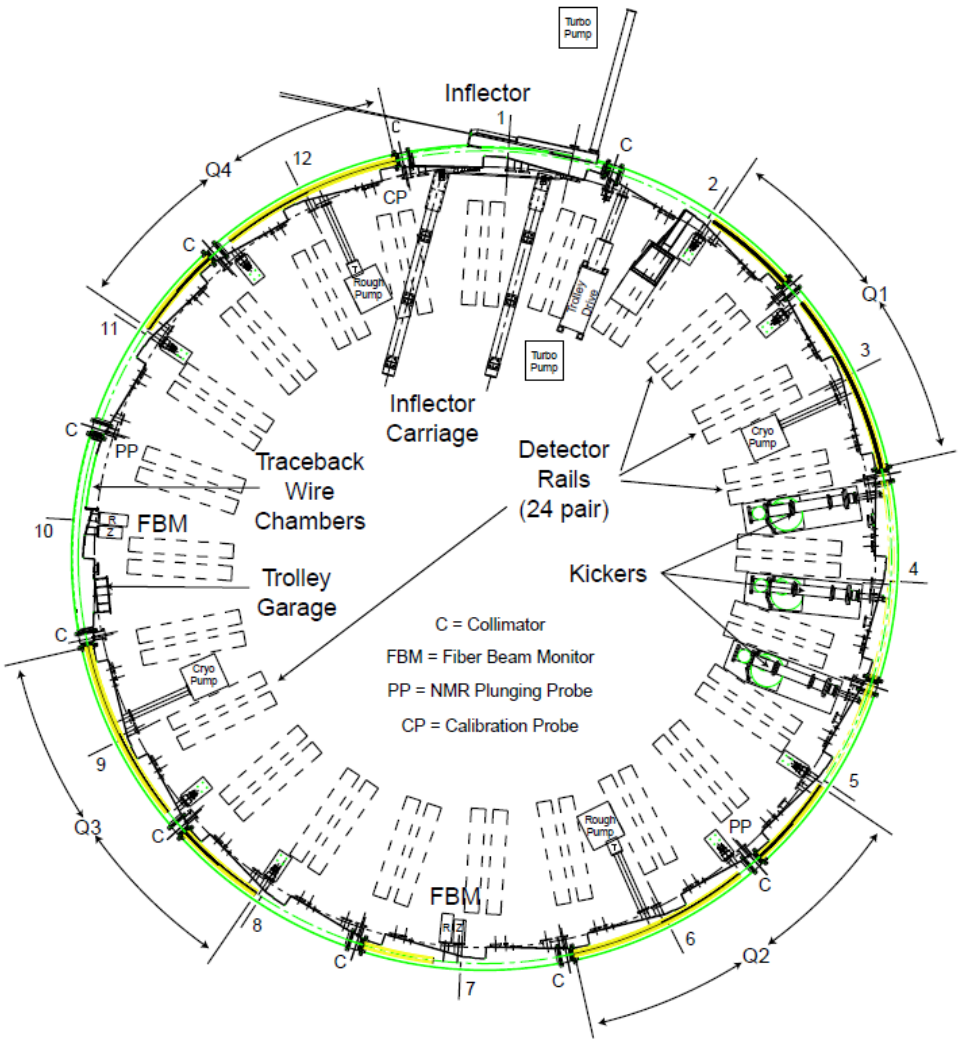

Figure 3.3.1: From Ref. [87]. Muons entered the back of the storage ring through the field-free channel of the inflector; 3 kickers provided a rapid current pulse which gave the muon bunch a transverse 10 mrad kick; 4 electrostatic quadrupoles vertically focused the beam; the 24 regularly spaced calorimeters detected the electrons from muon decay.

The 7.3 ppm error in the CERN III experiment was dominated by a statistical uncertainty of 7 ppm, whereas the systematic uncertainty was around 2 ppm, almost entirely due to limited knowledge of the magnetic field. At BNL, the plan was to measure the precession frequency ω_a

at 0.3 ppm, the magnetic field at 0.1 ppm, and keep the systematic uncertainties under 0.1 ppm.

The first goal was to produce a higher rate of muons, reaching a statistics 20 times as large as for CERN III: this was possible because the muon flux could be increased by approximately a factor of 400 thanks to the high luminosity of AGS.
A second improvement was a better way of injection: in CERN III, pions were injected in the ring and completed one orbit before impacting on the exterior wall of the inflector, thus muons emitted by pions were limited in number; in BNL, pions were allowed to decay in a long ($\sim$ 80 m) channel upstream of the storage ring, and then the muon beam was directly injected in the ring. In this way, a much larger number of muons was stored per AGS cycle, that delivered pulses of 7×10^{12} protons with 24 GeV/c momentum. In order to inject muons in the ideal orbit after the inflector, and to avoid interference between the muon beam and pions, a system of 3 pulsed electromagnetic kickers was implemented.
Another important improvement was that the storage ring of 7 m of diameter was composed of three continuously wound superconductors, instead of the 40 independent bending magnets of CERN III, which allowed the magnetic field to be much more uniform.
Finally, the 1.4513 T magnetic field was measured using pulsed NMR techniques: 17 NMR probes mounted inside a trolley were pulled through the storage ring to measure the field inside; in between trolley runs, a system of 378 fixed probes (identical to the trolley ones in design and shape), placed above and below the storage-ring volume in the walls of the vacuum chamber, continuously monitored the magnetic field during data taking [2].

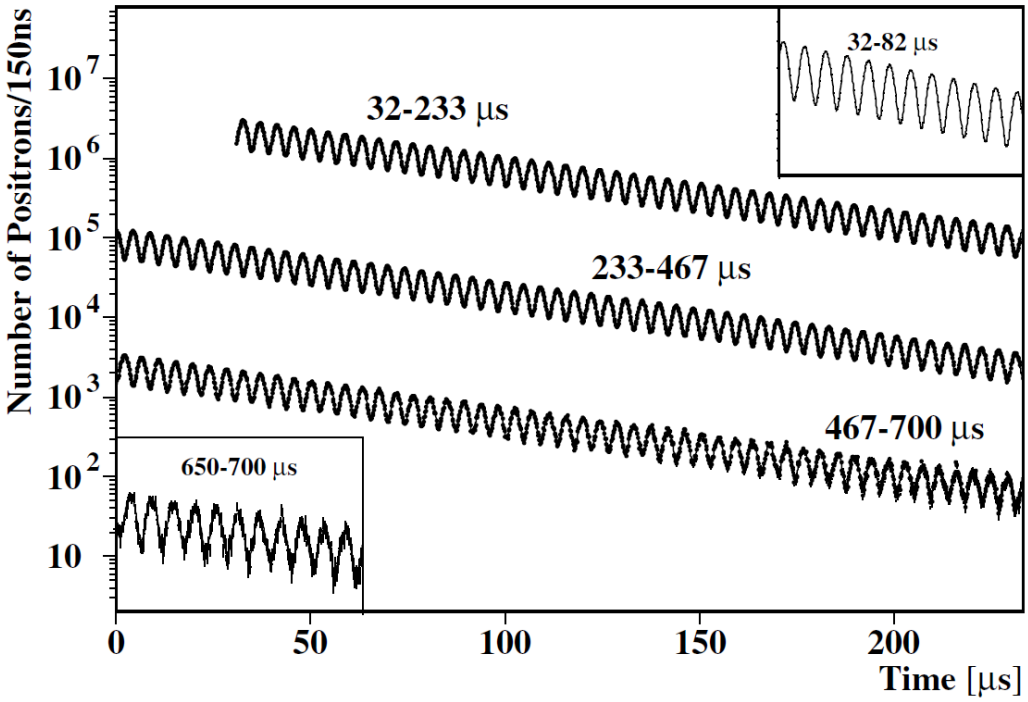

Figure 3.3.2: Time spectrum of positrons with energy above 2 GeV from 1999 data [88].

Figure 3.3.2 shows the decay positron counts from 1999 campaign as a function of time: positron signals in the lead-scintillating fiber electromagnetic calorimeters were recorded by waveform digitizers and stored for later analysis. The fit on data was performed with the eight-parameter function in Equation (3.2.4) as for CERN III, corrected for beam dynamics effects such as muon losses as function of time and coherent betatron oscillations; the storage time was increased to 700 μs thanks to all the improvements applied in the new experiment. Data taking started in 1997 and continued until 2000, when the final precision of 0.7 ppm was reached for positive

muons; in 2001, the experiment switched to negative muons, which required to invert the polarities of the storage ring, and some optimizations to maximize the flux of stored muons. The final results for BNL were [2]:

$$\begin{aligned} a_{\mu^+}^{\text{exp}}(\text{BNL},\ 2000) &= 0.0011659204(9) \rightarrow \pm 0.73\,\text{ppm} \\ a_{\mu^-}^{\text{exp}}(\text{BNL},\ 2001) &= 0.0011659214(9) \rightarrow \pm 0.72\,\text{ppm} \\ a_{\mu}^{\text{exp}}(\text{BNL},\ 2006) &= 0.00116592080(63) \rightarrow \pm 0.54\,\text{ppm} \end{aligned} \tag{3.3.1}$$

The final statistical and systematic uncertainties were 0.46 ppm and 0.28 ppm, respectively. Like CERN III, the E821 experiment served as a precise verification of the CPT theorem: the ratio $\mathcal{R} \equiv \omega_a/\omega_p$, where ω_p is the proton precession frequency from the magnetic field calibration, should be the same for μ^+ and μ^-. From the latest measurements at BNL, the CPT test yielded [2]:

$$\mathcal{R}_{\mu^-} - \mathcal{R}_{\mu^+} = 0.0037072083(26) - 0.0037072047(26) = 3.6 \pm 3.7 \times 10^{-9} \tag{3.3.2}$$

in good agreement with the expectation from CPT invariance, which allowed to take the average of a_{μ^+} and a_{μ^-}.
At the time, the best theoretical estimation of a_μ included the QED fifth power of (α/π), and the second order of EW and hadronic loops [2]. The difference between the experimental and the theoretical values was:

$$a_{\mu}^{\text{exp}}(\text{BNL},\ 2006) - a_{\mu}^{\text{th}} = 268.6(72.4) \times 10^{-11} \tag{3.3.3}$$

pointing out a non-negligible 3.7-standard deviation difference.

3.4 The E989 experiment at FNAL

In order to either confirm or disprove the discrepancy observed at BNL, a new experiment at Fermilab was proposed in 2009 [89], where the accelerator complex was capable of delivering a higher luminosity than the BNL AGS. The E821 superconducting magnetic ring was already a sufficiently accurate device for an improved measurement, so in the summer of 2013 it was moved from Brookhaven to Fermilab and relocated in the newly completed MC-1 building at Fermilab with a stable floor and good temperature control [90]. The goal of the new Muon $g-2$ experiment at Fermilab is to measure the muon magnetic anomaly with a precision of 0.14 ppm, by achieving statistical and systematic errors around 0.1 ppm (the Technical Design Report was published in 2015 and can be found in Ref. [4]). A detailed description of the experimental apparatus, as well as all the improvements in place to reduce the systematic effects, will be provided in Chapter 4. The experimental technique is similar to the one of the CERN and BNL experiments.
The Muon $g-2$ collaboration released our first measurement of a_μ in April 2021, based on the 2018 data campaign (Run-1). In August 2023, we released our second result, based on 2019 and 2020 data campaigns (Run-2/3). The new measured values are consistent with the previous BNL results [1, 3]:

$$\begin{aligned} a_{\mu}^{\text{exp}}(\text{FNAL},\ 2021) &= 0.00116592040(54) \rightarrow \pm 0.46\,\text{ppm} \\ a_{\mu}^{\text{exp}}(\text{FNAL},\ 2023) &= 0.00116592057(25) \rightarrow \pm 0.21\,\text{ppm} \end{aligned} \tag{3.4.1}$$

The detailed description of these two results will be presented in Sections 7.1 and 7.2.

Table 3.4.1 summarizes the history of $g-2$ experiments: the development of the experimental apparatus and method allowed the BNL experiment to achieve an impressive 14-fold improvement in precision with respect to the last CERN results; the experiment at FNAL aims to further improve this precision by a factor of ~ 4.

Experiment [Ref.]	Years of running	Particles	$a_\mu \times 10^{11}$	Precision [ppm]
CERN I [81]	1961	μ^+	$1162(5) \times 10^5$	4300
CERN II [82]	1962-1968	μ^+, μ^-	$116616(31) \times 10^3$	270
CERN III [85]	1974-1976	μ^+, μ^-	116592400(850)	7.3
BNL [2]	1997-2001	μ^+, μ^-	116592080(63)	0.54
FNAL [3]	2018-2023	μ^+	116592055(24)	0.20
Average [3]			116592059(22)	0.19

Table 3.4.1: Values of experimental measurements for a_μ from CERN I to the latest results at Fermilab. The value quoted for "FNAL" is the combination of the results from Run-1 and Run-2/3 data, in Equation (3.4.1).

3.5 Future experiment E34 at J-PARC

A new experiment is under preparation at the J-PARC muon facility in Japan, aiming to provide an independent measurement of a_μ and of the muon EDM (see Section 2.2.2) with a completely new approach. Contrarily to the previous experiments, at J-PARC they will not use muons at the "magic" momentum of $\sim 3.09\,\mathrm{GeV}/c$ to cancel the influence of electric fields to ω_a, as in the last term of Equation (1.3.9); instead, the experiment will not use electric fields at all, but it will use a technique that will not require to strongly focus the muon beam.

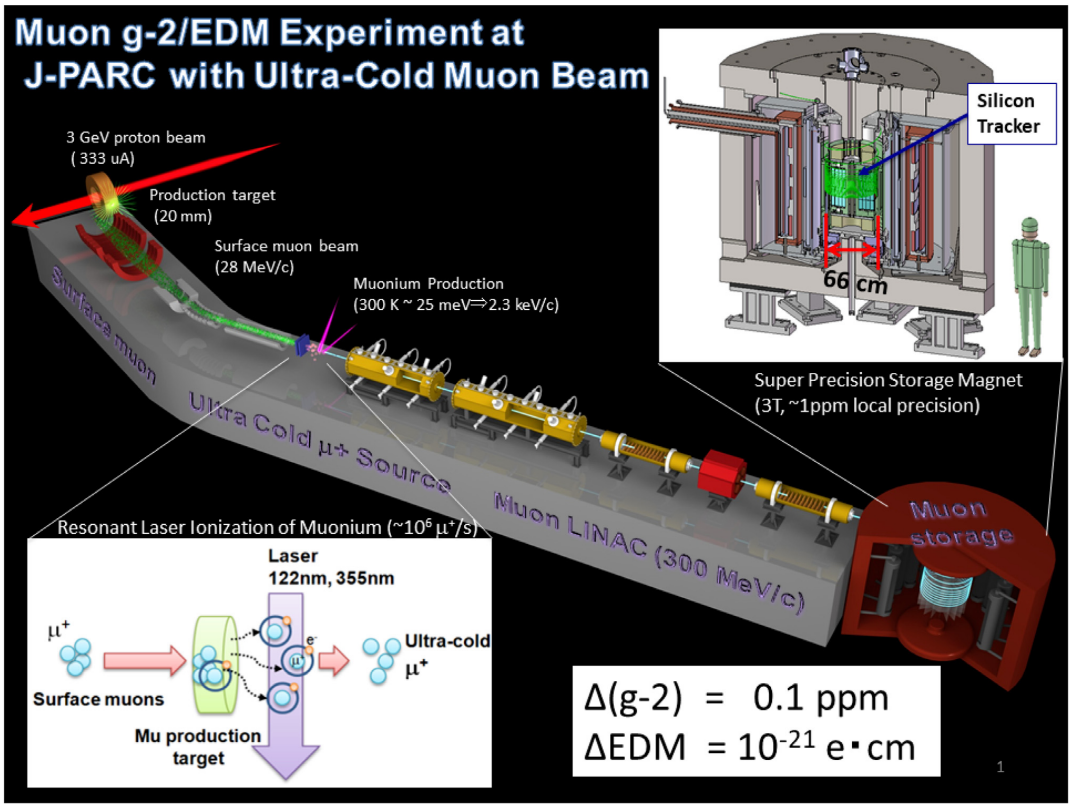

Figure 3.5.1: From Ref. [92]: overview of the J-PARC E34 experiment.

As a first step, a positively charged muon beam will be stopped at a silica aerogel target, where muonium, a bound state of e^- and μ^+, will be produced; muonium atoms will be ionized by laser excitation to produce room-temperature muons ($\sim 25\,\text{meV}$); finally, a linac will accelerate these muons to a momentum of $\sim 300\,\text{MeV}/c$, which will then be stored in a compact region with a highly uniform (1 ppm local uniformity) magnetic field. The advantage of reaccelerating thermal muons is that the produced beam has a factor of 1000 smaller transverse emittance than "conventional" muon beams from pion decay; in addition, muon losses during storage time and the pion background will be eliminated with this technique.
Figure 3.5.1 shows the schematic drawing of the E34 experiment at J-PARC. The muon beam will be stored in the presence of a 3.0 T magnetic field, in a storage ring that is 20 times smaller than the Fermilab one. The positrons from muon decay will be measured by a tracker detector composed of 40 silicon strip sensors arranged radially.
The summary paper of TDR was published in May 2019 [66], and the first phase of data taking after commissioning is expected to begin after 2027 [91] with an initial precision of about 0.45 ppm in a_μ, similar to that of BNL and of the Run-1 result from Fermilab. The goal in the next phase of the J-PARC E34 experiment will be to measure a_μ to a precision of 0.1 ppm [92], similar to the goal at Fermilab. In addition, they will search for muon EDM with a sensitivity of the order of $10^{-21}\,\text{e cm}$. As it can be seen from Equation (2.2.3), where the electric dipole d_μ term is perpendicular to the a_μ term in the $\vec{\omega}_a$ expression, a muon EDM will produce muon spin precession out of the horizontal plane that is defined by the ideal muon orbit, thus generating vertical motion of the spin. At J-PARC, they will extract the EDM term from the oscillation of the up and down asymmetry in the number of detected positrons over time. A major source of systematic uncertainty on EDM is detector misalignment with respect to the plane of the muon storage, which will be monitored with optical frequency comb technology. The estimated systematic uncertainty is $0.36 \cdot 10^{-21}\,\text{e cm}$. The effects of axial electric field and radial magnetic field will be both less than $10^{-24}\,\text{e cm}$, thus negligibly small.

Chapter 4

The Muon $g-2$ experiment at Fermilab

The new experiment E989 in operation at Fermi National Accelerator Laboratory (FNAL) aims to measure the muon magnetic anomaly with a precision of 0.14 ppm (or, equivalently, 140 ppb), a fourfold improvement in precision with respect to the previous E821 experiment at BNL. The design error of 140 ppb is obtained by equal contributions of statistical and systematic errors of 100 ppb [4]. This goal was chosen in order to bring down the significance of the discrepancy between theory and experiment observed at BNL, from $3.7\,\sigma$ to more than $6\,\sigma$ assuming the same central value, and provide a strong statistical evidence that new physics beyond the Standard Model contributes to a_μ at this level of precision.
The factor 4.6 of improvement in the statistical uncertainty from BNL required an event yield of 21 times the positrons accumulated in the previous experiment. As of now, the Fermilab experiment has collected 21.9 times the BNL statistics (see Section 5.1), thus surpassing the design goal, and it has ended its sixth and final year of data taking. The goal of 100 ppb of systematic uncertainty is split into a 70 ppb contribution from the anomalous precession frequency ω_a analysis, and 70 ppb from the magnetic field measurement, expressed in terms of ω_p, the Larmor precession frequency of protons in a water sample. The experimental technique at Fermilab is the same as the one in CERN III and BNL experiments, which has proven to be successful. While BNL greatly improved the CERN III apparatus - for example by directly injecting muons into the storage ring, instead of pions - the real challenge of E989 was to introduce a series of refinements in order to reduce the sources of systematic error. While the superconducting storage ring was moved from Brookhaven and installed at the end of the FNAL accelerator chain, a broad suite of new elements replaced or upgraded the old ones, for example 3 powerful electromagnetic kickers, 24 segmented calorimeters whose crystals are matched with silicon photomultipliers (SiPMs), and a state-of-the-art laser calibration system. More details about all systems will be provided throughout this Chapter. In the 2023 publication, the systematic contribution amounts to 70 ppb, divided into 47 ppb from ω_a and 52 ppb from the magnetic field measurement, thus already surpassing the design goal for the final systematic error [3]. Currently, the Fermilab experiment is performing final measurements of the magnetic field and of transient magnetic fields without storing μ^+ in the ring, which will further reduce the associated sources of systematics. More details about the field measurements will be provided in Sections 4.7.4 and 4.7.5.

We will now review the improvements needed for E989 to achieve the experimental goal of 100 ppb on statistical and systematic error:

- The Fermilab beam complex is able to provide an annual delivery of $\sim 2 \cdot 10^{20}$ protons

with an energy of 8 GeV, with a higher proton rate and less protons per bunch than E821[1]. The average rate of muon injection was 12 Hz, compared to only 4.4 Hz at BNL.

- A longer pion decay line (~ 2 km) with respect to the BNL one (~ 80 m). Only a negligible number of undecayed pions were injected into the storage ring, almost 10^5 times better than in the BNL experiment where a limiting factor was an enormous burst of neutrons produced when pions intercepted materials.

- A high precision laser calibration system to continuously re-calibrate the detectors, to precisely monitor gain fluctuations. At BNL, detector gain changes during muon storage were the highest systematic error on ω_a: the aim of E989 was to reduce this contribution by a factor 6, down to 20 ppb. In the latest publication, the gain systematic amounted to 5 ppb [3].

- Hardware and software improvements which reduce the rate of overlapping positron events (pileup) and the related systematic. A new tracking system was also able to monitor the muon distribution inside the storage ring, and precisely determine the beam dynamics corrections to ω_a that arise, for example, from electric field and vertical oscillations.

- Edge shims, wedge shims, top hats and steel foils (the latter were new over BNL) were placed around the ring in 2015-2016 to increase the magnetic field uniformity by a factor of 3 with respect to BNL. A precise monitoring of B-field variations was possible thanks to critical NMR probes placed in strategic locations and also to many trolley runs.

The E989 experiment at Fermilab used positively charged muons. Using μ^+ brought several advantages in the experimental setup [4]: for example, the vacuum could be more relaxed (10^{-6} Torr are needed in the vacuum chamber for μ^+, whereas 10^{-7} Torr for μ^-) and therefore the high voltage could be turned on for longer times; in the negative polarity, quadrupoles would require a very delicate and lengthy conditioning process, since low energy trapped electrons could cause sparking; in the last BNL run, trapped electrons caused the side support insulators to varnish, which required them to be cleaned and in some cases replaced for E989. The largest relevant difference in a negative muon run between Fermilab and Brookhaven is that the production ratio of μ^-/μ^+ was close to 1 at the 24 GeV AGS, but it is lower at the 8 GeV Fermilab beam complex. The μ^- yields were simulated: it was found that the rate of negative muons arriving at the experiment would be roughly 60% that of positives [93].
As we approached the statistical goal of the experiment, we studied the possibility to take a final run in the μ^- configuration, which would have been a great opportunity for a CPT test like BNL did, that the next experiment at J-PARC will not be able to perform. Unfortunately this was inconsistent with critical accelerator commissioning work for the Mu2e experiment at Fermilab. Ultimately, by running for our last year in the μ^+ configuration, we were able to collect data with a higher flux and bring the statistical uncertainty beyond the design goal, closer to the achieved systematic uncertainty.

4.1 Production and injection of the muon beam

In this section, we will review the production of muon beam at Fermilab. Figure 4.1.1 is an overview of the FNAL beam complex that produces muons for $g-2$.

[1] In the first 2 years of data taking we had a lower storage efficiency and lower running time, but the required statistics was eventually reached in about 6 years of data taking.

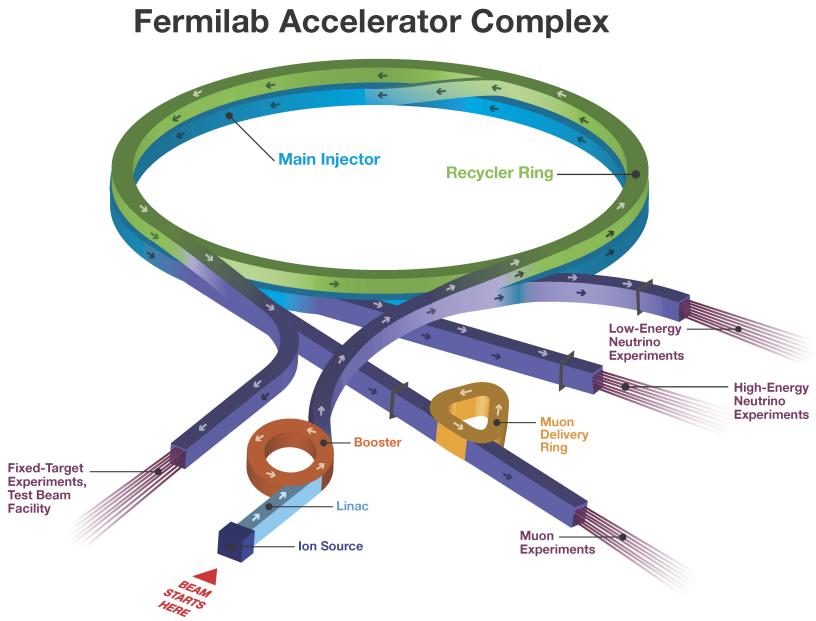

Figure 4.1.1: The Fermilab accelerator complex sends particle beams to numerous experiments and research and development stations. Protons travel through a chain of accelerators. They start at the Linac (linear accelerator) and head to the Booster, Recycler Ring and Main Injector before heading to their final destinations. Link to the original picture.

The Fermilab muon campus beamline can deliver pulses of highly polarized muons to the storage ring. This process starts with protons accelerated in the linear accelerator Linac up to 400 MeV and injected into the Booster, a 150-m diameter proton synchrotron that cycles at 15 Hz and accelerates protons to 8 GeV of kinetic energy. Protons then reach the Recycler ring, a 3-km diameter ring where they are grouped into bunches with approximately 4×10^{12} particles and a temporal width of $\sim$ 120 ns. Each bunch propagates to the AP0 target hall (the antiproton production hall used by the Tevatron), where protons collide on a cylindrical core made from a nickel-chromium-iron alloy called Inconel-600, encased by a thick layer of beryllium to resist beam interaction stress. From the collision of protons on target, $\mathcal{O}(10^9)$ secondary particles are produced, of which many are pions. An electrostatic lithium lens focuses the secondary beam which then goes through a momentum filter that selects a beam of particles at the so-called magic momentum of $p = 3.094\,\text{GeV}/c$ with 10% relative uncertainty. Through a series of beamlines, the secondary beam enters the 500-m circumference Delivery Ring, where two important steps for the preparation of pure muon bunches take place. Firstly, a spatial separation is created between the pions (together with the emitted muons) and protons, which are more massive and therefore have a smaller Lorentz boost factor given the same momentum. Protons with the magic momentum have $\gamma \approx 3.3$, whereas pions that didn't decay in the previous beamlines have $\gamma \approx 22$ and, as mentioned in Section 1.3.2, muons have $\gamma \approx 29.3$: after each turn, protons fall 25 m behind muons; 4 turns are enough to create a spatial separation of 100 m and a time delay of $\sim$ 200 ns, so protons can be kicked away cleanly in the abort channel, without disturbing the 120 ns muon bunch. Secondly, virtually all pions decay in the Delivery Ring, since in 4 turns they travel for a total of 2 km, which is more than 11 times the decay length of about $\sim$ 170 m. At this point, muon bunches travel

towards the Muon $g-2$ Storage ring: the final step is to use an inflector magnet to cancel the fringe field of the ring itself, which otherwise would deflect the beam into the magnetic iron and reduce injection efficiency; moreover, three kickers are needed to kick the beam of about 11 mrad (corresponding to a magnetic field of ~ 22 mT), since the trajectory at the exit of the inflector does not match the closed orbit of the ring (more details are given in Section 4.2).

At the time of injection, the distribution of delivered muons has the required momentum of 3.094 Gev/c (center value), with a root mean square (RMS) value of 2%, and a temporal length of 120 ns. The typical muon injection efficiency is 2×10^{-7} per proton on target. Stored muons have a maximum beam radius of 45 mm (which is the inner radius of collimators), an RMS value of 0.5% on the momentum centered at the magic value, an orbit radius of 7.112 m and are observed for about 700 µs after injection. A bunch of muons produced in the beamline is referred to as "fill": in E989, fills can deliver $\mathcal{O}(10^4)$ muons to the storage ring, with an average rate of 11.4 Hz, and about 500 positrons[2] are detected and counted in wiggle plots. Figure 4.1.2 shows the bunch time structure of each cycle, which provides 2 groups of 8 fills each every 1.4 s.

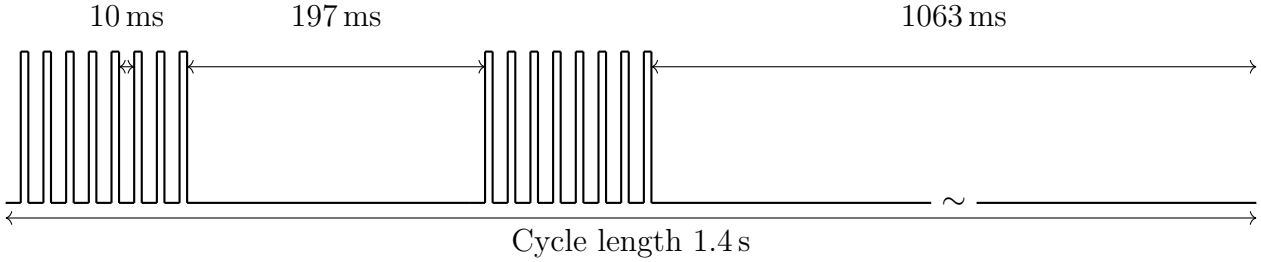

Figure 4.1.2: Bunch structure: two groups of eight fills each are delivered every 1.4 s, which means that the average rate is 11.4 fills per second. [4]

4.2 The ideal muon orbit

When the muon beam reaches the storage ring, it enters through a hole in the back-leg of the magnet where a field-free region is created by the superconducting inflector magnet. This has been a crucial step for injection efficiency since the CERN III experiment (Section 3.2.3): the inflector facilitates injection of the muon beam into the storage ring by canceling the main 1.45 T dipole field of the ring, so that injected muons are not deflected by the field as they enter the ring [94]. The exit of the inflector is placed 77 mm radially outwards from the center of the storage ring, so the muon beam does not start on the ideal trajectory but on a slightly different one: this is an issue that cannot be ignored, otherwise muons would impact against the inflector after one turn.
To correct the initial muon orbit, a series of three pulsed kicker plates is displaced $\sim 90°$ downstream of the inflector exit, to kick the muon beam. When it was designed, the kicker system had to meet several strict requirements, for instance: it could not contain ferrite or any other magnetic elements, because that would affect the uniformity of the magnetic field; it had to fit where the old E821 kicker system was placed, which was a series of three consecutive 1.7 m long spaces; the kicker pulses had to be shorter than ~ 149 ns, which was the cyclotron period; and, finally, any eddy currents produced due to kicker pulses should be negligible after ~ 20 µs after injection, or at least precisely corrected for in the final measurement. The kicker plates are connected to a high voltage transformer that allows up to 70 kV peak forward anode voltage,

[2] This was the maximum value that we achieved throughout the 6 years of running, but in general we detected a lower number of positrons, around 350 per fill.

15 kA maximal current, a 300 kA/µs rate rise and maximum repetition rate of 2 kHz [95].

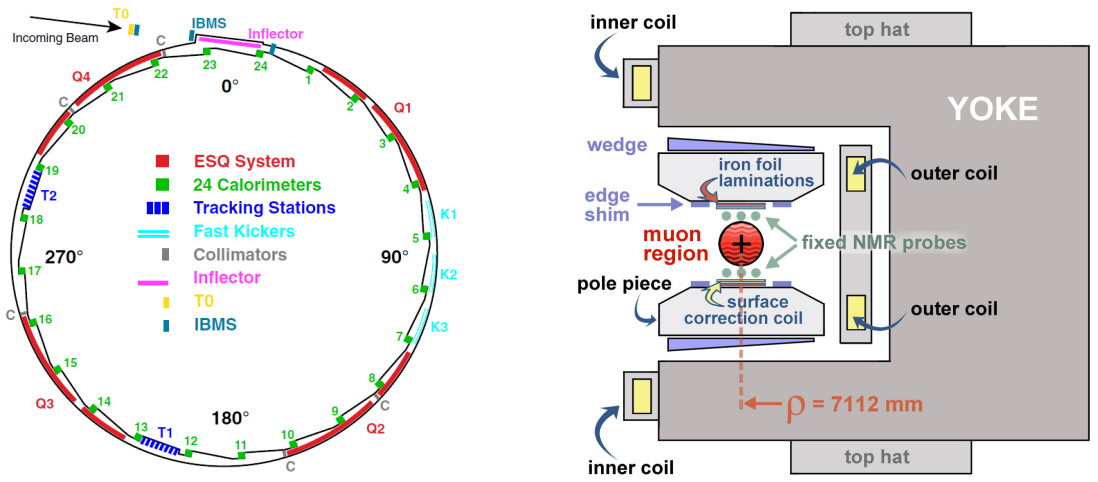

(a) **(b)**

Figure 4.2.1: (a) Plan view of the $g-2$ storage ring vacuum chamber and instrumentation: the beam circulates clockwise, starting from the inflector at the top of the figure [96]. (b) A cross section of the storage ring magnet featuring the components used to generate the highly uniform 1.45 T magnetic field [97].

Figure 4.2.1 shows the plan and cross sectional views of the storage ring. It is the same one used for E821 at BNL: three superconducting coils compose the 14 m diameter ring; the continuous "C"-shaped magnet yoke is built from twelve 30° segments of iron, which are designed to eliminate the end effects in magnets. Holes in the yoke would also affect the B-field at 1 ppm level, thus the only penetrations allowed are the back-leg through which the muon beam enters, and cryogenic services and power supplies connected to the inflector magnet and to the outer radius coil. The superconducting magnet operates at a 5170 A current, at a cryogenic temperature of 4.5 K, to produce a highly uniform field of 1.45 T. Over long timescales, the magnetic field's stability is driven by thermal expansion and contraction of the magnet steel in response to temperature changes in the experimental hall: the magnetic field is stabilized by feedback to the magnet current supply from a set of NMR probes, described in Section 4.7.4, distributed around the ring.

The anomalous precession frequency ω_a and the magnetic field are the main quantities to be measured in the E989 experiment. The principle of both measurements will be presented in Section 4.7. Recalling that $p/e = B \cdot R$, where $p = 3.094\,\mathrm{GeV}/c$ is the magic momentum, e is the elementary charge and R the radius of the orbit, one obtains that a B-field of 1.4513 T puts muons into a uniform circular motion with 7.112 m of radius. The B-field directly affects the spin precession frequency, the cyclotron frequency and ω_a - see Equations (1.3.8) and (1.3.9). In the E989 experiment, muons precess around the storage ring with a period of 149.2 ns, which means about 4690 orbits during fill time of 700 µs; the anomalous precession frequency is $\omega_a \approx 1.44\,\mathrm{rad}/\mu\mathrm{s}$, which is equivalent to a period of about 4.3 microseconds, so the spin takes about 30 orbits to fully precess around the muon momentum. The analysis of the magnetic field is weighted with the stored muon distribution, so it is also taken into account how the magnetic field itself affects the muon beam dynamics.

4.3 Vertical focusing with electrostatic quadrupoles

The storage ring acts as a weakly focusing betatron with electric quadrupoles that provide strong vertical focusing. Muons are injected with the magic momentum so that the E-field does not affect the anomalous precession frequency, as in Equation (1.3.9). Another important requirement for the muon trajectory is that $\vec{\beta}$ must be orthogonal to $\vec{B}$, so that the term proportional to $\vec{\beta} \cdot \vec{B}$ does not contribute to ω_a: to preserve a purely longitudinal muon path, quadrupole gradients are necessary to strongly focus the vertical waist of the beam shape. The electric field of the Electrostatic Quadrupole (ESQ) system provides a linear restoring force in the vertical direction; on the radial direction, instead, the electric field alone would have a defocusing effect on the beam shape, but it is combined with the effect of the dipolar magnetic field and the net resulting force radially restores the muon beam.
An important parameter when studying the beam motion along the ring is the field index n, defined as:

$$n \equiv \frac{\kappa R_0}{v B_0} \tag{4.3.1}$$

where κ is the electric quadrupole gradient, B_0 the dipole B-field, R_0 the storage ring magic radius of 7112 mm and v the speed of the muon beam. Typical values for n are of the order of $\mathcal{O}(0.1)$. In an ideal ring, vertical dipole magnetic fields and quadrupolar electric fields are uniform and cover the full azimuth, so muons undergo a simple harmonic motion (namely, betatron oscillation), in both the vertical and radial directions, that can be parametrized in terms of n. The effect of the coherent betatron oscillations of the muon beam and the study of the associated systematic error will be discussed in Sections 5.5.1 and 6.3.
Figure 4.2.1(a) shows the location of the most important components of the storage ring, discussed in this Chapter. In addition, collimators are shown, which are copper rings with inner radius of 45 mm, outer radius of 55 mm and thickness of 3 mm.

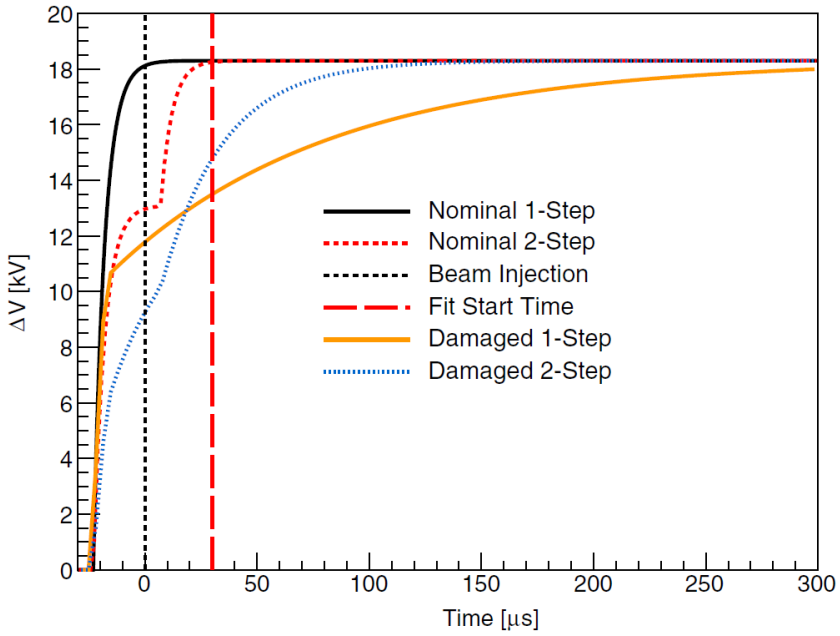

Figure 4.3.1: From Ref. [96]. Patterns of ESQ plates charging for the 30 nominal and for the 2 damaged ESQ resistors, measured after the end of Run-1.

The four ESQ stations are symmetrically placed around the ring, each with a short and a long section (shown by the red curves in Figure 4.2.1(a)). Each section consists of four plates

connected to power supplies through individual high voltage resistors, for a total of 32 plates and 32 resistors. Plates are charged prior to each fill and discharged at the end of the 700 µs storage time. Figure 4.3.1 (black and dotted red lines) shows the nominal procedure to charge ESQ plates: some of them are connected to 1-step power supplies that reach the design voltage of 18 kV with a lifetime of about 5 µs; others are connected to 2-step power supplies, that rise to 5 kV below the design voltage, and after 7 µs rise to the same voltage as the 1-step supplies. This procedure is called "scraping" and it is used in order to scatter away muons that exceed a 45 mm radius: the initial asymmetry displaces the muon beam horizontally and vertically; muons that are further away from the quadrupole center likely strike collimators, scatter, lose energy and drift away from the storage ring in a few turns; when the voltages are symmetrized, the muon beam relaxes back to the nominal center of the closed orbit. Scraping was designed in order to be completed by 30 µs after injection, which is the nominal start time of ω_a fits. However, following completion of the first data-taking campaign in 2018, Run-1, it was discovered that 2 out of 32 ESQ resistors were damaged and dynamically changed their resistances when high voltage was applied. The orange and dotted blue lines in Figure 4.3.1 show the charging patterns of these resistors at the end of Run-1, which strongly affected the muon beam dynamics, enhancing losses over time and increasing the systematic effects on ω_a. These damaged resistors were replaced before the start of Run-2.

4.4 The calorimeter system

When muons decay in the storage ring, the emitted positrons have a lower energy than the parent muons and a smaller orbit radius in the magnetic field, thus they curl towards the center of the ring and may be detected (Figure 4.4.1). There are 24 electromagnetic calorimeters stationed around the inner radius of the storage ring, as schematically shown in Figure 4.2.1(a), which measure the energies and arrival times of incident positrons. They are designed and optimized for the specific needs of ω_a measurement, and constantly calibrated over time, so that all fluctuations in their gain are corrected for (see Section 4.4.2).

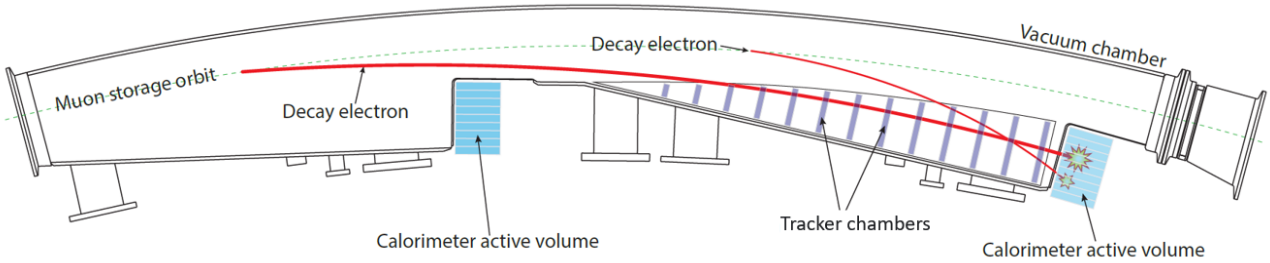

Figure 4.4.1: From Ref. [4]. Scalloped vacuum chamber with positions of calorimeters indicated. A high- (low-) energy decay positron trajectory is shown by the thick (thin) red line, which impinges on the front face of the calorimeter array.

Each segmented calorimeter features an array of 6×9 PbF_2 (lead-fluoride) crystals, with size $25 \times 25 \times 140\,mm^3$, transparent to visible light. Each crystal absorbs the energy of incoming positrons by generating an electromagnetic shower, which is contained thanks to $\sim 15X_0$ of length (for lead-fluoride, $X_0 \approx 0.93\,cm$) and a Molière radius of 1.8 cm. The generated charged particles travel faster than light in the crystal (the refractive index is approximately 1.8), so they generate Cherenkov photons. Each crystal is coupled to a silicon photomultiplier (SiPM) detector with 57344 pixels operating as Geiger counter, which responds to Cherenkov photons with electrical current; this current is then converted by a custom electronic board into voltage

signal, recorded by waveform digitizers and stored for offline analysis.

In order to contain the systematic effects on ω_a, the calorimeter system was designed to meet special requirements [4]. First of all, it was required that the relative energy resolution of reconstructed positron had to be better than 5% at 2 GeV, and, for any positron with energy greater than 100 MeV, the hit time resolution extracted from the SiPM pulse had to be better than 100 ps. As we will explain in Section 4.7.1, the purpose of the energy measurement is only to select events above a fixed threshold for wiggle plots (as it was in previous experiments), so the specification on the energy resolution is rather modest and the deposited energy is not a direct observable in the experiment. In the E821 experiment, the systematic effect associated to pileup amounted to 80 ppb; the goal in the E989 experiment was to lower it down to 40 ppb or below. For this requirement, the calorimeter system had to be able to resolve two different electromagnetic showers with 100% efficiency if they have time separations of 5 ns or more, 66% efficiency below 5 ns and still be able to further resolve showers spatially (thanks to the segmented structure of calorimeter made of 54 crystals, instead of unique blocks of lead-scintillating fibers in previous experiments). An illustration of different decay positrons trajectories, which depend on the decay energy, is given in Figure 4.4.1: high energy positrons are curled inward with a greater orbit radius than low energy positrons, so their trajectory is longer. Thus, two events close in time in the same calorimeter might carry (slightly) different information on the ω_a phase (the angle between muon spin and momentum) at the time of emission, according to their energy. If the events are reconstructed as a single positron, this can modify the wiggle plot counts and also affect the fitted initial phase, thus introducing a systematic uncertainty.

Each of the 24 calorimeters is placed on a movable platform that rides on a set of rails and allows for easy insertion of calorimeters into or out of the storage ring; it also provides sufficient cooling power to stabilize the temperature of all subsystems: the lead-fluoride absorbing crystals, the SiPMs for photodetection, the bias control and voltage amplifiers.

4.4.1 Crystals and SiPMs for photodetection

Incoming positrons deposit energy in each crystal by producing electromagnetic showers that emit Cherenkov radiation. Crystals function as absorbers and the chosen material is lead-fluoride (PbF_2). The advantage of detecting Cherenkov light is that it produces an almost instantaneous signal when positrons arrive, as opposed to scintillators, so a higher time resolution is achieved.

Crystal cross section	$2.5 \times 2.5\,\mathrm{cm}^2$
Array configuration	6 rows and 9 columns
Radiation length X_0	0.93 cm
Crystal length	14 cm ($15X_0$)
PbF_2 density	$7.77\,\mathrm{g/cm}^3$
Magnetic susceptibility	$-58.1 \times 10^{-6}\,\mathrm{cm}^3/\mathrm{mol}$
Molière radius R_M	2.2 cm
Molière radius R_M (Cherenkov only)	1.8 cm
Kinetic $E_{\mathrm{threshold}}$ for Cherenkov light	102 keV
Refraction index	1.8

Table 4.4.1: From Ref. [4]. Properties of PbF_2 crystals used in the E989 experiment.

Table 4.4.1 summarizes the most important characteristics of PbF_2 crystals used at Fermilab [4]. The very low magnetic susceptibility makes the calorimeters suitable for working in

the E989 experiment without perturbing the B-field; thanks to the crystal length of more than 15 radiation lengths and to a Molière radius of 1.8 cm for Cherenkov light, positrons typically deposit all of the energy within a crystal or two; the segmentation 6×9 decreases the likelihood that two decay events occur simultaneously in the same SiPM (double events are referred to as pileup). A refractive index of 1.8 makes sure that all positrons with kinetic energy above 100 keV produce Cherenkov radiation. Each crystal is wrapped in a black Tedlar® absorptive material: it was chosen after a series of tests on different wrapping materials (such as white reflecting Millipore paper and aluminum foil), with the primary goal to optimize the number of photons that reached the SiPMs as well as the distribution spread of the signal. Tedlar® was eventually chosen for the best quality of its sharp signal, that ensures a fast response of the crystal [98].

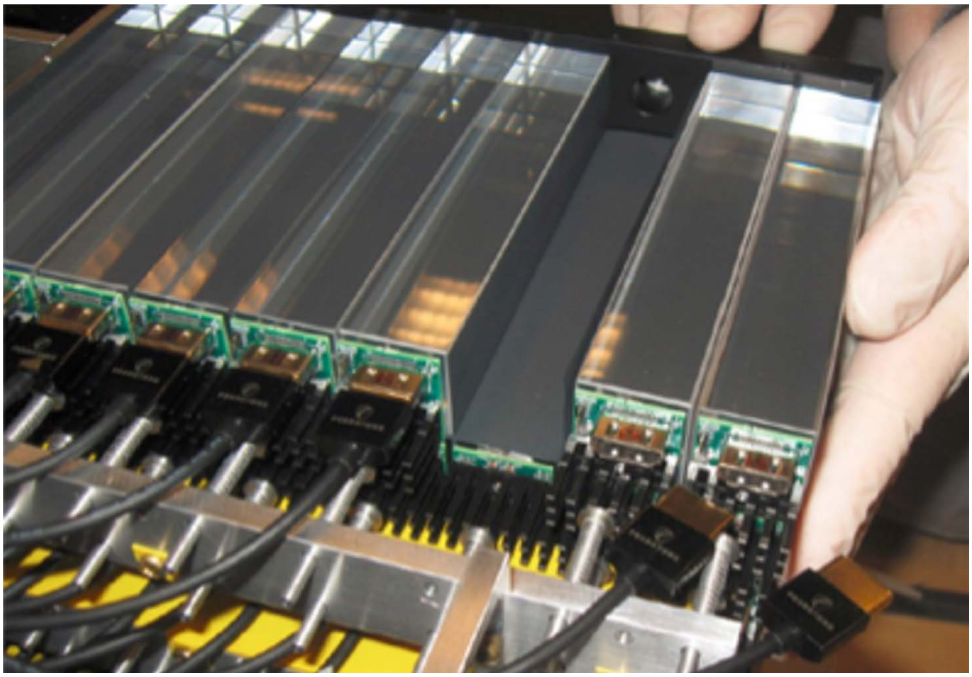

Figure 4.4.2: Picture of PbF_2 crystals taken during calorimeter assembly, each coupled to a SiPM board (green).

Figure 4.4.2 shows a rear view of crystals and SiPM boards. There are several reasons why SiPMs were preferred to photomultipliers (PMTs) as light detectors: they can be placed inside the storage ring field without perturbation, avoiding the long light guides that the E821 experiment used for remote PMTs; they can be mounted directly on the rear face of the PbF_2 crystals; they have a high photo-detection efficiency and they cost less than same-size PMTs. On the other hand, SiPMs are very sensitive to changes in temperature and bias voltage, so it is crucial to calibrate their gain over time.
The SiPMs work as Geiger-mode counters, made of 57344 pixels with a 50 µm pitch, for a total active area of $1.2 \times 1.2\,cm^2$. Each pixel contains a quenching resistor, in series with an avalanche photodiode: when a photon strikes a pixel, it causes an avalanche that is arrested by the resistor by dropping the bias voltage below the Geiger-mode breakdown threshold. The device recovers with a time constant of ~ 10 ns, whereas pixels that were not struck by light remain ready for the next pulse. The produced electric currents are added up for all pixels in a summing board to form the overall response: through a custom electronic readout board with a transimpedance amplifier, this current is converted into a voltage signal and recorded by 12-bit, 800 MS/s waveform digitizers [99]. Power supplies are one every 12-16 SiPMs and must supply a bias voltage in the 60-75 V region, while maintaining a time-averaged current of about

50 µA for each channel, even when higher instantaneous peak currents are present during fill time. Moreover, a stability of 1 mV or better must be achieved: gain shifts are approximately 0.12% per millivolt, which corresponds to a shift in the ω_a fit of 0.05 ppm.
In the "Geiger-mode" operation, a pixel can either fire (produce signal) or not: SiPMs are therefore intrinsically non-linear, because if a pixel is simultaneously hit by two or more photons, it only fires once. The SiPM response is in the linear regime if the number of emitted photons are not more than a few thousands, i.e. 5% of the total number of SiPM pixels. Results from the test beam campaign in 2016 at the SLAC End Station Test Beam facility [100] showed that the typical number of fired pixels was below 3000 for 3 GeV positrons. The calorimeter's energy and time resolutions were measured to be:

$$\frac{\sigma_E}{E} = \sqrt{C_E^2 + \frac{S_E^2}{E/\mathrm{GeV}}}; \qquad \sigma_t(E = 3\,\mathrm{GeV}) = 40\,\mathrm{ps} \tag{4.4.1}$$

where $C_E = (1.86 \pm 0.43)\%$ and $S_E = (3.56 \pm 0.77)\%$. The time resolution is reported in Equation (4.4.1) for an incoming beam energy of 3 GeV; in Ref. [100], the time resolution σ_t is also reported as a function of the incoming beam energy expressed as the number of photo-electrons fired, starting from a value as high as 80 ps at $E \approx 600$ MeV, and decreasing like $1/\sqrt{E}$. It was hence verified that the calorimeter system met the desired resolution goals from the Technical Design Report [4].

4.4.2 The laser calibration system

The E989 experiment requires continuous monitoring and calibration of the SiPMs over the muon fill time-scale of 700 µs, where the rate of detected events changes by 4 orders of magnitude. Monitoring of the gain over longer terms (months or even years, mostly due to external temperature changes) is also achieved at sub per-mill level. These requirements ensure that the systematic error on ω_a due to gain changes, which amounted to 120 ppb in the E821 experiment and was hence the main source systematics, does not exceed 20 ppb in the E989 experiment. For this purpose, a state-of-the-art laser calibration system was designed and built by the INFN group in collaboration with CNR-INO (Istituto Nazionale di Ottica). The system sends simultaneous calibration pulses onto each of the 1296 crystals of the electromagnetic calorimeters. Laser pulses must be stable in intensity and timing; they are generated by 6 identical laser diode heads (Picoquant, mod. LDH-P-C-405M), 700 pJ/pulse, 600 ps (FWHM) duration, each one serving 4 calorimeters. The muon beam cycle was schematically sketched in Figure 4.1.2: laser calibration pulses can be sent before and after fills (in which case they are called Out-of-Fill Pulses, or OOF) or within a fill (the so-called In-Fill-Gain pulses, or IFG). A diffusing system sends the light pulses to all 54 detectors of each of the 24 calorimeters and a cascaded distribution system monitors the pulses at different stages: a Source Monitor, placed directly at each laser head, keeps the stability of the laser source under control; a Local Monitor is placed after each diffusing system to monitor its stability.
Most of the laser apparatus is in a dedicated room, the Laser Hut, located inside the $g-2$ experimental hall. It is a 4 by 4-meter wide, light-tight, acoustically isolated and thermally controlled room, from where laser calibration pulses are sent to calorimeters through 24 launching optical fibers (Polymicro, mod. FDP400440480), 25 m long and 400 µm of diameter, as seen in Figure 4.4.3. Laser monitoring signals from calorimeters are sent back to the Hut by 48 fibers: 24 are 1 mm of diameter PMMA fibers (Mitsubishi Eska, mod. GK40) and 24 are 600 µm of diameter silica fibers (Thorlabs, mod. FP600URT). The launching fiber and the two monitoring fibers of each calorimeter are inserted into protective, semi-rigid plastic tubes that guide them inside the ring to each calorimeter, keeping them separated from the other electric cables.

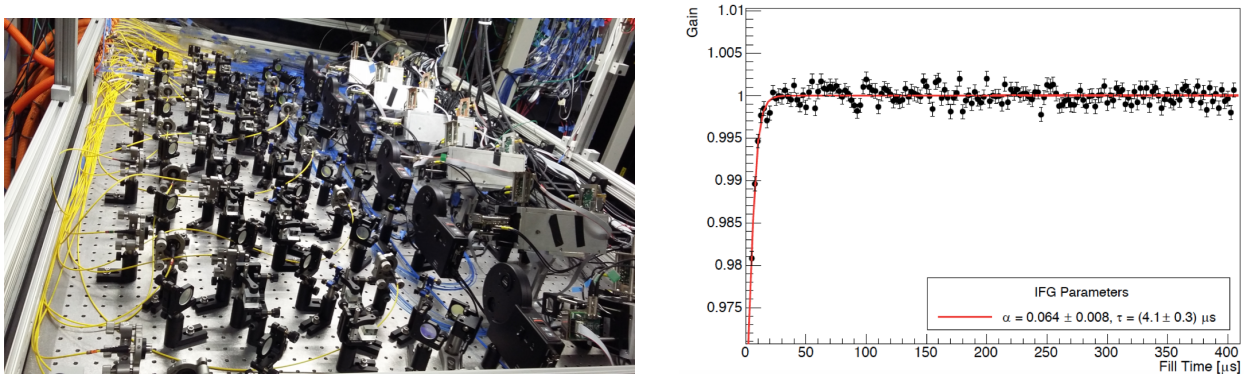

(a) **(b)**

Figure 4.4.3: (a): Picture overviewing the optical table. On the right side, the 6 laser heads are partially hidden by the 6 Source Monitors (silver aluminum boxes). On the left, the 25-meter-long optical fibers bring light to the 24 calorimeters. (b): Example of In-Fill-Gain function for a single SiPM, with an exponential fit (overlapped in red) to extract IFG constants for energy calibration.

The choice to serve 4 calorimeters with each laser head was conservative, as the laser power available exceeds what is actually required by over a factor 4, but it allows special calibration modes: the first one is the Standard Mode, in which 4 laser pulses with a relative delay of about 200 µs are sent in $\sim 9\%$ of the fills, each pulse shifted by 2.5 µs during the next fill, so that the four pulses sweep the entire 700 µs of storage time in 93 fills; the second one is the Double Pulse Mode, in which laser lights are re-directed by means of movable mirrors, in such way that 2 laser beams slightly separated in time hit the same crystal of a calorimeter.
The Standard Mode is used to provide the In-Fill-Gain and Out-of-Fill Gain corrections - IFG and OOF, respectively - and to synchronize the different detectors, frontend electronics and DAQ. Figure 4.4.3(b) shows an example of how the gain of a SiPM changes within a fill: the initial flash of particles causes charge depletion in the first microseconds, so the SiPM gain reaches its asymptotic value on a timescale of $\mathcal{O}(1\,\mu s)$. The IFG function is modeled with an exponential function $G(t;a,\tau) \equiv 1 - a\exp(-t/\tau)$, and data collected by laser calibration is fitted to determine the (a,τ) parameters. Energies deposited on each crystal at time t are therefore divided by $G(t)$, to correct for this effect.
The Double Pulse Mode is used to study the response of SiPMs when two positrons hit the same calorimeter within a few nanoseconds: the expectation is that the first pulse causes a systematic reduction in the measured energy of the second signal due to charge depletion in the capacitive components of the system's electronics [99].

More details about the laser system and the optics to diffuse the laser light to calorimeters are provided in the papers in Ref. [101]. The gain corrections applied to detected positron energies in the event reconstruction are described in full in Section 5.2.2, whereas the systematic associated to gain corrections that affect ω_a are described in Section 6.1.

4.5 The tracker system

In the design of the E989 experiment, two tracking stations [102] are placed around the storage ring at approximately 180° and 270° after the injection point, in front of calorimeters 13 and 19 as in Figure 4.2.1(a). These locations are advantageous because they are unobstructed by quadrupoles or collimators. Each tracking station consists of 8 tracking modules, that are

inserted in the vacuum chamber in a "staircase" arrangement, as shown in Figure 4.5.1(a). Each module has four layers of drift tubes: the straws are arranged in a stereo pattern, with a stereo angle of $\pm 7.5°$ from the vertical direction, to provide information on both x and y positions of the track, with a resolution of at least 1 mm on impact parameter. Each straw is 10 cm long and has a 5 mm diameter; the total thickness of the wall, made of two layers of Mylar (a special type of stretched polyester film) separated by an adhesive layer, is 15 µm. Sense wires, centered in the straws, are made of 25 µm of gold-plated tungsten and are held at a voltage of 1800 V. Drift gas in the tubes are a mixture of 50:50 Argon:Ethane at 1 atm pressure, which provides a $\sim 2 \times 10^6$ gain. The flow of tracker data processing starts with the induced signal on sense wires; a hierarchical system of analog and digital frontend electronics and backend aggregator electronics boards is used to make the data flow and eventually reconstruct particle tracks and extrapolate muon decay vertices. Figure 4.5.1 shows the location and schematic of tracking modules, placed in the scallop region of the vacuum chamber in front of calorimeters. Tracking detectors have three important physics goals [4]:

1. Measure the muon beam profile at two locations around the storage ring as a function of time;
2. Improve the understanding of systematic uncertainties on ω_a, that are derived from calorimeter data;
3. Make auxiliary measurements of other properties of the muon, for example its electric dipole moment (EDM).

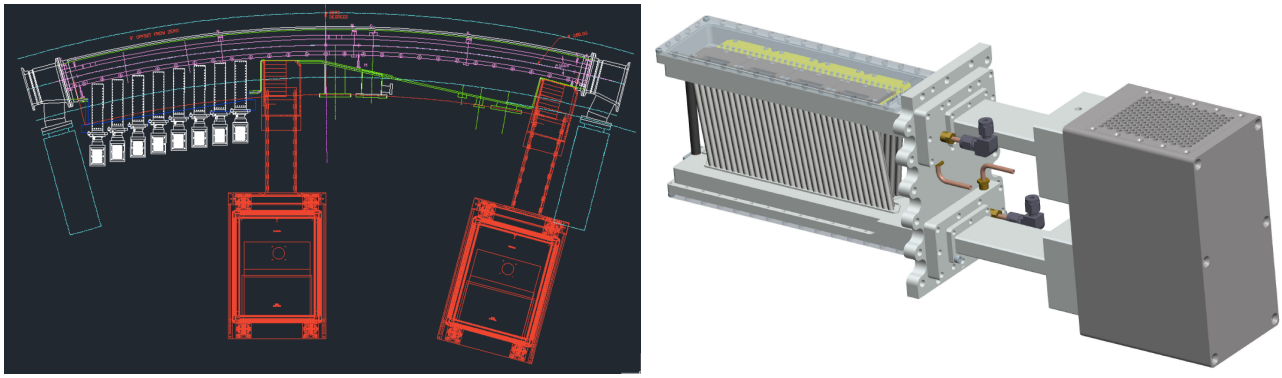

(a) **(b)**

Figure 4.5.1: From Ref. [4]. (a) Placement of 8 straw tracking modules in one of the 12 vacuum chambers. (b) Diagram of a 32-straw-wide tracking module together with the readout electronics attached.

There are several reasons why the muon beam distributions must be tracked precisely over fill time. Firstly, momentum spread and betatron motion of the beam lead to beam dynamics corrections to ω_a (discussed in Section 4.7.3) of the order of hundreds of ppb, because the beam motion is not exactly perpendicular to the B-field and in general the momentum can slightly differ from the magic value of 3.094 GeV/c. Secondly, the coherent betatron motion causes changes in calorimeter counts which must be taken into consideration when fitting wiggle plots to extract the precession frequency, and trackers play a key role in the correct parametrization of this effect (the procedure is explained in Section 5.5.1). Lastly, the muon spatial distribution must be convoluted with the measured magnetic field map, to obtain the effective field felt by the beam in the storage ring (this will be discussed in Section 4.7.4).
Trackers can also isolate short time windows that have multiple positrons hitting the same

calorimeter, so that an independent measurement of the momentum of incident muons is possible: this provides an independent validation of techniques used on calorimeter data to estimate the systematic uncertainties, such as the number of muon losses over time (see Section 5.2.4) based solely on calorimeter data.
Finally, trackers can determine if there is any tilt in the muon precession plane away from the vertical orientation: this could be indicative of radial or longitudinal components of the storage ring B-field, or the presence of a permanent EDM of the muon. The technique for this measurement was explained in Section 2.2.2.

4.6 Auxiliary detectors

Several other detectors are placed around the ring, to provide us with information on the stored beam. The measurements from these detectors play an important role in systematics studies, or during preparation of new data acquisition campaigns every year, when we performed the initial detector calibrations.

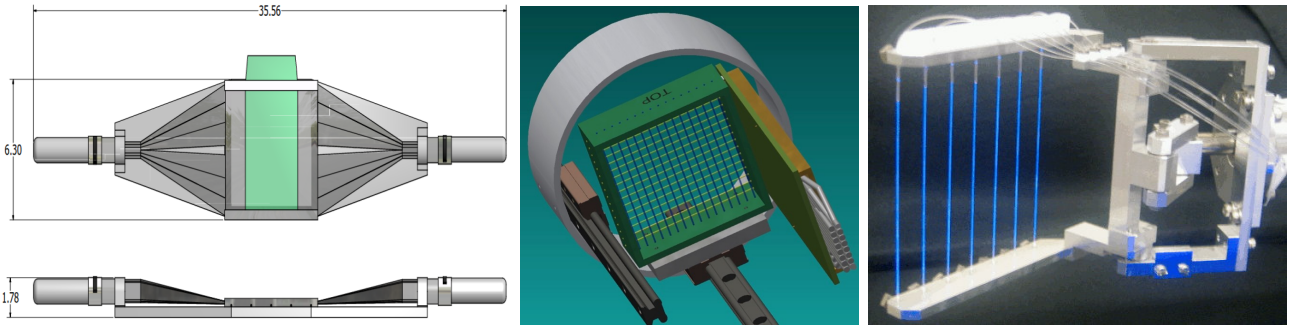

(a) **(b)** **(c)**

Figure 4.6.1: (a) CAD drawing of the T0 detector. The muon beam passes through the plastic scintillator (green). (b) CAD drawing of the IBMS detector. (c) The 180° x-profile monitor, glowing under ultraviolet illumination in the laboratory.

The T0 detector is a paddle composed of a 1 mm thick plastic scintillator coupled to two PMTs, as shown in Figure 4.6.1(a). It is placed right before the inflector, so it precisely measures the time at which the muon beam is injected into the magnet. It also measures the beam time profile, which can be integrated to monitor the storage efficiency (when compared to the number of detected positrons for each muon fill) and data quality across the data taking period.
The Inflector Beam Monitoring System (IBMS) is a series of three detectors, each made of a 16×16 grid of scintillating fibers read by a $1\,\text{mm}^2$ Hamamatsu SiPM. Two of them are placed before the inflector: one before the hole in the yoke, one right before the inflector, as seen in Figure 4.2.1(a). These two detectors monitor the beam profile in the x-axis and y-axis, after the final focusing before injection. The third IBMS detector is installed right after the inflector and only has the vertical fibers to measure the x-axis profile; in normal running conditions, the third detector is retracted as, otherwise, it would destroy the muon beam after several turns.
The Fiber Harps are planes of vertical and horizontal scintillating fibers that can be placed in the path of the muon beam in two different locations, at $\sim 180°$ and $\sim 270°$, right before each tracking station. They can destructively measure the beam $x-y$ profile and therefore they are used only in dedicated runs and not during normal data taking. Figure 4.6.1(c) shows a picture of the x Fiber Harp detector. When inserted, they can measure the beam momentum distribution, the cyclotron frequency and the debunching of the muon beam over time.

4.7 Measurement principle of a_μ in the Fermilab experiment

The goal of the Muon $g-2$ experiment at Fermilab is to measure the muon magnetic anomaly a_μ at the 0.14 ppm level of precision, a fourfold improvement with respect to the previous experiment. Section 1.3.2 introduced the measurement principle on which the experiment is based: when muons are injected in a magnetic field $\vec{B}$, their spin vector precesses around the momentum vector with the so-called anomalous precession frequency ω_a. If the motion is perpendicular to the B-field so that $\vec{\beta} \cdot \vec{B} = 0$, and if muons have the magic momentum $p = 3.094\,\mathrm{GeV}/c$ that cancels the effect of focusing electric fields on ω_a, then Equation (1.3.9) becomes:

$$\vec{\omega}_a = -a_\mu \frac{QeB}{m} \tag{4.7.1}$$

where Q is the particle charge ($Q = -1$ or $Q = +1$, for muons and antimuons, respectively) and $e > 0$ is the absolute value of elementary electric charge. Two different measurements of high precision are needed to extract a_μ: the first one is ω_a, which can be fitted from the time distribution of decay positrons detected by calorimeters; the second one is the magnetic field, expressed by means of the Larmor precession frequency of free protons in the same B-field felt by muons, via $\omega_p = 2\mu_p|\vec{B}|$. Expressing the magnetic field as a function of ω_p and using $\mu_e = g_e e\ /4m_e$, with g_e from Ref. [20], Equation (1.3.7) can be rearranged:

$$a_\mu = \frac{\omega_a}{\omega_p}\,\frac{\mu_p}{\mu_e}\,\frac{m_\mu}{m_e}\,\frac{g_e}{2} \tag{4.7.2}$$

The first ratio ω_a/ω_p is obtained directly in the E989 experiment, measuring ω_a through the wiggle plot fit and ω_p with nuclear magnetic resonance (NMR) probes. The other quantities are well-known constants from other experiments, which carry a small overall uncertainty of ~ 25 ppb. The actual complete formula for a_μ is more complicated [3] and it will be explained throughout this Section:

$$a_\mu = \underbrace{\left[\frac{f_{\mathrm{clock}} \cdot \omega_a^m \left(1 + C_e + C_p + C_{pa} + C_{dd} + C_{ml}\right)}{f_{\mathrm{calib}} \cdot \langle \omega_p'(\vec{r}) \times M(\vec{r}) \rangle \left(1 + B_q + B_k\right)}\right]}_{\mathcal{R}_\mu} \frac{\mu_p(T_r)}{\mu_e(H)}\,\frac{\mu_e(H)}{\mu_e}\,\frac{m_\mu}{m_e}\,\frac{g_e}{2} \tag{4.7.3}$$

At the numerator, ω_a^m is the measured value of the precession frequency from wiggle plot fits, and it is multiplied by correction factors C_i that come from beam dynamics. At the denominator, the shielded ω_p' is weighted by the muon beam spatial distributions, and corrected by two fast magnetic transients B_i, from kickers and quadrupoles, synchronized to the beam injection. The unblinding factor f_{clock} is set and monitored by external and unknown people to the Muon $g-2$ collaboration, and it is in the range ± 25 ppm, to prevent any conscious or unconscious biases on our measurement. $T_r = 34.7°$ is the reference temperature at which the shielded proton-to-electron magnetic moment $\mu_p(T_r)/\mu_e(H)$ is measured [103]. The QED factor $\mu_e(H)/\mu_e$ is the ratio of the magnetic momentum of the electron in a hydrogen atom to the magnetic momentum of the free electron in vacuum [104]. The ratio in masses m_μ/m_e was measured to 22 ppb with muonium spectroscopy [105], and new precise measurements from several experiments (such as MuSEUM at J-PARC [106] and Mu-MASS at PSI [107]) are expected soon.

4.7.1 Measurement of ω_a

In the E989 experiment, a beam of polarized muons is injected into the storage ring in presence of a magnetic field. The anomalous precession frequency ω_a is the rate at which the angle

between the muon spin and muon momentum precesses over the fill time of 700 µs. This frequency is approximately equal to 1.43 rad/µs, corresponding to a period of ~ 4.365 µs. The analysis procedure is to identify individual decay positrons that hit the calorimeters, record their energy and arrival time, and plot the time distribution of positrons above a fixed energy threshold to build the so-called "wiggle plot" (an example is in Figure 4.7.1(a)).

As anticipated in Section 1.3.3, the number of positrons detected above a certain threshold E_{th} is given by a function like Equation (1.3.21):

$$N(t) = N_0(E_{th})e^{-t/\gamma\tau}\left[1 + A(E_{th})\cos(\omega_a t + \phi)\right] \tag{4.7.4}$$

where the normalization parameter N_0 and the asymmetry A depend on E_{th}. Figure 1.3.6 in Section 1.3.3 plotted these parameters in the ideal case; in our analysis, we fit these parameters as they are affected by detector acceptance and beam dynamics of the muon beam (see Section 5.5).

There are several ways to build wiggle plots, according to how we weight positron events depending on their energies: each method has a different statistical power as a function of the energy threshold. At the end of Section 1.3.3, we anticipated that the optimal threshold is the one that maximizes a Figure of Merit (FOM) and minimizes the statistical uncertainty $\delta\omega_a$ on the anomalous precession frequency. Detailed studies [26] showed that $\delta\omega_a$ can be parametrized as:

$$\delta\omega_a = \sqrt{\frac{2}{N(\gamma\tau)^2}\cdot\frac{\langle p^2\rangle_{E_{th}}}{\langle pA\rangle^2_{E_{th}}}} \tag{4.7.5}$$

where N is the integrated number of decay positrons in the analysis; p is the function that we choose to weight positrons according to their energy E, and that characterizes each different method; the notation $\langle\cdot\rangle_{E_{th}}$ means that we take the average over all detected positrons above the energy threshold. The method discussed in Section 1.3.3 was the so-called T-method, where all positrons above threshold are equally weighted, i.e. $p(E) = 1$, and the FOM reduces to NA^2 which is maximum around 1.86 GeV.

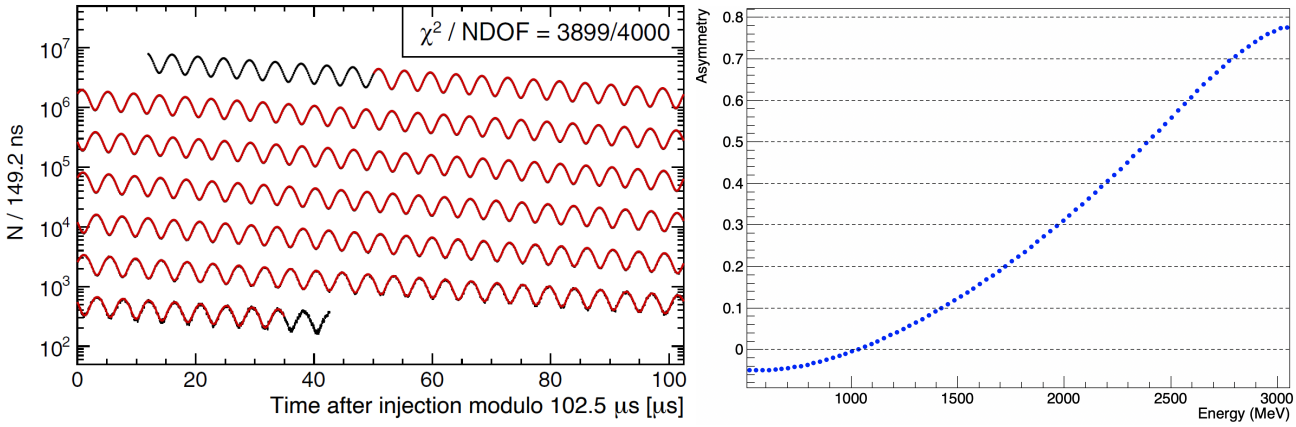

(a) Run-1 T-method wiggle plot.

(b) A-Method energy weights.

Figure 4.7.1: (a): wiggle plot built for ω_a fit in Run-1 [108]. (b): $A(E)$ asymmetry parameter fitted from T-Method wiggle plots for each energy bin.

The main two methods in Run-1 analysis were:

- **Threshold Method** or **T-Method**: all positron events are integrated in energy above a fixed threshold, with equal weights ($p(E) = 1$). An example is in Figure 4.7.1(a), taken from the Run-1 result. The shape of oscillations is such that the histogram has been historically called "wiggle plot", and it is typically convoluted many times so that it can fit in one plot. For this method, it was found that the statistical uncertainty on ω_a is minimum if we integrate energies above 1.7 GeV (see Section 5.2.6).

- **Asymmetry Weighted Method** or **A-Method**: each positron event is weighted with the asymmetry function $A(E)$ as a function of the positron energy. In the ideal case, this function is represented by Equation (1.3.16) and plotted in Figure 1.3.5. The function obtained by Run-1 data is plotted in Figure 4.7.1(b). Visually, the A-Method wiggle plot is very similar to the T-Method one. This technique yields the maximum possible statistical power, lowering the optimal energy threshold to 1 GeV and the statistical uncertainty on ω_a to $\sim 10\%$ less than the T-Method.

In Run-1 there were two other methods developed to build wiggle plots, not used for the combination of ω_a results but for consistency checks and evaluation of systematic uncertainties:

- **Integrated Energy Method** or **Q-Method**: in this alternative approach, the detector current is used as a proxy for the deposited positron energy. Individual positron events are not identified, which suppresses the pileup systematic and allows for a very low energy threshold. The statistical power of this approach almost reaches that of the T-method. Further details on the Run-1 and Run-2/3 analysis are found in [109, 110].

- **Ratio method** or **R-Method**: an alternative approach which consists in randomly splitting positron events into 4 separate groups, shifting some of them in time, and combining them in order to cancel out the exponential term in the 5-parameter function. This method will be explained in much more detail in Section 5.3. In general, it reduces the sensitivity of ω_a to all "slow" terms (i.e. the ones that change within 700 µs) and therefore the associated systematics. Its statistical power is similar to that of the T-method.

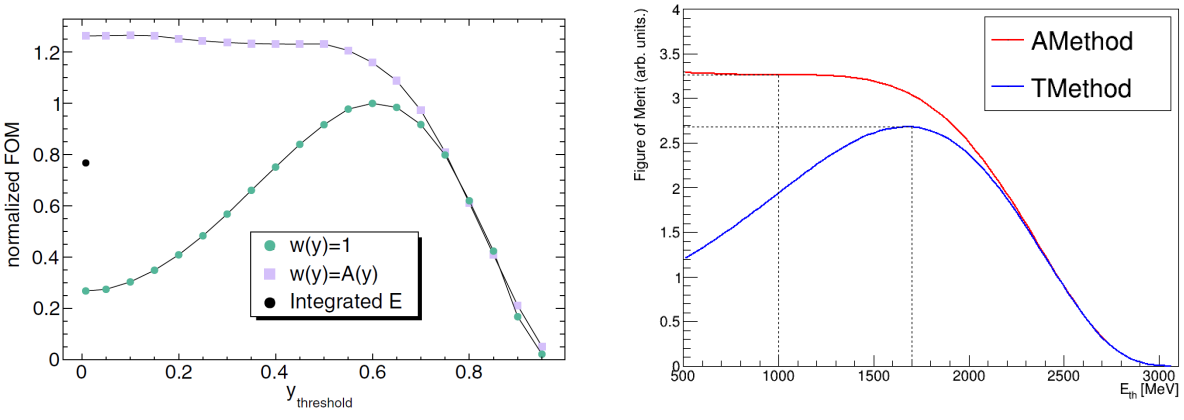

(a) **(b)**

Figure 4.7.2: (a): From Ref. [4]. The statistical figures of merit are calculated using a Monte Carlo simulation for the T/A Methods as a function of the energy threshold E_{th}. The simulation included basic detector acceptance. y is the positron energy normalized to the maximum value of 3.1 GeV in the laboratory frame. The isolated black point indicates the corresponding figure of merit for the Q-Method. (b): ω_a figure of merit as a function of the energy threshold E_{th} for the Run-2 T-Method and A-Method fits.

Figure 4.7.2(a) shows the results of FOM for T/A/Q Methods, obtained thanks to a Monte Carlo simulation. Figure 4.7.2(b) shows the FOM obtained from Run-2 data.
In Run-2/3, we developed another method which is the "asymmetry weighted" version of the R-Method and yields a statistical uncertainty similar to A-Method results: the so-called **RA-Method**. This has been my major contribution in my analysis group, and I will describe it in detail in Section 5.3.

4.7.2 Coherent Betatron Oscillation and other beam dynamics effects

Assuming that vertical dipole magnetic fields and quadrupolar electric fields are uniform and cover the full azimuth, stored muons undergo a simple harmonic motion called "betatron oscillation" in both the vertical and radial directions. The horizontal and vertical motions have different frequencies, determined by the cyclotron frequency ω_C and by the field index n (defined by Equation (4.3.1)):

$$\omega_x = \omega_C\sqrt{1-n}; \qquad \omega_y = \omega_C\sqrt{n} \tag{4.7.6}$$

The cyclotron period in the Muon $g-2$ experiment is 149.2 ns, and $n \approx 0.1$ (see Section 5.1), which means that $\omega_C \approx 42$rad/µs, $\omega_x \approx 40$rad/µs and $\omega_y \approx 14$rad/µs. It is important that the betatron wavelengths are not simple multiples of the circumference, otherwise ring imperfections or higher multipoles could drive resonances and cause a great particle loss from the storage ring.
The beam oscillations introduce a time-dependent modulation in the number of detected positrons due to the radial and vertical acceptance of the detectors. Figure 4.7.3 helps to understand this effect: a bunch of muons starts in $s = 0$ (s is the arc length along the trajectory) and oscillates in the radial direction with frequency $\omega_x < \omega_C$, such that $\lambda_x > 2\pi\rho$ where $2\pi\rho$ is the circumference of the ring. Several successive revolutions around the ring are shown, so the vertical axis (which shows the radial coordinate of the bunch) is repeated several times and so is the position of one of the calorimeters.

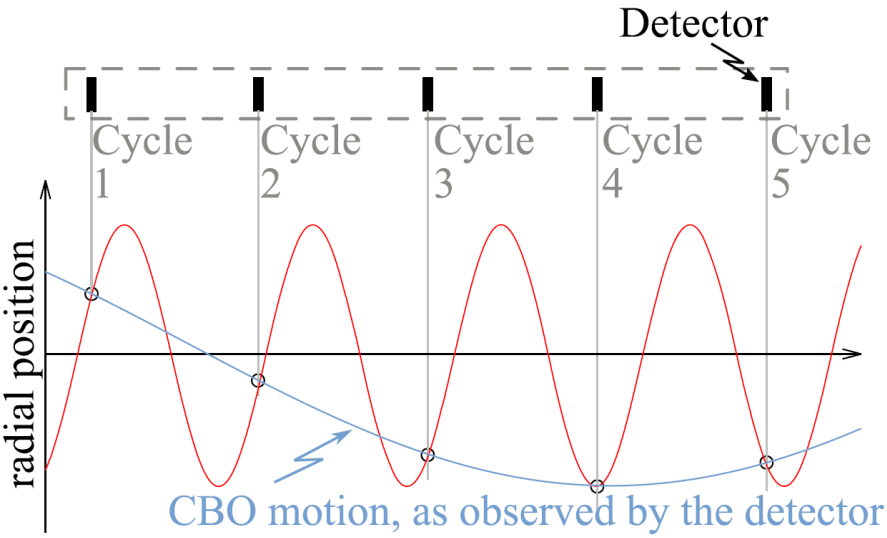

Figure 4.7.3: From Ref. [111]. Illustration of the radial beam motion in the storage ring, showing successive turns in the ring. The betatron oscillation (red) frequency is adjusted to be less than the cyclotron frequency. A detector sees the motion at the CBO frequency. The location of a single detector is shown.

The rate at which the muon bunch moves toward and then away from the detector is given by the Coherent Betatron Oscillation (CBO) frequency: $\omega_{CBO} \equiv \omega_C - \omega_x$. In other words, since $\omega_x > \omega_C/2$, the Nyquist-Shannon sampling theorem states that ω_x is not directly measurable, but the aliased frequency ω_{CBO} is. The radial motion of the beam has also got components at $2\omega_x$, so in the ω_a analysis the $2\omega_{CBO}$ frequency is observed as well. Things are different in the vertical direction: ω_y is less than $\omega_C/2$ and thus it is observed unchanged; however, the components at $2\omega_y$ introduce the frequency $\omega_{VW} \equiv \omega_C - 2\omega_y$, where VW stands for Vertical Waist, i.e. the position where the beam's vertical width is at minimum. The Vertical Waist travels along the ring with ω_{VW} frequency, which is observed in our wiggle plot data. The values of all the above-mentioned frequencies are listed in Table 4.7.1 for the Run-2 value of the field index $n = 0.108$ (see Section 5.1.1).

Quantity	Expression	Frequency [MHz]	Frequency [rad/μs]	Period [ns]
ω_a	$ea_\mu B/m$	0.23	1.439	4365
ω_C	v/R_0	6.7	42.0	149.2
ω_x	$\omega_C\sqrt{1-n}$	6.3	39.7	158.0
ω_y	$\omega_C\sqrt{n}$	2.2	13.8	454.2
ω_{CBO}	$\omega_C - \omega_x$	0.37	2.33	2686
ω_{VW}	$\omega_C - 2\omega_y$	2.3	14.4	435.3

Table 4.7.1: Frequencies in the $g-2$ storage ring, assuming the quadrupole field is uniform in azimuth and that $n = 0.108$ (Run-2).

4.7.3 Beam dynamics corrections C_i

The anomalous precession frequency ω_a is extracted from wiggle plot fits. The quantity that we measure, indicated with ω_a^m in Equation (4.7.3), is not exactly the precession frequency ω_a because there are deviations from the ideal formula due to beam dynamics effects. The electric field C_e and pitch C_p corrections make the spin precess slower than in the ideal experiment; the phase acceptance C_{pa}, differential decay C_{dd} and muon losses C_{ml} corrections affect the average muon initial phase ϕ of Equation (4.7.4) over fill time, thus biasing ω_a. In general, if the phase ϕ changes early-to-late, i.e. varies within the fill time of 700 μs and takes the form $\phi(t)$, then it can be expanded into $\phi(t) \approx \phi(0) + \frac{d\phi(0)}{dt}t$ and the wiggle plot fit will not measure the real value of ω_a, but $\omega_a + \frac{d\phi(0)}{dt}$. Ref. [112] reviews in great detail the beam dynamics effects and in particular the C_{pa} correction in the Run-1 and Run-2/3 results.
Many results presented in this Section incorporate comparisons with dedicated beam simulations, described in detail in Ref. [96]: the GEANT4-based GM2RINGSIM models the storage ring, the final focus beamline used to steer the beam into the ring, all of the active detectors and most of the passive components installed in the storage ring [113]. The COSY INFINITY is a data-driven simulation, that recreates the injected muon with high fidelity by representing the magnetic and electric guide fields in the storage region based on measurements of the beam [114].

Electric field correction C_e

In the ideal case, the anomalous precession frequency is proportional to the magnetic anomaly and to the B-field, as in Equation (4.7.1): this proportionality is only valid if the muon beam travels at the magic momentum, so that the effects of the quadrupole electric field are cancelled, and that the muon velocity is always perpendicular to the storage ring magnetic field. In the more general case, the anomalous precession frequency contains a term proportional to the E-field, as in Equation (1.3.9). For muons at the magic momentum of $p_\mu = 3.094\,\mathrm{GeV}/c$

(relativistic boost of $\gamma_\mu \approx 29.3$), this term vanishes and the electric field does not contribute to ω_a. In our experiment, the storage ring has a momentum acceptance of $\pm 0.5\%$, which means that not all muons travel exactly at the magic momentum. Therefore, the radial component of the electric field E_r modifies ω_a:

$$\omega_a^m = a_\mu \frac{e}{m} B \left[1 - \beta \frac{E_r}{cB_y} \left(1 - \frac{m^2 c^2}{a_\mu p^2} \right) \right] \tag{4.7.7}$$

where B_y is the y-axis component of the B-field, and p is the muon momentum. The mean radial electric field experienced by a muon oscillating around an equilibrium radius x_e is:

$$E_r = \kappa x = \frac{n\beta c B_y}{R_0} x, \qquad \langle E_r \rangle = \kappa x_e = \frac{n\beta c B_y}{R_0} x_e \tag{4.7.8}$$

where κ is the electric quadrupole gradient and n the field index, defined in Section 4.3, and R_0 is the magic orbital radius. The electric field correction that needs to be applied to ω_a^m can be expressed in terms of the beam radial distribution [4]:

$$C_e = -\langle \frac{\Delta\omega_a}{\omega_a} \rangle = 2 \frac{\beta \langle E_r \rangle}{cB_y} \frac{\Delta p}{p_0} \approx 2n(1-n)\beta_0^2 \frac{\langle x_e^2 \rangle}{R_0^2} \tag{4.7.9}$$

where β_0 is the speed of the muons with magic momentum, and $\Delta p/p_0$ is the momentum spread around the magic momentum, equal to $\Delta p/p_0 = (1-n)x_e/R_0$. It follows that C_e is always positive, meaning that the electric field effect reduces the value of the measured precession frequency from the ideal one.
The beam distribution x_e is measured by analyzing the cyclotron motion of the muons using the calorimeter data, exploiting the fact that x_e is related to the revolution frequency:

$$\omega_C = \frac{c\beta}{R_0 + x_e} \tag{4.7.10}$$

so x_e is actually defined to be zero when the equilibrium radius is the magic radius R_0. $\langle x_e^2 \rangle$ is the time-average of x_e^2. Figure 4.7.4(a) shows the measured distribution for the four different datasets. The value of C_e was 489(53) ppb in Run-1 and 451(32) ppb in Run-2/3 [1, 3].

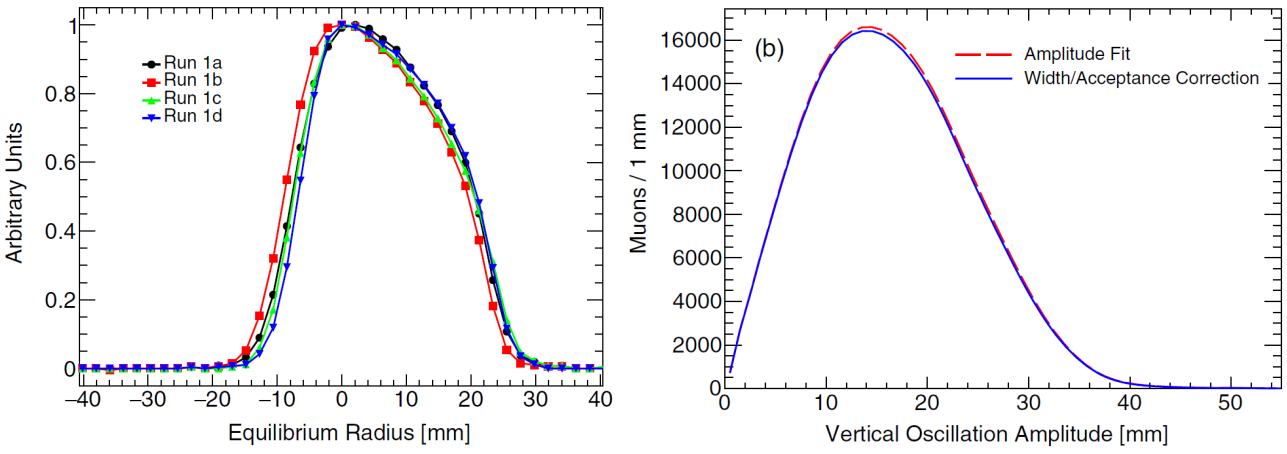

(a) **(b)**

Figure 4.7.4: From Ref. [96]. (a): radial distribution of the muon beam as determined by the Fourier method [115], Run-1 data. The equilibrium radius is defined to be 0 mm at the magic momentum. (b): the fitted distribution of vertical oscillation amplitudes, before and after the azimuthal averaging and calorimeter acceptance corrections described in the paper.

Pitch correction C_p

The pitch correction is related to the vertical betatron oscillation of stored muons, that breaks the assumption that $\vec{\beta}\cdot\vec{B}=0$. This means that the term proportional to $(\vec{\beta}\cdot\vec{B})\vec{\beta}$ in Equation (1.3.9) does not cancel out, and ω_a is affected by it. The term is quadratic in $\vec{\beta}$, so its contribution to the precession frequency will not generally average to zero. Vertical oscillations are the only significant correction to the precession frequency: thus the name "pitch correction", since the pitch angle is the one between the momentum and the horizontal plane. Figure 4.7.5 shows the pitch angle ψ between the muon momentum and the horizontal plane; two dashed lines indicate the directions parallel and orthogonal to $\vec{\beta}$.

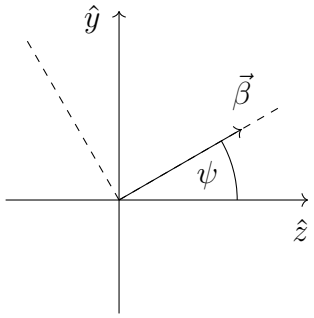

Figure 4.7.5: The coordinate system of the pitching muon. The angle ψ varies harmonically. The vertical direction is $\hat{y}$, whereas $\hat{z}$ is the azimuthal (beam) direction.

We adopt the system of coordinates in Figure 4.7.5, which rotates along the storage ring, in such way that $\hat{z}$ is the direction of propagation. Then, we can write the magnetic field as $\vec{B}=B_y\hat{y}$ and the velocity as $\vec{\beta}=\beta_y\hat{y}+\beta_z\hat{z}=\beta\sin\psi\,\hat{y}+\beta\cos\psi\,\hat{z}$. Assuming that ψ is small enough to approximate $\sin\psi\approx\psi$ and $\cos\psi\approx 1-\psi^2/2$, we find:

$$\omega^m_{a,\,y}=a_\mu\frac{e}{m}B\left[1-\left(\frac{\gamma-1}{\gamma}\right)\psi^2\right];\qquad \omega^m_{a,\,z}=-a_\mu\frac{e}{m}B\left(\frac{\gamma-1}{\gamma}\right)\psi \tag{4.7.11}$$

Equation (4.7.11) projects $\vec{\omega}^m_a$ onto the y-axis and z-axis; it can also be projected onto the parallel and perpendicular axes to $\vec{\beta}$. Since the pitch angle oscillates rapidly with the vertical betatron frequency ω_y, much larger than ω_a (see Equation (4.7.6)), the parallel component of $\vec{\omega}^m_a$ cancels out in the time average. Therefore, $\omega^m_a\approx\omega_\perp$ and taking the time average yields a pitch correction [96, 116]:

$$C_P=\frac{n}{2}\frac{\langle y^2\rangle}{R_0^2} \tag{4.7.12}$$

The quantity $\langle y^2\rangle$ can be determined experimentally from tracker measurements of the beam motion: Figure 4.7.4(b) shows the measured distribution from Run-1. Like the electric field correction, this effect reduces the precession frequency so that the measured value is lower than the ideal experiment, thus C_p is always a positive correction. The value of C_p was 180(13) ppb in Run-1 and 170(10) ppb in Run-2/3 [1, 3].

Phase acceptance correction C_{pa}

The $g-2$ initial phase ϕ in the 5-parameter expression of Equation (4.7.4) represents the average phase of the muons at the time of injection. As already stated at the beginning of Section 4.7.1, in the real experiment the parameters N_0, A and ϕ are time dependent due to effects like detector acceptance and beam dynamics. The phase ϕ is originally related to the phase of muon spin vector relative to momentum at the time of injection into the storage ring, but also

has other components such as the drift time of decay positrons according to their energies, and calorimeter acceptance versus time.
It is easy to derive that higher energy positrons have a larger radius of curvature and therefore a longer trajectory path toward the calorimeters (see Figure 4.4.1). A detected positron at time t was therefore produced at $t' < t$, when the angle between muon spin and momentum was slightly different. Since the precession frequency is approximately 1.44 rad/µs, a drift time (defined as $t - t'$) of 1 ns accounts for a shift in phase of 1.44 mrad. A typical shift in phase due to drift time, for positrons with energies of $1.5 \div 2.5$ GeV, is $10 \div 15$ mrad. For higher energy positrons, near 3 GeV, this can reach $30 \div 40$ mrad.
The measured phase also depends on the position of the decay vertex. Firstly, if a muon decays closer to the calorimeters, the emitted positron will travel a shorter path on average with respect to the ones that are emitted more radially outwards. Secondly, since positrons curl radially inwards when they are emitted, the configuration that maximizes detector acceptance is not when the muon spin is parallel to the momentum, but when it is slightly rotated inwards. These two effects are a function of the coordinates x and y on the transverse profile of the muon beam, and of the positron energy E, so they generate an effective phase shift $\phi_{pa}(x, y, E)$. Figures 4.7.6(a) and 4.7.6(b) show, respectively, the azimuthally averaged transverse distribution measured in Run-1, and GM2RINGSIM simulation of the transverse "phase map" averaged over the azimuth angle [96].

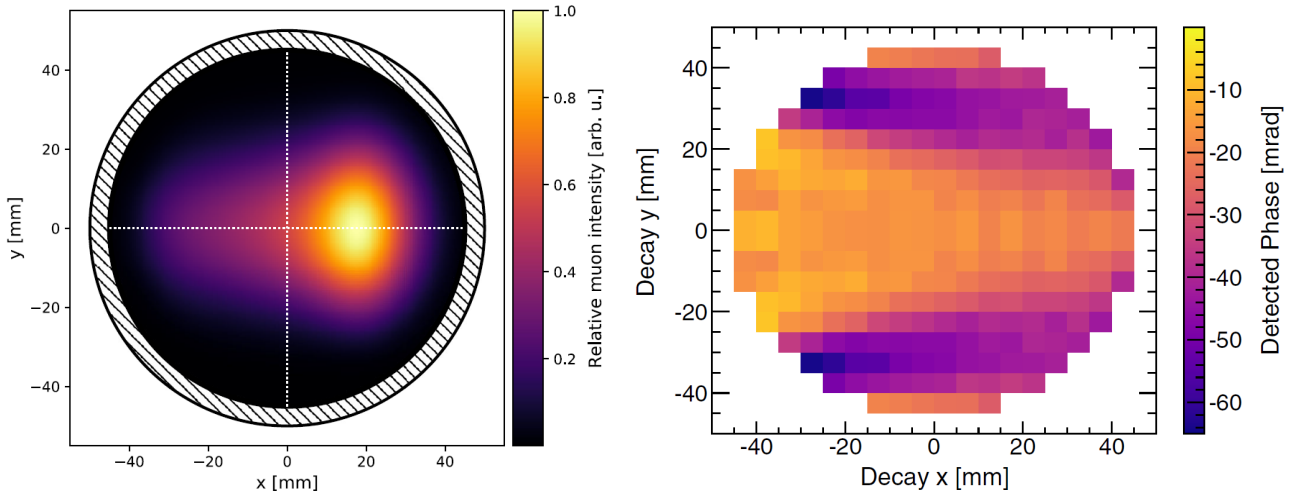

(a) **(b)**

Figure 4.7.6: From Ref. [96]. (a): an azimuthally averaged muon spatial distribution measured by the trackers in Run-1. (b): the azimuthally averaged phase map $\phi(x, y)$, generated by GEANT4-GM2RINGSIM, integrated over energy by the A-Method weights.

If the muon beam did not have any motion inside the storage ring, the phase acceptance effect would not bias the measured value of ω_a. However, the radial and vertical betatron oscillations generate a time-varying phase that biases ω_a and needs to be accounted for. This effect was enhanced in Run-1 due to the damaged ESQ resistors described in Section 4.3, which caused additional vertical beam movements with a lifetime of tens of µs.
The phase acceptance correction is extracted by measuring the beam distribution with the two tracker stations and extrapolating the phase maps to all the azimuth angles corresponding to the calorimeter locations with simulation [96]. For each calorimeter, the phase variation $\phi_{pa}(t)$ is extracted as a function of time. A wiggle plot is generated with the full ω_a function described in Section 5.5 (more complex than the 5-parameter function of Equation (4.7.4), to include beam dynamics effects), which includes the phase variation $\phi_{pa}(t)$ summed directly to

the ϕ parameter. The correction C_{pa} is extracted by taking the difference between ω_a fitted with the full fit function that keeps ϕ constant, and the ω_a value used to generate the wiggle plot with a time-varying phase. The value of C_{pa} was $-158(75)$ ppb in Run-1 and $-27(13)$ ppb in Run-2/3 [1, 3]: the damaged ESQ resistors in Run-1 were fixed before the start of Run-2/3 campaigns, which greatly reduced the phase acceptance effect on ω_a.

Differential decay correction C_{dd}

The muon decay rate depends on the relativistic boost γ_μ, which is distributed around the magic value of 29.3: $\Gamma = 1/(\gamma_\mu \tau)$. As muons decay with a different rate according to their momentum, the average momentum of the muon distribution will shift with time. If there is a correlation between the initial spin phase of the muon and its momentum, ϕ will have a time dependency, biasing ω_a. This effect is called differential decay, and is corrected for by C_{dd} in Equation (4.7.3). Although it was a known effect at the time of Run-1 analysis, it was not applied to the Run-1 result because preliminary results showed that C_{dd} and its uncertainty was much smaller than the other corrections.
There are three independent contributions to the phase dependency on the muon momentum, $d\phi/dp$: the first one is generated by the upstream beamline, after muons are emitted from pions in the Delivery Ring; the second one is due to momentum-orbit correlations that develop during beam injection; the third one is due to the fact that a muon bunch is 120 ns long when injected, and muons at the head of the bunch start precessing sooner than those at the end.
The C_{dd} correction is calculated using this formula:

$$C_{dd} = -\frac{\Delta\omega_a}{\omega_a} = \frac{1}{\omega_a}\frac{d\phi}{dt} = \frac{1}{\omega_a}\frac{d\phi}{dp}\left(\frac{dp}{dt}\right)_{dd} \tag{4.7.13}$$

where $(dp/dt)_{dd}$ represent how the beam momentum changes in time, as muons with different lifetimes decay. Summing the three contributions, the value of C_{dd} was found to be $-15(17)$ ppb in Run-2/3 [3].

Muon loss correction C_{ml}

Some of the muons that circulate in the storage ring are lost before decaying into positrons. In general, this happens when they strike one the collimators that limit the transverse region and the momentum acceptance. The collimators have an aperture of 45 mm in radius and are centered on the magic orbit. Muons hitting a collimator lose some energy, and start curling inward until they exit the storage region.
The time distribution of lost muons induces a distortion in the exponential decay shape as observed by the calorimeters. In the ω_a analysis, this is handled with a term in the full fit function which accounts for the losses throughout fill time (see Section 5.2.4). As in the case of differential decay, the C_{ml} correction is needed because a correlation exists between the injected muon average spin phase ϕ and the particle momentum [96]. As the probability of hitting a collimator depends on the muon momentum, the population of muons that are lost is correlated to the ω_a phase observed by the calorimeters. Since the muons are not lost uniformly across the storage time, a slow drift in the ω_a phase is induced. The magnitude of the effect is directly proportional to the number of lost muons, which was especially high during Run-1 because of the damaged quadrupole resistors, fixed before Run-2, and a non-optimized kick fixed during Run-3 (see Section 5.1).
The correction for the muon loss effect has been evaluated by taking special acquisition runs where the strength of the magnetic field was slightly changed from its nominal value, resulting in different momentum acceptances of the storage ring, allowing us to select a different portion of the original beam momentum distribution. The ω_a analysis was performed for each special run, to extract the average phase of the muon beam. The measured phase-momentum correlation

was (-10.0 ± 1.6) mrad/(%$\Delta p/p$) in Run-1 and (-13.5 ± 1.4) mrad/(%$\Delta p/p$) in Run-2/3. As for the phase acceptance, the C_{ml} correction is extracted by generating wiggle plots with a time-varying phase $\phi(t)$, fitting them with a constant phase and taking the difference of ω_a results from the ω_a value at generation step. The value of C_{ml} was found to be $-11(5)$ ppb in Run-1 and $0(3)$ ppb in Run-2/3 [1, 3]: the losses in Run-2/3 were reduced by an order of magnitude with respect to Run-1, which led to a sub-ppb correction.

4.7.4 Measurement of $\tilde{\omega}'_p$

As mentioned at the beginning of this Chapter, after moving the superconducting ring from BNL to Fermilab there was a campaign in 2015-2016 to increase the magnetic field uniformity by a factor of 3 with respect to the E821 experiment: 72 high-purity steel poles were used to increase the homogeneity; 864 wedges (12 for each pole piece) affected the dipole and quadrupole fields; 144 edge shims affected the quadrupole and sextupole fields; finally, 48 iron top hats and 8000 surface iron foils changed the local fields to achieve the desired uniformity [117]. Figure 4.7.7 compares the initial and final plots of the magnetic dipole field: the shimming campaign achieved a peak-to-peak variation of ± 25 ppm and a standard deviation of 15 ppm throughout the azimuthal angle of the ring. An "active" shimming is also ongoing as long as the experiment runs: 200 wires (100 on top and 100 on bottom), called surface current coils, make dynamic changes to the azimuthally averaged field by driving controllable currents.

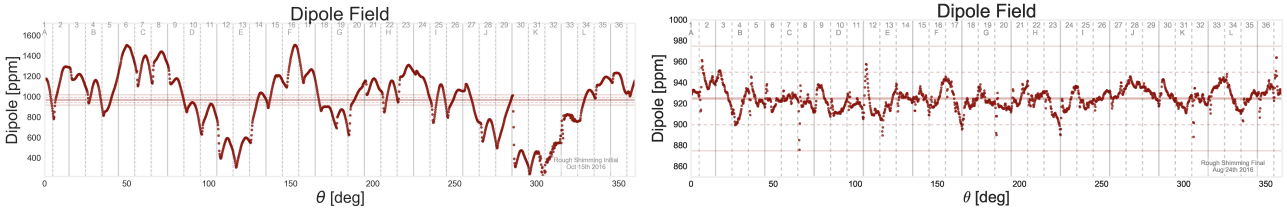

(a) **(b)**

Figure 4.7.7: (a): initial dipole magnetic field when it was first fully measured at Fermilab. The peak-to-peak variation was around 1400 ppm [117]. (b): the final rough shimming result for E989. The dashed bands at 900 ppm and 950 ppm indicate ± 25 ppm around the central value, which was the target for E989 (private communication with M. W. Smith.

In the E989 experiment, the B-field has to be measured precisely in order to obtain a_μ. As already stated, it is measured in terms of the shielded proton precession frequency, or Larmor frequency. During data taking, ω'_p is constantly measured by 378 nuclear magnetic resonance (NMR) fixed probes, placed along the ring in 72 strategic locations 7.7 cm above and below the storage volume. About once every three days, a trolley run is performed with no muon beam stored, where a cylinder equipped with 17 NMR probes is moved on rails inside the vacuum chamber along all the ring with the purpose to produce a three dimensional map of the magnetic field that the muons experience: the probes are displaced in a circle of 9 cm in diameter, which is the storage cross section, and they measure the field in 9000 azimuthal positions (once every ~ 0.5 cm). The fixed probes monitor the field stability between two consecutive trolley runs, and some of them also serve to provide feedback to the magnet supply to actively stabilize the field strength over time.

The NMR technique uses a radio frequency (RF) pulse applied to the proton sample in petroleum jelly, in order to rotate the proton spin of 90° such that it lies in the plane perpendicular to the storage ring B-field. When the RF pulse is turned off, the sample polarization starts precessing in the storage ring magnetic field until the net magnetization of the sample

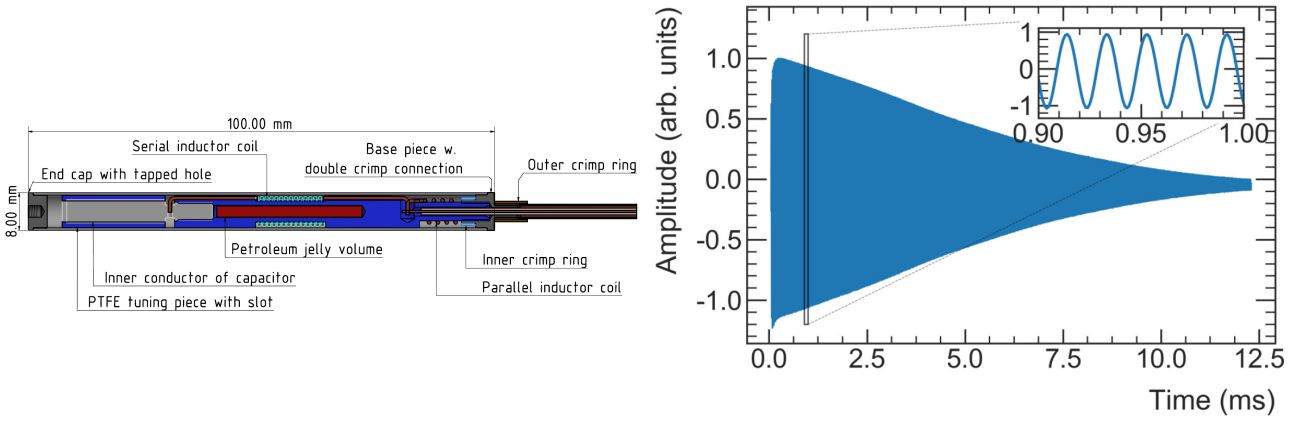

(a) **(b)**

Figure 4.7.8: From Ref. [97]. (a): schematic drawing of the NMR probe for field mapping and monitoring. (b): a typical free induction decay (FID) from a trolley probe. The zoomed inset shows the periodic behaviour that is fitted to extract the signal frequency.

returns to being aligned with the external field. Pickup coils oriented perpendicularly to the magnetic field are connected to waveform digitizers that save the current induced in the coils by the precessing protons: this current is the so-called free induction decay (FID) signal, and measuring it over time gives information about the magnetic field. The Larmor precession frequency is about 61.79 MHz in the $g-2$ storage ring, and it is mixed down to ~ 50 kHz prior to digitization [97]. Figures 4.7.8(a) and 4.7.8(b) show, respectively, the design of the trolley and fixed probes, based on a similar design from the BNL E821 experiment, and an example of the FID signal [97]. Both the trolley and fixed probes are calibrated with a water-sample probe that is installed on a translation stage in the ring vacuum, and that can be positioned in the same locations as the trolley probes. This step provides absolute calibration of the field measurement, providing the offsets f_{calib} that are present due to diamagnetic shielding effects of the petroleum jelly samples, trolley body and shape.

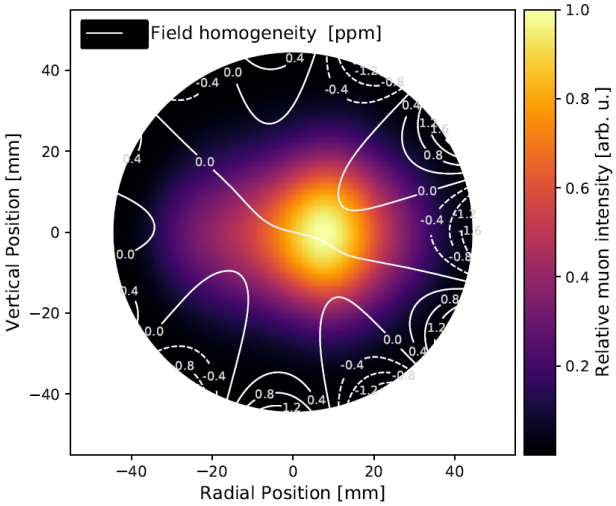

Figure 4.7.9: From Ref. [3]. Azimuthally averaged magnetic field contours, overlaid on the time and azimuthally averaged muon distribution at the end of Run-3.

The final value of ω_p' required in Equation (4.7.3) is the average magnetic field $\tilde{\omega}_p'$ experienced by the muons as they precess around the ring, obtained by weighting the ω_p' map with the muon beam distribution $M(\vec{r},t)$ measured by the trackers, and by integrating over time and space.

Figure 4.7.9 shows an example of the three-dimensional map of the magnetic field inside the chamber.
The NMR technique allows to bring down the systematic uncertainty on $\tilde{\omega}'_p$ to 70 ppb, whereas the statistical error is completely negligible.

4.7.5 Transient magnetic fields B_i

During muon storage, two time-dependent magnetic fields are induced by the pulsed magnetic and electric fields from the kicker and quadrupoles that are synchronized with each muon fill. These transient magnetic fields are not present during the trolley runs; the fixed probes only measure the field at time intervals of ~ 1 s asynchronously with respect to muon injection, whereas the fast transients change on the µs timescales, so they must be included as corrections to ω_p at the denominator of Equation (4.7.3). Contrarily to beam dynamic corrections C_i, the corrections B_i due to transients increase the ratio ω_a/ω_p if they are negative, and decrease it if they are positive.

Electrostatic quadrupole transient fields B_q

The transient associated with the ESQ field was discovered during Run-1 studies of correlations between the fixed probe measurements and the muon injection [97]. These fields are caused by mechanical vibrations of the charged plates induced by ESQ pulsing, and generate a perturbation that needs to be measured by a dedicated set of NMR probes. Such probes are sealed inside polyether ether ketone (PEEK) plastic tubes for vacuum compatibility and read out through the fixed probe NMR system, synchronized to the ESQ pulsing system. During normal running, the quadrupoles are triggered by the upcoming beam and they discharge about 700 µs after the trigger. As shown in Figure 4.1.2, this structure happens in a series of 8 muon bunches, then a pause of ~ 200 ms, then 8 more muon bunches, and the entire series of 16 beam injections happens every ~ 1.4 s.

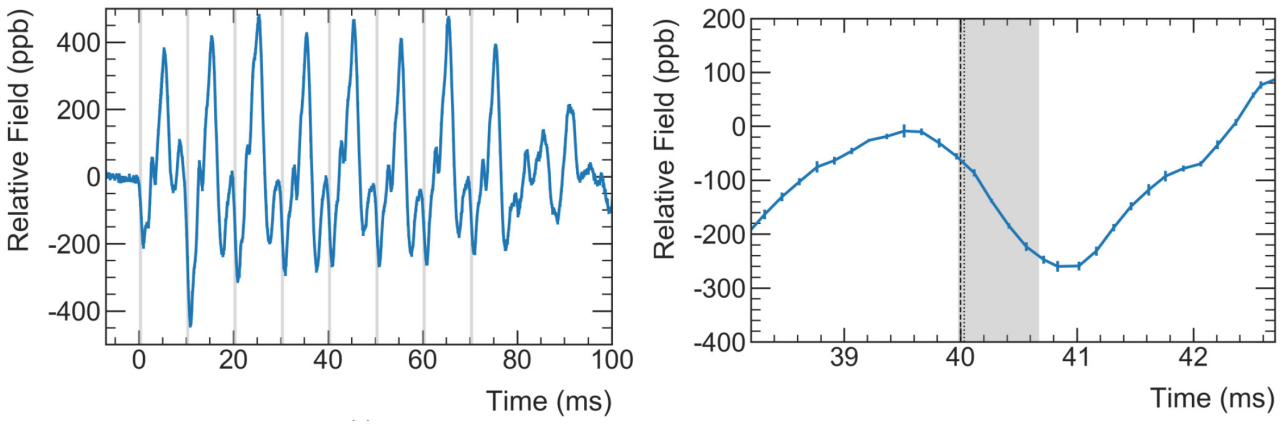

(a) **(b)**

Figure 4.7.10: From Ref. [97]. (a): the time structure of the ESQ transients measured by NMR probes (for the first 8 out of 16 bunches). In the grey regions, the ESQ are charged during muon storage. (b): the ESQ time structure zoomed in to a single beam pulse, where the black dashed line is the time of muon injection.

The transient quadrupole fields were measured by varying the delay time between the ESQ trigger and the NMR measurement, performed at several positions corresponding to quadrupole locations. Figure 4.7.10 shows the structure of ESQ transients measured in Run-1, when the

number of measurement locations was limited; in Run-2/3, NMR probes measured ESQ transients on the trolley rails, allowing for a full mapping of all quadrupole stations. The value of B_q was $-17(92)$ ppb in Run-1 (indeed, it was the largest systematic contribution to the result) and $-21(20)$ ppb in Run-2/3 [1, 3].

Kicker transient fields B_k

As explained in Section 4.2, kickers deflect the injected muon beam towards the ideal orbit, by reducing the magnetic field by ~ 22 mT for 150 ns. The pulsed field induces eddy currents in the surrounding metal, leading to field perturbations during muon storage. The fixed NMR probes are shielded from this rapid transient field by the skin depth effect of the aluminum vacuum chambers [97], so dedicated measurements were carried out by two Faraday magnetometers, in order to account for this effect.
The magnetometers exploit the rotation of the polarization angle θ of linear polarized light when passing trough a dielectric material submerged in a magnetic field. If the field is parallel to the direction of propagation of the light, the polarization rotates by:

$$\Delta\theta(t) = V \cdot B(t) \cdot L \tag{4.7.14}$$

where V is the Verdet constant of the dielectric material and L is the length of the material. The magnetometers consist of a terbium gallium garnet (TGG) crystal placed vertically between the kicker plates and supported by a structure built without any metal parts; for this material, the Verdet constant is approximately 450 rad/Tm. The polarized light is brought to the crystals with optical fibers for the magnetometer by UMass (shown in Figure 4.7.11(a)), whereas, for the other one by INFN, light travels through free space and is brought to the crystal by mirrors.

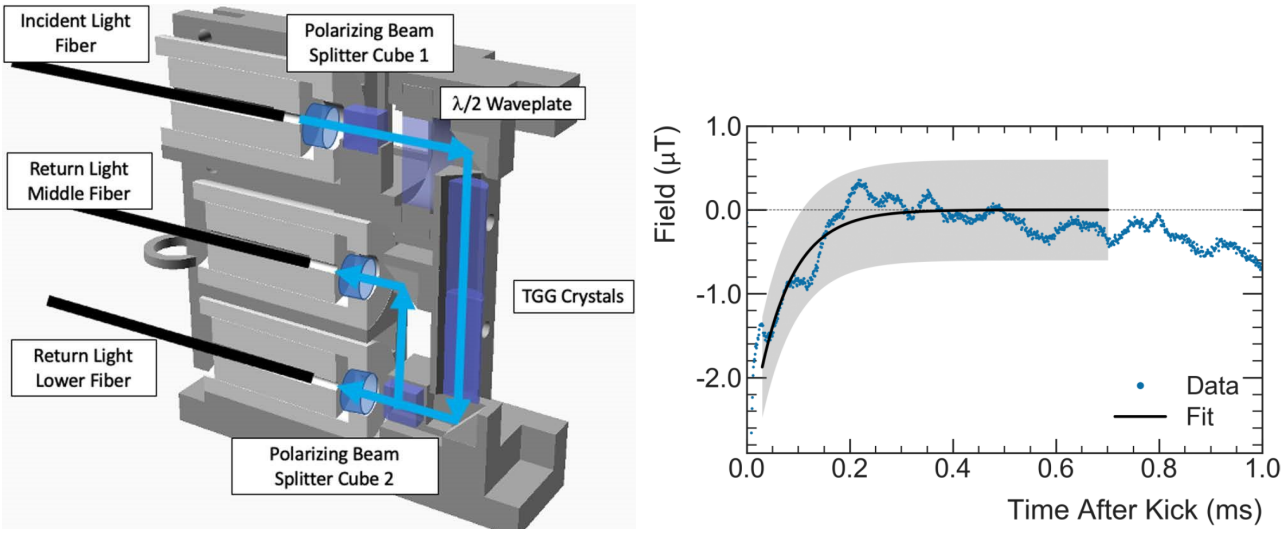

(a) **(b)**

Figure 4.7.11: From Ref. [97]. (a): schematic of the fiber magnetometer inserted between the kicker plates. (b): the field perturbation caused by the eddy currents as measured by the fiber magnetometer. The grey shaded band represents the associated uncertainty of ± 0.6 μT.

The Run-1 measurement result is shown in Figure 4.7.11(b). Field perturbation is obtained by fitting the data with an exponential function between the ω_a fit start time t_0 (which was around 30 μs in Run-1/2/3) and 700 μs:

$$\Delta B(t) = \Delta B(t_0) e^{-(t-t_0)/\tau_B} \tag{4.7.15}$$

The fractional effect on the muon anomalous precession frequency measurement depends on the fitted lifetime τ_B of Equation (4.7.15):

$$B_k = \frac{\Delta\omega_a}{\omega_a} \approx \frac{\Delta B(t_0) \cdot k}{1.45\,\mathrm{T}} \left(\frac{\tau_B}{\tau_B + \tau_\mu} \right)^2 \tag{4.7.16}$$

where k is a scaling factor that takes into account the azimuthal coverage of kickers in the storage ring, approximately equal to $(3 \cdot 1.27\,\mathrm{m})/(2\pi \cdot 7.112\,\mathrm{m}) \approx 0.085$. The value of B_k was $-27(37)$ ppb in Run-1 and $-21(13)$ ppb in Run-2/3 [1, 3].

4.7.6 Blinding of the analysis

There is one more term present in Equation (4.7.3): the secret blinding frequency f_{clock}, that is applied to our ω_a results during analysis, in order to prevent any unconscious biases of the analyzers when processing and fitting the data. The blinding procedure artificially shifts ω_a with respect to the true value, and it is applied in two different ways: at the hardware level, where the secret shift is set and monitored by people external to the Muon $g-2$ collaboration, and at the software level, where the secret shift is chosen by ω_a analyzers and is different for each analysis group.

Hardware blinding

The clock timing of the experiment's detectors is provided by a 10 MHz Rubidium "master" clock. The Rubidium source provides the short-term oscillation stability, while a GPS receiver provides the long-term stability. The master clock generates a signal for two precision synthesizers, Stanford Research Systems (SRS) SG-382, which in turn generate the 60 MHz clock for the field measurement and the 40 MHz primary clock for the calorimeters. The latter is up-scaled to the sampling rate of 800 MHz in the calorimeter front-ends, which defines the unit of 1 c.t. (clock tick) equal to 1.25 ns. The hardware blinding consists in detuning the master clock frequency, in the interval $[39.997, 39.999]$ MHz, thus introducing an intrinsic bias on the measured frequency of ± 25 ppm, hundreds of times larger then the precision on a_μ. The secret frequencies are noted in two sealed envelopes: only upon completion of the analysis, crosschecks and systematic evaluations, and after the unanimous decision of the collaboration to unblind the result, the secret frequencies are revealed and applied to the formula to extract a_μ.

Software blinding

During the analysis, a further level of blinding is applied to the ω_a fitting procedure, in order to prevent biases at the stage of comparing fit results among the analysis teams. When wiggle plots are fitted to extract ω_a, the fit routine replaces ω_a with an adimensional parameter R, defined as the fractional offset, in ppm, of the fitted ω_a from a secret reference value:

$$\omega_a(R) \equiv 2\pi \cdot (0.2291\,\mathrm{MHz}) \cdot \left[1 + (R + \delta R) \cdot 10^{-6}\right] \tag{4.7.17}$$

where δR is the secret reference value that differs for each analysis group, and 0.2291 MHz is the inverse of the ω_a period of $\sim 4.365\,\mu$s. δR is randomly generated in the range $[-24, +24]$ ppm starting from a passphrase that the analysis group chooses, and using a `MD5` hash algorithm [108]. After the ω_a analysis is complete, and before the secret hardware frequency is revealed, all groups apply a common software blinding that allows to perform cross-checks on the results.

Chapter 5

The Run-2/3 measurement of the anomalous precession frequency ω_a

The anomalous precession frequency ω_a measurement is the main topic of this Thesis: it is measured by counting the number of positrons above a fixed energy threshold which are detected by the calorimeters over time, and it is performed independently by several analysis groups which will be presented in this Chapter. Each analysis group introduces a secret blinding offset to their ω_a fits with the procedure described in Section 4.7.6, to prevent biases when comparing results in the early stage of the analysis. When presenting the results of ω_a fits, we will always report the blinded values; the unblinded average among all teams, used for the Run-2/3 publication, will be shown in Chapter 7.

5.1 Overview of the Run-2/3 ω_a analysis

5.1.1 Run-1/2/3 campaigns and running conditions

In the 6 years of running, the E989 experiment at Fermilab collected 21.9 times the number of positrons that the previous experiment E821 at Brookhaven had collected and analyzed. This allowed us to reach and hopefully surpass the design goal for the statistical uncertainty on a_μ, set to 100 ppb by the Technical Design Report [4]. Figure 5.1.1 shows how our data is split into 6 campaigns, called Run-X datasets (with X ranging from 1 to 6), from 2018 to 2023. Each dataset is characterized by different running conditions: ESQ voltage, kicker settings, muon beam dynamics, muon storing efficiency, and so on.
In this Section, I will describe the main differences between each Run, and any upgrades or changes in the experimental setup. In the rest of this Thesis, I will use the term "dataset" to refer indistinctly to a whole Run, or to its subsets that will be presented in each of the following Sections.

Run-1 data was collected from April to June 2018 and it was divided in 4 major datasets for analysis, labelled from Run-1a to Run-1d. Run-2 data was collected from March to July 2019 and Run-3 data was collected from November to March 2020, although it was planned to last until July 2020 with more datasets, but ended before due to the COVID-19 pandemic. Run-2/3 were divided into a total of 20 datasets, but, thanks to the improved stability of the hardware conditions with respect to Run-1, many datasets were combined to allow higher statistics in the ω_a and reduction of the statistical uncertainties of some systematic effects. Thus, Run-2/3 were divided into three major datasets for analysis: Run-2, Run-3a and Run-3b. On the B-field side, a total of 25 and 44 trolley runs have been performed for Run-2 and Run-3, respectively,

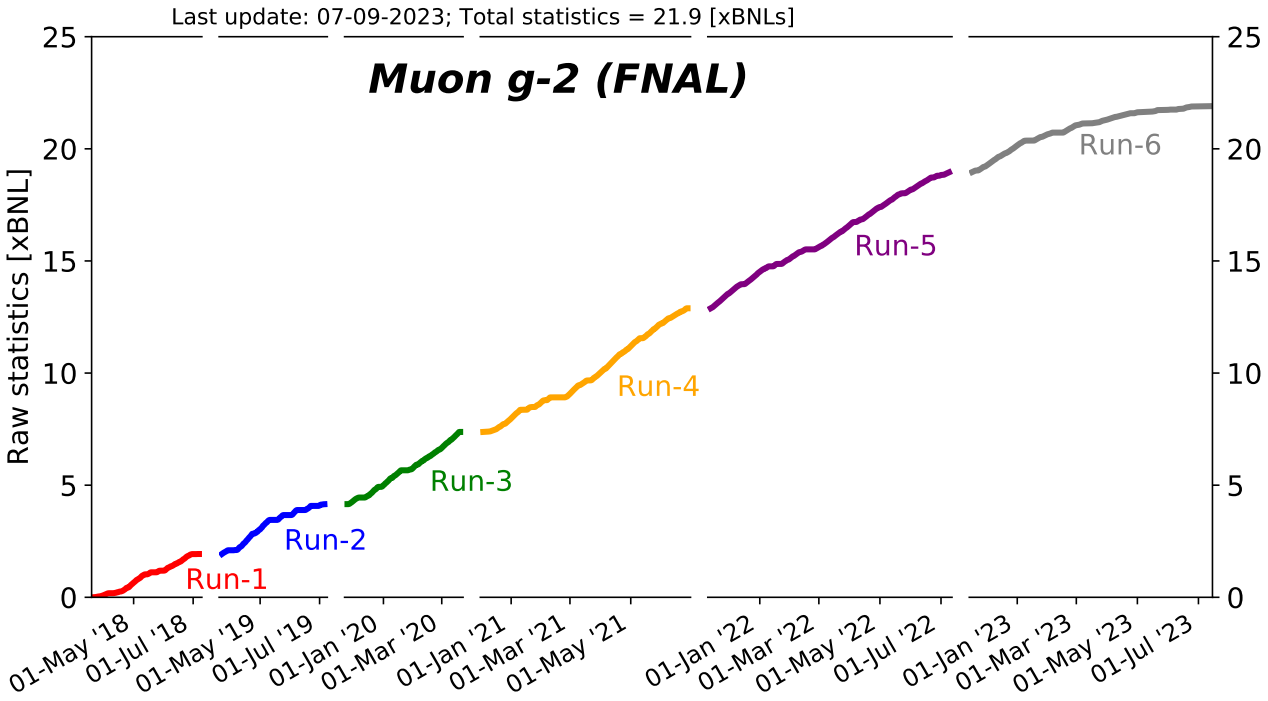

Figure 5.1.1: The 6 run periods of the E989 experiment, with labels indicating the periods in which each data acquisition campaign took place. The last day of acquisition is reported in the top, with the total number of collected positrons in terms of the E821 BNL statistics.

as opposed to 19 trolley runs in Run-1.

The analyzed positrons from muon decay included in the final datasets were selected according to Data Quality Cuts (DQC)[1]. The DQC cuts select fills based on the stability of the magnetic field and of the ESQ system; they also check that the kicker amplitude and timing were at nominal during data acquisition, and that beam profiles from the T0 detector and laser synchronization pulses were present. Final selection cuts were applied based on the average rate of lost muons and on the number of positrons detected (normalized by T0 integral).

Table 5.1.1 reports the field index n and kicker strength for each dataset, along with the number of reconstructed positrons with energies above 1.7 GeV which were analyzed by the ω_aEuropa team.

Dataset	T-Method e^+ [$\times 10^9$]	Field index n	Kicker [kV]
Run-1a	0.96	0.108	130
Run-1b	1.34	0.120	137
Run-1c	2.05	0.120	130
Run-1d	4.09	0.107	125
Run-2	11.32	0.108	142
Run-3a	15.04	0.107	142
Run-3b	5.96	0.107	165

Table 5.1.1: Dataset statistics and hardware conditions for Run-2/3 compared to Run-1. The number of analyzed positrons (e^+) is reported for the ω_aEuropa T-Method fits.

[1]This has been one of my major service works for the experiment, as I have been managing this stage of dataset reconstruction since 2021.

Some of the significant improvements and changes for Run-2/3 with respect to Run-1 were the following:

- During Run-1 there were two damaged resistors in the ESQ plates. The resistors were replaced after Run-1, improving the stability of radial and vertical betatron oscillations and reducing the phase acceptance correction C_{pa} in Run-2/3 significantly (as discussed in Section 4.7.3).
- The kicker strengths for Run-1, Run-2 and Run-3a were limited to 142 kV by the cables used at that time: as a result, the beam was not perfectly centered in the storage region. At the end of Run-3a, the cables were upgraded and the kicker voltage was increased to 165 kV in Run-3b to achieve optimal kick. This resulted in a better-centered muon beam which reduced the electric field C_e correction. The difference in the muon beam profile before and after the kicker upgrades can be seen by comparing Figures 4.7.6(a) and 4.7.9.
- Between Run-1 and Run-2 the magnet yokes have been covered with a thermal insulating blanket to mitigate day-night field oscillations due to temperature drifts. In addition, the experimental hall's air conditioning system has been upgraded after Run-2 to further stabilize the temperature of both the magnet yokes and the detector electronics to better than $\pm 0.5\,^{\circ}\mathrm{C}$.
- The number of lost muons was greatly reduced in Run-2/3 thanks to two upgrades. Firstly, the operational high-voltage set points for the ESQ system were lowered, in order to avoid betatron resonances for beam stability. Secondly, all 5 collimators shown in Figure 4.2.1(a) were used in Run-2/3, whereas only 2 were used in Run-1: this allowed for better beam scraping.

It's worth mentioning a number of further differences in the analysis across the Run-1/2/3 periods:

- There were three different hardware blindings (see Section 4.7.6) for each Run (Run-1/2/3). This allowed to publish the Run-1 result in 2021 while Run-2 was still at its early stages of reconstruction and analysis. Before releasing the Run-2/3 result, we performed a "relative" unblinding between Run-2 and Run-3 which allowed to compare the datasets directly with a common blinding offset.
- Towards the end of Run-3, there was a change in the configuration of In-Fill-Gain (IFG) laser pulses (described in Section 4.4.2). In the initial configuration, 4 laser pulses covered the entire 700 µs of storage time moving by a step of 2.5 µs per fill, for a total of 93 steps before the pulses moved back to their starting point; in the new configuration, the step was reduced to 1.5 µs to allow for a finer scan of the fill time, and the number of total steps was increased to 117.
- In Run-1a/1b/1c, and in Run-2/3, the ω_a fit range was $[30, 650]$ µs. For Run-1d, the fit start time had to be increased to 50 µs because the effect of damaged resistors got worse towards the end of Run-1, and choosing a higher start time would reduced the related systematic effect despite increasing the statistical uncertainty.

5.1.2 Organization of ω_a analysis teams

In Run-2/3, the ω_a analysis was conducted by seven independent teams using a number of different strategies for the positron reconstruction, subtraction of pileup, and treatment of beam dynamics effects. Table 5.1.2 describes some of the main characteristics of the seven teams, which are labelled as follows: Boston University (BU), Cornell University (CU), Europa (ω_aEuropa), Illinois Ratio Method Analysis (IRMA), University of Kentucky (UKy), Shanghai Jiao Tong University (SJTU) and University of Washington (UW).

	BU	CU	ω_aEuropa	IRMA	UKy	SJTU	UW
Pulse fitting and clustering	Local $\Delta t'$	Global	ReconITA	Global	Q	Local	Local $\Delta t'$
Pileup subtraction	Empirical	Empirical	Semi-empirical	Empirical	-	Shadow	Empirical
Analysis methods	T, A, R, RA	T, A	T, A, R, RA	T, A, R	Q, RQ	T, A	T, A

Table 5.1.2: Main details of the procedures to build and fit wiggle plots for each of the seven analysis teams in Run-2/3. The Q-Method, Local and Global reconstruction procedures are described in Ref. [108], whereas the ReconITA and Local $\Delta t'$ are described in Ref. [118] and [119], respectively. The Pileup row refers to how multiple hits on the same crystals are handled when building doublet and triplet events: the Empirical and Shadow methods were described in Ref. [108], whereas the ω_aEuropa Semi-empirical will be described in Section 5.2.3. The "Ratio" versions of A-Method and Q-Method (RA and RQ, respectively) are new with respect to Run-1.

In the following, I will focus on my contributions, consisting in the development of the Ratio-Asymmetry Method, new with respect to Run-1, in the Run-2/3 fits to wiggle plots. The ω_a results and systematic errors from this method were included in the 2023 publication [3]. This work has been done within the ω_aEuropa team.

5.1.3 Europa ω_a analysis workflow

In the Run-2/3 analysis, ω_aEuropa developed the "ReconITA" reconstruction with the aim of reducing the major Run-1 ω_a systematics, such as the pileup effect which amounted to 35 ppb. Details on the new reconstruction will be provided in the following Sections (a full description can be found at [118]).

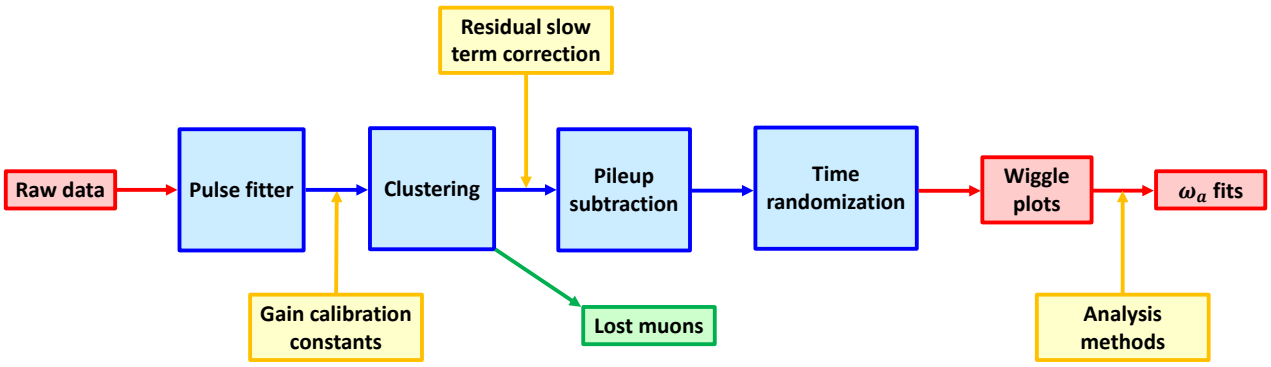

Figure 5.1.2: Run-2/3 ω_aEuropa analysis workflow.

The chart in Figure 5.1.2 describes the procedures employed in the ω_aEuropa team, to reconstruct positron events from raw SiPM data and build wiggle plots.

5.2 Procedure to reconstruct positron events

5.2.1 New clustering for the Europa ω_a analysis

The first step in the reconstruction of positron events involves a fit on crystal traces. Given the high linearity of the SiPMs with respect to deposited energy (see Section 4.4.1), we extract templates for each of the 1296 crystals before the beginning of each Run, and scale them in amplitude so that they fit the waveforms of positron hits, like the example in Figure 5.2.1.

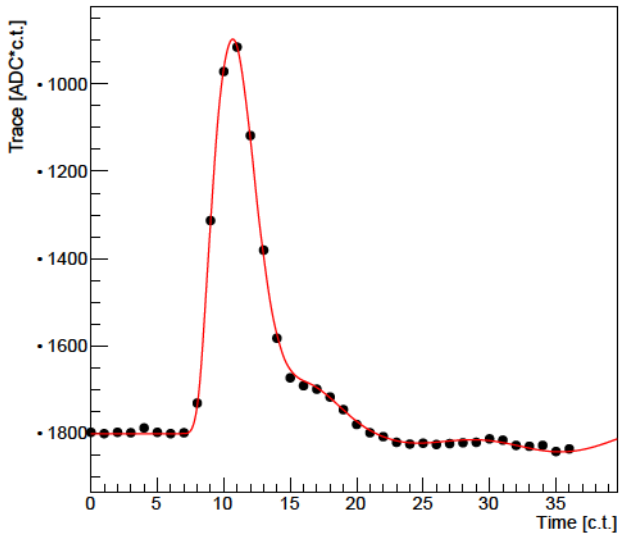

Figure 5.2.1: Simulated trace of a positron hitting a crystal, fitted with a predetermined template to obtain the time and deposited energy of the event. 1 clock tick (c.t.) is equal to 1.25 ns (see Section 4.7.6).

For each event in which a positron has released energy in the calorimeters, we perform these template fits and assign the corresponding hit times and amplitudes (in arbitrary units, before energy calibration) to each crystal that contained a waveform. At this point, we calibrate the hits in energy (see Section 5.2.2 that follows), and we synchronize all crystals of all calorimeters in time, using the laser pulses that are normally shot in Standard Mode during data acquisition a few µs before muon injection. At last, our clustering procedure reassembles all of the crystal hits and reconstructs a candidate for positron event. The new ReconITA clustering algorithm is an improvement with respect to the Run-1 clustering (the one referred to as *local-fitting* in Ref. [108]), which was modified in order to use the time information of the crystal hits as an input to the clustering.

All crystal hits are passed as the input of the so-called *seed-and-propagation* algorithm. This procedure finds the most energetic hit among all crystals in a calorimeter, and uses it as the cluster "seed": the time of the seed determines the cluster time, since dedicated studies on the time distribution of crystal hits showed that most of the energy deposition is localized in that crystal [118]. From these studies, the width of the distribution $\sigma(E)$ was obtained, by taking the root mean square (RMS) of the time difference between all hits in a cluster and the cluster seed. This function decreases with the crystal hit energy: $\sigma(E) = 0.198 + 70.4/E$, with energies in MeV units. Then, the algorithm propagates the cluster according to times and energies of adjacent crystals: positron hits that are n_C crystals apart are merged into a single cluster, if they fall within the time window Δt_{ij}, defined in clock tick units (1 c.t. = 1.25 ns) as:

$$\Delta t_{ij}\,[\text{c.t.}] < \sigma(E_i, E_j) + 0.03 n_C, \qquad \sigma(E_i, E_j) = \sqrt{\sigma^2(E_i) + \sigma^2(E_j)} \tag{5.2.1}$$

where $\sigma(E_i, E_j)$ adds in quadrature the two width functions for each couple of crystal hits i, j, and the parameter $0.03 n_C$ is used to include a spatial input in the time window Δt_{ij}.
All these steps are repeated for the remaining crystal hits that were not included in the first cluster, starting from a new seed. At the end of this procedure, any remaining low energy hits ($< 100\,\text{MeV}$) are assigned to the closest cluster, but only if they meet the same time criterion reported above, otherwise they create new independent clusters.
In general, there is the possibility that there are two or more positron hits fitted on the same crystal waveform. These hits are treated independently, and may be included in the same cluster, or they may be separated, according to the time window criterion in Equation (5.2.1). As a very last step of the clustering procedure, if the seed of a cluster has a second hit on the same crystal that was not associated to any other cluster, then the second hit is included in the same cluster as the first hit. This feature handles rare occurrencies in which the template fitter incorrectly recognizes two positron hits in the same waveform close in time: the second hit is re-absorbed into the cluster of the first hit, so that the total energy of the hit can be measured correctly.

At the end of the clustering algorithm, each cluster is identified as a positron event: the reconstructed time of the event is the one of the cluster seed, and the reconstructed energy is the sum of all the crystal energies that compose the cluster. Figure 5.2.2 compares the energy spectrum of reconstructed positron events between the Run-1 algorithm and the improved ReconITA Run-2/3 algorithm. The energy region above $\sim 3.1\,\text{GeV}$ is nonphysical, because positrons are emitted from muons at the magic momentum of $\sim 3.1\,\text{GeV}/c$, so they cannot have more energy than the parent particle. The events in the nonphysical region are explained by the presence of pileup, i.e. two or more positron events that occur at the same time in a calorimeter, which are misidentified as a single event. With the improved Run-2/3 algorithm, the reconstruction is able to better resolve pileup events and reduce their number by a factor of ~ 2, estimated from the integral of the red and blue curves after 3.1 GeV. Section 5.2.3 will describe how we subtract pileup to reduce the curve to 0 in the nonphysical region.

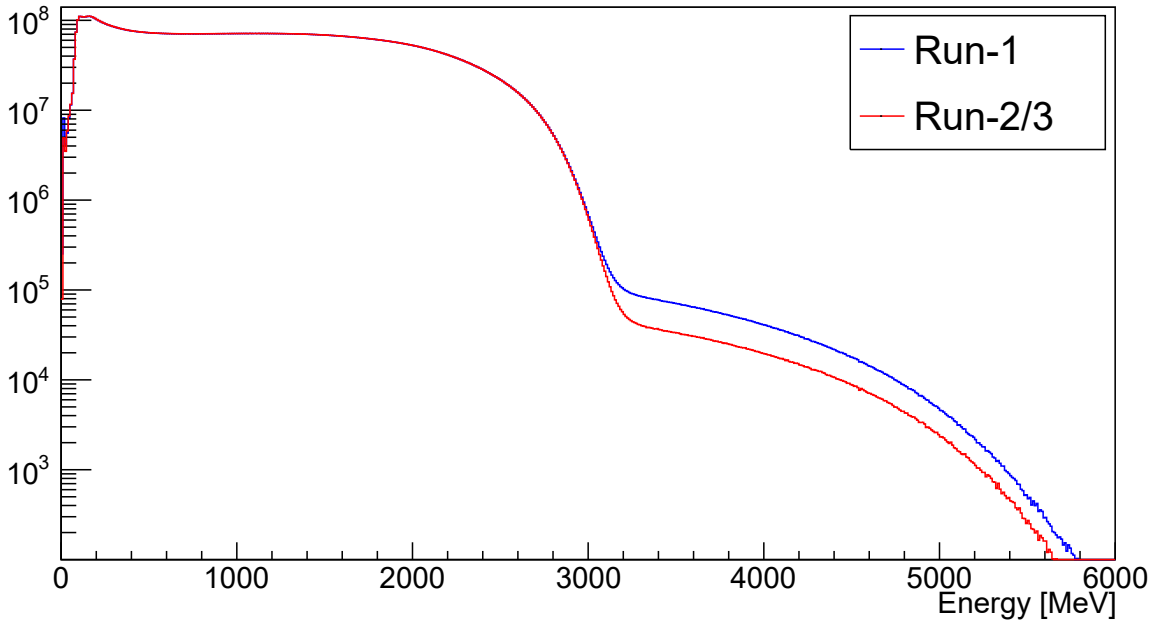

Figure 5.2.2: Cluster energy spectrum before pileup correction: comparison between Run-1 (blue) and Run-2/3 (red) clustering algorithms.

5.2.2 Gain corrections

When positrons hit calorimeters, the SiPM signals are recorded by analog-to-digital (ADC) waveform digitizers, and stored for analysis: "gain" is the conversion factor between the ADC values and the physical energy deposited by positrons. The state-of-the-art laser calibration system described in Section 4.4.2 can measure the gain at a sub per-mill precision over a wide range of timescales: from tens of nanoseconds to weeks.

Short-Term Double-Pulse (STDP) correction

When two positrons hit the same crystal in a short interval of time (within $\sim \mathcal{O}(10\,\text{ns})$) a gain drop occurs: this is because when a SiPM is hit, it delivers charge that comes from all available source, including the SiPM array itself which behaves like a charged capacitor; the bias voltage momentarily drops, until the charge is recovered. More details on how the SiPM response depends on the frontend electronics are reported in [99]. To account for this effect, the so-called Double Pulse operation mode is used, where the light from two laser heads is redirected on the same crystal and two laser pulses are fired with a set time delay ranging from 0 to 100 ns. The Double Pulse Mode simulates the physics case in which two positrons hit the same crystal within tens of nanosecond: the first pulse causes the bias voltage drop and the consequent gain sag, while the second pulse is a probe for the size of the sag. In dedicated STDP campaigns before the beginning of each Run, we fix the energies E_1 and E_2 of the two laser pulses, and vary the time delay Δt to reconstruct the gain function of the SiPM and fit it with an exponential:

$$G(\Delta t, E_1) = 1 - \alpha E_1 e^{-\Delta t/\tau} \tag{5.2.2}$$

Figure 5.2.3 shows an example of fit on the STDP data. Typical values for the fit parameters in Run-2/3 were $\alpha \sim 2\%/\text{GeV}$, $\tau \sim 15\,\text{ns}$, both with an average relative uncertainty of 2%. When two positrons events are reconstructed close in time in the same crystal, the energy of the second one is thus rescaled: $E_2' = E_2/G(\Delta t, E_1)$.

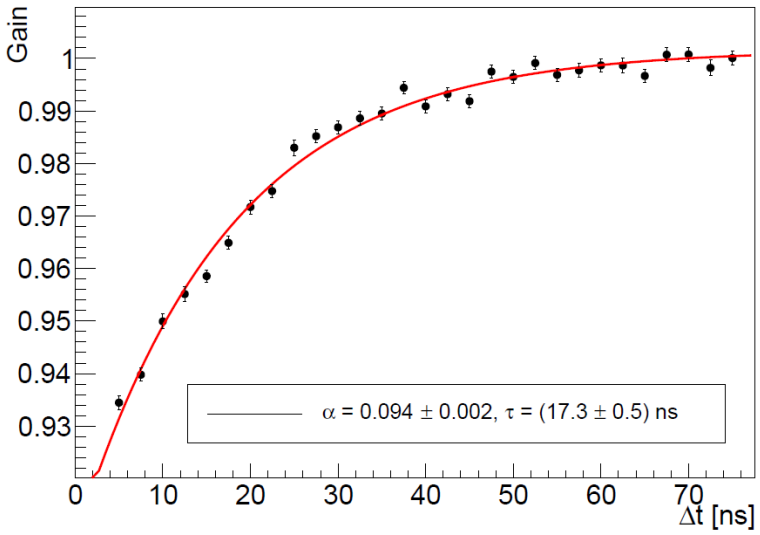

Figure 5.2.3: Example of short-term gain sag for a crystal, fitted with Equation (5.2.2).

In-Fill-Gain (IFG) correction and Long-Term Double-Pulse (LTDP) campaigns

Two types of transient effects in the 700 µs window of storage time contribute to in-fill variations of the detector gain, which is the most significant source of systematic effect in the ω_a analysis among the gain-related ones. Firstly, upon beam injection, a big "flash" of particles hit the calorimeters in the first few µs, making them temporarily blind. These particles mostly deposit their energy in the first calorimeters and quickly exit the storage region. Secondly, in the time range of $[30, 700]$ µs of ω_a analysis, the muon decay rate drops by more than four orders of magnitude because of the 64.4 µs lifetime in the laboratory frame. The SiPM power supplies are affected by these two facts, and the gain sag resulting from charge depletion is restored with the SiPM electronics recovery time of $3\,\mu s \div 8\,\mu s$.
The in-fill gain correction for each crystal is extracted by sending in-fill laser shots at the same time of muon beam in a fraction of fills, and measure the laser energy detected the SiPMs, equalized using the Local Monitor (see Section 4.4.2). The ratio between the laser energy that we send and the one measured by SiPMs is then normalized by the same ratio calculated with out-of-fill pulses (described further in this Section), in order to correct for long term gain fluctuations, since we combine many fills together - collected over many days or even weeks - to extract the parameters of IFG correction.

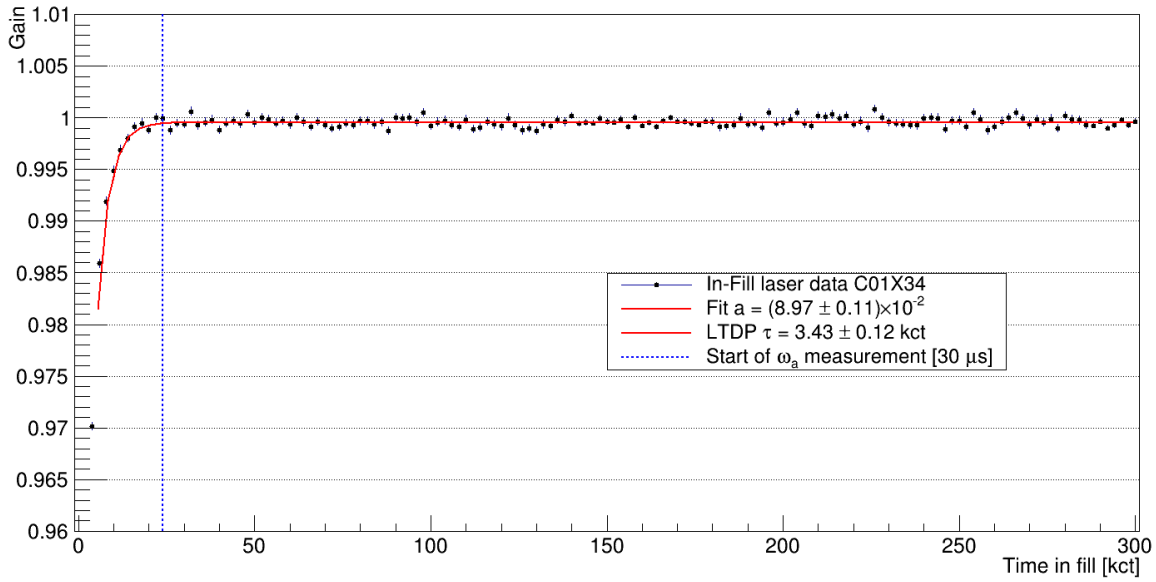

Figure 5.2.4: From Ref. [118]. Example of an IFG function for a particular crystal in Run-3. In the exponential fit (red) the lifetime is fixed from LTDP studies. The dashed line at 24 kc.t. (30 µs) represents the start of the ω_a measurement period.

A typical IFG function is shown in Figure 5.2.4, fitted with an exponential of the form:

$$G(t) = N\left(1 - a_{IFG}\, e^{-t/\tau_{IFG}}\right) \tag{5.2.3}$$

where a_{IFG} is the amplitude of the sag and τ_{IFG} is the recovery time of the electronics. The asymptote N is a free parameter since the complexity of the measurements can bring small deviations from 1, typically of the order of $10^{-4} \div 10^{-3}$. In Run-2/3, the average value of a_{IFG} was around $2\% \div 3\%$, but it could reach $10\% \div 15\%$ for the first calorimeters which saw a greater amount of flash particles at injection; τ_{IFG} has a bi-modal distribution around 4 and 8, which was understood as a specific pattern of the SiPMs electronics [120].

The N and a_{IFG} parameters of Equation (5.2.3) are free in the fit, whereas τ_{IFG} is fixed from dedicated Long-Term Double-Pulse (LTDP) studies [101, 118], in order to avoid correlations between the two parameters (which will be useful for assessing the systematic uncertainty, as explained in Section 6.1) and also because for some crystals the amplitude is so small that it's difficult to extract the lifetime. Like the STDP campaigns, the LTDP studies occur before the beginning of every Run, in the absence of muon beam: to mimic the effect of the particle flash at injection, a burst of ~ 100 laser pulses are shot between 0 and 8 µs; a laser pulse is then sent with a variable delay, ranging from a few µs to hundreds of µs, to serve as a probe of the SiPM gain.

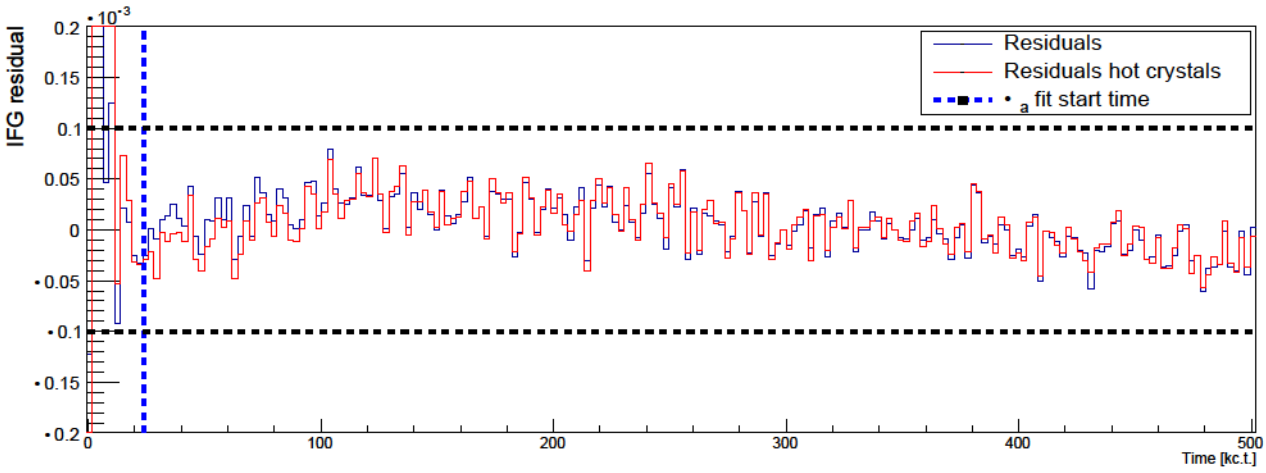

Figure 5.2.5: In-Fill-Gain fit residuals, obtained by summing over the 1296 SiPMs over all the Run-2/3 datasets. The red histogram shows only the contribution from the 16 "hottest" crystals, which are closest to the beam storage region and therefore detect positrons with a higher rate.

Figure 5.2.5 shows the accumulated fit residual obtained by summing over the 1296 SiPMs for all the 20 datasets of Run-2/3. The contribution from the highest-rate crystals of each calorimeter is also shown. The horizontal black bands are placed at $\pm 10^{-4}$, which is the level of precision needed to limit the gain systematics below the design goal of 20 ppb. The residuals after 30 µs (relevant for the ω_a analysis) are well contained within these bands, giving us confidence that IFG function that we use properly accounts for the in-fill changes of SiPM gains.

Out-Of-Fill (OOF) correction

As described in Section 4.4.1, SiPMs have the advantage of being very stable in the presence of strong electric and magnetic fields; however, they are also very sensitive to temperature variations, so their gain must be calibrated on the timescales of days and months. In Section 4.7.3, the concept of early-to-late effects which bias ω_a was introduced. The long-term fluctuation of SiPM gains is not an early-to-late effect so it does not directly affect the ω_a measurement, but it complicates the analysis because different subsets of the data will have a different effective energy threshold to build wiggle plots. For this reason, the laser system fires a series of Out-Of-Fill (OOF) pulses, between each muon fill and the next. This provides a continuous monitoring of the SiPM performance and allows to build a long-term gain correction. The OOF correction is extracted by averaging $\mathcal{O}(500)$ pulses and comparing the measured energies with the reference from the Source Monitor:

$$G_{OOF} = \frac{\langle E_{OOF} \rangle}{\langle E_{SM} \rangle} \tag{5.2.4}$$

Absolute gain calibration

The STDP, IFG and OOF corrections calibrate the detector gain over a wide range of timescales and correct for effects that cause a gain sag; however, they still leave the recorded positron energies in ADC units. The last step of the energy calibration is to equalize SiPM response, and set the absolute scale. For this purpose, we have dedicated runs before the start of each Run where the Fiber Harps (described in Section 4.6) are inserted with a destructive effect on the muon beam, thus enhancing muon losses: the muons that are scattered towards the inside of the storage ring can typically hit multiple calorimeters in their trajectory because they are minimum ionizing particles (MIPs) and release a small amount of energy on individual crystals, with a time delay of ~ 6.2 ns between each calorimeter hit. We reconstruct scattered ("lost") muons by selecting single-crystal hits coincidences on consecutive calorimeters; for each crystal, we build the distribution of released energies, which have a gaussian shape. We equalize SiPM gains by fitting each gaussian and imposing that the peak position is the same for all crystals. The absolute scale, instead, was obtained from positron signals collected during Run-1: the T-Method wiggle plots was built, scanning for different energy thresholds and performing a 5-parameter fit with a function like Equation (4.7.4), where N_0, τ, A, ω_a and ϕ were left free to float; the energy threshold that minimized the statistical uncertainty on ω_a was set to 1700 MeV, and this calibration was used for following runs. Figure 5.2.6 shows that the minimum was still at 1700 MeV in Run-2 data.

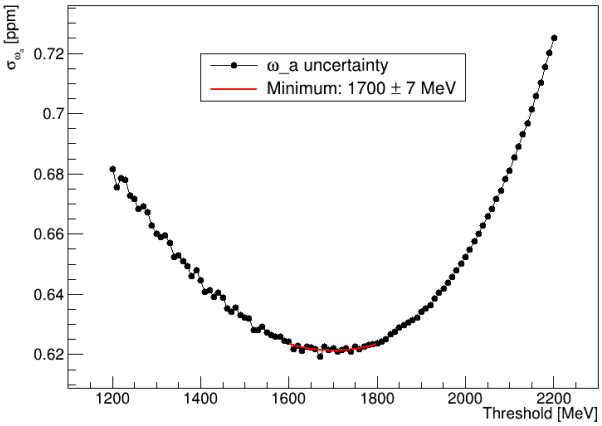

Figure 5.2.6: Statistical uncertainty of ω_a as a function of the energy threshold E_{th} for the T-Method fits (from a subset of Run-2).

5.2.3 Pileup subtraction

When two or more positrons hit the same calorimeter within $\mathcal{O}(10\,\text{ns})$, the reconstruction algorithm is not always able to separate the two events: the incident particles are reconstructed as a single hit, whose energy is the sum of the deposited energies. This is the pileup effect and it distorts the number of positron counts and the time and energy spectra. The reason why pileup is a problem when fitting ω_a is schematically explained in Figure 5.2.7: two low-energy positrons arrive on the same calorimeter at the same time, and can be mistaken for a high-energy hit; but a high-energy positron that arrives on the same calorimeter would decay from the red muon which has a different $g-2$ phase, instead. Thus, pileup affects the fit to the initial phase ϕ in Equation (4.7.4); more importantly, it does so in a time-dependent way, because the rate of double-events is proportional to the square of the rate of detected positrons, so it has a lifetime of $\sim 32\,\mu$s (half of the muon lifetime in the lab frame). This early-to-late modification

of ϕ introduces a systematic bias in ω_a, so we need to subtract pileup from our reconstructed events before attempting to fit the anomalous precession frequency.

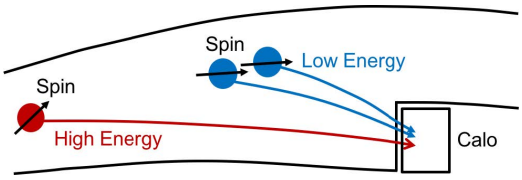

Figure 5.2.7: The blue muons decay later than the red muon, so they have a different precession angle (here the difference in angles is exaggerated on purpose). Due to pileup, two positrons that hit a calorimeter might be mistaken for a single positron that decayed earlier in time, with higher energy.

We will now review our "shadow window" method to subtract pileup. It is an algorithm that assumes that the probability of observing a "doublet" (pileup between two positrons) equals that for observing two "singlets" that are separated in time by an amount much smaller than the experiment's timescales. For every cluster in a calorimeter during a muon fill, the algorithm defines a time window of $T_D = 5\,\text{ns}$ that starts after a gap time $T_G = 149.2\,\text{ns}$ (equal to the cyclotron period), and searches for another cluster in that window: if it finds one, we say it identified a "doublet". In Run-2/3 analysis, we have added the search for triple events: if a positron event is found in the first shadow window, a second shadow window after the first is defined as well, with the same T_D and T_G; if we find another cluster, we identify a "triplet"; if we do not find another cluster, we check that the doublet wasn't part of a previous triplet, otherwise we won't count it. Figure 5.2.8 shows how the shadow windows are defined after the trigger positron event, to search for doublets and triplets.

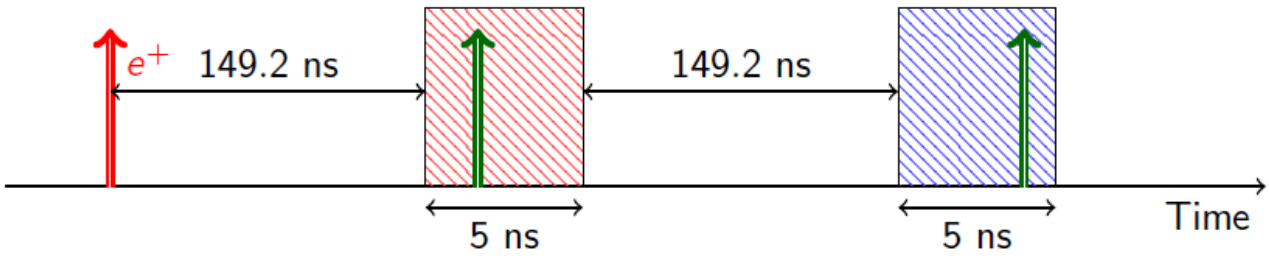

Figure 5.2.8: Example of shadow windows to search for double and triple pileup events, after a trigger positron event. The blue shadow is built only if an event is found in the red shadow. We also check that the positron found in the red band was not part of a previous triplet.

If we find a cluster in the shadow window(s), we retrieve the list of crystal times and energies that formed the trigger (T) and shadow (S) clusters, and we merge this shifting the shadow times back by $-T_G$ and $-2T_G$ for doublets and triplets respectively. We pass the merged list as an input to our clustering algorithm and check if it splits the list into two (or three clusters) or not. If the clustering splits the list, we move to the following trigger. We say that we have a pileup event if our clustering is not able to split the list: in that case, we keep record of the individual energies and times (E_T, t_T) (for trigger clusters) and $(E_{S_{1/2}}, t_{S_{1/2}})$ (for shadow clusters), and also build a "pileup" event with energy and time (E_2, t_2) (for doublets) or (E_3, t_3) (for triplets). The combined energy is the sum of individual cluster energies, whereas the combined time is the energy-weighted average of individual times, as in Equation (5.2.5):

$$
\begin{aligned}
E_2 &= (E_T + E_{S_1}) & t_2 &= \frac{(t_T + T_G/2)E_T + (t_{S_1} - T_G/2)E_{S_1}}{E_T + E_{S_1}} \\
E_3 &= (E_T + E_{S_1} + E_{S_2}) & t_3 &= \frac{(t_T + T_G)E_T + t_{S_1}E_{S_1} + (t_{S_2} - T_G)E_{S_2}}{E_T + E_{S_1} + E_{S_2}}
\end{aligned}
\tag{5.2.5}
$$

The reason why we shifted trigger and shadow times by $\pm T_G/2$ (doublets) and $\pm, T_G$ (triplets) is to account for the muon flux drop during the gap time(s). Calling $\rho(t)$ the probability for detecting positrons at time t, we can define the times t' and t'' such that the following relations hold for doublets and triplets, respectively:

$$
\begin{aligned}
\rho(t)\rho(t + T_G) &\equiv \rho^2(t') \\
\rho(t)\rho(t + T_G)\rho(t + 2T_G) &\equiv \rho^3(t'')
\end{aligned}
\tag{5.2.6}
$$

Assuming $\rho(t) \propto \exp(-t/\tau)$, we can solve Equation (5.2.6) and obtain $t' = T_G/2$, $t'' = T_G$. We repeat this procedure using all clusters as triggers, and then we populate four two-dimensional histograms filling them with the assigned energies and times from Equation (5.2.5): doublets are filled with (E_2, t_2), their related singlets with (E_T, t_T) and (E_{S_1}, t_{S_1}); triplets are filled with (E_3, t_3), their related singlets with (E_T, t_T), (E_{S_1}, t_{S_1}) and (E_{S_2}, t_{S_2}). From the two-dimensional histograms of positron events obtained with the clustering procedure described in Section 5.2.1, we subtract double and triple pileup events for each time and energy bin, and add singlets.

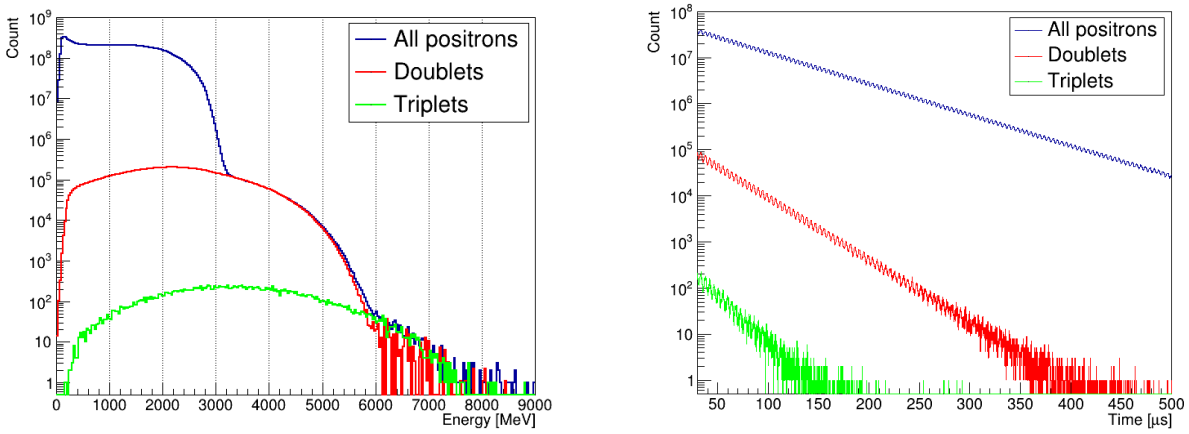

(a) **(b)**

Figure 5.2.9: Pileup energy (a) and time (b) distributions.

Figure 5.2.9 shows the time and energy distributions of the double and triple pileup corrections for the ReconITA clustering for a subset of Run-2. The double pileup contamination at $t = 30\,\mu s$ is $\sim 2 \times 10^{-3}$ and decays as $\tau_D \approx 32.2\,\mu s$, while the triple pileup contamination is $\sim 4 \times 10^{-6}$ and decays as $\tau_T \approx 21.5\,\mu s$. Almost all the energy spectrum above 3.1 GeV disappears after pileup subtraction: the systematic associated to how well we have corrected for pileup will be discussed in Section 6.2. In Run-1, the procedure to subtract triple events was not implemented and this was treated as a further systematic effect, which is not present anymore in Run-2/3. In Ref. [118], there are also more details on how we avoid double counting doublets and triplets, for instance in the case in which one of the positrons (trigger or shadow) used to build a doublet was, in fact, a pileup event itself.

There is a further detail that we take into account within the ω_aEuropa pileup subtraction, which handles the real-case scenario when two positron signals overlap on the same crystal, and which defines the "semi-empirical" label in Table 5.1.2. In this situation, the SiPM will receive two signals so close in time that the reconstruction algorithm might not be able to distinguish them, fitting a single pulse instead. Unless the two pulses are exactly simultaneous, the energy determined by fitting a single pulse will be slightly lower than the sum of the two pulses. Figure 5.2.10 shows an example of two overlapping pulses of equal energy which are 1 c.t. apart. The fit using a single pulse results underestimates the energy by $\sim 2.3\%$.

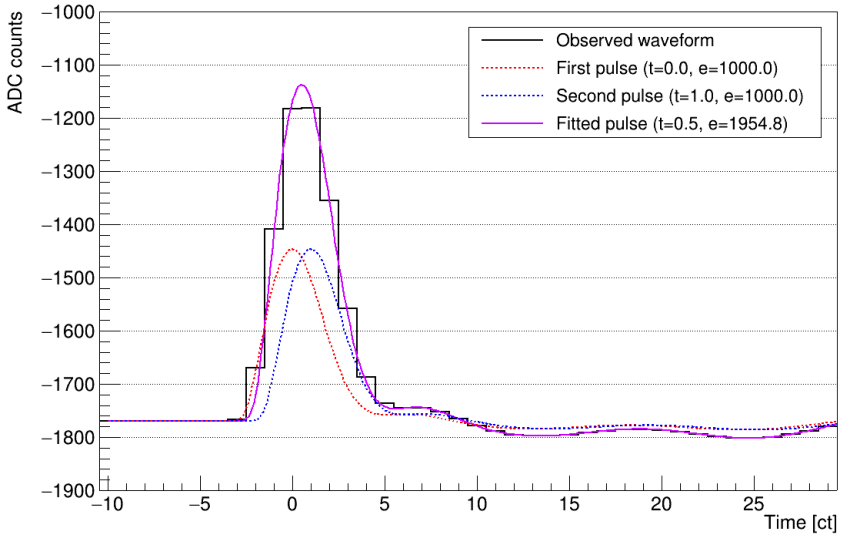

Figure 5.2.10: Template fit of two pulses when they are $\Delta t = 1$ c.t. (1.25 ns) apart. A single template fit is performed as the reconstruction is not able to distinguish between the two underlying pulses. The measured energy ($E_{fit} = 1954.8$ ADC*c.t.) is smaller than the sum of the two underlying pulses.

When doublets and triplets are built from trigger and shadow clusters with multiple hits on the same crystals, we need to reproduce this effect to avoid a systematic bias on the observed energy. To study it, real SiPM pulses were used to create artificial traces by summing two pulses with arbitrary time separation and energies. The traces were then sampled at 800 MHz (as a reminder, 1 c.t. corresponds to 1.25 ns sampling time) and the points were multiplied by a smearing factor that represents the SiPM noise. This factor was randomly extracted from a Gaussian distribution of mean 1 and variance $\sigma^2 = 0.003^2$, where 0.003 was the RMS value we observed from waveform fits residuals. Finally, the artificial trace points were digitized into integer ADC values and the result was stored in a format which could be processed by the reconstruction algorithm as if it were real raw data. We provided the artificial signal as an input to our pulse fitter and we analyzed the fitter response, to check whether or not the pulses were being split, and, if not, which were the reconstructed energies and times. From this study, we extracted the following parameters as a function of the time separation Δt between the original pulses, and their energies E_1 and E_2:

1. The efficiency of separating the two pulses;
2. The bias in energy of the single fitted pulse;
3. The bias in time of the single fitted pulse.

Figure 5.2.11 shows these corrections on average. When there are two or more pulses on the same SiPM in a shadow window coincidence, they are merged into one pulse according to the probability of Figure 5.2.11(a). If merged, the following corrections are applied:

$$E' = f_{corr}(E_1 + E_2), \qquad t' = \frac{t_1 E_1 + t_2 E_2}{E_1 + E_2} + t_{corr} \tag{5.2.7}$$

where both f_{corr} and t_{corr} depend on Δt, E_1, and E_2, according to the corrections of Figures 5.2.11(b) and 5.2.11(c) respectively.

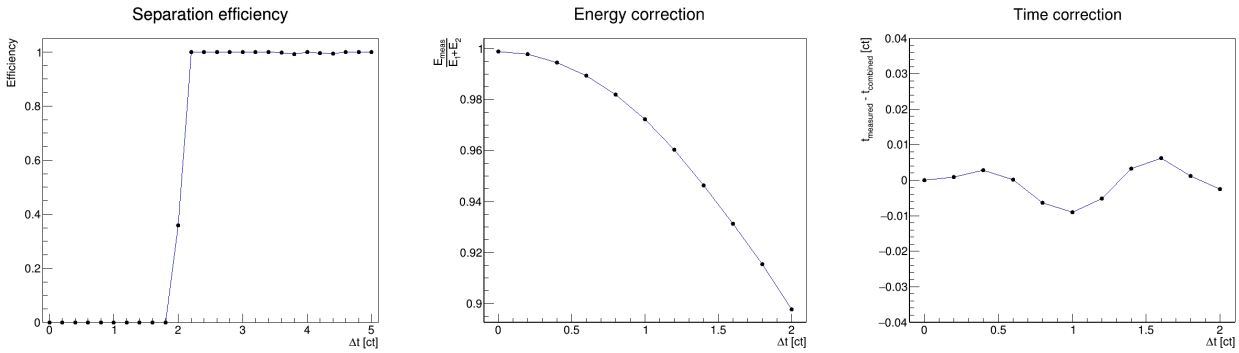

(a) **(b)** **(c)**

Figure 5.2.11: Pulse fit average corrections for multi-hit crystals in a pileup coincidence. (a) is the efficiency of separating the two individual pulses, (b) is the ratio between the fitted energy and the sum of the two pulses, and (c) is the difference between the fitted time and the energy-weighted average of the two pulses.

5.2.4 Lost muons

In the ω_a analysis, we need to take into account the number of muons which are lost from the stored beam before they can decay into positrons, the so-called "lost muons", introduced in Sections 4.7.3 and 5.2.2.

The procedure with which we build the lost muons function in the ω_aEuropa analysis has not changed since Run-1, and it is described in Ref. [118, 121, 122]. As anticipated in previous Sections, we can easily identify lost muons with calorimeters and trackers thanks to the characteristic signature of the traces they leave: they have a momentum close to 3.1 GeV/c which can be measured by trackers, and deposit $\sim$ 170 MeV of energy in the calorimeters, which is the typical energy deposit for a MIP particle travelling in 14 cm of PbF_2; their trajectory is almost perpendicular to the calorimeter's face, so they only deposit energy in a single crystal and can hit several consecutive calorimeters, with a time of flight between two calorimeters $\approx$ 6.2 ns. Therefore, in the ω_aEuropa analysis we used data from the two trackers, and from the calorimeters behind them, to build likelihood functions based on the deposited energy, position distribution and time of flight with respect to the previous and to the next calorimeter. We built the $L(t)$ histograms by counting events that satisfied the likelihood cuts in 2, 3, 4 or even 5 consecutive calorimeters. Figure 5.2.12(a) shows the $L(t)$ function obtained by summing triple, quadruple and quintuple coincidences. We compared the functions for Run-2/3 datasets with the one from Run-1d, where losses were enhanced by the damaged ESQ resistors that greatly affected beam dynamics in Run-1. The double coincidences are not included in our $L(t)$, as they were found to contain some residual positron background; however, they are used as a cross check of the systematics related to our partial knowledge of the "true" lost muons distribution (see Section 6.4). The four $L(t)$ functions for Run-1d and Run-2/3 have a similar shape at later times (t 200 µs) but early-in-fill Run-2 is different: a bump is present and peaked at around 70 µs, with a size that was found to be correlated with magnet parameters, such as the yoke temperature and feedback current.

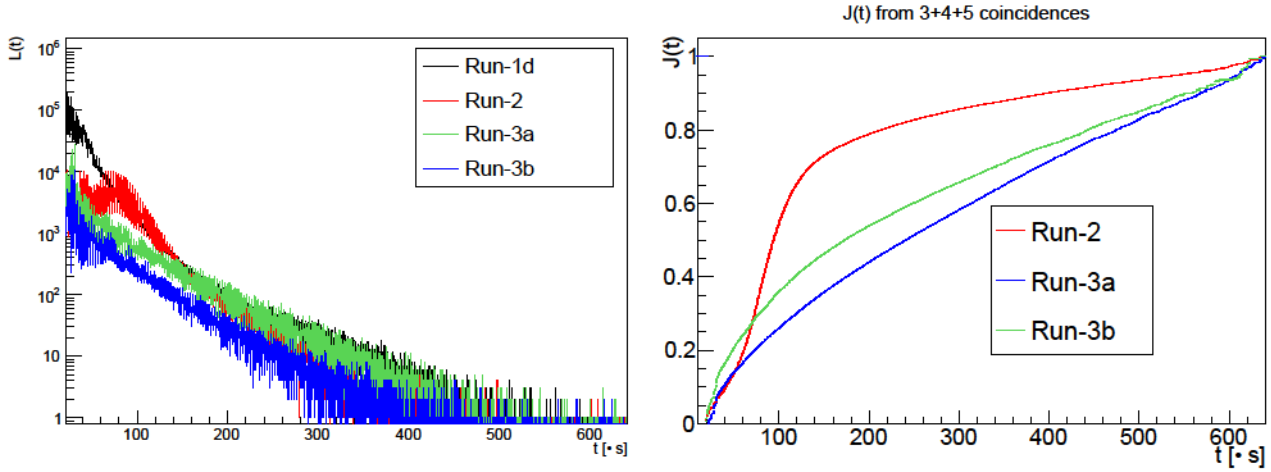

(a) (b)

Figure 5.2.12: Run-1d dataset compared with Run-2/3 datasets: (a) $L(t)$ histograms with lost muons counts from $3+4+5$ coincidences, and (b) the integrated lost muons functions $J(t)$.

The consequence of losing muons during storage time is that the observed decay rate deviates from a pure exponential with 64.4 µs of lifetime. By solving a differential equation, we obtain:

$$\begin{aligned} \frac{dN}{dt} &= -\frac{N}{\gamma\tau} - L(t) \\ N(t) &= N_0 e^{-t/\gamma\tau}\left(1 - k_{LM}\int_0^t L(t')e^{t'/\gamma\tau}dt'\right) \equiv N_0 e^{-t/\gamma\tau}\left(1 - k_{LM}J(t)\right) \end{aligned} \tag{5.2.8}$$

where N_0 is the initial number of stored muons, and the scale factor k_{LM} is a parameter that takes into account the efficiency of the muons selection algorithm, and included in the ω_a fit (see Section 5.5.2). Figure 5.2.12(b) shows the three $J(t)$ curves for the Run-2/3 datasets, where in the Run-2 case the $L(t)$ is peaked at around 70 µs. We chose to normalize the $J(t)$ functions such that they are equal to 1 for $t = 650.0644$ µs (see Section 5.5.6): by doing so, the fitted k_{LM} does not depend on the dataset size.

5.2.5 Residual slow term correction

Since the Run-1 analysis, we have been affected by a residual early-to-late (or "slow") effect in our ω_a fits, whose source is still under investigation [3, 108]. In our preliminary Run-2/3 fits, we observed several hints of this effect, most of them also present in Run-1. When performing T/A-Methods fits selecting slices of energy (30 MeV bins), the k_{LM} parameter was not constant, but it drifted downwards and reached negative values as the energy increased. A negative k_{LM} would be nonphysical, because it would mean that muons were somehow added to the stored beam much later than injection. Moreover, in Run-3 fits k_{LM} was even starting from a negative value at low energies: as shown in Figure 5.2.12(a), losses were much reduced in Run-3 so it was easier for a slow effect to pull k_{LM} towards negative values, rather than in Run-2 where a big bump near 70 µs placed a strict constraint on k_{LM}. Another hint of a slow term was the typical value of the reduced χ^2 (the χ^2 normalized by the number of degrees of freedom, that we will indicate as χ^2/n.d.o.f. in the rest of this Thesis). In our preliminary fits, the χ^2/n.d.o.f. was always around 1.08 with n.d.o.f. $= 4133$, suggesting that there was a term that we were not accounting for; in the fast fourier transform (FFT, see Section 5.5.4), a peak at near-zero

frequencies in the residuals was present, hinting at the slow nature of the unaccounted effect, rather than a missing oscillation in the fit function.

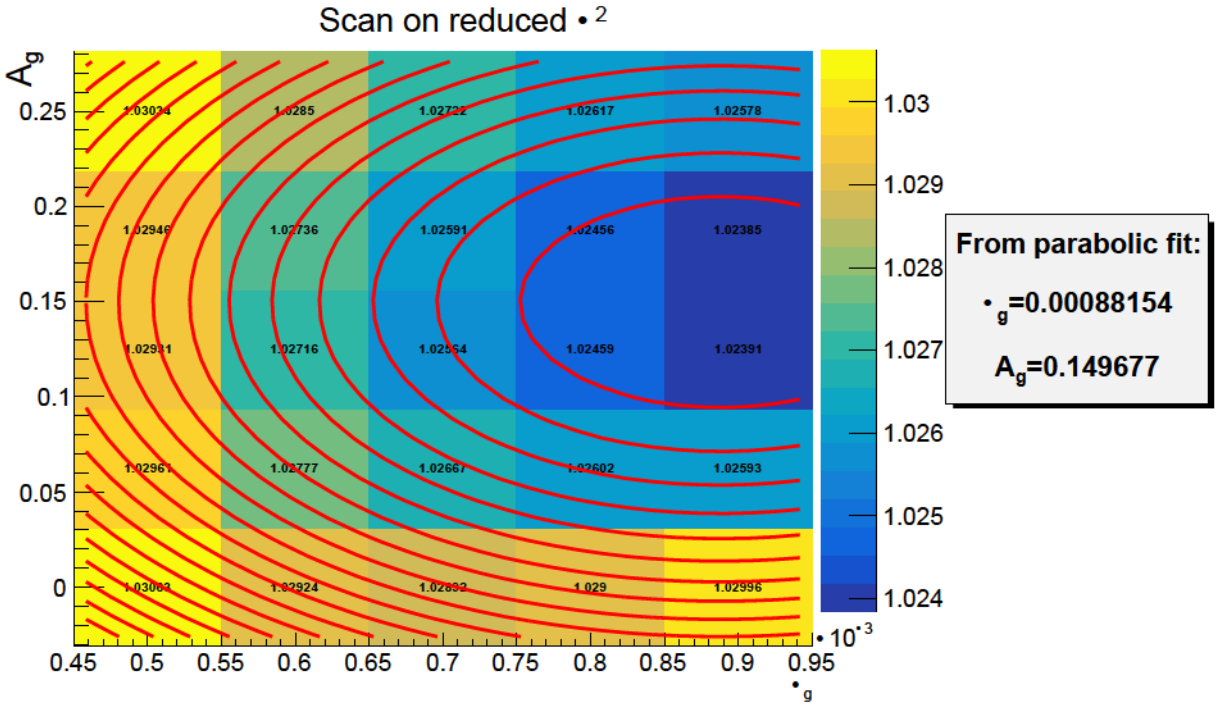

Figure 5.2.13: Scan on the χ^2/n.d.o.f. for Run-2 preliminary T-Method fits, to extract the optimal parameters of the residual slow term correction.

To correct for this residual slow term, different groups have taken different approaches since Run-1. In the ω_aEuropa analysis, we chose to apply an "Ad-Hoc correction" which consists in scaling each cluster's energy by a function that depends on the time of the cluster, in the assumption that the residual slow effect is a rate-dependent perturbation of the energies. Therefore, a function in the form of Equation (5.2.9) is a suitable candidate to account for the slow effect and fix the problems reported above.

$$G(t) = 1 + \delta_g e^{-t/\gamma\tau} \left[1 + A_g \cos\left(\omega_a t - \phi\right)\right] \tag{5.2.9}$$

From preliminary fits, the muon lifetime $\gamma\tau$ was fixed to the fitted Run-2 value of 64.43 µs, ω_a to 1.43939 rad/µs, and ϕ to 4.117 rad. $\gamma\tau$ actually varied across Run-2/3 datasets, but the shift on ω_a due to the choice of its value was found to be negligible and included in the systematics (see Section 6.5). Still from preliminary fits to T-Method wiggle plots, we performed a scan on the δ_g and A_g parameters in order to see which values minimized the χ^2/n.d.o.f.
δ_g was scanned in the range $[5, 9] \times 10^{-4}$ at steps of 10^{-4}, and A_g in the range $[0, 0.25]$ at steps of 0.0625. We fitted the 5×5 scan on χ^2/n.d.o.f. with a quadratic function of the form $p_0 (x - p_1)^2 + p_2 (y - p_3)^2 + p_4$, to extract the optimal (δ_g, A_g) from the minimum (p_1, p_3) of the paraboloid. The optimal values for Run-2 were found to be $\delta_g = 0.8815 \cdot 10^{-3}$ and $A_g = 0.1497$, as shown in Figure 5.2.13. This was not the most generic quadratic expression to extract the minimum because it is missing $x \cdot y$ terms, but this choice was motivated by the fact that we did not observe cross terms $\delta_g \cdot A_g$. The optimal δ_g value for Run-2 was found at the edge of the interval: a further scan on δ_g with a bigger step and larger interval was also performed, which ensured that the value we found was indeed a minimum.
Figure 5.2.14 shows the k_{LM} parameter as a function of the cluster energy, comparing the case in which the residual slow term correction is applied with the case in which it is not.

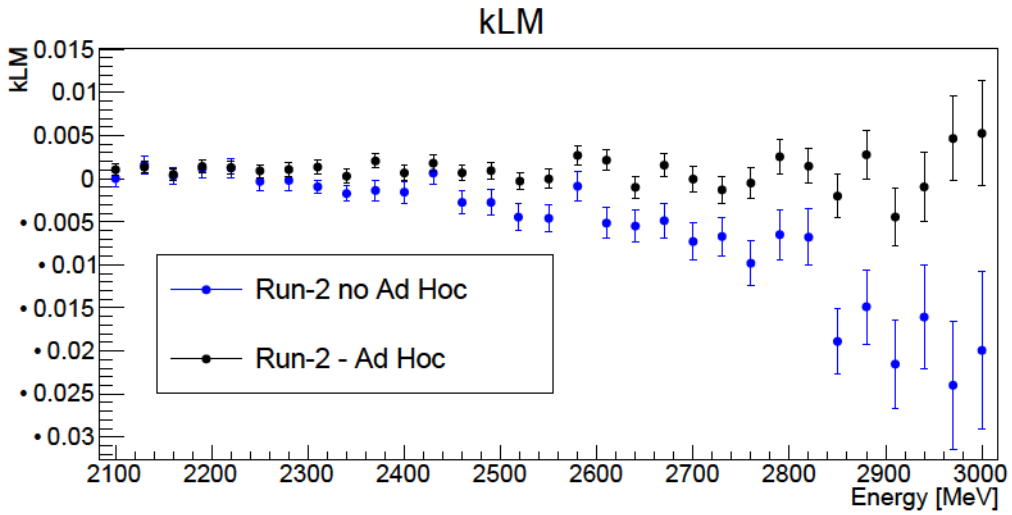

Figure 5.2.14: Energy binned fits on Run-2 data, T-Method, to extract the k_{LM} parameter as a function of the energy. One of the results of the residual slow term correction is to make k_{LM} more stable at higher energies and keep it above 0.

For Run-3a and Run-3b, a similar procedure to obtain the optimal parameters from the minimization of the χ^2/n.d.o.f. yielded the following results: $\delta_g = 0.00035$ and $A_g = 0.1192$. However, for these choices of the slow term correction parameters, k_{LM} was not flat but instead it drifted towards lower values at higher energies. The choice was made to determine the optimal value for δ_g that made k_{LM} more stable as a function of the energy. Figure 5.2.15 shows that both $\delta_g = 5 \times 10^{-4}$ and $\delta_g = 7.5 \times 10^{-4}$ stabilize k_{LM}, so we chose the intermediate value $\delta_g = 6.25 \times 10^{-4}$ for Run-3 data, whereas we kept the $A_g = 0.1192$ from the fit that minimized χ^2/n.d.o.f.
The A_g parameter does not affect significantly the k_{LM} shape as a function of the energy, but it can shift ω_a and also the fit χ^2/n.d.o.f., which will be handled as a systematic error in Section 6.5.

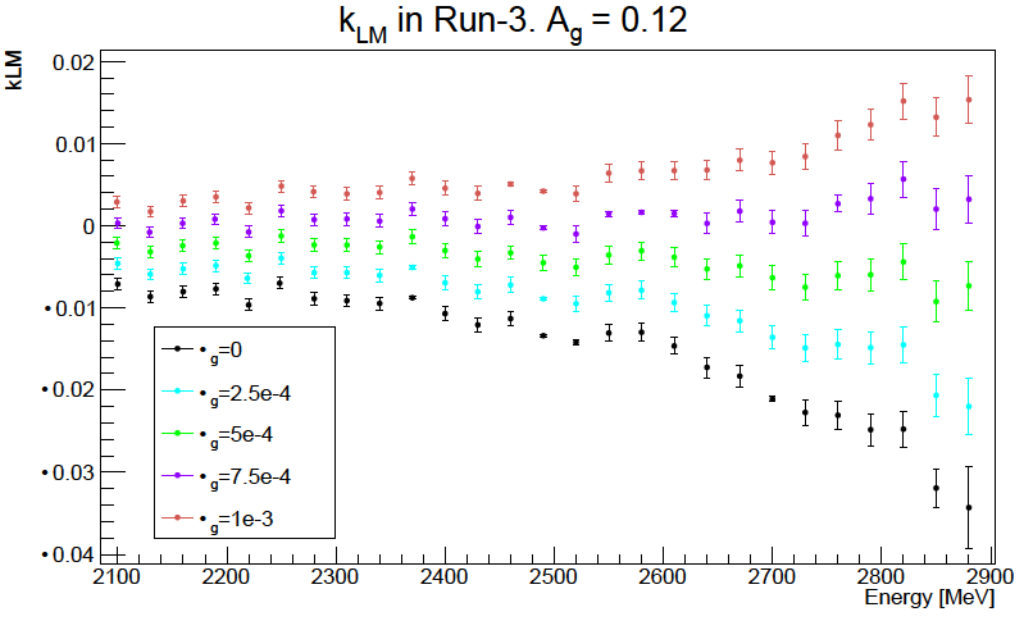

Figure 5.2.15: Energy binned fits on Run-3 data where Run-3a and Run-3b were combined, in order to improve the statistical uncertainty on the results. The parameter δ_g was chosen to flatten k_{LM} even if it remained at negative values.

Since $\delta_g \sim 10^{-3}$, we can infer that the size of the residual slow term is $\sim 10^{-3}\text{GeV} = \mathcal{O}(\text{MeV})$. When the first hints of the slow term were found, it was suggested that the rate-dependent effect could be due to an incorrect parametrization of the IFG correction (see Section 5.2.2). In Figure 5.2.5 we showed that, combining all of the Run-2/3 residuals between the laser data points and our IFG fits, no effect as large as $0.5 \cdot 10^{-4}$ can be observed: an incorrect evaluation of the IFG correction can only lead to a $\mathcal{O}(50\,\text{keV})$ effect in our data, much smaller than the observed residual slow term.

5.2.6 Time randomization and energy selections

After reconstructing positron events with our clustering algorithm, we build two-dimensional histograms that are filled with the time (x-axis) and energy (y-axis) of clusters. These histograms combine data from all 24 calorimeters, but we have the possibility to build separate histograms for individual calorimeters. When injected into the storage ring, the muon beam is a bunch of $\sim 120\,\text{ns}$ which is shorter than the cyclotron period of $T_c = 149.2\,\text{ns}$, so the number of detected positrons in each calorimeter is modulated by the cyclotron frequency. This is called the "fast rotation" effect: it is an additional frequency in the time distribution of the decay positrons, which can affect the fit of ω_a if we do not take it into account. The strategy to suppress this effect is to choose a time binning on the time-axis equal to the cyclotron period T_c. We therefore build histograms with 4691 bins that go from 0 to 699.8972 µs.
As in Run-1, a second strategy to remove the fast rotation effect in the ω_a analysis is to apply a time randomization to all positron hit times when filling the Run-2/3 histograms. In the ω_aEuropa group, we used the random engine `CLHEP::Ranlux64` with luxury level 2, that was found to have a good performance and computational speed [123], to generate a random shift in the range $[-T_c/2, +T_c/2]$ for each positron event. Since the random number generator initialization is based on a seed, and the choice of the seed can bias ω_a, the ω_a analysis is repeated for many seeds, and the average of the resulting ω_a per-seed distribution is quoted as our final result. The statistical uncertainty associated to the randomization procedure is taken as:

$$\sigma_{Rand} = \frac{\sigma_R}{\sqrt{n_S - 1}} \tag{5.2.10}$$

where σ_R is the standard deviation of the per-seed ω_a distribution, and n_S the total number of seeds used.

On the y-axis of our two-dimensional histograms, the energy binning is set to 10 MeV: we have 1053 bins that go from 0 to 10530 MeV. We integrate positron counts on the energy axis to build our wiggle plots: for the T-Method, we chose a lower energy threshold of 1700 MeV which minimizes the statistical uncertainty on ω_a, and no upper threshold. In principle, for the A-Method analysis we could include positrons of all energies, even the ones whose direction of emission is anti-correlated with the muon spin, by weighting their contribution to the fit with the asymmetry value corresponding to the specific energy. The figure of merit (FOM) that has to be maximized in order to minimize the statistical uncertainty on ω_a is proportional to NA^2 (see Section 1.3.3 and Ref. [26]). Figure 4.7.2(b) showed the NA^2 scans for ω_aEuropa as a function of the energy threshold, both for the T-Method and for the A-Method. The choice was made to only use positrons with positive asymmetry for the A-Method, which means that the lower energy threshold is 1000 MeV: this choice avoids problems of energy resolution, electronic noise and contamination from lost muons. As shown in Figure 4.7.2(b), the gain in precision from a lower threshold would be negligible. For the A-Method there was an agreement amongst all the ω_a analsyses to also apply an upper energy threshold, set to 3000 MeV, a value that is close enough to the physical limit of 3.1 GeV of positron energy from muon decay, above which the asymmetry is not well defined.

5.3 Ratio Method to build wiggle plots

In Section 4.7.1, we introduced the Ratio Method, a technique to build wiggle plots, alternative to the T/A-Method, that aims at reducing the sensitivity of ω_a to slow effects. It was used in the previous experiment at BNL [87, 124, 125], and also in the Fermilab Run-1 result as a test of robustness, but not for the final combination of ω_a values [108, 126]. A full description of the mathematical background can be found in Appendix B. In this Section, we will show how the exponential decay with the boosted muon lifetime vanishes by construction.
The technique consists in randomly splitting positron events into 4 different sub-groups, so that each one will contain $\sim$ 25% of the total events. Four histograms (one for each sub-group) are built and filled with the detected times of decay positrons. The first two histograms are labelled $v_{1,2}(t)$ and leave the positron times unchanged; the other two are labelled $u_{\pm}(t)$, where the subscript means that the positron times are shifted by $\mp T_a/2$ (T_a is the $g-2$ period, $\sim 4.365\,\mu$s), so that the time distribution $N(t)$ of positrons becomes $N(t \pm T_a/2)$. This procedure is called "Quartering" and, since it is random, it uses an input random seed. We can then define two histograms, $U(t) \equiv u_+(t) + u_-(t)$ and $V(t) \equiv v_1(t) + v_2(t)$, and the ratio $R(t) \equiv (V(t) - U(t))/(V(t) + U(t))$. Assuming that the time distribution $N(t)$ of positrons is given by a simple 5-parameter function:

$$N(t) = N_0 e^{-t/\gamma\tau} \left[1 + A\cos\left(\omega_a t + \phi\right)\right] \tag{5.3.1}$$

then $R(t)$ is equal to:

$$R(t) = \frac{2N(t) - N(t + T_a/2) - N(t - T_a/2)}{2N(t) + N(t + T_a/2) + N(t - T_a/2)} \tag{5.3.2}$$

Since $T_a/2 \ll \gamma\tau$, the exponential terms at the numerator and denominator almost cancel out perfectly in the ratio. The shift in time by $\pm T_a/2$ is such that all terms with $\cos\left(\omega_a t \pm \omega_a T_a/2\right)$ are equal to $-\cos\left(\omega_a t\right)$. Thus, to the first order approximation, Equation (5.3.2) becomes a 3-parameter function:

$$R(t) \approx A\cos\left(\omega_a t + \phi\right) \tag{5.3.3}$$

where the normalization parameter N_0 and the boosted muon lifetime $\gamma\tau$ from Equation (5.3.1) are not present anymore. In Section 6.6, we will evaluate the systematic error arising from the assumption that the value chosen *a priori* for T_a (which, in principle, depends on the ω_a fit) is the one that exactly simplifies $\omega_a T_a/2 = \pi$. In the Run-1 studies in Ref. [126], it was shown that an incorrect guess of T_a could lead to an effect of $d\omega_a/dT_a \quad 0.1$ ppb/ppm. In Section 6.6, we will show similar results for the Run-2/3 datasets and report a related systematic error of the order of a few parts per billion.

The R-Method wiggle plots use random seeds as input for three types of time randomization: during the Quartering step, positron events are randomly assigned to four histograms, two of which shift their times by $\pm T_a/2$; the fast rotation signal is cancelled by applying a random time shift in the uniform range $[-T_c/2, T_c/2]$, as described in Section 5.2.6; also the vertical oscillation frequency is removed from the data, with a similar technique as the fast rotation.
Table 4.7.1 shows that the vertical waist (VW) frequency ω_{VW} is very close to 10 times the ω_a frequency: because of how the R-Method wiggle plots are built, all oscillating effects whose frequencies are even multiples of ω_a are highly suppressed [126, 127]. This is the reason why, in the ω_aEuropa analysis, we randomize the VW frequency instead of fitting it in the data where the amplitude would be too small for a meaningful fit. In this procedure, the VW period T_{VW} is fixed to 440.63 ns which is the value obtained in a preliminary analysis of the T-Method wiggle

plots. Thus, in addition to the fast rotation randomization, positron times are also shifted by a random value extracted by a uniform distribution in the range $[-T_{VW}/2, +T_{VW}/2]$.

5.4 Building T/A/R/RA-Methods wiggle plots: data weights and bin errors

In the first part of this Chapter, we have described all the steps for positron reconstruction in the ω_aEuropa analysis: crystal waveforms are calibrated in time with laser synchronization pulses, and in energy with all the corrections described in Section 5.2.2); our new clustering algorithm identifies positron events and assigns time and energy of calorimeter detection; the residual slow term correction described in Section 5.2.5 rescales the positrons' energies, in order to account for the residual slow term that would otherwise affect our data; pileup histograms (doublets, triplets, and all the associated singlets) are built and subtracted to our positron data, as described in Section 5.2.3. We will now review how we transform our two-dimensional histograms with times and energies information into the so-called "wiggle plots", typical of the Muon $g-2$ experiments.

For each time and energy bin of our positron histograms, the error assigned to the pileup-corrected value is the following:

$$\delta N(t,E) = \sqrt{N'(t,E) + P(t,E)} \tag{5.4.1}$$

where N' is the observed number of positrons, P is the pileup correction applied (we remove doublets and triplets, and add the associated singlets), N is the corrected number of positrons. We assume that the number of observed positrons N' and that of pileup events P follow Poisson distributions, so that the variances are also equal to N' and P, respectively.
To build the T-method wiggle plot, the pileup-corrected histograms are integrated above a fixed energy threshold E_{th}: for each time bin on the x-axis, we sum all the energy bin's contents; the error assigned to this sum in the final histogram is the sum in quadrature of the individual energy bins' errors in the two-dimensional histogram. As explained in Section 5.2.6, the energy threshold is chosen to be the one that minimizes the uncertainty on the fitted ω_a frequency, which is 1700 MeV for the T-Method.
In Sections 4.7.1 and 5.2.6, we described the principle of the A-Method technique, that allows to lower the energy threshold of the wiggle plots and achieve a smaller statistical uncertainty on ω_a. This method consists in extracting the asymmetry function versus energy (a function like the one shown in Figure 1.3.5) and weighting each positron event with energy E with the corresponding asymmetry $A(E)$. In practice, in the ω_aEuropa analysis we build a histogram $A(E)$ with small energy bins, by measuring the amplitude of the $g-2$ oscillation from wiggle plots that only use events in each energy bin. The effective asymmetry is a convolution between the theoretical function of Equation (1.3.16) and the detector acceptance. As a first step, we obtained 87 wiggle plots, where each one integrated the pileup-corrected positrons in a similar way as the T-Method but only over 30 MeV of energy, starting from 495 MeV until we reached 3105 MeV. We performed fits with the full T-Method function (described in the Section 5.5) to obtain the asymmetry versus energy $A(E)$ histograms.
Figure 5.4.1 shows the comparison between Run-2/3 asymmetry functions and the theoretical one: due to detector acceptance effects, the maximum value reached for $A(E)$ is lower than 1 (around 0.8) and the energy at which $A(E) = 0$ is about 300 MeV lower than the theoretical calculation. We have used these functions to weight the A-Method (and, as it will be explained later, also the RA-Method) wiggle plots: right after pileup subtraction, we weighted each bin in

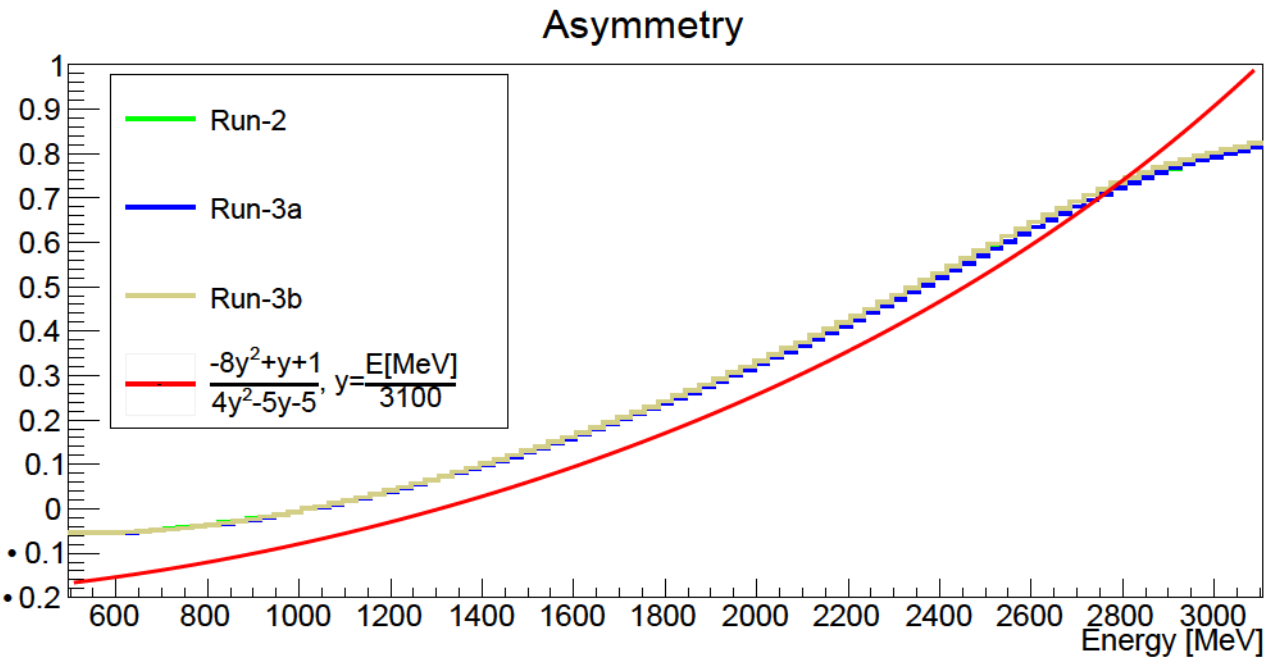

Figure 5.4.1: Asymmetry functions for the Run-2/3 datasets. The red curve is the theoretical asymmetry in the lab frame from Equation (1.3.16), where y is the positron energy normalized to the maximum value of ~ 3.1 GeV.

the two-dimensional positron histogram with the asymmetry $A(E)$ corresponding to the energy value, and rescaled the bin error according to the following formula:

$$\delta N_{A/RA}(t, E) = A(E)\, \delta N_{T/R}(t, E) \tag{5.4.2}$$

where $\delta N_{T/R}(t, E)$ is the bin error obtained from Equation (5.4.1), and the subscripts T, R, A and RA stand for the corresponding methods. As previously stated, the two-dimensional pileup-corrected histograms have energy bins of 10 MeV of width, but the $A(E)$ histogram was built integrating over 30 MeV intervals to ensure that there was enough statistics for a meaningful fit. Therefore, the energy E in Equation (5.4.2) is the center value of 10 MeV energy bins, and the value of the asymmetry for that energy is extrapolated by linear interpolation from the 30 MeV points.
After weighting with the asymmetry, we integrated the two-dimensional histogram over energy bins with the same procedure as T-Method, but with the lower and upper energy thresholds of 1 GeV and 3 GeV.

To build the Ratio and Ratio-Asymmetry Methods wiggle plots (R/RA-Methods), we started from two-dimensional histograms of positron counts, built with the same time and energy binnings as the T/A-Methods. The statistical uncertainty on ω_a does not change significantly between R/RA and T/A: hence, the R-Method has a lower energy threshold of 1700 MeV and no upper threshold, like the T-Method; the RA-Method has a lower energy threshold of 1000 MeV and an upper threshold of 3000 MeV, like the A-Method. To build the R-Method wiggle plot, we first split positrons into four sub-groups, namely v_1, v_2, u_+ and u_-, with equal probabilities of 25% each. As described in Section 5.3, u_+ and u_- shift the positrons' times by a fixed value of $\mp T_a/2$ respectively, where T_a is obtained as the period of the ω_a frequency reference value 1.43939 rad/µs. After splitting the data into four sub-groups, we combined v_1 and v_2 into a two-dimensional histogram V, and u_+ and u_- into a two-dimensional histogram U. Before this Quartering step, we built pileup singlets, doublets and triplets events with the shadow method, and built separate pileup histograms for V and U, labelled V_{pileup} and U_{pileup}

respectively, with a similar Quartering procedure; for pileup events, we made sure that the two singlets associated with a doublet were assigned to the same sub-group as the doublet, and likewise for the three singlets associated with a triplet. We subtracted pileup from V and U histograms, and assigned bin errors with the same formulas that we used for the T-Method; then we integrated V and U over energy to project them into one-dimensional histograms $V(t)$ and $U(t)$ with the same procedure and energy thresholds as the T-Method. Finally, we took the following ratio to construct the R-Method wiggle plot $R(t)$:

$$R(t) = \frac{V(t) - U(t)}{V(t) + U(t)}, \qquad \delta R(t) = \frac{2V(t)U(t)}{(V(t) + U(t))^2}\sqrt{\left(\frac{\delta V(t)}{V(t)}\right)^2 + \left(\frac{\delta U(t)}{U(t)}\right)^2} \tag{5.4.3}$$

The formulas for bin errors come from error propagation: in the case of Poissonian counts, $\delta V(t) = \sqrt{V(t)}$ and $\delta U(t) = \sqrt{U(t)}$, so the formula for the bin error can be simplified as $\delta R(t) = \sqrt{(1 - R^2(t))/(U(t) + V(t))}$; but, as stated before, in general we do not have Poissonian counts due to pileup correction, and also because of $A(E)$ weights in the case of A/RA-Methods. For RA-Method histograms, we first performed the same procedure as the R-Method to build two-dimensional V and U histograms, and then weighted each bin with the asymmetry $A(E)$ and assigned bin errors with the same formula as Equation (5.4.2) for the A-Method; then we projected them to $V(t)$ and $U(t)$ with the energy thresholds of the A-Method. For each time bin of the RA-Method wiggle plot, the error is assigned according to Equation (5.4.3).

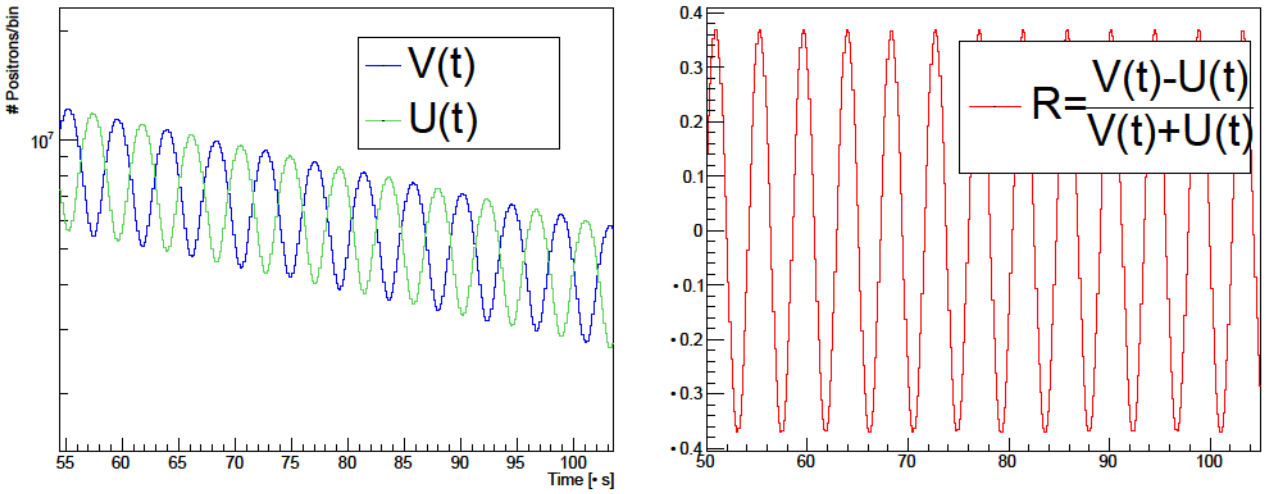

(a) (b)

Figure 5.4.2: Examples of Ratio-Method histograms from a subset of Run-2 in the $[55, 105]$ µs range: (a) $V(t)$ and $U(t)$ after pileup correction, (b) the Ratio wiggle plot $R(t)$.

Figure 5.4.2(a) shows the pileup-corrected, one-dimensional histograms $V(t)$ and $U(t)$, where the exponential decay due to the muon lifetime is still present in the data; Figure 5.4.2(b) shows the R-Method wiggle plot $R(t)$, where, by construction, the exponential decay is cancelled out. As described in Section 5.3, the R/RA-Methods split clusters into four different groups of approximately equal size, one of which shifts cluster times by $+T_a/2$ and another one by $-T_a/2$, where T_a is the anomalous precession period, ~ 4365 ns. This means that, in the R/RA-Methods, approximately 25% of the clusters whose times are within ~ 2.18 µs before the nominal fit start time are included in the analysis, and approximately 25% of the clusters within ~ 2.18 µs after the nominal fit start time are excluded from the analysis. The opposite thing happens for clusters within $\pm \sim 2.18$ µs of the nominal fit end time, but the events in that region are much less than the ones at the beginning of the fit window, so the contribution

is negligible. This does not happen in the T/A-Methods, so in general the number of positron events in the T/A and R/RA wiggle plots can be different: the allowed statistical differences were studied with dedicated Monte Carlo, and found to scale as $\sim 1/\sqrt{N}$, where N is the number of positrons in the analysis [128, 127].

5.5 Fit function

For each method, the wiggle plot is fitted to extract the anomalous precession frequency ω_a, the main parameter of interest. Since ω_aEuropa, like all ω_a analyses, applies a software blinding procedure described in Section 4.7.6, all ω_a fit values reported in this Thesis are actually the blinded R values from Equation (4.7.17).

The fit procedure is based on the χ^2 minimization method using the `TMinuit2` minimizer included in the `ROOT` software. The minimization algotrithm is `MnMigrad` and the `TMinuit::mnimpr` option is used to improve the local minimum [129] identification. Uncertainties on the parameters are computed using the `MnHesse` algorithm (default in `MnMigrad`) for greater speed. However, for the final values quoted in this Thesis, the `MnMinos` technique has been used to improve the error estimation.
The fitting code proceeds in steps, going from a simple 5- (3-) parameter function to the full 28- (16-) parameter function, for the T/A- (R/RA-) Methods. In each step, we use the parameters found in the previous one as initial guesses. The parameters are added in order to eliminate, at each step, the highest frequency peak in the fast fourier transform (FFT) of fit residuals (see Section 5.5.4).
The nominal fit for Run-2/3 will have additional terms with respect to Run-1 [108], to account for new effects observed in the coherent betatron oscillation (CBO) beam dynamics that will be explained in the following.
The full fitting equation used for Run-2/3 is:

$$\begin{aligned} N(t) = \boldsymbol{N_0}\, e^{-t/\gamma\tau}\, [1 \,+\, \boldsymbol{A}\, A_{BD}(t)\, \cos\left(\boldsymbol{\omega_a}\, t + \phi_{BD}(t) \,-\, \boldsymbol{\phi_0}\right)] \times \\ \times\; N_{CBO}(t)\, N_{VW}(t)\, N_y(t)\, N_{2CBO}(t)\, \Lambda(t)\, N_{CBOVW}(t) \end{aligned} \tag{5.5.1}$$

where the terms $A_{BD}(t)$, $\phi_{BD}(t)$ in the first row represent the beam dynamics effect that affect the amplitude and phase of the oscillation over time, and $N_{CBO}(t)$, $N_{VW}(t)$, $N_y(t)$, $N_{2CBO}(t)$, $\Lambda(t)$ and $N_{CBOVW}(t)$ in the second row represent the beam dynamics effects on the total number of detected positrons. These terms will all be described in detail and motivated in the following paragraphs. All free parameters will be highlighted in bold and red. The convention was to use a minus sign in front of free parameters that represented phases.

5.5.1 Coherent Betatron Oscillation

The muon beam radial motion and the CBO effect were introduced in Section 4.7.2. The CBO term is modeled with the oscillation function of Equation (5.5.2), where the amplitude varies in time because the muon ensemble decoheres late-in-fill, thus it is modulated by a decoherence function $D_{CBO}(t)$.

$$N_{CBO}(t) = 1 + \boldsymbol{A_{CBO}}\, D_{CBO}(t)\, \cos\left(\omega_{CBO}(t)\, t - \boldsymbol{\phi_{CBO}}\right) \tag{5.5.2}$$

The decoherence term used in the Run-2/3 analysis has the following form:

$$D_{CBO}(t) = e^{-t/\boldsymbol{\tau_{CBO}}} + \boldsymbol{C_{CBO}} \tag{5.5.3}$$

In Run-1, only an exponential term was used to fit the data [108]. For Run-3b, where the stronger kick changed beam dynamics as explained in Section 5.1.1, it was found that the shape of the CBO envelope required an additional constant term. Our group decided to include the constant C_{CBO} in the CBO envelope for all Run-2/3 datasets, although it is almost compatible with 0 within the fit error for Run-2/3a. Our studies on the CBO envelope will be presented in Section 6.3, together with the systematics associated to this effect.
In Equation (5.5.2), $\omega_{CBO}(t)$ is a function of time that asymptotically reaches the constant fitted value $\boldsymbol{\omega^0_{CBO}}$. As explained in Section 4.7.2, the beam frequencies depend on the quadrupole field index n, that in turn depends on the voltage applied to the ESQ plates, so in general frequencies vary with time as quadrupoles charge, and they stabilize after the quadrupoles reach their nominal voltage.
In Run-1, because of the damaged resistors in the charging circuit, the lifetime of the charging process was longer than the expected 5 µs (see Figure 4.3.1) and the beam oscillation frequencies acquired an exponential time dependence which extended well into the ω_a fit region. The tracker system had the possibility of directly measuring this additional contribution: two representative plots of $\omega_{CBO}(t)$ in Run-1b/1c are shown in Figure 5.5.1.

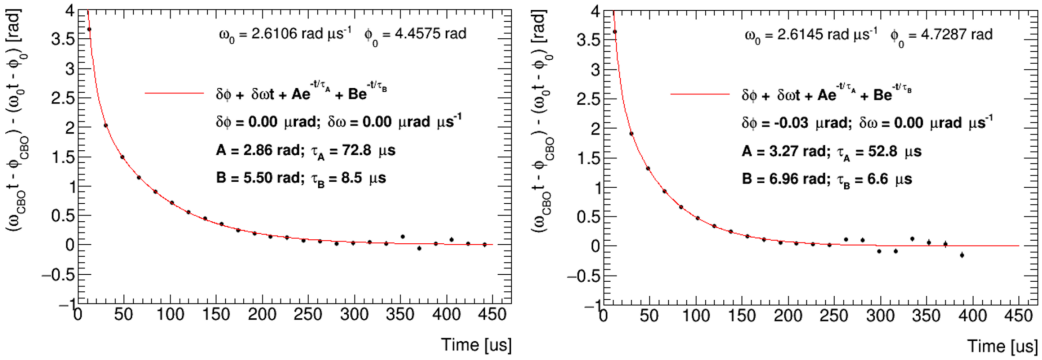

Figure 5.5.1: Tracker station 12 measurements of the varying CBO frequency due to damaged ESQ resistors in Run-1b and Run-1c.

The frequency variation in Run-1 was modeled as a double exponential function

$$\omega_{CBO}(t) = \boldsymbol{\omega^0_{CBO}} + \frac{A\, e^{-t/\tau_A}}{t} + \frac{B\, e^{-t/\tau_B}}{t} \tag{5.5.4}$$

where A, B, τ_A and τ_B were fixed from dedicated studies; in particular, $\tau_B \sim 6$ µs represented the nominal quadrupole charging lifetime and $\tau_A \sim 60$ µs the slower lifetime due to the faulty resistors.
Before the start of Run-2 acquisition, the quadrupoles resistors were fixed, so a long lifetime in the $\omega_{CBO}(t)$ modeling is not needed anymore. However, it was observed that the CBO frequency still had a drift with a lifetime longer than ~ 6 µs in wiggle plots, especially evident in individual calorimeters plots (see Figure 5.5.2(a)). In the ω_aEuropa group, we found that we could model the varying CBO frequency as:

$$\omega_{CBO}(t) = \boldsymbol{\omega^0_{CBO}} + \frac{A\, e^{-t/\tau_A}}{t} \tag{5.5.5}$$

where the parameters A and τ_A were extracted from a dedicated study using the T-Method analysis for each dataset. In these studies, we built about 65 wiggle plots selecting positrons from 10 µs time intervals, and we performed fits on each wiggle plot taking $\omega_{CBO}(t)$ as constant. In this way, we could measure how its value varied from early-to-late during the muon fills. Since the CBO phase ϕ_{CBO} could vary as well, we took the precaution of taking the difference

$(\omega_{CBO}\,t - \phi_{CBO})$ for each time interval. In order to extract A and τ_A, for each time bin we plotted the difference $(\omega_{CBO}\,t - \phi_{CBO})$ with respect to its value $(\omega_0\,t - \phi_0)$ at $t = 650\,\mu s$. Figure 5.5.2 shows the results of our study for Run-2, and Table 5.5.1 reports the values of A and τ_A that we fixed in our fits.

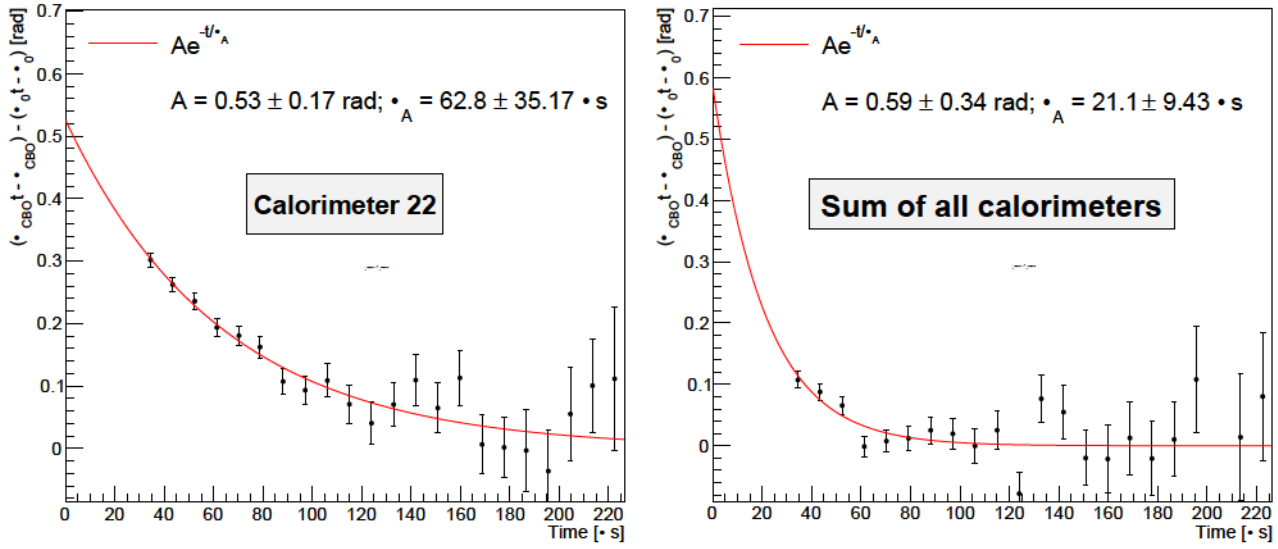

(a) (b)

Figure 5.5.2: Run-2 fits to extract the varying CBO parameters for (a) a single calorimeter, where the effect is more pronounced, and (b) the sum of all calorimeters.

Dataset	A [rad]	τ_A [μs]
Run-2	0.59 ± 0.34	21.1 ± 9.4
Run-3	0.50 ± 1.04	12.9 ± 10.9

Table 5.5.1: Results of our study to extract the varying CBO parameters for Run-2/3 and Figure 5.5.2). Run-3a and Run-3b were combined to decrease the uncertainty on the parameters.

These long lifetimes in the CBO data arise from the interplay between quadrupole scraping and calorimeter acceptance. In principle, since beam dynamics changed during the course of Run-3, A and τ_A could be different between Run-3a and Run-3b. However, given the low statistics of Run-3b, we combined the two Run-3 datasets together to increase the statistics of the study, which otherwise would have been too low for Run-3b. Nonetheless, we verified that, for the calorimeters where the effect was larger in Run-3a, the A and τ_A parameters were compatible within the errors between Run-3a and Run-3b. When looking at sum of all calorimeters, the amplitude of the varying CBO frequency is smaller because the CBO oscillations in one calorimeter tend to compensate the ones in the calorimeter 180° across the ring [108].
For all methods, we fixed the A and τ_A fit parameters from Table 5.5.1: the systematic related to the uncertainties of such parameters is discussed in Section 6.3. One of the results that proved the need for an exponential term in Equation (5.5.5) was the start time scan of the ω^0_{CBO} parameter, that will be shown in Section 5.7: without the exponential term in Equation (5.5.5), this parameter drifted towards greater values when fitting wiggle plots from later times.

After the $g-2$ oscillation at the ω_a frequency, the CBO oscillation is the dominant contribution to wiggle plots: if $N_{CBO}(t)$ is removed from the fit function, R changes by $\sim 2\,$ppm and the χ^2/n.d.o.f. increases by ≥ 10 units.

5.5.2 Lost muons

The lost muons term was described in Equation (5.2.8) of Section 5.2.4: the function $L(t)$ counts how many muons were lost during storage time, and its integral $J(t)$ is built in order to take the lost muons into account when fitting our data. We can define the fit term $\Lambda(t)$:

$$\Lambda(t) = 1 - \boldsymbol{k_{LM}}\, J(t) \tag{5.5.6}$$

where $J(t)$ functions are built for each Run-2/3 dataset, and k_{LM} is the parameter that accounts for the efficiency of our lost muons selection algorithm. Only positive values for k_{LM} have a physical meaning, and $J(t)$ is normalized in such way that k_{LM} does not depend on the wiggle plot statistics, so it can be compared across the different datasets of Run-2/3.

5.5.3 Higher-order beam dynamics

The dominant oscillation in our data is the first-order CBO term in Equation (5.5.2). There are additional contributions from beam dynamics, as described in Section 4.7.2. Firstly, the oscillation at twice the CBO frequency is parametrized as follows:

$$N_{2CBO}(t) = 1 + \boldsymbol{A_{2CBO}}\, D^2_{CBO}(t)\, \cos\left(2\,\omega_{CBO}(t)\,t - \boldsymbol{\phi_{2CBO}}\right) \tag{5.5.7}$$

There are other frequencies present in our calorimeter data and listed in Table 4.7.1. To account for the vertical waist frequency at $\sim 2.3\,\mathrm{MHz}$, we have the exponentially decaying sinusoidal term:

$$N_{VW}(t) = 1 + \boldsymbol{A_{VW}} \cos\left(\omega_{VW}(t)\,t - \boldsymbol{\phi_{VW}}\right) e^{-t/\tau_{VW}} \tag{5.5.8}$$

where τ_{VW} is the vertical waist decoherence lifetime. The mean vertical oscillation correction is given by:

$$N_y(t) = 1 + \boldsymbol{A_y} \cos\left(\omega_y(t)\,t - \boldsymbol{\phi_y}\right) e^{-t/\tau_y} \tag{5.5.9}$$

where the decoherence lifetimes are in relation:

$$\tau_{VW} = \frac{\tau_y}{2} \tag{5.5.10}$$

The y-oscillation frequency is related to the cyclotron and CBO frequencies, and it is described by:

$$\omega_y(t) = \boldsymbol{F_y}\,\omega_{CBO}(t)\sqrt{\frac{2\,\omega_C}{\boldsymbol{F_y}\,\omega_{CBO}(t)} - 1} \tag{5.5.11}$$

which comes from the expressions in Table 4.7.1. In the ideal experiment, $F_y = 1$: this term is a correction factor, free to float in the final fit, that takes into account the non-uniform quadrupoles coverage and the non-linearities inside the ring [130]. Equation (5.5.11) allows to further reduce the number of fitted parameters without the need to directly measure the time dependence of the vertical oscillation.
The vertical waist frequency can be expressed in terms of the mean vertical oscillation:

$$\omega_{VW}(t) = \omega_C - 2\,\omega_y(t) \tag{5.5.12}$$

and used in the final fitting function to account also for the time dependent variations of vertical waist. $\omega_{CBO}(t)$, $\omega_y(t)$ and $\omega_{VW}(t)$ are therefore related in such way that they can all be described by the same parameter ω^0_{CBO}.

High order terms need to be included in the asymmetry and phase terms of Equation (5.5.1) as well:

$$\begin{aligned} A_{BD}(t) &= 1 + \boldsymbol{A_A}\, D_{CBO}(t)\, \cos\left(\omega_{CBO}(t)\, t - \boldsymbol{\phi_A}\right) \\ \phi_{BD}(t) &= \boldsymbol{A_\phi}\, D_{CBO}(t)\, \cos\left(\omega_{CBO}(t)\, t - \boldsymbol{\phi_\phi}\right) \end{aligned} \tag{5.5.13}$$

5.5.4 Fast fourier transform of fit residuals: VW-CBO peak

A technique that we use to identify which oscillating terms we need to include in our ω_a fits is looking at the fit residuals, and taking their fast fourier transform, where several peaks may arise mainly due to beam dynamics frequencies present in the data. Figure 5.5.3(a) shows the case of Run-1 data. Since time bins are wide $\delta t = 149.2\,\text{ns}$, the range of frequencies that can be explored with this technique stretches from 0 to $f_{\text{FFT}}^{max} = 1/(2\delta t) \approx 3.35\,\text{MHz}$.

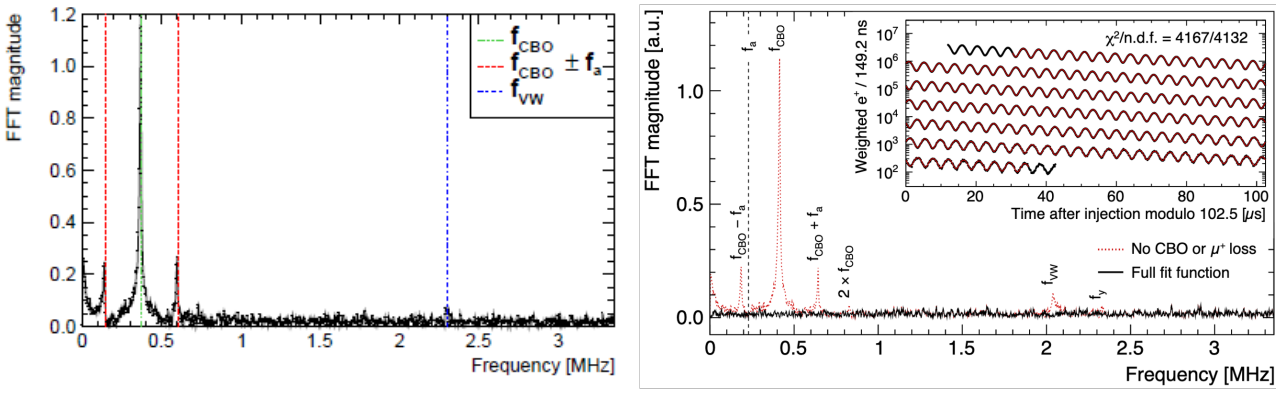

(a) **(b)**

Figure 5.5.3: FFT of residuals from Run-1 [108]. (a): 5-parameter fit, where the vertical coloured lines show how the expected frequencies from beam dynamics (see Table 4.7.1) match the observed peaks, the most important one being the CBO term. (b): complete fit function, where no more characteristic frequencies remained in the spectrum.

With the great amount of statistics in the Run-2/3 datasets, a new effect appeared in the FFT of the residuals: a small peak centered near 1.9 MHz when fitting with the complete Run-1 function. Figure 5.5.4 shows the fit results and residuals for Run-2, A-Method.
The new peak is one of the beating frequencies between the CBO and vertical waist terms:

$$\omega_\pm(t) \equiv \omega_{VW \pm CBO}(t) = \omega_{VW}(t) \pm \omega_{CBO}(t) \tag{5.5.14}$$

From the values of Table 4.7.1, $\omega_+(t) = 2.67\,\text{MHz}$ and $\omega_-(t) = 1.93\,\text{MHz}$, where the latter corresponds to the new peak observed in the FFT. Thus, a new term is present in the ω_a function of Equation (5.5.1), parametrized as follows:

$$N_{CBOVW}(t) = 1 + \left[\boldsymbol{A_+} \cos\left(\omega_+(t)\, t - \boldsymbol{\phi_+}\right) + \boldsymbol{A_-} \cos\left(\omega_-(t)\, t - \boldsymbol{\phi_-}\right)\right] e^{-t/\boldsymbol{\tau_{CBOVW}}} \tag{5.5.15}$$

where the $+$ and $-$ subscripts refer to the $VW + CBO$ and $VW - CBO$ terms respectively. The $VW + CBO$ peak is only visible in the FFT plot of individual calorimeters and not in the sum of 24 calorimeters [127, 119], but both beating frequencies are included in the full ω_a fit. This increases the number of floating parameters with respect to Run-1 by 5 parameters.

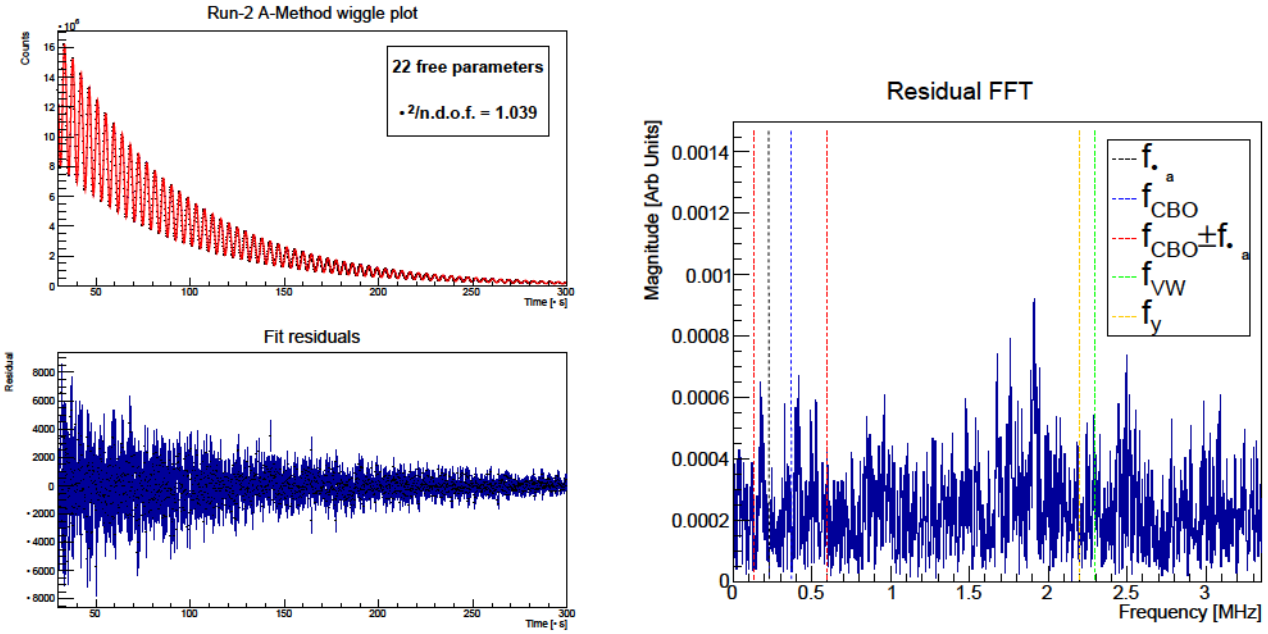

Figure 5.5.4: The top left plot shows the Run-2 A-Method wiggle plot fitted with the Run-1 fit function ($N_{CBOVW}(t)$ not included). The fit residuals are shown in the bottom left plot, whereas the fast fourier transform (FFT) of the residuals is shown on the right plot, with a residual peak near 1.9 MHz.

5.5.5 Ratio method fit function

The function used to fit the R/RA-Methods wiggle plot is very similar to the T/A-Methods, but with notable differences. Firstly, vertical waist and vertical oscillation effects are not included in the fit, because these frequencies are eliminated by the randomization procedure described in Section 5.3, otherwise their amplitudes would be too small to be fitted in the Ratio wiggle plots. Thus, the terms $N_{VW}(t)$, $N_y(t)$ and $N_{CBOVW}(t)$ are not included in the fit function, eliminating 11 floating parameters. The normalization N_0 is also not present in the fit function because it cancels out in the ratio of Equation (5.4.3), as it is also shown in Figure 5.4.2(b), bringing the total number of parameters to 16 in the R/RA fit function. Secondly, since the wiggle plot is built starting from four subsets, two of which shift the clusters' time by a fixed value of $\pm T_a/2$, we build three versions of the fit function: $N(t)$, $N(t+T_a/2)$ and $N(t-T_a/2)$, where in this case $N(t)$ is the same expression as in Equation (5.5.1), without the terms that are not necessary in the R/RA-Methods fits. The complete R/RA fit function is:

$$R(t) = \frac{2N(t) - N(t+T_a/2) - N(t-T_a/2)}{2N(t) + N(t+T_a/2) + N(t-T_a/2)} \tag{5.5.16}$$

that resembles Equation (5.4.3), which is the way R/RA wiggle plots are built.
Lastly, for the R/RA fits, the muon lifetime $\gamma\tau$ and the constant C_{CBO} in the CBO decoherence term are actually fixed to the values obtained from T/A fits, respectively. From the Ratio wiggle plot in Figure 5.4.2(b), it is evident that the exponential decay with the $\gamma\tau$ muon lifetime is not present in the R/RA histograms, but in Section 5.3 it was stressed that the exponential function does not cancel out perfectly and the Ratio formula of Equation (5.3.3) is just an approximation. In Appendix B, the first order correction to this approximation is derived, where the leading term is an offset of the order of 10^{-4}. One way to remove the offset, which was adopted in Run-1 [108], is to choose the four subsets in the relative proportions $v_1 : v_2 : u_+ : u_- = 1 : 1 : e^{T_a/2\gamma\tau} : e^{-T_a/2\gamma\tau}$, so that the exponential functions at the numerator and denominator cancel out exactly in the ratio; with this choice, the R/RA fit function does

not require the parameter $\gamma\tau$. A different way to account for the offset, chosen for the ω_aEuropa Run-2/3 analysis, is to assign equal probabilities to each of the four Ratio histograms during the Quartering step, and keep the exponential term in the $N(t)$ functions of Equation (5.3.2), fixing $\gamma\tau$ from the T/A fits. The reason for this choice was to make it easier to repeat the fits for different values of $\gamma\tau$, if needed.

By construction, the exponential decay is absent from the R/RA wiggle plots, and in general these methods are much less sensitive than the T/A-Methods to all "slow terms": for instance, the shape of the CBO decoherence that decays over time. Therefore, the fit errors on τ_{CBO} and C_{CBO} parameters of Equation (5.5.3) are larger than the ones from T/A. To prevent the offset C_{CBO} from drifting towards negative values in the R/RA fits, we fixed it from T/A values, which also improved the fit error on τ_{CBO}.

5.5.6 Nominal fitting window

The fitting window has been carefully chosen in order to balance the statistical power gained including more data with the systematic effects. In particular, there are some fit start times that minimize the systematic associated with the IFG correction: for all of the datasets in Run-2/3, the fit start time has been fixed to 30.1384 µs (similarly to Run-1a/1b/1c), which is the lower edge of a time bin in the wiggle plot given that the bin width is 0.1492 µs. The fit end time was instead chosen to extend the measurement window as much as possible, but excluding the low-populated bins at the end of the spectrum: it was therefore fixed to 650.0644 µs, which is the upper edge of the last bin in the wiggle plot that we build.

5.6 Run-2/3 A/RA-Methods fit results

Tables 5.6.1 and 5.6.2 show the results for a selection of fit parameters in the A-Method and RA-Method, for all Run-2/3 datasets. In the first three rows, the parameters of the per-seed R and χ^2/n.d.o.f. distributions are reported. The rest of the parameters are reported for the so-called "representative seed", which is the one for which the blinded R value is closest to the average of the per-seed distribution $\langle R \rangle$. Tables with full results for all datasets and methods are shown in the Appendix C, together with the correlations between each pair of parameters for the A/RA-Methods.

In Run-3, the k_{LM} parameter is fitted to a negative value as anticipated in Section 5.2.5. In Section 6.5, we will report the estimations of how much R and τ are affected by the negativity of k_{LM}, also comparing τ with the results from Fast Rotation analysis. C_{CBO}, the constant term in the CBO decoherence envelope, is compatible with 0 for the Run-2/3a dataset, whereas it is significantly larger in Run-3b. The initial phase ϕ_0 is fitted to ~ 4.1 rad in all cases, and this is consistent with the values predicted by beam simulations in the accelerator complex: positive muons are first emitted with $\phi_0 = \pi$ (see Figure 1.3.2) and then precess for about 4 turns in the Delivery Ring where they are emitted from pions (as described in Section 4.1), with an anomalous precession of ~ 0.9 rad before being injected into the Muon $g-2$ Storage ring.

Fit parameter	Run-2	Run-3a	Run-3b
$\langle\chi^2/\text{n.d.o.f.}\rangle$	1.02664	0.997004	0.999528
$\langle R\rangle$ [ppm]	-80.626	-71.390	-70.396
σ_R [ppb]	35	26	48
$\chi^2/\text{n.d.o.f.}$	4225.91/4127	3981.24/4127	4154.14/4127
p-value	0.13842	0.94699	0.38003
N_0	20140739 ± 299	27021394 ± 562	10487162 ± 431
$\gamma\tau \times 10^3$ [μs]	64430 ± 1	64415 ± 3	64392 ± 3
$A \times 10^5$	36064 ± 1	36252 ± 1	36126.2 ± 1.5
R [ppm]	-80.628 ± 0.337	-71.393 ± 0.291	-70.397 ± 0.468
$\phi_0 \times 10^5$ [rad]	411775 ± 6	412089 ± 5	410803 ± 8
$A_{CBO} \times 10^4$	37 ± 2	29.4 ± 1.6	13.6 ± 0.8
$\omega^0_{CBO} \times 10^4$ [rad/μs]	23412.2 ± 1.0	23292.0 ± 1.0	23318 ± 3
$\phi_{CBO} \times 10^3$ [rad]	6027 ± 8	6143 ± 9	6100 ± 20
τ_{CBO} [μs]	242 ± 27	213 ± 24	88 ± 18
C_{CBO}	0.04 ± 0.07	0.09 ± 0.07	0.47 ± 0.08
$k_{LM} \times 10^5$	106 ± 7	-90 ± 30	-90 ± 30

Table 5.6.1: A-Method fit results.

Fit parameter	Run-2	Run-3a	Run-3b
$\langle\chi^2/\text{n.d.o.f.}\rangle$	0.999067	1.00046	0.997689
$\langle R\rangle$ [ppm]	-80.583	-71.435	-70.368
σ_R [ppb]	85	62	123
$\chi^2/\text{n.d.o.f.}$	4191.42/4141	4184.78/4141	4106.18/4141
p-value	0.28804	0.31323	0.64668
$\gamma\tau$ [μs]	64.430 (fixed)	64.415 (fixed)	64.392 (fixed)
$A \times 10^5$	35479 ± 1	35641 ± 1	35515.6 ± 1.5
R [ppm]	-80.583 ± 0.345	-71.435 ± 0.301	-70.369 ± 0.480
$\phi_0 \times 10^5$ [rad]	411815 ± 6	412125 ± 5	410840 ± 8
$A_{CBO} \times 10^5$	362 ± 11	272 ± 8	160 ± 20
$\omega^0_{CBO} \times 10^4$ [rad/μs]	23415 ± 3	23292 ± 4	23322 ± 9
ϕ_{CBO} [rad]	6.05 ± 0.03	6.17 ± 0.03	6.14 ± 0.08
τ_{CBO} [μs]	228 ± 19	222 ± 21	56 ± 18
C_{CBO}	0.04 (fixed)	0.09 (fixed)	0.47 (fixed)
$k_{LM} \times 10^3$	13 ± 19	-8 ± 11	-7 ± 14

Table 5.6.2: RA-Method fit results.

5.7 Internal consistency: per-calorimeter and start time scans

In this Section, we will present some consistency checks that were performed on the ω_aEuropa data, that added confidence in our results and that could reveal potentially hidden systematic effects.

As a first check, we have carried out a per-calorimeter analysis: for each of the 24 calorimeters, we repeated the procedure of building pileup-subtracted wiggle plots and fitting with the full function described in Section 5.5. As in the nominal procedure, we did not constrain any of the 28 (16) floating parameters, but the initial values were set to those from the sum of all calorimeters.
In Figure 5.7.1, we compare the Run-3a A-Method per-calorimeter fits (the ones with most statistics amongst Run-2/3), with and without applying the time randomization described in Section 5.2.6. In particular, we highlighted the amplitude of the so-called "R-Wave", which is the sinusoidal fluctuation of R along the azimuthal position of the calorimeters, due to the Fast Rotation signal that is not completely eliminated by choosing a time bin width of $T_c = 149.2\,\text{ns}$. We fitted this oscillation with a fixed frequency of $2\pi/24$: when we randomize positron times to remove the fast rotation signal, the amplitude of the R-Wave is strongly suppressed. In this example, the seed used for randomization is different from the representative one reported in Table 5.6.1, so the average blinded R is also different.

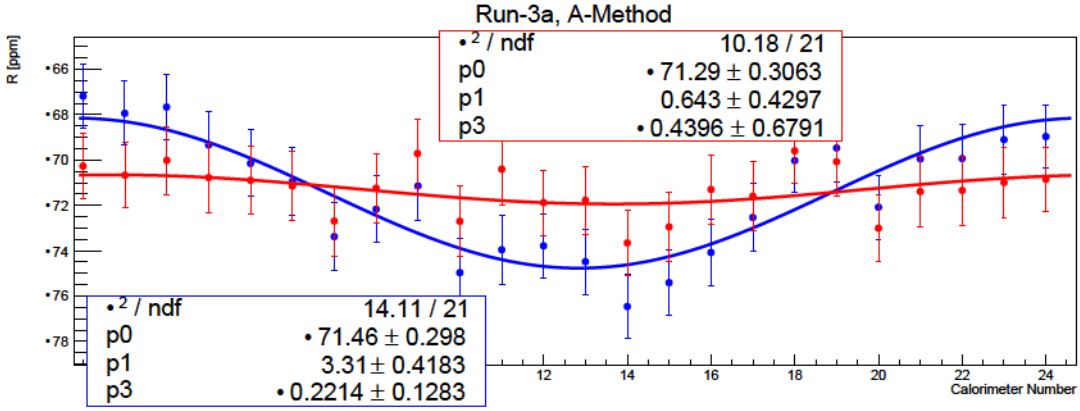

Figure 5.7.1: A-Method Run-3a per-calorimeter scan, with (red) and without (blue) time randomization. The R-Wave is fitted with a model $p_0 + p_1 \cos(p_2\, t + p_3)$.

As a second check, we performed scans on R and χ^2/n.d.o.f. as a function of the fit start time. The start times that we used ranged from the nominal value of 30.1384 µs to 100.1132 µs, in steps of 1.0444 µs so that the fit would always start from the lower edge of the wiggle plot's bins. For each point in the scan, to allow our fits to converge well at later start times with less statistics, we fixed the following beam dynamics parameters to the values from the nominal fit: A_{CBO}, τ_{CBO}, ϕ_{CBO}, C_{CBO}, A_A, ϕ_A, A_ϕ, ϕ_ϕ, A_{2CBO} and ϕ_{2CBO}. The other parameters, not fixed, were only used as initial values for the fits. Figure 5.7.2 shows, for dataset Run-3a, the behaviour of χ^2/n.d.o.f. and blinded R as a function of the fit start time. For each point in the scan, we reported the statistical uncertainty from the fit, and also an upper and lower band that represent the $1\,\sigma$ allowed statistical fluctuation due to a lower number of positrons for later fit start times.

As mentioned in Section 5.5.1, the fits on individual calorimeters have a greater CBO effect, so they can be used to study, for instance, the parametrization of the CBO varying frequency

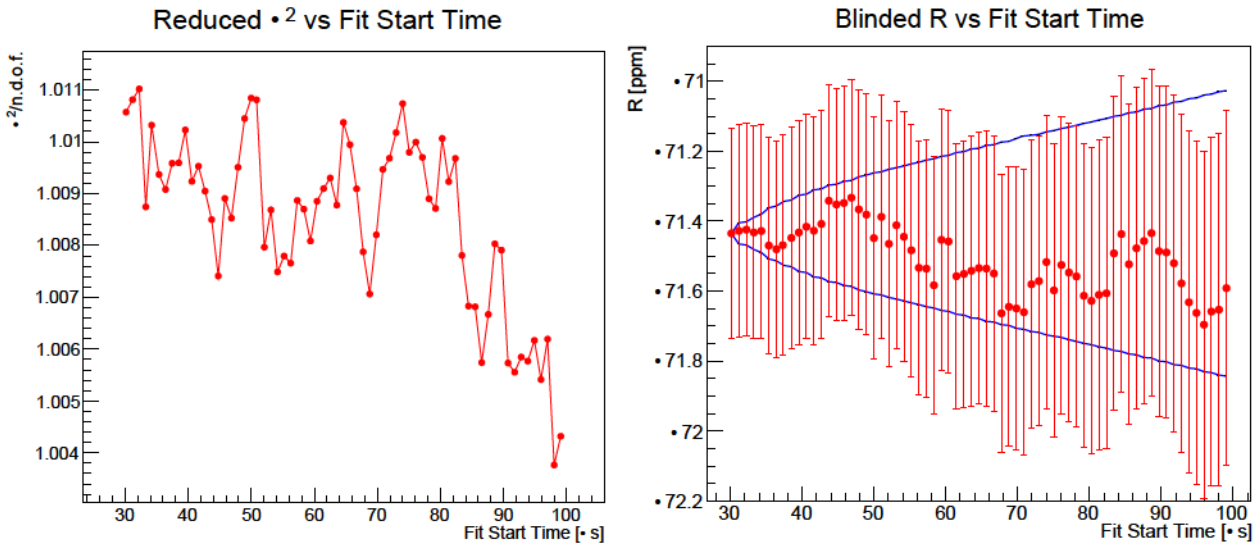

Figure 5.7.2: Run-3a, RA-Method start time scans of χ^2/n.d.o.f. and R. The blue bands are the $1\,\sigma$ allowed statistical differences from the start point.

and the model in Equation (5.5.5). As a last consistency check, we report an example for calorimeter 22 in Run-2, where the CBO drift was more pronounced. Figure 5.5.2(a) shows that the fitted ω^0_{CBO} frequency drifts out of the allowed $1\,\sigma$ bands when the exponential term Ae^{-t/τ_A} of Equation (5.5.5) is missing; instead, when we fixed A and τ_A from the results shown in Figure 5.7.3, ω^0_{CBO} remained more stable within the allowed $1\,\sigma$ statistical bands.

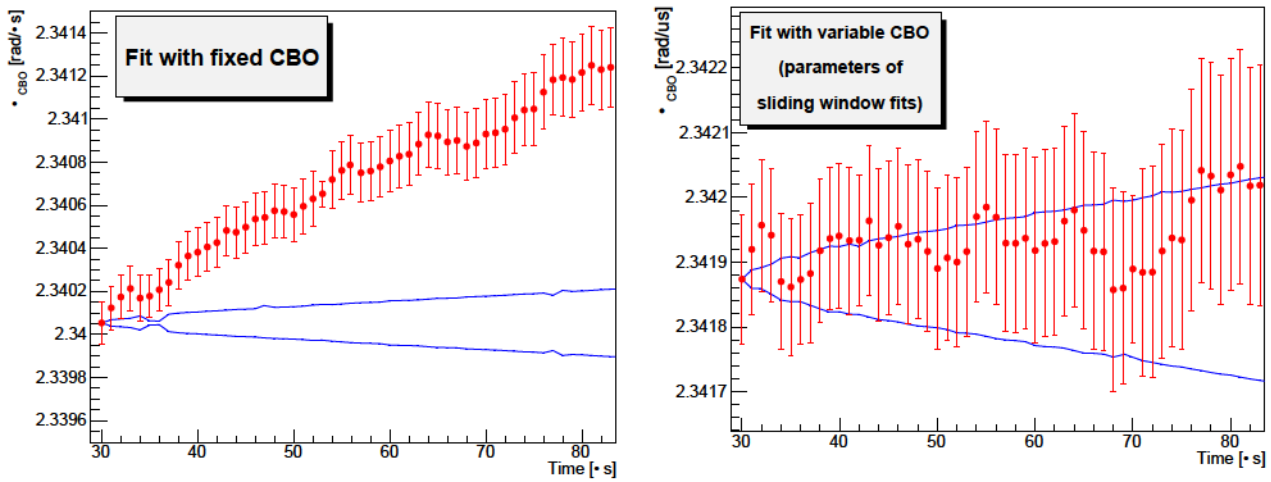

Figure 5.7.3: A-Method Run-2 fit for calorimeter 22, with a constant ω^0_{CBO} term (left plot) and with the additional exponential terms of Equation (5.5.5) (right plot). The blue bands are the $1\,\sigma$ allowed statistical differences from the start point.

Chapter 6

Sources of systematic uncertainty on ω_a for the Run-2/3 analysis

In this Chapter, the different sources of systematics contributions to the ω_a analysis, evaluated within the ω_aEuropa team, will be described.

6.1 Gain correction

This Section will present the ω_aEuropa approach for the systematic errors related to the SiPM gain correction in Run-2/3.
Both the IFG and STDP corrections are parametrized with an exponential function with amplitudes a and lifetimes τ, extracted from dedicated laser studies. The typical values for the amplitudes a_{IFG} and a_{STDP} are around 10%, whereas the lifetimes have different orders of magnitude: τ_{IFG} can span from a few µs to 10 µs depending on the SiPM, and τ_{STDP} is typically around 10 nanoseconds.
In order to evaluate the systematic effects of the gain corrections, scans of the amplitude and lifetime parameters were performed. For each cluster, we removed the nominal energy correction on each crystal, then we applied a new gain correction with a different amplitude or lifetime. The procedure in the ω_aEuropa team is to scale the parameter of each crystal taking the uncertainty into account, according to the following formula:

$$a' = a + m\sigma_a \qquad \text{or} \qquad \tau' = \tau + m\sigma_\tau \tag{6.1.1}$$

where a and τ are the nominal amplitude and lifetime parameters, a' and τ' are the scaled ones, σ_a and σ_τ are the uncertainties on these parameters from gain studies, and the m parameter is a scaling factor referred to as "sigma multiplier", that can range from negative to positive values ($m = 0$ is the nominal gain correction). In this procedure to evaluate the gain systematics, we assumed that the amplitude and lifetime parameters of the gain correction were under- or over-estimated by a multiple m of their uncertainty; the systematic was taken as the difference of R from nominal, when the a and τ parameters changed by $\pm$1-σ. Thus, the systematic uncertainty was obtained from the slope of R versus m. After applying the modified gain correction with the sigma-method for all crystals' of each cluster, the whole procedure for building wiggle plots was repeated, and we fitted R for each value of the scaling parameter m.

Figure 6.1.1 compares the results of the sigma-multiplier method for T-Method and R-Method IFG amplitude scans: for each point of the interval we have reported the difference with respect to the nominal $m = 0$ value. The slope in the R-Method is ~ 3.5 times smaller, indicating that it is less sensitive to early-to-late effects like gain corrections.

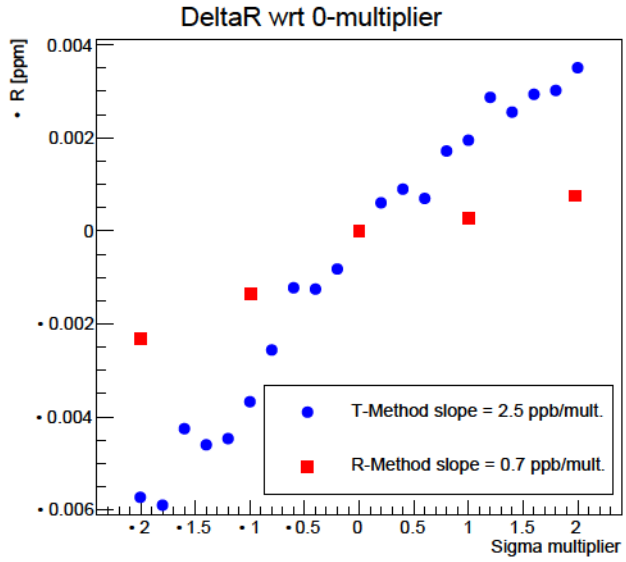

Figure 6.1.1: Run-2 T/R-Methods: the slope for the R-Method is notably smaller, because the Ratio wiggle plots are less sensitive to slow systematic effects.

Table 6.1.1 reports the IFG systematic uncertainties, which are evaluated as the p_1 slopes for each method and dataset of Run-2/3. For Run-3 datasets, the systematic errors related to the IFG lifetimes are slightly larger than Run-2, because a fewer number of laser campaigns were performed and therefore the extracted IFG lifetimes had a bigger uncertainty.

IFG amplitude systematics [ppb]				IFG lifetime systematics [ppb]			
Method	Run-2	Run-3a	Run-3b	Method	Run-2	Run-3a	Run-3b
A	2.6	2.4	1.6	A	2.7	3.7	4.0
RA	0.08	0.1	0.1	RA	0.01	0.3	0.3

Table 6.1.1: In-Fill Gain systematics.

STDP amplitude systematics [ppb]				STDP lifetime systematics [ppb]			
Method	Run-2	Run-3a	Run-3b	Method	Run-2	Run-3a	Run-3b
A	0.08	0.15	0.25	A	0.25	0.26	0.34
RA	0.05	0.26	0.41	RA	0.19	0.39	0.49

Table 6.1.2: Short-Term Double-Pulse Gain systematics.

The procedure for the STDP systematics is very similar to the one for IFG. There is only a small difference in the implementation of the study, because the STDP correction is only applied when two or more positron hits are close in time, within $\mathcal{O}(100\,\text{ns})$. In Table 6.1.1 the systematic uncertainties are reported for each method and dataset of Run-2/3. The changes in R are much smaller than for the IFG systematics (always less than 1 ppb), and the systematics for the R/RA-Methods are typically of the same size as the T/A-Methods.

For each method and each dataset of Run-2/3, we combined the four systematic uncertainties due to amplitude and lifetime of IFG and STDP into a single number. In the nominal reconstruction procedures, the amplitudes and lifetimes of the gain corrections are extracted from independent fits, so for each type of gain correction we added the two systematic errors

in quadrature. We conservatively assumed that the overall IFG and STDP systematics were fully correlated, thus added them linearly, and the results of this combination procedure are reported in Table 6.1.3.

Combined Gain systematics [ppb]			
Method	Run-2	Run-3a	Run-3b
A	4.0	4.7	4.7
RA	0.28	0.78	0.96

Table 6.1.3: Total gain-related systematics for the Run-2/3 datasets.

6.2 Pileup subtraction

In this Section, the following contributions to the systematics related to pileup subtraction will be described: the pileup amplitude uncertainty; the cluster time and energy model in the ω_aEuropa nominal procedure, represented by Equation (5.2.7); a systematic uncertainty related to residual events above 3.1 GeV after pileup subtraction. These three contributions are conservatively assumed to be fully correlated with each other, thus they are added linearly to obtain the total value reported in Table 6.7.1.

Pileup amplitude

The pileup subtraction in the ω_aEuropa analysis was described in Section 5.2.3. In principle, our procedure could under- or over-estimate the number of doublets and triplets for each time and energy bin. The pileup subtraction can be modulated by a scaling parameter f_{scale}, which multiplies the number of pileup events and is set to 1 in the nominal procedure. As the systematic study, f_{scale} can be varied around 1 to extract the slope of R as a function of this parameter. We varied f_{scale} from 0.5 to 1.5 in steps of 0.25: for each point of the interval, we repeated our nominal procedure for building and fitting wiggle plots, to extract the slope of R versus f_{scale}.

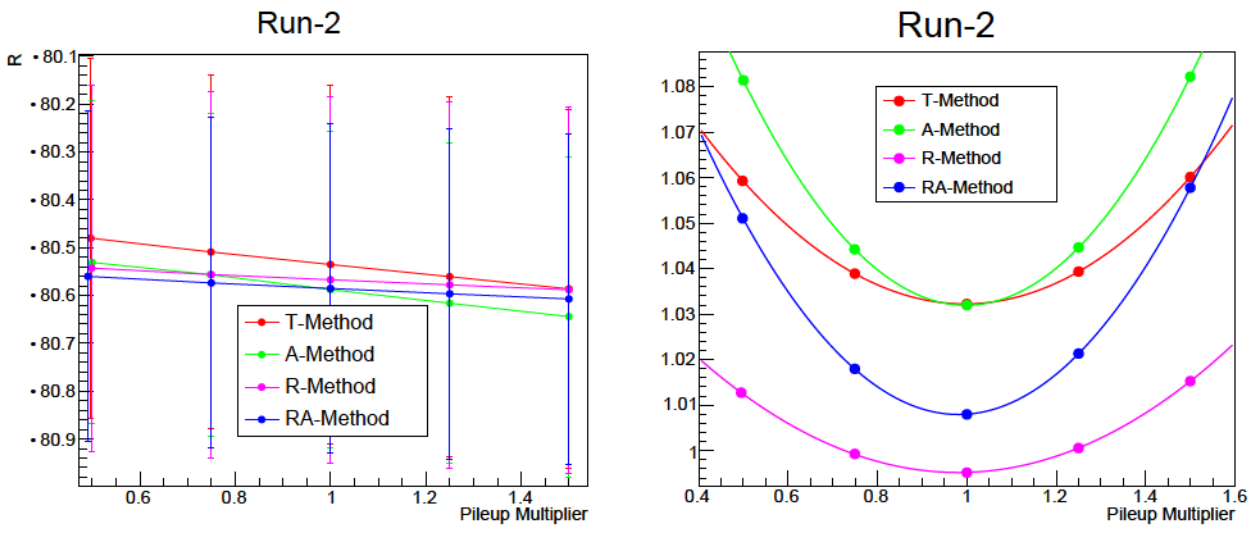

Figure 6.2.1: Scans of R and χ^2/n.d.o.f. as a function of the f_{scale} amplitude multiplier.

In Figure 6.2.1, the variations of R and χ^2/n.d.o.f. as a function of the pileup multiplier f_{scale} are shown: the minimum of the χ^2 is always centered around the nominal $f_{scale} = 1$, within ± 0.05; the fitted slopes, reported in Table 6.2.1, are all negative and typically of the order of hundreds of ppb/multiplier.

Dataset	Method	Slope of R versus f_{scale} [ppb/mult]	Systematic [ppb]
Run-2	A	-113	0.6
	RA	-45	0.9
Run-3a	A	-78	2.7
	RA	-78	1.7
Run-3b	A	-109	1.6
	RA	-227	3.2

Table 6.2.1: Pileup systematics related to the uncertainty on the overall amplitude, tuned by f_{scale}.

To evaluate the systematic uncertainty, the slopes of R as a function of f_{scale} are multiplied by the fractional residual pileup contamination, shown in Figure 6.2.2 and defined as follows: the pileup-corrected energy spectrum in the nominal procedure (with $f_{scale} = 1$) is divided by the energy spectrum before pileup subtraction; the region between 3.4 GeV and 4.2 GeV is fitted with a constant parameter p_0. For the R/RA-Methods, there are two energy spectra, one for the $U(t)$ and one of the $V(t)$ histograms, and the fractional residual pileup is chosen as the biggest p_0 from the two fits.

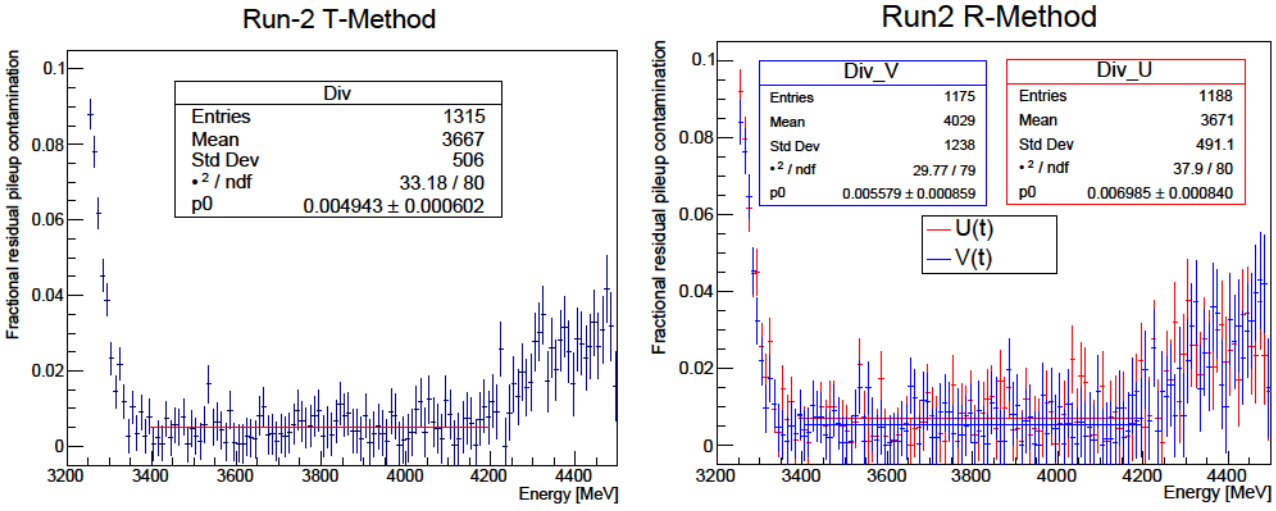

Figure 6.2.2: Run-2 dataset energy spectra, ratio between pileup- corrected and uncorrected histograms: the region from 3.4 GeV to 4.2 GeV is fitted with a constant to extract the fractional residual pileup contamination, reported in Table 6.2.1.

Cluster time and energy model

When two positrons hit the same SiPM with a separation time of ~ 4 ns, the ω_aEuropa reconstruction algorithm can separate them but it might assign wrong energies or times. In Section 5.2.3 we reported our a study on artificial islands to extract the efficiency of our algorithm as

a function of the time separation between the two hits. A systematic effect might arise if the corrections shown in Figure 5.2.11 are not estimated properly. As a systematic check, we have repeated the nominal pileup procedure and fits on wiggle plots: the first time, we set $f_{corr} = 1$ in Equation (5.2.7), to remove the energy model; the second time, we restored the nominal value of f_{corr} but removed the time model, setting $t_{corr} = 0$.

Dataset	Method	ΔR when $f_{corr} = 1$ [ppb]	ΔR when $t_{corr} = 0$ [ppb]	Systematic [ppb]
Run-2	A	−1.0	−0.8	1.3
	RA	−0.3	−0.5	0.6
Run-3a	A	1.3	0.5	1.4
	RA	1.1	0.4	1.2
Run-3b	A	1.3	2.6	2.9
	RA	0.8	−1.0	1.3

Table 6.2.2: Pileup systematics related to the f_{corr} and t_{corr} in Equation (5.2.7).

Table 6.2.2 reports the differences of R, with respect to the nominal fit, when removing the energy and time corrections to build pileup events. The systematic uncertainty is the sum in quadrature of the two variations, assumed to be independent.

Excess of residual events around 5 GeV

In Figure 6.2.2, a notable number of residual events after 3 GeV is present in the pileup-subtracted energy spectrum after 4.2 GeV. These residual events are peaked at ~ 5 GeV. In the energy region above 6.2 GeV, where only coincidences between three or more positron hits are present, the spectrum is flat as expected. The presence of a relatively small number of residual events after the ω_aEuropa pileup subtraction has not been understood yet, but we plan to study it with future Monte Carlo tests; at the moment, it is thought to be due to a possible bias in the evaluation of doublet events energies. In the following, we describe a way to correct for this effect, which accounts for the last source of systematic uncertainty related to pileup.

The blue histogram in Figure 6.2.3 represents the pileup-subtracted energy spectrum for Run-2. As a conservative way to estimate the systematic due to this excess, a further subtraction has been applied from 0 to 6.2 GeV to obtain the black histogram: for each time bin, we added a number of events that scaled linearly with energy, with a negative slope of $3 \cdot 10^{-5}$/MeV; this subtraction greatly reduced the events after 4.2 GeV, but it increased the number of positron events below 3.1 GeV that are used in the A/RA-Methods wiggle plots. The difference is notable in the pileup region above 3 GeV, shown in Figure 6.2.3, but not significant between 1 GeV and 3 GeV where the number of events is of the order of 10^8.

We have compared the R results between the nominal fits and the wiggle plots built with the additional pileup subtraction. Table 6.2.3 reports the differences in R, in parts per billion, which are taken as an evaluation of the systematic error.

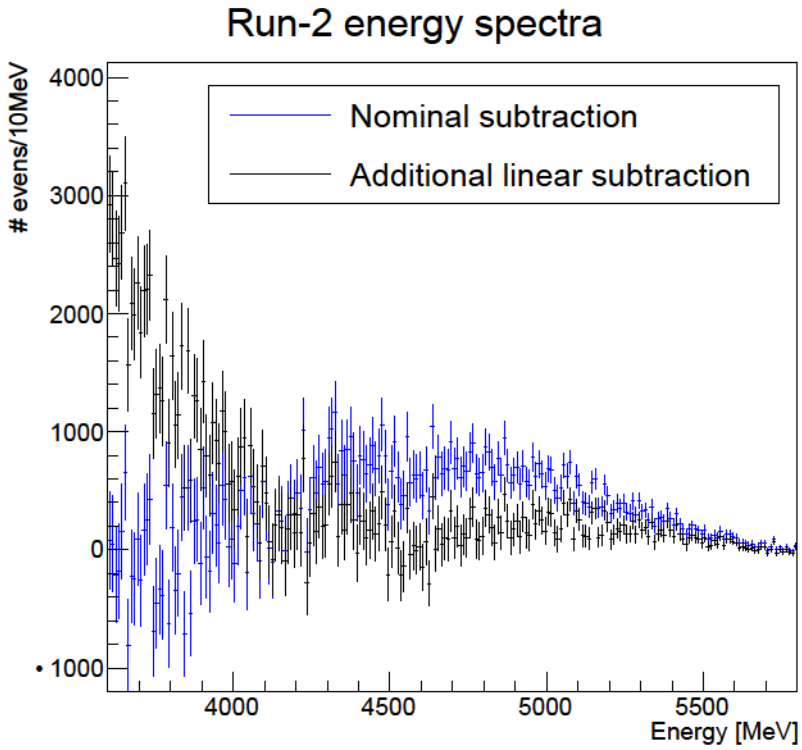

Figure 6.2.3: Run-2 pileup-subtracted energy spectra from 3.5 GeV to 5.8 GeV. The spectrum from the ω_aEuropa nominal procedure (blue) was modified to further subtract events around 5 GeV (black).

Dataset	Method	Systematic [ppb]
Run-2	A	4.3
	RA	1.4
Run-3a	A	3.6
	RA	1.8
Run-3b	A	4.7
	RA	2.4

Table 6.2.3: Systematic uncertainty related to the excess of residual pileup events in the range [4.2, 5.5] GeV.

6.3 Coherent Betatron Oscillation

In this Section, the three sources of systematic uncertainty related to CBO will be described: the model for decoherence envelope $D(t)$ in the nominal fit function; the amplitude A and lifetime τ_A parameters of the varying CBO frequency, extracted from dedicated studies and reported in Table 5.5.1; the lifetimes of higher-order CBO terms, that are fixed to the same values of the leading CBO function in our nominal fit function.

CBO decoherence envelope

In Run-1, the decoherence envelope $D(t)$ was chosen as an exponential function in the ω_aEuropa; in Run-2/3 it was observed that for Run-3b this was not a good model for the CBO envelope, and a costant offset was added to the exponential function, as in Equation (5.5.3).
Figure 6.3.1 shows fits on 8 µs time bins for A-Method wiggle plots, where the CBO frequency has been fitted with an amplitude A_{CBO} without any exponential term, in order to extract

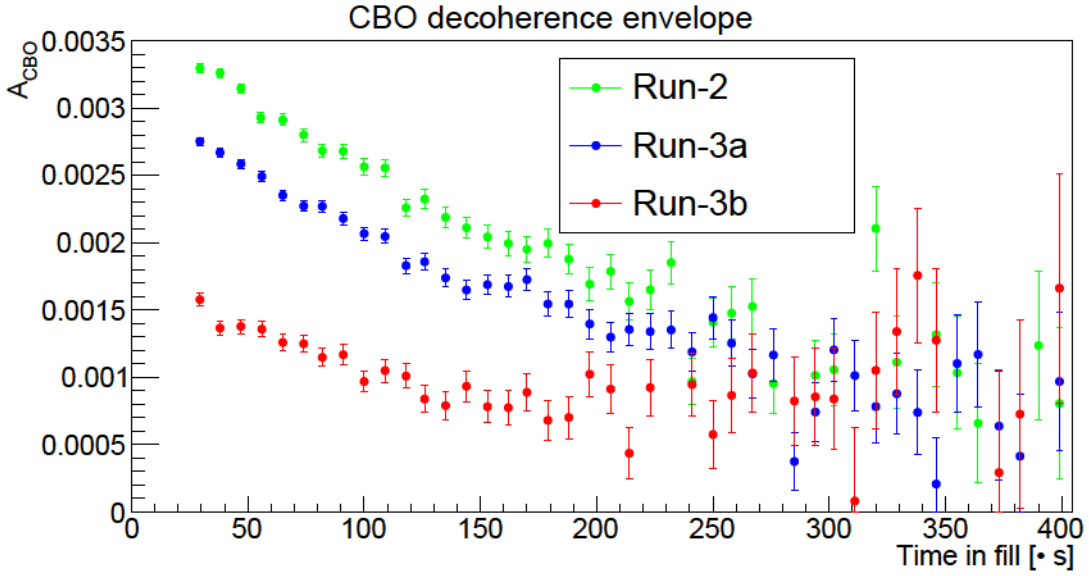

Figure 6.3.1: A-Method fits for small time intervals to extract the CBO decoherence envelope as a function of time.

the shape of the CBO decoherence as a function of time: at the fit start time, the values of A_{CBO} are compatible with the ones reported in Table 5.6.1; for Run-3b, A_{CBO} remains constant starting from 150 µs, which is a hint that an exponential model is not sufficient to describe the envelope in this case. Many models of the decoherence envelope have been developed from tracker data and simulation, and we will report the effects on R from the fit to representative seeds when testing different envelopes.
Figure 6.3.2 shows the shapes of 6 different envelope models that were tested in our wiggle plot fits (with the A/RA-Methods). The so-called "Generic envelope" is a function motivated by tracker studies on beam dynamics, repoted in Equation (6.3.1):

$$D^2_{\text{generic}}(t) = \left[\frac{p_1^2}{p_1^2 + (t - 30\,\mu\text{s})^2} - \frac{p_2}{p_3^2} G(t - 30\,\mu\text{s}, 0, p_3)\right]^2 + \\ + \left[p_4 G(t - 30\,\mu\text{s}, 0, p_5) + \frac{p_6}{p_7^2} G(t - 30\,\mu\text{s}, 0, p_7)\right]^2 \tag{6.3.1}$$

where $G(t, 0, p_i)$ is the Gaussian distribution calculated at time t, centered in 0, with standard deviation p_i. Three of the parameters, p_2, p_6 and p_7 in Figure 6.3.2(f), were fixed by tracker data. For each dataset and each method, the systematic uncertainty related to CBO decoherence was taken as the largest difference of R between the nominal procedure (with an exponential plus constant evenlope) and each of the different envelopes tested. Among all ω_a analysis groups, a common strategy was implemented to reject fit results for "unreasonable decoherence envelopes" for each dataset and method, i.e. those for which the fit χ^2/n.d.o.f. was much worse than the nominal fits. For each envelope, the fit χ^2 was corrected for the different number of degrees of freedom: if $(\chi^2 - \text{n.d.o.f.})\,|_{\text{envelope}} \leq 3 + (\chi^2 - \text{n.d.o.f.})\,|_{\text{nominal}}$, the envelope was taken into account for the evaluation of the decoherence systematic. The cut at 3 was selected from dedicated studies where CBO decoherence envelopes that did not fit our data were forced into the fit function on purpose, to observe the χ^2/n.d.o.f. behaviour.
Tables 6.3.1 reports the systematic uncertainty for the A/RA-Methods, for each of the Run-2/3 datasets.

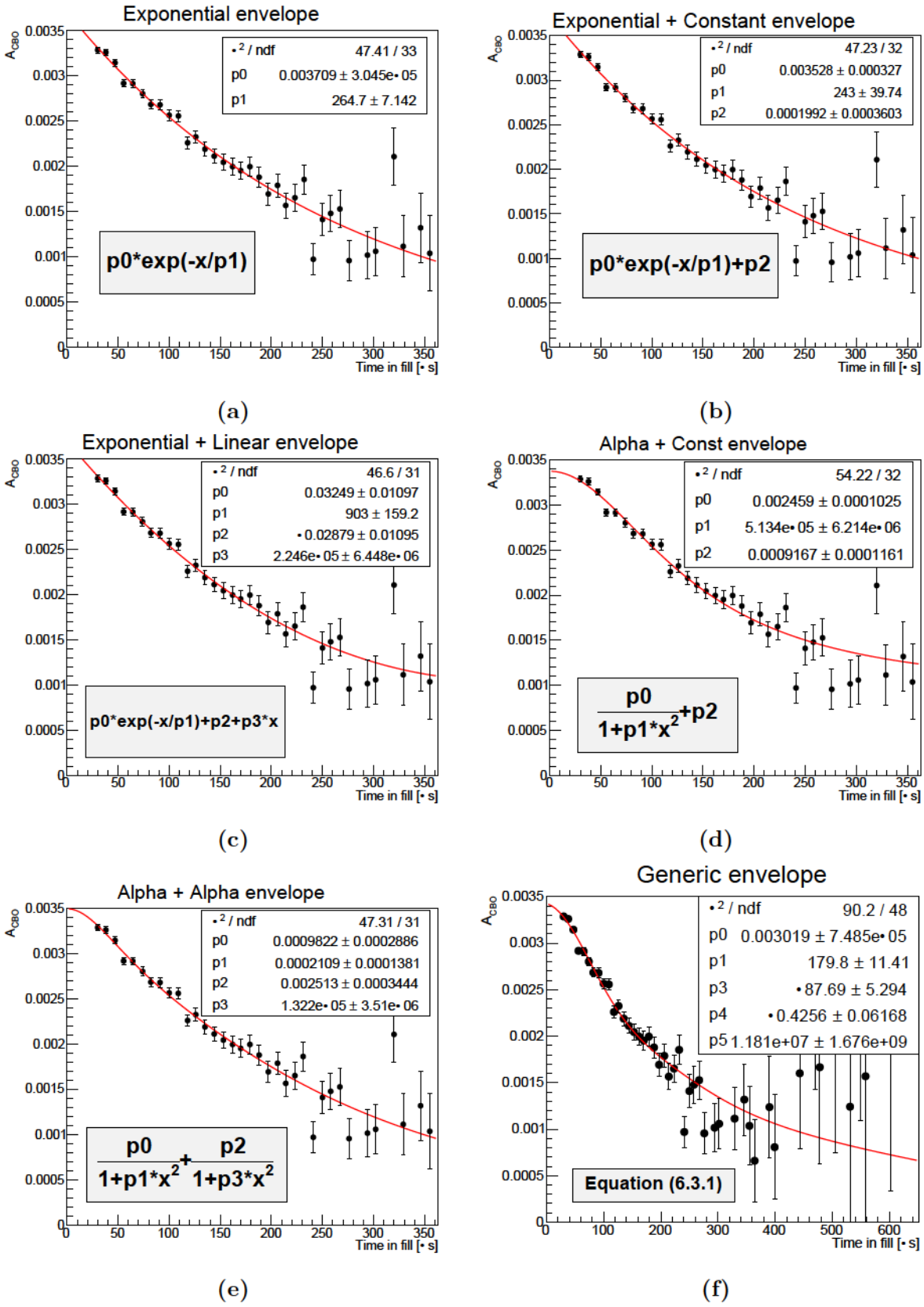

Figure 6.3.2: Decoherence models tested on Run-2, A-Method A_{CBO} envelope obtained with fits on calorimeter data with 8 μs bin width.

Varying CBO frequency

In our nominal procedure, we parametrized the drifting CBO frequency as an exponential plus a constant function (Equation (5.5.5)): the values of the amplitude and lifetime (A, τ_A) were

CBO decoherence systematics [ppb]			
Method	Run-2	Run-3a	Run-3b
A	26	12	20
RA	15	7	15

Table 6.3.1: Systematic uncertainty related to the decoherence function $D(t)$ that parametrizes the CBO amplitude.

extracted separately from Run-2 and Run-3 data and reported in Table 5.5.1.
Within the ω_aEuropa team, we estimated the systematic associated to the uncertainty on A and τ_A in the following way: we randomly sampled 100 values of A and τ_A from a multivariate Gaussian distribution, where the mean and standard deviation for A and τ_A were set from Table 5.5.1, and the two parameters were assumed to be fully anti-correlated[1]. We repeated the 28/16-parameter fits of A/RA-Methods wiggle plots fixing A and τ_A to the randomly generated values, and extracted R from fits. Figure 6.3.3 shows the results in Run-2: the standard deviation of the distribution of R values was taken as the systematic uncertainty, and reported in Table 6.3.2.

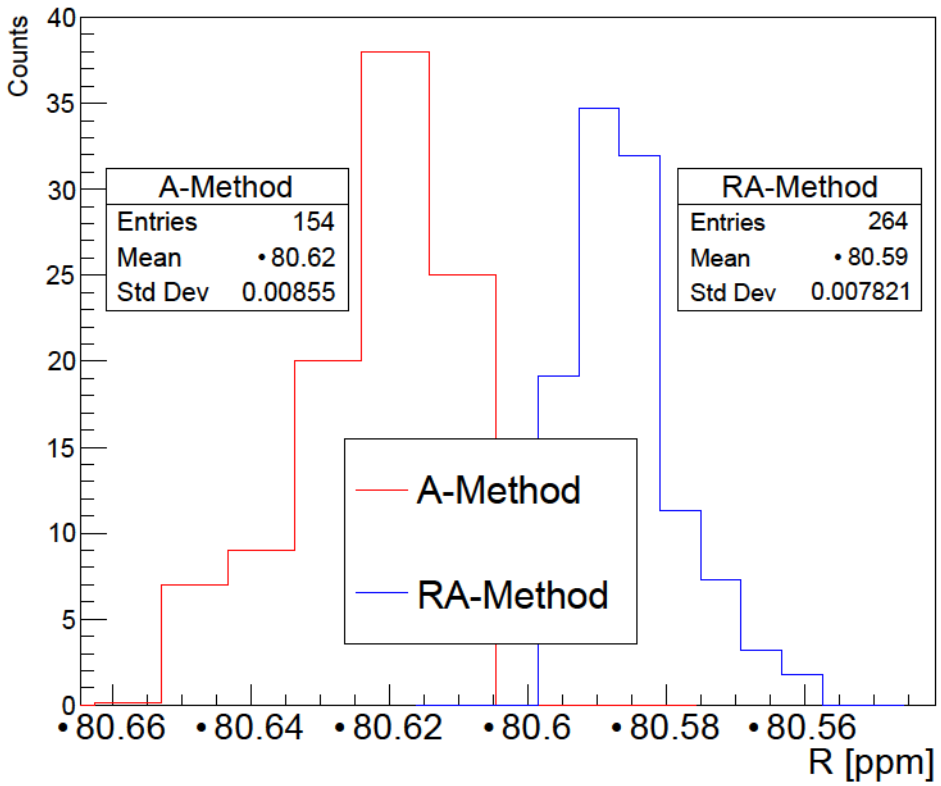

Figure 6.3.3: Run-2 data: 100 extractions of the varying CBO parameters and resulting distributions of fitted R values.

Dedicated studies carried out by other analysis teams proved that the two effects described so far, the CBO decoherence model and the varying CBO frequency, are uncorrelated and can be added in quadrature when combining the total CBO systematic. The last contribution, reported in the following, is instead assumed to be fully correlated, thus added linearly to the combination of the first two.

[1]From the fit in Figure 5.5.2(b), the correlation was found to be -0.98.

Varying CBO systematics [ppb]			
Method	Run-2	Run-3a	Run-3b
A	7.2	8.6	3.7
RA	3.6	0.8	0.9

Table 6.3.2: Systematic variation on R due to varying CBO parameters, taken as the standard deviation of the distributions like the ones in Figure 6.3.3.

Higher-order CBO time constants

In the nominal ω_aEuropa fit function, the decay time τ_{CBO} is assumed to be the same for the three fit terms $N_{CBO}(t)$, $A_{BD}(t)$, $\phi_{BD}(t)$. However, since Run-1 our $g-2$ simulations suggested that the time constants for the last two terms can differ from the lifetime of $N_{CBO}(t)$, and actually reach values that are $\pm 50\%$ of τ_{CBO}. To evaluate this systematic contribution in Run-2/3, we have repeated our A/RA-Methods fits fixing the time constants of $A_{BD}(t)$ and $\phi_{BD}(t)$ independently, as $0.5\tau_{CBO}$ or $1.5\tau_{CBO}$, for a total of 4 new fits in addition to the nominal one. For each dataset and method, we extracted the largest variation in R with respect to the nominal result, and took it as our systematic evaluation, reported in Table 6.3.3.

Higher-order CBO time constants [ppb]			
Method	Run-2	Run-3a	Run-3b
A	4.6	1.3	2.1
RA	5.8	3.9	3.8

Table 6.3.3: Systematic error obtained by changing the $A_{BD}(t)$ and $\phi_{BD}(t)$ lifetime constants by $\pm 50\%$ with respect to τ_{CBO}.

6.4 Lost muons model

In this Section we will present the different sources of systematic contributions from our lost muons model, based on the selection of triple, quadruple and quintuple calorimeter coincidences. In order to assign a systematic uncertainty, we compared our fit results with the nominal lost muon function with two other procedures: the first one is the lost muons function obtained by selecting only double coincidences in two consecutive calorimeters; the second one is the lost muons function that another analysis team, IRMA, built with their own procedure to select triple coincidences.
Figure 6.4.1 shows the comparison between the nominal $J(t)$ and the two other lost muons function that we tested, in the case of Run-2. Table 6.4.1 reports the shifts in R and k_{LM} with respect to the nominal representative fits. The systematic uncertainty has been taken as the largest difference ΔR between the standard $J(t)$ from $3+4+5$ coincidences and the other models that were tested.

The k_{LM} values from double coincidences and from IRMA function are typically similar in size, because of the similar normalization of $J(t)$ that can be observed in Figure 6.4.1. The final systematic errors for the R/RA-Methods are larger than the T/A-Methods, and this could be caused by the fact that k_{LM} parameter is fitted with greater uncertainty in R/RA fits, so it is

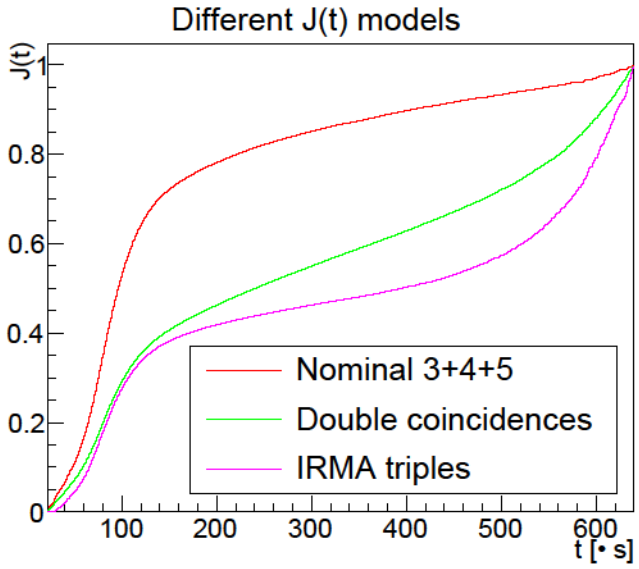

Figure 6.4.1: Different functions for the Run-2 lost muons: our nominal $J(t)$ has a different efficiency than the one built in the IRMA analysis or by selecting double coincidences, which results in a different value of the k_{LM} parameter. The difference in R depends on the shape of $J(t)$ and not on the normalization.

Case	Parameter	2 A	3a A	3b A
Nominal	k_{LM}	0.00106(7)	−0.0009(3)	−0.0009(3)
Doubles	ΔR [ppb]	0.0	−1.9	−1.2
	k_{LM}	0.0023(1)	−0.0022(8)	−0.0026(9)
IRMA	ΔR [ppb]	0.2	−0.7	0.0
	k_{LM}	0.0019(3)	−0.0019(8)	−0.0022(8)
Systematic [ppb]	–	0.2	1.9	1.2

Case	Parameter	2 RA	3a RA	3b RA
Nominal	k_{LM}	0.013(19)	−0.008(11)	−0.007(14)
Doubles	ΔR [ppb]	−0.1	−4.2	0.5
	k_{LM}	0.03(4)	−0.02(3)	−0.03(5)
IRMA	ΔR [ppb]	−2.6	−0.6	3.4
	k_{LM}	0.04(6)	−0.03(4)	−0.03(6)
Systematic [ppb]	–	2.6	4.2	3.4

Table 6.4.1: Different lost muons models tested on Run-2/3 datasets, for A/RA-Methods. ΔR shifts are calculated with respect to nominal fits in Tables 5.6.1 and 5.6.2.

allowed to fluctuate more, resulting in a larger bias on R.

In the nominal ω_aEuropa procedure, we fixed the lifetime $\gamma\tau$ to 64.4 µs in the integral of Equation (5.2.8) to build $J(t)$ for all Run-2/3 datasets. The choice of this value did not affect ω_a significantly: we repeated the wiggle plot analysis varying $\gamma\tau$ in Equation (5.2.8) by ±30 ns, which was the total change across the Run-2/3 datasets, and the systematic error on ω_a was less than 0.1 ppb for all fits.

The systematic related to the fact that k_{LM} converges to negative values in Run-3 will be discussed in Section 6.5.

6.5 Residual slow term

In the nominal ω_aEuropa reconstruction procedure, we apply a residual slow term correction that rescales the clusters' energies, to account for a slow term that affects our data in multiple ways - for example, it induces the drift towards negative values of k_{LM} as a function of the positron energy. The correction is parametrized according to Equation (5.2.9), where the δ_g sets the absolute size of the correction, and the ω_a oscillation is modulated by the asymmetry A_g. In the following, we will assess the systematics on ω_a due to the uncertainties on the δ_g and A_g parameters. We will do this in a similar way as the gain systematics: we will extract the dependence R on each parameter, and multiply it by the parameter's uncertainty.

Slow term correction asymmetry A_g

The nominal value of A_g in the ω_aEuropa procedure was 0.1497 for Run-2 and 0.1192 for Run-3a/3b. The choices were made based on preliminary T-Method scans of R versus A_g, with the goal of minimizing the χ^2/n.d.o.f.
In order to extract the sensitivity of R to this parameter and the related systematic, we varied A_g from 0 to 0.48, in steps of 0.04 for T/A-Methods; and from 0 to 0.45 in steps of 0.075 for R/RA-Methods. For each choice of A_g, the procedure to build and fit wiggle plots was repeated.

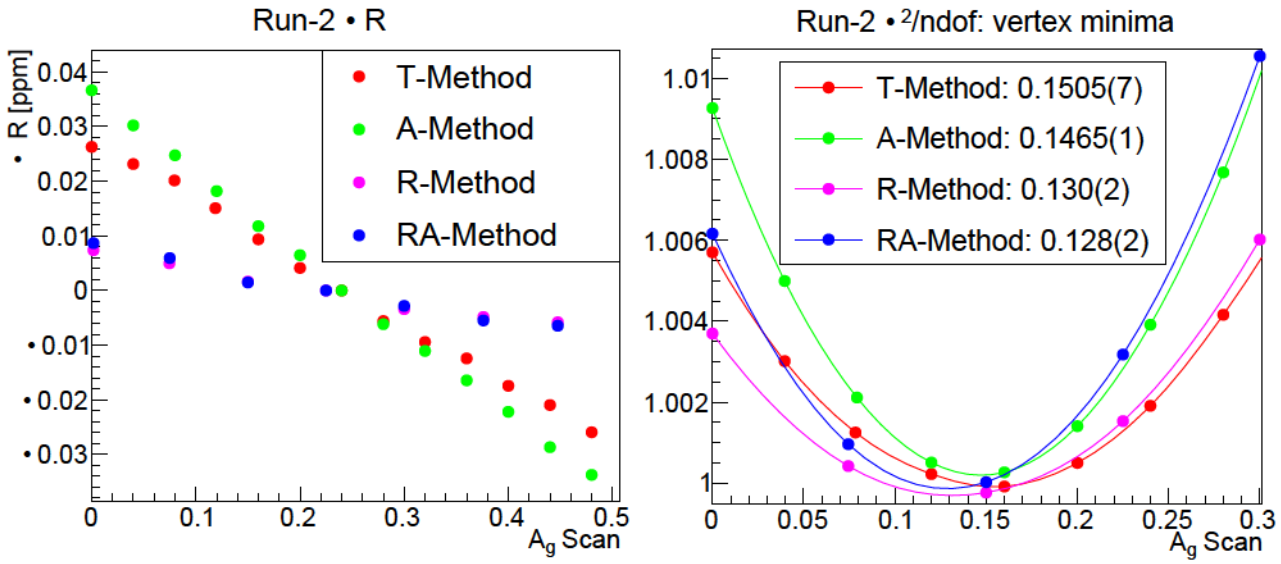

(a) (b)

Figure 6.5.1: (a) Run-2 scan of R versus A_g: to display all methods in the same plot, we applied an offset on R such that it is 0 for the central point of the study. (b) Run-2 scan of χ^2/n.d.o.f. versus A_g, where the value of the minimum is fitted with a quadratic formula and reported in the legend with its error: to display all methods in the same plot, we applied an offset on χ^2/n.d.o.f. such that it is ~ 1 for the vertex of the parabola.

Figures 6.5.1(a) and 6.5.1(b) show the R and χ^2/n.d.o.f. results for all methods in Run-2: the slopes of R were always negative, but smaller in absolute value for the R/RA-Methods; the χ^2/n.d.o.f. plots were fitted with a quadratic formula to extract the value of the vertex minimum, reported with the fit error. All the fitted slopes are reported in Table 6.5.1. To extract the systematic related to the A_g parameter, we multiplied the slope of R versus A_g by the uncertainty on A_g, which could be estimated in two ways: the difference between the χ^2/n.d.o.f. minimum and the nominal A_g value for each of the Run-2/3 reconstruction; or the change in A_g that increased the χ^2 by 1 unit. The uncertainty was chosen as the maximum value between these two methods.

The systematic related to the A_g parameter is reported in Table 6.5.1 for A/RA-Methods, together with the slopes of R.

Slow term correction amplitude δ_g

The nominal value of δ_g in our procedure was $8.815 \cdot 10^{-4}$ for Run-2 and $6.250 \cdot 10^{-4}$ for Run-3a/3b. The choices were made based on preliminary T-Method studies on the δ_g parameter, with the goal of making the k_{LM} parameter more stable as a function of the cluster energy. In order to extract the sensitivity of R to this parameter and the related systematic, we varied δ_g from 0 to $1.5 \cdot 10^{-3}$, in steps of $1.25 \cdot 10^{-4}$ for T/A-Methods and steps of $2.5 \cdot 10^{-4}$ for R/RA-Methods, to extract the slopes of R as for the δ_g parameter.

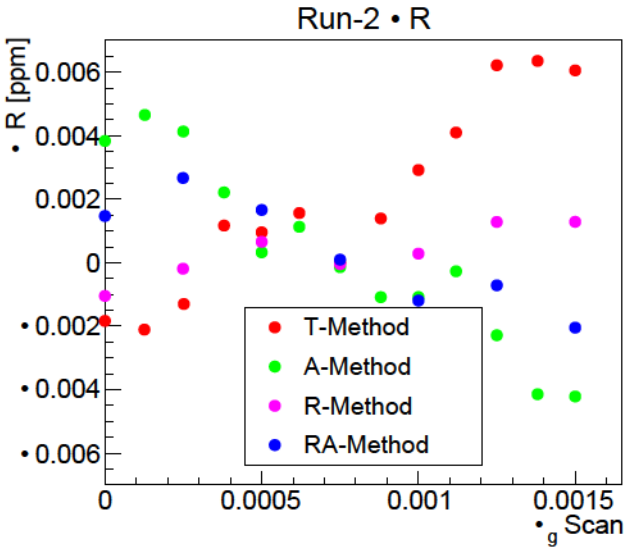

Figure 6.5.2: Run-2 scan of ΔR versus δ_g: to display all methods in the same plot, we applied an offset on R such that it is 0 for the central point of the interval.

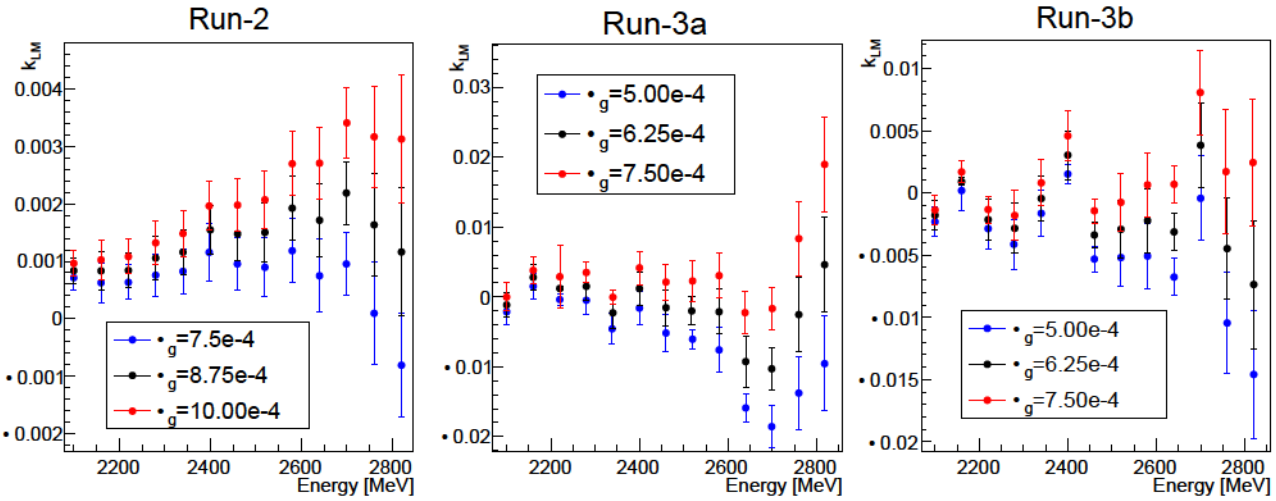

(a) (b) (c)

Figure 6.5.3: Energy binned fit of k_{LM} parameter for Run-2/3 dataset, T-Method. The residual slow term correction parameter δ_g is varied around the nominal value, to test if k_{LM} versus energy remains flat.

Figures 6.5.2 shows the R results for all methods in Run-2: the slopes of R are positive for the T/R-Methods and negative for the A/RA-Methods, which could be caused by the different energy thresholds; all the fitted slopes of R/δ_g are reported in Table 6.5.1.
The choice of δ_g was based on the values that made k_{LM} more stable as a function of the energy. Figure 6.5.3 shows k_{LM} versus energy for different choices of δ_g around the nominal value for each of the Run-2/3 datasets: k_{LM} is flat for the central value and tends to drift upwards/downwards for the upper/lower values of the δ_g interval. To be conservative, in order to evaluate the systematic contribution due to δ_g we multiplied the slopes of R by $1.25 \cdot 10^{-4}$, which was the T/A-Methods step in δ_g. Table 6.5.1 reports the resulting systematic error related to the choice of δ_g for all datasets of Run-2/3.

Slope of R versus A_g [ppb]			
Method	Run-2	Run-3a	Run-3b
A	−146	−182	−96
RA	−34	−146	−32

A_g-related systematics [ppb]			
Method	Run-2	Run-3a	Run-3b
A	3.5	6.6	3.2
RA	0.9	3.2	2.3

Slope of R versus δ_g [ppb/10^{-3}]			
Method	Run-2	Run-3a	Run-3b
A	−5.72	−120	−45.33
RA	−2.90	−16.21	−15.20

δ_g-related systematics [ppb]			
Method	Run-2	Run-3a	Run-3b
A	0.7	15.0	5.7
RA	0.4	2.0	1.9

Table 6.5.1: Slopes of R and systematics related to the uncertainties on A_g and δ_g.

Other parameters of the slow term correction

When building the residual slow correction of Equation (5.2.9), the muon lifetime was fixed to the value of 64.43 µs obtained in Run-2 T-Method fits, and also the ω_a parameter was fixed *a priori* to 1.43939 rad/µs, but in principle the R value from fits could change according to this parameter. In this paragraph, we report the results obtained when changing $\gamma\tau$ and ω_a conservatively by a value that is larger than their uncertainty. We changed $\gamma\tau$ from 64.43 µs to 64.40 µs (closer to the Run-3 value) and ω_a by ±10 ppm: the differences of R with respect to the nominal fits are reported in Table 6.5.2.

ΔR due to $\delta\tau_\mu = 30$ ns [ppb]			
Method	Run-2	Run-3a	Run-3b
A	2.5	0.4	−0.5
RA	2.8	−3.5	1.9

ΔR due to $\delta\omega_a = 10$ ppm [ppb]			
Method	Run-2	Run-3a	Run-3b
A	2.9	1.8	−1.6
RA	2.3	−1.1	1.4

Table 6.5.2: Systematics associated to the parameters ω_a and τ choices for the slow term correction.

Negative k_{LM} in Run-3a/3b fits

In Run-3a/3b, the fitted values of k_{LM} were always negative, despite the residual slow correction that made their behaviour more stable as a function of the positron energy. In the A-Method results of Table 5.6.1, k_{LM} was negative and not compatible with 0 within the fit error, whereas

it was compatible with 0 for the RA-Method in Table 5.6.2. In this paragraph we will discuss the last systematic error related to the residual slow term, only for the Run-3a/3b A-Method. In Table 6.5.3 we report the shift in R and χ^2/n.d.o.f. when fixing k_{LM} to 0 or to 10^{-3} (close to the Run-2 value); since k_{LM} is highly correlated to $\gamma\tau$, we also report the shift in the muon lifetime when fixing k_{LM}. Differently from the systematics in Table 6.4.1, in this study the lost muons model $J(t)$ is always the nominal ω_aEuropa one.

Dataset	k_{LM}	χ^2/n.d.o.f.	R [ppm]	$\gamma\tau$ [µs]
Run-3a	Floating	3981.24/4127	-71.393 ± 0.290	64.415 ± 0.003
	0	3988.57/4128	-71.401 ± 0.290	64.4223 ± 0.0005
	0.001	4012.36/4128	-71.409 ± 0.290	64.4300 ± 0.0005
Run-3b	Floating	4154.14/4127	-70.397 ± 0.468	64.392 ± 0.003
	0	4162.76/4128	-70.404 ± 0.468	64.4002 ± 0.0007
	0.001	4192.28/4128	-70.411 ± 0.468	64.4088 ± 0.0007

Table 6.5.3: A-Method slow term systematics for Run-3 datasets due to k_{LM} being negative.

For each dataset, the $\gamma\tau$ fit error is reduced when fixing k_{LM}. From an independent study of the Fast Rotation signal that the beam dynamics groups performed, the $\gamma\tau$ parameter was found to be 64.418 ± 0.009 µs for Run-3a and 64.384 ± 0.009 µs for Run-3b [131]. In our nominal fits with negative k_{LM}, $\gamma\tau$ is compatible with the Fast Rotation values within $1\,\sigma$; instead, as shown in Table 6.5.3, $\gamma\tau$ becomes more than $1\,\sigma$ larger than the Fast Rotation values when fixing k_{LM} to the Run-2 value. For this reason, as a systematic error for the A-Methods, we take the difference between the nominal value of R and the fit for $k_{LM} = 0$, which is equal to 8 ppb for both Run-3 datasets.

Combined Slow term systematics [ppb]			
Method	Run-2	Run-3a	Run-3b
A	5.2	18.3	10.4
RA	3.8	5.3	3.8

Table 6.5.4: Sum in quadrature of all residual slow term systematics.

Table 6.5.4 reports the combined slow term systematics for each dataset and each method, where we have added in quadrature the contributions from A_g, δ_g, other parameters of the residual slow term correction, and the behaviour of k_{LM} for Run-3a/3b T/A-Methods, assuming these contributions are all independent. The values for Run-3a are larger than 10 ppb mostly from the contribution of the A_g and δ_g systematics, and from the negative value of k_{LM} in the case of the A-Method.

6.6 R/RA-Methods related systematics

There is a class of systematic uncertainty that only affects the R/RA-Methods, because it is related to two parameters that are fixed before building wiggle plots: the T_a anomalous precession period in the Quartering procedure, because in principle its choice *a priori* could

affect the fit results of R, and the T_{VW} that is used for time randomization of R/RA-Methods. We have repeated the nominal procedure for the representative seeds to extract the shifts in R when changing T_a by 10 ppm (to be conservative, like Table 6.5.2 of the residual slow term correction systematics), and T_{VW} by 2 ns (approximately 0.5%), which corresponds to how much it varies among the three Run-2/3 datasets from Table 5.6.1. The shifts in R due to the choices of T_a and T_{VW} were found to be of the order of ~ 3 ppb and are reported for all datasets in Table 6.6.1.

ΔR due to $\delta T_a = 10$ ppm [ppb]				ΔR due to $\delta T_{VW} = 0.5\%$ [ppb]			
Method	Run-2	Run-3a	Run-3b	Method	Run-2	Run-3a	Run-3b
R	2.1	2.5	1.9	R	2.1	1.7	2.4
RA	1.3	1.1	1.5	RA	−0.9	0.7	0.5

Table 6.6.1: Shifts in R for the representative R/RA-Methods seeds, when conservatively varying the T_a and T_{VW} parameters that are fixed *a priori* when building the R/RA wiggle plots.

6.7 Summary of all systematic contributions

Table 6.7.1 summarizes the statistical and systematic contributions for the different datasets of Run-2/3. These results were averaged with those from other groups, as it will be explained in Chapter 7. The "Time randomization" uncertainty is considered to be independent (thus uncorrelated) from each analysis. It is obtained from σ_R (the width of the per-seed distribution of R fits) reported in Table 5.6.1 and 5.6.2, through Equation (5.2.10). To keep this uncertainty below ~ 5 ppb, 100 seeds were used for the A-Method and 540 for the RA-Method, where the additional Quartering and vertical waist randomizations in the Ratio wiggle plots enhanced σ_R.

Contribution [ppb]	A-Method			RA-Method		
	Run-2	Run-3a	Run-3b	Run-2	Run-3a	Run-3b
Statistical	337	291	468	345	301	480
Time randomization	3.5	2.6	4.8	3.7	2.7	5.3
Gain	4.0	4.7	4.7	0.3	0.8	1.0
Pileup	6.1	7.7	9.2	2.9	4.7	6.9
CBO	31.6	16.1	21.6	20.5	16.6	21.3
Lost muons	0.2	1.9	1.2	2.6	4.2	3.4
Residual slow term	5.2	18.3	10.4	3.8	5.3	3.8
Ratio approximations	–	–	–	1.6	1.3	1.6
Total systematic	32.8	26.0	26.1	21.3	18.6	23.0

Table 6.7.1: Run-2/3 statistical and systematic uncertainties for A/RA-Method in the ω_aEuropa analysis.

Chapter 7

Measurement of the magnetic anomaly a_μ to 203 ppb

In this Chapter, we will present the result for a_μ with Run-2/3 data according to Equation (4.7.3). We will start by reminding our first result released in 2021, and then we will review the consistency checks that were performed.

7.1 Run-1 result

The Run-1 measurement was released in 2021 with a total precision of 462 ppb: the statistical error amounted to 434 ppb and was limited by the number of analyzed positrons; the systematic error amounted to 157 ppb and was dominated by the transient ESQ fields B_q and the phase acceptance effect C_{pa}, that was enhanced by damaged ESQ resistors. All of these large contributions were reduced in Run-2/3, thanks to the improvements described in Section 5.1.1. The uncertainties on the magnetic field and on the transient kicker field were limited by the number of measurements that were performed at the time. Within the ω_a analysis, there was the unsolved puzzles of the residual slow term effect and its interplay with k_{LM}, which required a conservative estimate of the associated systematic error. The CBO and pileup effects amounted to 38 ppb and 35 ppb respectively, dominating the total ω_a^m systematic error. Table 7.1.1 reports the published values for each contribution. The differential decay C_{dd} was not applied at the time, and preliminary estimations of its uncertainty were found to be negligible with respect to other beam dynamics effects.

With the Run-1 analysis, we performed a measurement of a_μ to 462 ppb, which was in agreement with the previous result at the E821 experiment in BNL:

$$a_\mu^{E989}\ (\text{Run-1}, 2021) = (116592040\ \pm\ 54) \times 10^{-11} \tag{7.1.1}$$

Combining the Run-1 result with the previous one at E821, the experimental average in 2021 was:

$$a_\mu^{exp}\ (\text{average}, 2021) = (116592061\ \pm\ 41) \times 10^{-11} \tag{7.1.2}$$

reaching the precision of 351 ppb. Figure 7.1.1 shows the comparison between the 2021 experimental average and the theoretical value recommended by the Theory Initiative in the 2020 White Paper [5], described in Chapter 2.

Quantity	Correction [ppb]	Uncertainty [ppb]
ω_a^m (statistical)	···	434
ω_a^m (systematic)	···	56
C_e	489	53
C_p	180	13
C_{pa}	-158	75
C_{dd}	···	···
C_{ml}	-11	5
$f_{\text{calib}} \cdot \langle \omega_p'(\vec{r}) \times M(\vec{r}) \rangle$	···	56
B_q	-17	92
B_k	-27	37
External fundamental factors	···	25
Total systematic	···	157

Table 7.1.1: From Ref. [1]. Run-1 summary of the statistical and systematic errors on different contributions to a_μ in Equation (4.7.3): the measured anomalous precession frequency and magnetic field, the values and uncertainties on the correction terms of due to beam dynamics and field transients, and the total fundamental factors.

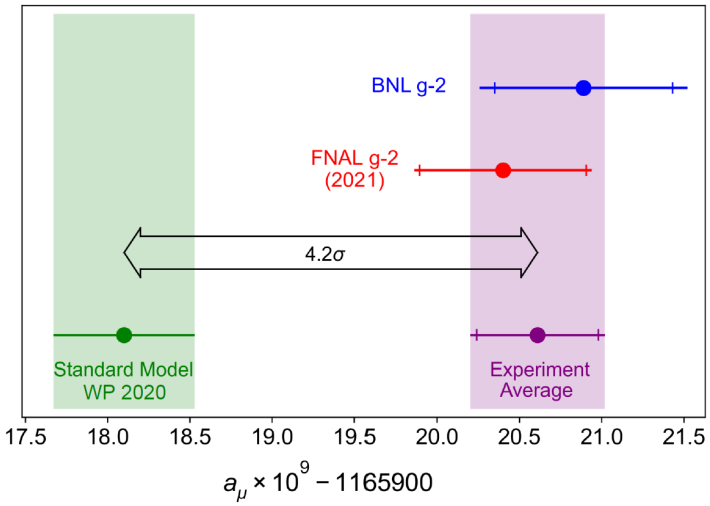

Figure 7.1.1: From Ref. [1]. The experimental values of a_μ from the E821 experiment at BNL (blue), the Run-1 measurement at Fermilab (red) and the combined average (purple band) are compared with the Muon $g-2$ Theory Initiative recommended value for the Standard Model. The inner tick marks indicate the statistical contribution to the total uncertainties.

7.2 Run-2/3 result

There were two different hardware blinding in Run-2 and Run-3, thus there were two unknown values of f_{clock} that prevented any comparisons with the Run-1 result during the analysis. Furthermore, each of the seven ω_a analysis teams applied a software blinding with a secret offset to their ω_a results, according to Equation (4.7.17).
There were three steps towards the release of the Run-2/3 result: the first was the software unblinding amongst analyses, the second was a "relative" unblinding to compare Run-2/3 with a common secret offset, and the last one was the hardware unblinding of Run-2/3. We will now discuss some comparisons done after the software unblinding, to investigate potential outliers and study the allowed statistical variations between each reconstruction or each method of building wiggle plots.

7.2.1 Consistency checks of ω_a results across different analysis groups

Once the software blinding was removed, different analysis teams could compare their result for ω_a within the same dataset, whereas a hardware blinding was still in place between Run-2 and Run-3. As a cross check, several analyzers sent their wiggle plot histograms to other analyzers from different teams, who extracted ω_a with their own fit function. The aim of this procedure was to spot any differences in the ω_a results when fitting the same wiggle plot with different functions: in case this happened, it was important to track down the origin of such a difference, to clarify whether it was due to reasonable choices in the analysis (e.g., different values of A and τ_A that parametrized the varying CBO frequency in Equation (5.5.5)), or instead due to a possible error in the code.

Within the ω_aEuropa group, we exchanged histograms and performed these checks with two groups: BU and SJTU. The exchange with BU was crucial for the RA-Method, since ω_aEuropa and BU were the only two groups that used that method in Run-2/3 (see Table 5.1.2). BU's procedure for the A-Method wiggle plots involved the time randomization of vertical oscillation frequencies, which removed the need to parametrize the vertical waist (VW), y-oscillations and VW-CBO effects in their fit function. In the ω_aEuropa team, this type of randomization was applied to the R/RA-Methods, but not for T/A-Methods. Thus, the exchange with SJTU histograms was an important test for the vertical oscillation frequencies in the ω_a fit function, and in particular for the VW-CBO term of Equation (5.5.15), which was new with respect to Run-1.
The procedure to perform this type of check was the following:

1. A first fit was performed by each group with their own nominal fit function, on the same wiggle plot with the associated lost muons function. For instance: as a first step, both ω_aEuropa and BU fitted BU's RA-Method wiggle plot, each with their own fit functions; in this case, for the lost muons parametrization, both groups used BU's $J(t)$ function obtained in their nominal procedure; then both groups repeated this procedure on ω_aEuropa's wiggle plots.

2. These first fits served as a baseline for the comparison: typical differences of R were of the order of 20 ppb, but could reach up to 30 ppb, and large differences of R were associated with differences in the reduced χ^2 by 30 or more units.

3. To track down the differences, we began to standardize our fit functions step-by-step. The most relevant changes on R and χ^2/n.d.o.f. occurred when both groups used the same parameters for the CBO decoherence envelope and for the varying CBO frequency. Other changes improved the comparisons significantly: in the BU fits, k_{LM} was fixed to positive values in Run-3; in the nominal SJTU function, the lifetime parameter of the VW-CBO effect was fixed instead of being kept as a free parameter. In both cases, when we implemented these fit strategies in the ω_aEuropa fit function, there was an overall reduction of the R and χ^2/n.d.o.f. differences.

With standardized fit functions, we were able to obtain very similar results between ω_aEuropa and BU teams when fitting ω_aEuropa and BU wiggle plots, and likewise between ω_aEuropa and SJTU. For each dataset and method, the final differences in R were less than 1 ppb, and in χ^2/n.d.o.f. less than 0.5 units.

Figure 7.2.1 shows the software-unblinded ω_a results for the total of 19 analysis methods across the seven ω_a analysis teams, reported in Table 5.1.2. Because of the different blinding, there is a ~ 10 ppm difference between Run-2 and Run-3 values.

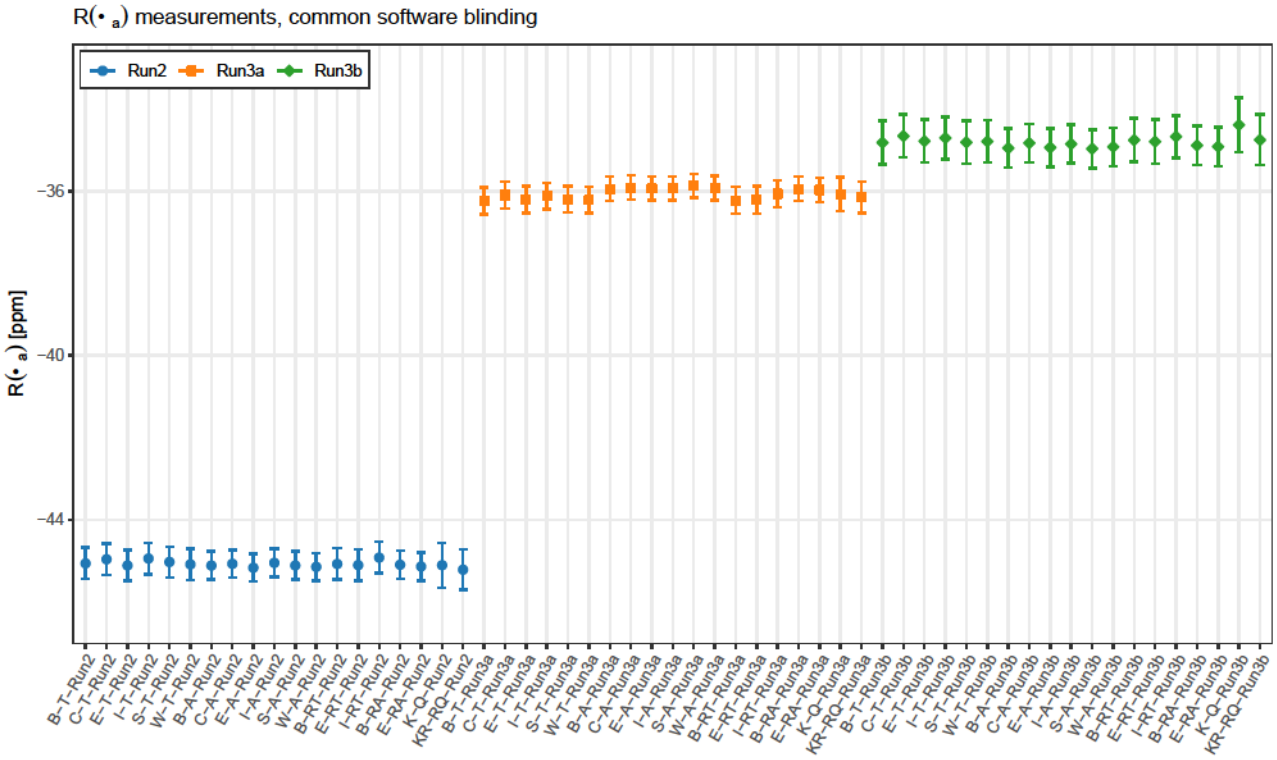

Figure 7.2.1: For each of the three Run-2/3 datasets, the 19 measurements of ω_a from the seven analysis teams with different methods are shown. These results have the same ω_a software unblinding within a given dataset, but there is still a different hardware blinding between Run-2 and Run-3. The error bars represent the statistical uncertainties.

Within each dataset, the 19 distinct ω_a analyses agree with each other within the allowed statistical and systematic uncertainties, that we will refer to as σ_{ij} for each pair of analyses i, j. We can define the pulls between each pair as $(y_i - y_j)/\sigma_{ij}$, where y_i is the ω_a determination for the i^{th} analysis. Figure 7.2.2 shows the pulls for the A/RA-Methods ω_a results, which are used for the average. There are $6 \times 5/2 = 15$ distinct pairs for each dataset, for a total of 45 entries. The standard deviation for the distribution is 1.09, close to 1 as expected.

7.2.2 Combination of ω_a results

For each of the three Run-2/3a/3b datasets, a single measured value of ω_a was obtained by averaging the results of six Asymmetry-Weighted Methods, one for each analysis team. For CU, IRMA, SJTU and UW, the A-Method was chosen; for the two groups that performed both an A-Method and a RA-Method analysis, ω_aEuropa and BU, the RA-Method was chosen as it reduced the systematic uncertainties. Results from the T/Q/RQ-Methods were not considered in the average, because their statistical uncertainty was significantly larger, nonetheless they helped for the consistency checks.

For each dataset, the conservative choice was made to assume that the statistical and systematic uncertainty contributions of the six measurements used in the average were fully correlated. This choice was justified by studying the correlations between each pair of analyses, performed with Monte Carlo and bootstrap techniques, where the correlations among the six analyses were found to be ~ 0.99. Under this assumption, for each dataset the average of the statistical and systematic uncertainties are the averages of the contributions from each of the six analyses. When combining the three dataset, the statistical uncertainty for Run-2/3 becomes 201 ppb,

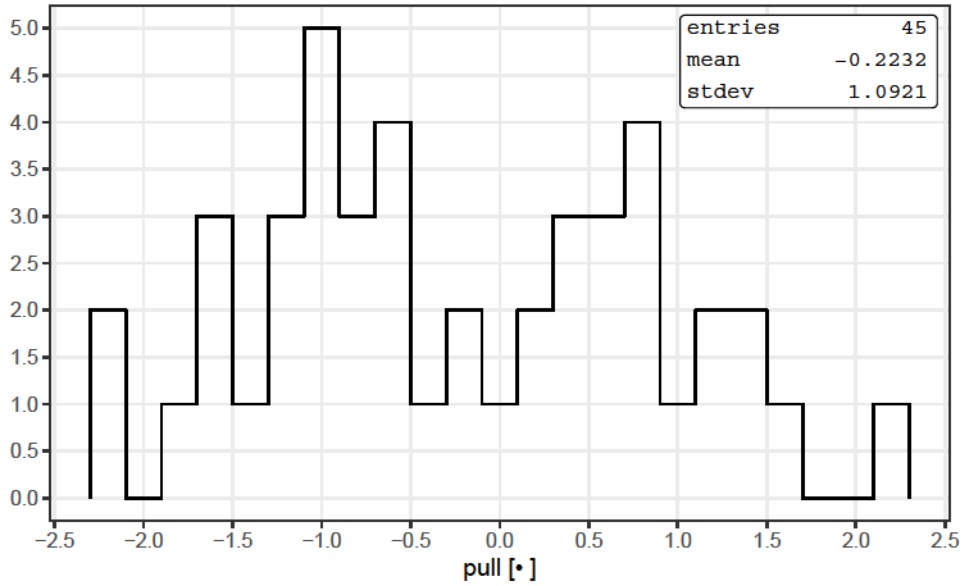

Figure 7.2.2: Pulls between the 45 pairs of A/RA-Methods measurements that are used in the ω_a averages of the Run-2/3 datasets.

whereas, for the systematic uncertainties, the conservative assumption is made that the same contributions are fully correlated among datasets[1].

7.2.3 Consistency checks of $\mathcal{R}_\mu$

After the hardware unblinding, many consistency checks on the $\mathcal{R}_\mu$ ratio of Equation (4.7.3) have been perform, to identify any unexpected correlations to external variables such as the temperature of the muon storage ring or the magnet current. For the purpose of these tests, for each external variable the Run-2/3 data have been divided into many slices, and for each slice the ratio $\omega_a/\tilde{\omega}'_p$ was obtained. Typically, the division into slices was carried out in order to have the same variable range for each slice, but in some cases this led to ω_a fits with too small statistics, so for a few external variables it was preferred to split data into slices with the same number of analyzed positrons. In this consistency study, none of the $\mathcal{R}_\mu$ ratio values showed a dependency on the external variables that were investigated. For each variable, a χ^2 minimization fit on the $\mathcal{R}_\mu$ versus slice was performed, and the fit p-values were typically above 0.75.

An additional consistency check was performed to examine the correlation of $\mathcal{R}_\mu$ versus each of the 20 datasets of Run-2/3. The results of this test are shown in Figure 7.2.3(a): no inconsistencies were observed, but two datasets (Run-2F and Run-2H) had higher $\mathcal{R}_\mu$ ratio values compared to the other datasets. In light of this difference, further analysis cross checks were performed for these two datasets by ω_a and ω_p analyzers, but no anomalies were discovered, giving us confidence that the higher $\mathcal{R}_\mu$ ratio values for Run-2F and Run-2H were due to statistical fluctuations. The results of a χ^2 minimization fit are shown, with a p-value of 44%.

For each of the three datasets Run-2/3a/3b, the ratio $\mathcal{R}_\mu$ was computed through Equation (4.7.3), including the corrections that arise from beam dynamics and transient magnetic fields. The three ratio values were found to be statistically consistent and fitted to obtain the measured

[1] Further details on the combination will be described in full in a future paper, that is currently in preparation for submission to Physical Review D.

$R_\mu(T_r)$ for the Run-2/3 combination (where T_r is the reference temperature in Equation (4.7.3)) with a p-value around 20%. The results are shown in Figure 7.2.3(b)

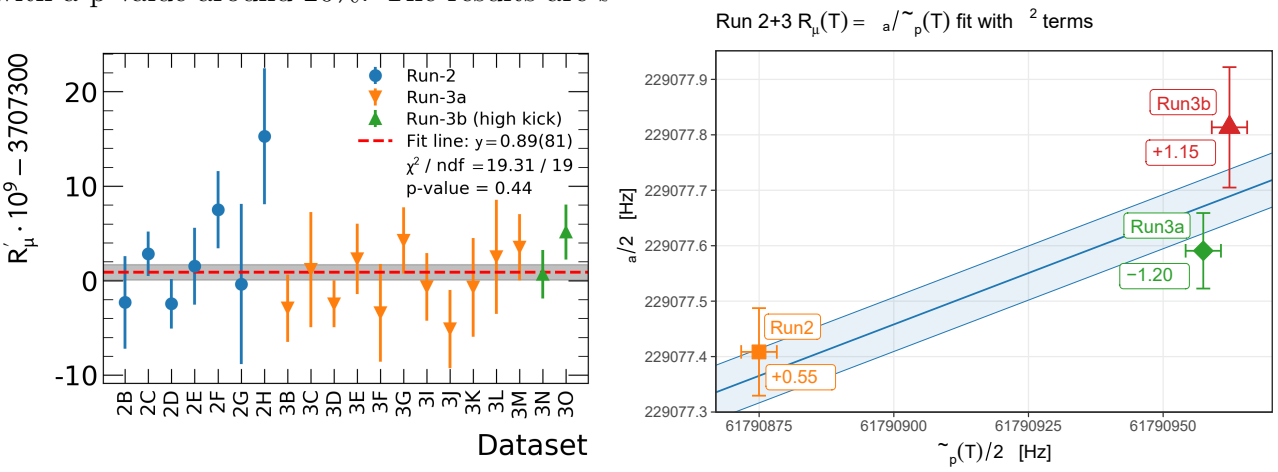

(a) (b)

Figure 7.2.3: (a): value of $\mathcal{R}_\mu$ from Equation (4.7.3) as a function of the 20 Run-2/3 datasets. The horizontal dashed line is the result of a χ^2 minimization fit. (b): Run-2/3 measurements of ω_a and $\tilde{\omega}'_p$, after applying all corrections of Equation (4.7.3), and fit to their ratio.

7.2.4 Run-2/3 measurement of a_μ

Table 7.2.1 reports the final values for each contribution to a_μ in the Run-2/3 result. The uncertainties are dominated by the statistical contribution, as for Run-1. The larger number of analyzed positrons and better running conditions (described in Section 5.1.1) improved both the statistical and the systematic uncertainties by a factor of ~ 2.2 with respect to Run-1. The major change in the apparatus was the repair of damaged ESQ resistors, which strongly affected the muon beam dynamics and enhanced the phase acceptance effect.
The largest beam dynamics correction is C_e, due to the electric fields of the ESQ system, which depends on the momentum spread of the muon beam. The muon momentum distribution is determined from the frequency distribution and debunching rate of the injected beam using calorimeter data, and the radial distribution of stored muons over a betatron period is obtained from tracker data. In Run-2/3, the debunching analysis took into account differences in momentum spread along the injected bunch length that were not included in the Run-1 analysis. Accounting for this difference and using complementary tracker information reduced the C_e uncertainty by a factor of ~ 0.6.
There was also a great reduction of the transient field systematic effects. In Run-1, the correction from the magnetic field transient due to vibrations caused by ESQ pulsing, B_q, was measured at a limited number of locations around the ring. Thanks to a nonconductive movable device, NMR probes were used in Run-2/3 to map the transient fields in the storage region between the ESQ plates, on a larger number of azimuthal locations. This mapping, in combination with improved methodology and repeated measurements over time, reduced the B_q systematic effect by more than a factor of 4 with respect to Run-1. An improved magnetometer setup with less vibration noise also reduced the systematic error on B_k, caused by kicker-induced eddy currents, by a factor of ~ 3.
With the Run-2/3 analysis, we performed a measurement of a_μ to 215 ppb, which was in agreement with the previous results of Run-1 at Fermilab and of the E821 experiment at BNL:

$$a_\mu^{E989}\ (\text{Run-2/3}, 2023) = (116592057 \pm 25) \times 10^{-11} \tag{7.2.1}$$

Quantity	Correction [ppb]	Uncertainty [ppb]
ω_a^m (statistical)	···	201
ω_a^m (systematic)	···	25
C_e	451	32
C_p	170	10
C_{pa}	-27	13
C_{dd}	-15	17
C_{ml}	0	3
$f_{\text{calib}} \cdot \langle \omega_p'(\vec{r}) \times M(\vec{r}) \rangle$	···	46
B_q	-21	20
B_k	-21	13
External fundamental factors	···	25
Total systematic	···	70

Table 7.2.1: From Ref. [3]. Run-2/3 summary of the statistical and systematic errors on different contributions to a_μ in Equation (4.7.3): the measured anomalous precession frequency and magnetic field, the values and uncertainties on the correction terms of due to beam dynamics and field transients, and the total fundamental factors.

Combining the Run-1 and Run-2/3 results, we obtained the new Fermilab average with a precision of 203 ppb:

$$a_\mu^{E989}\ (\text{Run-1/2/3}, 2023) = (116592055 \pm 24) \times 10^{-11} \tag{7.2.2}$$

Including the E821 result at BNL, the experimental average in 2023 has reached the unprecedented precision of 190 ppb:

$$a_\mu^{exp}\ (\text{average}, 2023) = (116592059 \pm 22) \times 10^{-11} \tag{7.2.3}$$

The results are displayed in Figure 7.2.4.

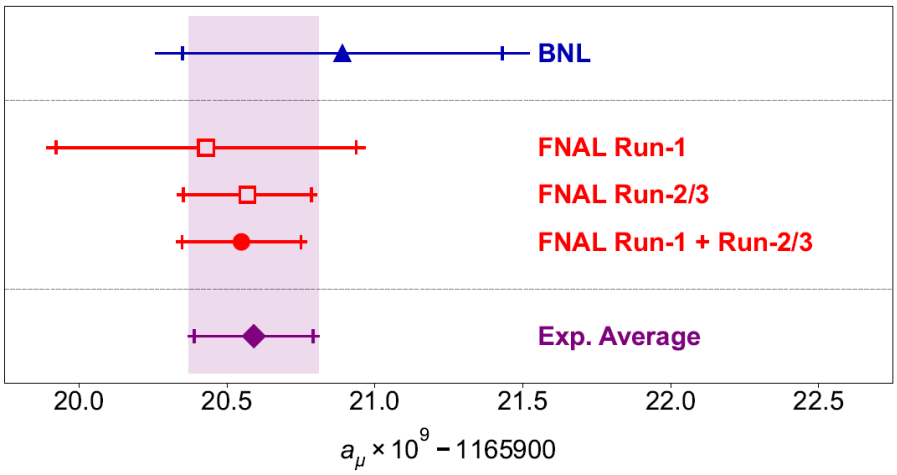

Figure 7.2.4: From Ref. [3]. The experimental values of a_μ from the E821 experiment at BNL (blue), from the E989 experiment at Fermilab (red) and the new combined average (purple band). The inner tick marks indicate the statistical contribution to the total uncertainties.

7.2.5 Theory comparison

The current scenario in the theoretical prediction of a_μ and the puzzles in the QCD sector of the Standard Model (SM) were reported in Section 2.1.3. In the last 20 years, since the previous experiment at BNL observed a $3.7\,\sigma$ discrepancy with respect to the theoretical prediction at the time, there has been a world-wide effort of experiments working on e^+e^- to hadrons data in the energy range below a few GeV, that allowed to achieve a remarkable uncertainty of 0.6% on the leading order hadronic vacuum polarization a_μ^{HVP-LO} [5, 35].
As we already mentioned, in the 2020 White Paper the Theory Initiative recommended a value for the Standard Model prediction based on e^+e^- to hadrons data [5]. The first result at Fermilab from Run-1 data confirmed the discrepancy, which provided a hint of new physics beyond the SM. The discrepancy between the experimental value of a_μ and the 2020 White Paper was strengthened to $5.1\,\sigma$ with the release of the Run-2/3 result.
In 2021, the BMW collaboration published a first lattice calculation of a_μ^{HVP-LO} with sub-percent accuracy [6], which was closer to the experimental value, compatible with a "no new physics" scenario, and discrepant with the dispersive approach based on e^+e^- data. While the evaluation of the whole a_μ^{HVP-LO} from the other lattice groups is in progress, an excellent agreement between different lattice results is found for the so-called intermediate window observable [47]. The evaluation of this intermediate window observable shows a $4\,\sigma$ discrepancy between the lattice and the data-driven computation. On the e^+e^- to hadrons side, in addition to the known discrepancy between KLOE and BaBar, the recent CMD-3 [7] data has shown a discrepancy at $(2.5-5)\sigma$ level with all previous measurements used in the 2020 White Paper [5]. The origin of this discrepancy is currently unknown.
In view of the current theory situation, a firm comparison between the 2023 Run-2/3 result and the theory cannot be established.

Chapter 8

Preliminary analysis of the Run-4/5/6 dataset

In this Chapter, we will present an overview of the Run-4/5/6 running conditions, and discuss the status of the ω_a analysis for these last three datasets which is expected to be completed by 2025.

8.1 Run-4/5/6 data campaigns and running conditions

In the last three data campaigns Run-4/5/6, from December 2020 to July 2023, we collected enough statistics to achieve our goal of ≥ 21 times the total statistics collected in the previous experiment at BNL. Thanks to this amount of data, we expect to exceed the design goal for the statistical uncertainty of 100 ppb. Figure 8.1.1 shows the number of collected positrons over the Run-1-to-Run-6 campaigns from 2018 to 2023, and the projected statistical uncertainty on ω_a with the A-Method.

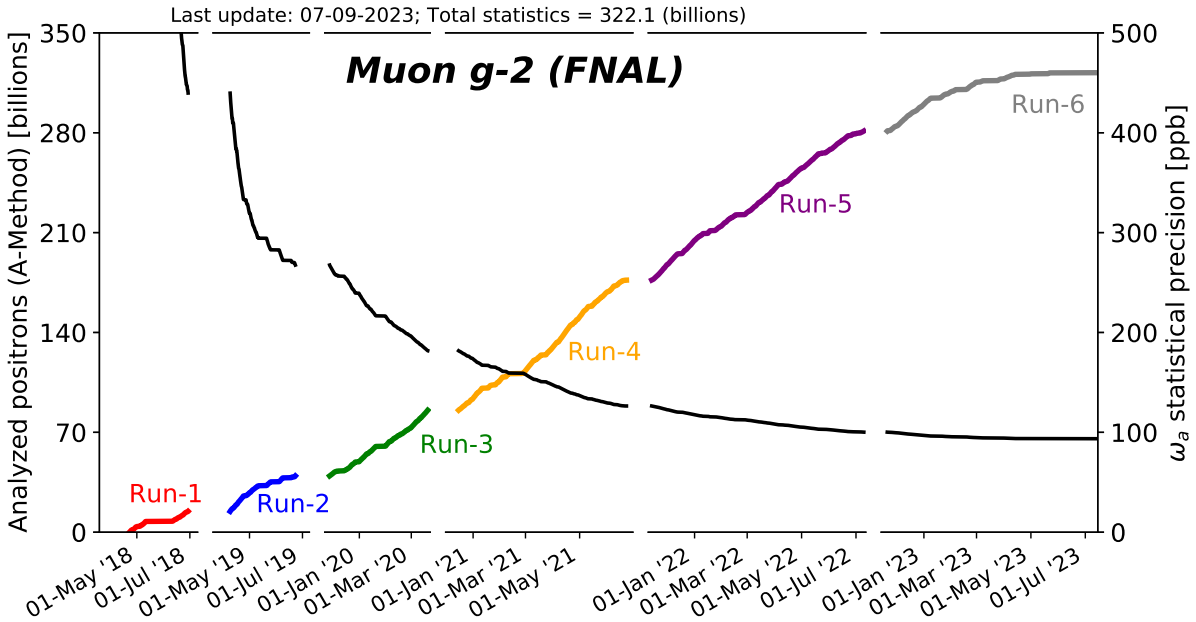

Figure 8.1.1: The 6 run periods of the E989 experiment, with labels indicating the periods in which each data acquisition campaign took place. The last day of acquisition is reported in the top, with the total number of collected positrons. The black curve is the projected statistical uncertainty on ω_a as a function of the cumulative number of positrons, analyzed with the A-Method.

There have been significant changes in the Run-4/5/6 experimental setup, described in the following, that will influence the analysis (for instance, the CBO effect in wiggle plots) thus requiring to modify the analysis procedures to take the differences into account.

Run	Dataset(s)	Muon fills [$\times 10^6$]	Quad RF configuration
Run-4	All	78	No RF
Run-5	A	3	No RF
	B-L	54	Horizontal RF
	M-U	58	Horizontal+Vertical RF
Run-6	All	54	Horizontal+Vertical RF

Table 8.1.1: Run-4/5/6 configurations, along with the number of muon fills (each fill corresponds to 700 µs of data acquisition).

At the time of writing, it has not yet been decided how to combine our data into major datasets for the analysis, but proposals are being made based on the data reported in Table 8.1.1. Soon after the beginning of Run-5, after the first $\sim 2.6\%$ of the dataset was collected, we transitioned to a new configuration of the ESQ system, where a radio frequency (RF) electric field is applied at the ESQ plates simultaneously with the high voltage. This technique was proposed in 2003 after the BNL experiment had finished collecting data, with the goal of reducing the Coherent Betatron Oscillation (CBO) effect (introduced in Section 4.7.2) and the muon losses in the data, which were dominating the beam dynamics systematic uncertainties. The so-called "Quad RF" technique is explained in detail in Ref. [111]: the RF field applies a harmonic modulation of the betatron oscillations, acting as a counter-perturbation on the CBO in a similar way as a forced harmonic oscillator.
During Run-5, the Quad RF was switched on initially for the horizontal oscillations and then also to reduce the vertical motion of the beam. It was observed that the CBO amplitude changed from 5 mm to 1 mm with RF on, and the muon losses were reduced by a factor of 5, only at the expense of a 5% drop in stored muons (because, with this way of optimizing the beam phase space with RF scraping, there are less particles near the limits of the storage ring acceptance).

A few more details are worth mentioning about the Run-4/5/6 datasets.
After Run-4, there were a couple of changes in the configuration of In-Fill-Gain (IFG) laser pulses (described in Section 4.4.2). In the Run-4 configuration, 4 laser pulses covered the entire 700 µs of storage time moving by a step of 1.5 µs per fill, for a total of 117 steps before the pulses moved back to their starting point; IFG laser pulses were shot only in $\sim 9\%$ of the muon fills, i.e. 1 fill every 11. Firstly, in the last month of Run-4 the rate of IFG laser shots was decreased to 1 fill every 22, in order to increase the percentage of muon fills without laser pulses that could be analyzed. Thanks to a series of preliminary studies that we conducted, it was found that this new rate would still allow to keep the gain fluctuation systematics below the design goal of 20 ppb, given the high statistics of Run-4. Secondly, at the beginning of Run-5 the step between laser pulses was changed: the first laser pulse sweeping from 0 to 50 µs had a step of 0.2 µs with 250 repetitions; the step of the other three lasers pulses was instead set to 1.0 µs, with 250 repetitions. This allowed to finely scan the first microseconds of laser data, where the gain sag shown in Figure 5.2.4 occurs, and extract the exponential parameters from the fit with more accuracy.
For Run-4 and Run-5, the same hardware blinding (secret clock frequency described in Section 4.7.6) was chosen, because it was foreseen that these two runs would be analyzed and published together. Before the beginning of Run-6 data acquisition, it was not known if Run-4/5 and Run-6 would be published separately or together; if we kept the same hardware blinding, we

would have been forced to analyze and publish Run-6 together with Run-4/5, and there were concerns that this could delay the publication, so a different hardware blinding was set for Run-6. These concerns have mitigated since the reconstruction of Run-6 datasets finished a few months after the end of data acquisition, thanks to many upgrades in the production chain (for instance: Run-6 was the only dataset in which the data reconstruction happened in real time with data acquisition). At the time of writing, the proposal to relatively unblind Run-6 with respect to Run-4/5 during the early stages of ω_a is being discussed, and the tools to do so are being implemented: the main advantage is that Run-6 can be combined with the last part of Run-5, since they have the same configuration as shown in Table 8.1.1, increasing the wiggle plot statistics.

8.2 Preliminary ω_a fits and systematic studies

In Figure 5.2.5, we showed the accumulated fit residuals of the exponential fits on laser data, to extract the IFG correction in Run-2/3. The residuals after 30 µs are in the time window of the ω_a analysis, and are well contained within $\pm 10^{-4}$, giving us confidence in the parameters that we used for the IFG correction. A similar plot is shown in Ref. [118] for Run-4. In Run-5, the step of laser pulses in the first 50 µs was changed from 1.5 µs to 0.2 µs, to allow a finer binning of the laser data in the region where most of the gain sag occurs. In Figure 8.2.1, the accumulated residuals are shown for the whole Run-5 dataset, where the finer binning is evident in the first 50 µs and the residuals are still well contained within $\pm 10^{-4}$.

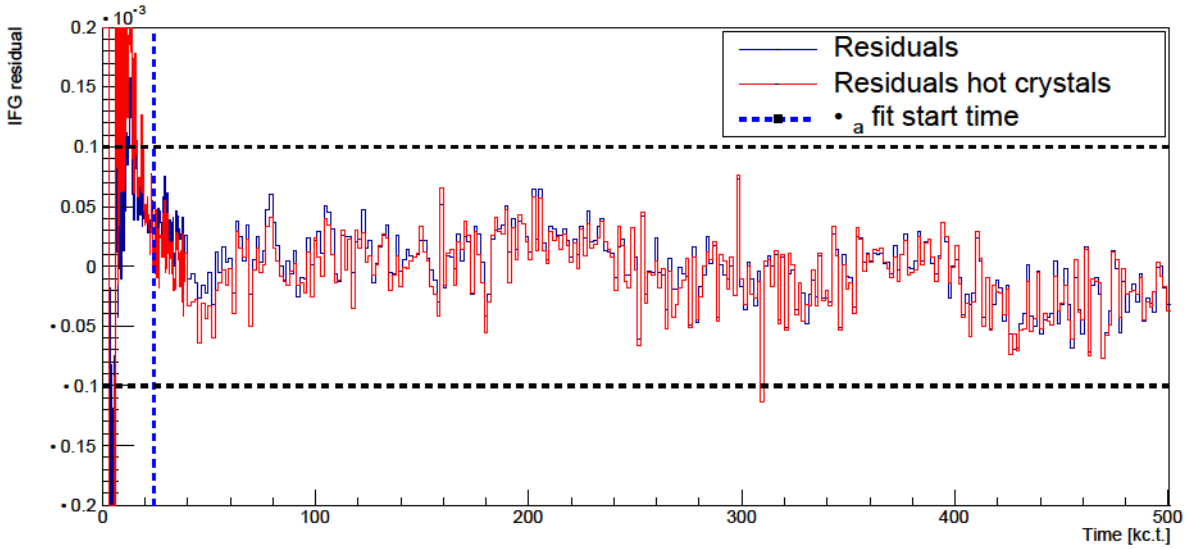

Figure 8.2.1: In-Fill-Gain fit residuals, obtained by summing over the 1296 SiPMs over all the Run-5 dataset. The red histogram shows only the contribution from the 16 "hottest" crystals, which are closest to the beam storage region and therefore detect positrons with a higher rate.

This result gives us confidence that a potentially incorrect calibration of SiPM In-Fill-Gain changes cannot be the main source of the residual slow term, observed in the ω_a analysis. Before the start of Run-4 data reconstruction, it was found that the common pulse fitter of Local/Local $\Delta t'$ and ReconITA reconstructions was missing some crystal hits in the case of two positrons detected within tens of ns. The number of missing hits was proportional to the rate of pileup, and it was partially responsible for the slow term in Run-2/3. The algorithm of the pulse fitter was revisited by its developers in view of Run-4/5/6, in order to overcome the limits observed in the Run-2/3 version. In the ω_aEuropa team, an improved version of

the ReconITA algorithm was being developed in parallel with the Run-2/3 analysis, which was finalized and used for Run-4/5/6 and which also managed to address the issue of missing hits. In the improved version, a new pulse fitting technique is implemented after the first round of pulse fitting and clustering[1]. In the second iteration, the fit on crystal waveforms searches for positron hits using the time constraint of clusters that were found in the first iteration: even if two positrons on the same calorimeter were already clearly separated, the algorithm manages to recover any previously missed hits belonging to the second positron. Thus, the new algorithm further separates pileup clusters that overlap spatially and generate multiple hits on the same SiPM. Figure 8.2.2 shows the new workflow, which is an upgrade in the ω_aEuropa analysis with respect to the Run-2/3 chain shown in Figure 5.1.2. Full details about the new reconstruction are provided in Ref. [118].

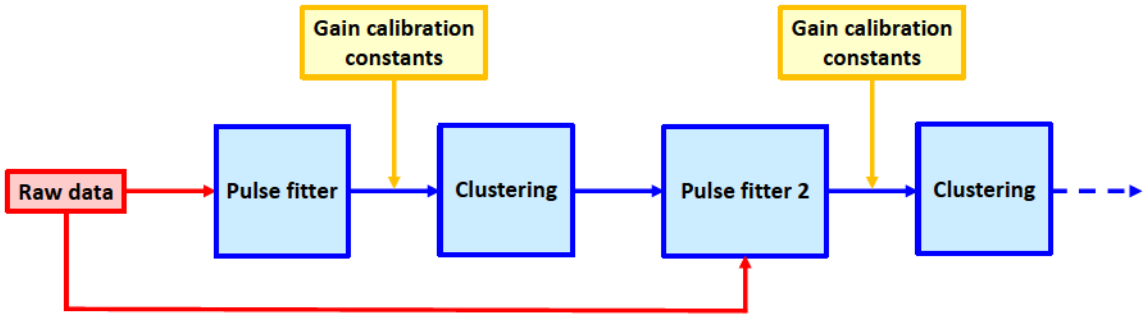

Figure 8.2.2: Run-4/5/6 ω_aEuropa analysis workflow. After the second round of clustering, the workflow continues as in Figure 5.1.2.

To investigate the impact of the new ReconITA reconstruction on the residual slow term effect, a preliminary energy binned analysis on Run-2C data has been performed to extract the behaviour of k_{LM} at high energies. Figure 8.2.3 shows that, with the upgraded ReconITA pulse fitter, k_{LM} is positive up to almost 2500 MeV, and the drift towards negative values is reduced by a factor or $\sim 66\%$. We therefore expect to reduce the systematic associated to the slow term in the Run-4/5/6 result.

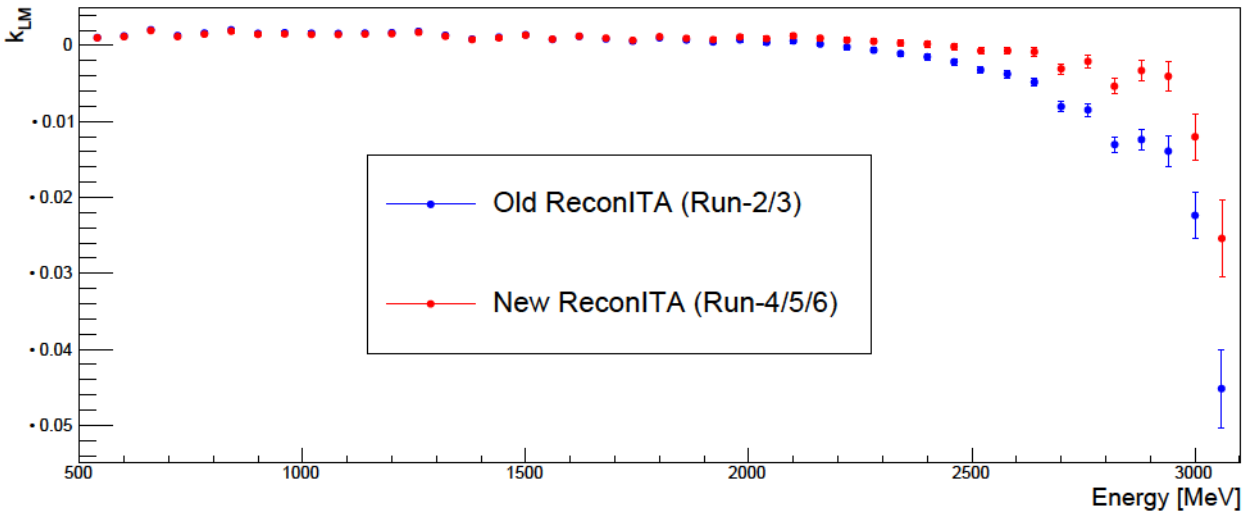

Figure 8.2.3: k_{LM} as a function of the energy in the Run-2C dataset for the old (blue) and new (red) ReconITA analysis. The drift towards negative values is reduced with the improvements that will be used for the Run-4/5/6 reconstruction.

[1]This work constituted one of my main contributions during the first year of PhD.

Since Run-5, the Quad RF technique has greatly suppressed the CBO radial oscillations of the muon beam: this is reflected in the shape of wiggle plots, where the rate of detected positron events is affected by beam dynamics frequencies, so we can also expect a reduction of this systematic contribution to ω_a. Figure 8.2.4 shows the fast fourier transform of residuals when wiggle plots are fitted with the 5-parameter function of Equation (4.7.4), and it compares the Run-3a dataset with the Run-5JK combined datasets. The peak at CBO frequencies is greatly reduced, and this is expected to decrease the systematic uncertainty related to the CBO effect, which is dominant in Run-2/3.

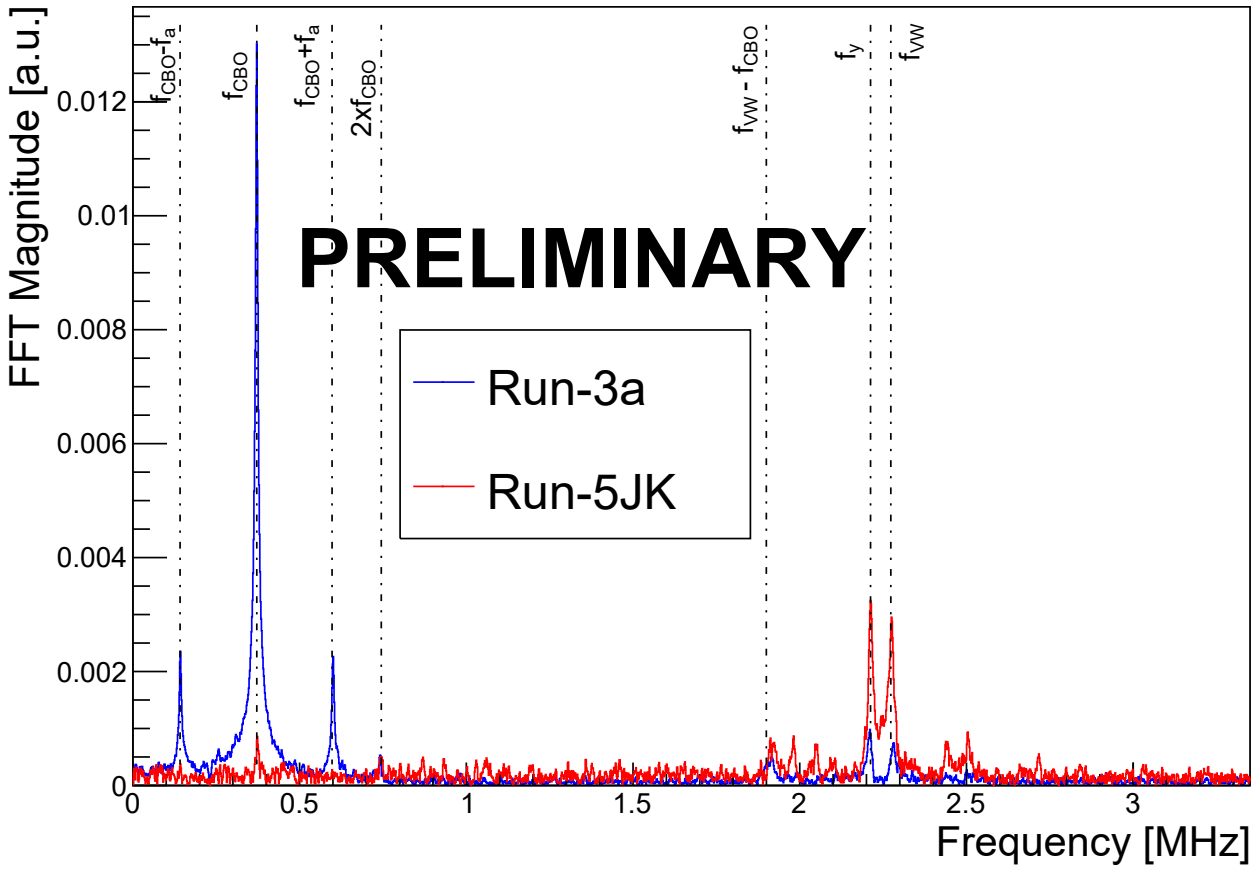

Figure 8.2.4: FFT of residuals with a 5-parameter fit. The peak in the Run-3a FFT (blue) is located at the characteristic CBO frequency. This peak is highly reduced in Run-5 (red). Some peaks near the vertical waist and y-oscillation frequencies are also present. The vertical Quad RF which was turned on in Run-5M is expected to also reduce these peaks.

We currently expect to release our next and final result, based on Run-4/5/6 data, in 2025. The reconstruction of all datasets has recently been completed, and the analyses of ω_a, ω_p and all corrections in Equation (4.7.3) have already started for Run-4/5 data. Two task forces within the ω_a teams were formed to work on the CBO effect and on the residual slow term, which were the largest systematic contributions to Run-2/3. With a collective effort from all analyzers, these effects will be investigated to reduce the systematic error and also to potentially identify new puzzles in the analysis, which might arise due to the different running conditions with respect to Run-2/3 (e.g., the introduction of the Quad RF technique). As explained in Section 8.1, during Run-6 a different hardware blinding than Run-4/5 was used, but a procedure is being developed to analyze Run-6 with the same blinding as Run-4/5 in order to combine data into bigger datasets. The analysis of Run-6 will start as soon as the collaboration will have agreed on this procedure.

Conclusions

The measurement of the muon magnetic anomaly $a_\mu = (g_\mu - 2)/2$, where g_μ is the g-factor of the muon, is a precision test of the Standard Model (SM), where a significant discrepancy between the measurement and the SM prediction has persisted for more than 20 years. The Muon $g-2$ experiment at Fermilab has published two measurements based on the first three years of data taking (Run-1 was published in 2021 and Run-2/3 in 2023), bringing down the precision on the experimental value of a_μ to 190 parts per billion (ppb). The newest result confirms the one from Run-1 in 2021 and the previous one at BNL, bringing the test of SM to unprecedented precision. The discrepancy between the experimental value of a_μ and the 2020 theoretical value recommended by the Theory Initiative White Paper was strengthened to $5.1\,\sigma$.

In this Thesis we presented the analysis of the anomalous precession frequency of the muon, ω_a, for the Run-2/3 result, which was a main ingredient together with the B-field for the measurement of a_μ. The "Ratio-Asymmetry" analysis method, new with respect to Run-1, was developed to analyze the anomalous ω_a frequency and to evaluate the systematic uncertainties: this constituted my major contribution to the Run-2/3 result, and my original work of this Thesis. The results that we presented for the ω_aEuropa analysis team were averaged with the ones from 5 other groups, each with their independent event reconstruction and fitting procedures. We were able to reduce the statistical and sytematic uncertainties on ω_a by a factor of ~ 2.2 with respect to Run-1, achieving 201 ppb and 25 ppb, respectively. Thanks to the improvements on ω_a, on the beam dynamics corrections and on the magnetic field, we were able to measure a_μ to 203 ppb for the combined Run-1/2/3 datasets.

Currently, there are puzzles in the theoretical prediction of a_μ, especially in the leading order hadronic vacuum polarization contribution, a_μ^{HVP-LO}, which prevent a solid comparison with the experimental value. The 2020 White Paper prediction was based on the dispersive approach, that takes e^+e^- to hadrons data as an input. In 2021, the BMW collaboration published a first lattice calculation of a_μ^{HVP-LO} with sub-percent accuracy, which is closer to the experimental value and discrepant with the dispersive approach. While the evaluation of the whole a_μ^{HVP-LO} from the other lattice groups is in progress, an excellent agreement among the different lattice groups is found for the so-called intermediate window observable. Inputs from lattice groups, and analyses of experimental cross sections of e^+e^- to hadrons, should allow to clarify the theoretical situation in the next years, while, on a longer term, new methods like the MUonE experiment currently proposed at CERN should reinforce the theoretical prediction.

On the experimental side, the analysis of Run-4/5/6 data of the Muon $g-2$ experiment at Fermilab has started, and the last result is expected to be published in about 2 years. This will bring down the uncertainty on the experimental measurement of a_μ to the design goal of 140 ppb. In addition, a new experiment at J-PARC (Japan), E34, with a completely different approach, is currently under construction with the goal to start data taking in the next few years. At the same time, progress is expected on the theory side using current and new methods which, hopefully, will clarify the present puzzles.

Appendix A

Schwinger calculation: $a = \alpha/2\pi$

High order, radiative QED predictions for the magnetic anomaly $a_l = (g_l - 2)/2$, where l stands for a generic lepton, can be written as a sum over terms of order $\frac{\alpha}{\pi}$. The first term comes from a 1-loop diagram, it accounts for $\sim 99\%$ of the anomaly and it is universal for all leptons (electron, muon, tau): its Feynman diagram is shown in Figure A.1(c).

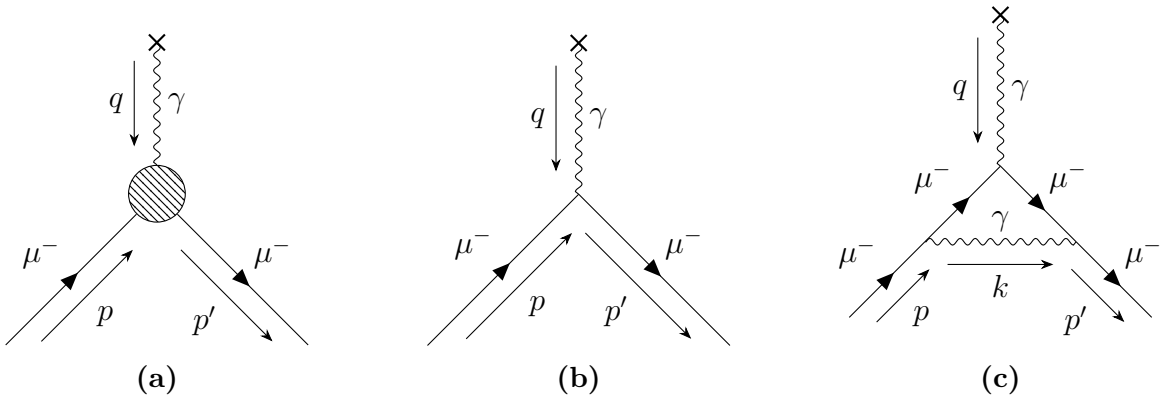

Figure A.1: QED prediction for the muon magnetic anomaly: (a) is the general form of diagrams that contribute to the anomaly, (b) is the tree-order contribution which yields $g = 2$ and (c) is the 1-loop Feynman diagram that leads to the first radiative correction.

Using Feynman rules for QED, the matrix element for the tree-order diagram in Figure A.1(b) is:

$$i\mathcal{M}_{\text{Tree}} = -ie\bar{u}(\vec{p}\,')\gamma^{\mu}u(\vec{p})\tilde{A}_{\mu}(q) \tag{A.1}$$

where $p+q = p'$ and $\tilde{A}_{\mu}(q)$ is the Fourier transform of the classical electromagnetic field $A_{\mu}(x)$. The aim of this calculation is to find a way to express the 1-loop correction to the matrix element as:

$$i\mathcal{M}_{1-\text{loop}} = -ie\bar{u}(\vec{p}\,')\Gamma^{\mu}u(\vec{p})\tilde{A}_{\mu}(q) \tag{A.2}$$

In Equation (A.2), Γ^{μ} can be a function of the muon mass and of the 4-momenta of the incoming and outgoing muon; it cannot contain terms proportional to γ^5 or $\epsilon^{\mu\nu\rho\sigma}$, since QED preserves parity. It can be shown, using Lorentz-invariance, applying Dirac's equation to spinor functions u and $\bar{u}$, recalling Ward identity for QED ($q_{\mu}\Gamma^{\mu} = 0$) and defining $\sigma^{\mu\nu} \equiv \frac{i}{2}[\gamma^{\mu}, \gamma\nu]$, that:

$$\Gamma^{\mu}(p', p) = \gamma^{\mu}F_1(q^2) + \frac{i\sigma^{\mu\nu}q_{\nu}}{2m}F_2(q^2) \tag{A.3}$$

where $F_1(q^2)$ and $F_2(q^2)$ are called "form factors". We will now use Born's approximation that relates $i\mathcal{M}$ to the Fourier transform of the electromagnetic potential $\tilde{V}(\vec{q})$:

$$-2\pi i\tilde{V}(\vec{q})\delta(E(\vec{p}\,') - E(\vec{p})) = (2\pi)^4 i\delta^4(p' - p)\mathcal{M} \tag{A.4}$$

Finally, by exploiting the algebra of γ^μ matrices, combining Equations (A.2) and (A.3), and comparing with Equation (A.4), we can relate $\tilde{V}(\vec{q})$ to the form factors. It can be shown that, taking the inverse Fourier transform and comparing with Equation (1.1.5) for the potential energy, the g-factor can be expressed as:

$$g = 2\left[F_1(0) + F_2(0)\right] \tag{A.5}$$

At tree level, Γ^μ becomes γ^μ (compare Equations (A.1) and (A.2)), so from Equation (A.3) $F_1(0) = 1$ and $F_2(0) = 0$, which predicts $g = 2$. It can be shown, thanks to the Ward identity, that $F_1(0) \equiv 1$ at all perturbation orders; what is left to compute is $F_2(0)$ at 1-loop. The major issue is that Feynman's diagram in Figure A.1(c) contains a divergent integral $\sim \int d^4k/k^4$: the dimensional regularization is one of the possible ways to parametrize the divergence and obtain a simple expression for the form factor $F_2(0)$:

$$F_2^{(1-\text{loop})}(0) = \frac{\alpha}{\pi}\int_0^1 dz \int_0^1 dy \int_0^1 dx\delta(1-x-y-z)\frac{z}{1-z} = \frac{\alpha}{\pi}\int_0^1 z dz = \frac{\alpha}{2\pi} \tag{A.6}$$

Thus the Schwinger term: at 1-loop order, QED predicts that $g = (2 + \frac{\alpha}{\pi})$ and therefore that the magnetic anomaly of electrons, muons and tau particles is $a^{(1-\text{loop})} = \frac{\alpha}{2\pi}$.

It should be mentioned that the diagram in Figure A.1(c) is not the only possible 1-loop diagram when a muon interacts with the magnetic field: Figure A.2 shows the other three possibilities, which however do not contribute to a_μ but only correct the propagators.

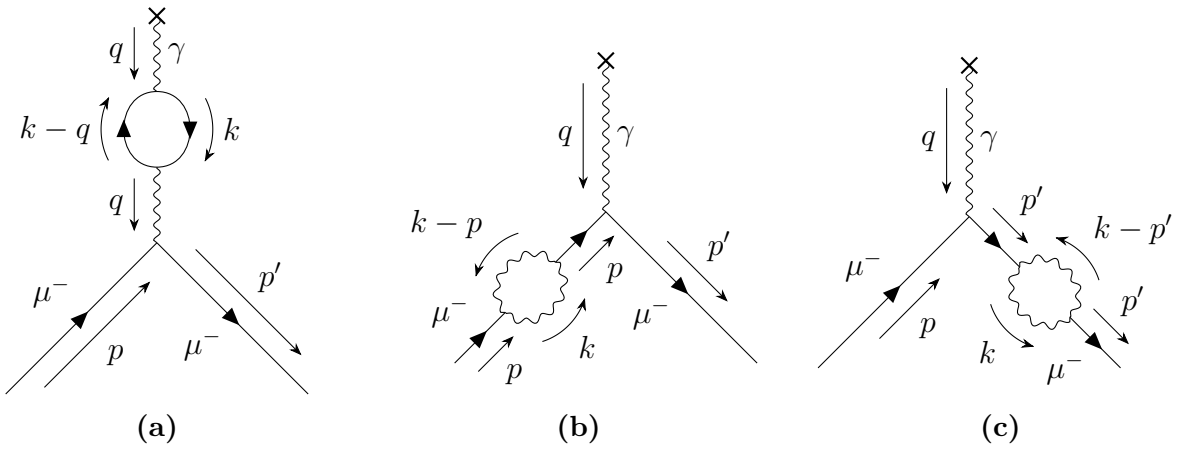

Figure A.2: 1-loop QED diagrams that do not contribute to a_μ: the loop in (a) modifies the photon propagator, the ones in (b) and (c) modify the fermion propagator.

The three diagrams in Figure A.2 can be studied in order to renormalize QED at 1 loop, and the first one (the diagram in Figure A.2(a)) is responsible for the so-called "Vacuum Polarization". This effect is the quantum analogous of the polarization of molecules in a dielectric when an external electric field is applied: the distorted molecules produce an electric field which reduces the external one. The same happens in QED when the interaction between two charges is studied: the photon propagator is affected, at 1-loop order, by virtual pairs of fermion-antifermion that screen and reduce the electromagnetic field felt by charges. The effective potential can be written as $V(r) = \pm\frac{\alpha_{\text{eff}}}{r}$ where the $\pm$ depends on the charges' sign and α_{eff} is a function of the distance r. At large distances, α_{eff} monotonously decreases until, in the limit of $r \to +\infty$, it becomes equal to the fine structure constant α.

Appendix B

Derivation of the Ratio Method to build wiggle plots

The Ratio Method technique consists in randomly splitting positron events into four different sub-groups, so that each one will contain $\sim 25\%$ of the total events. The technique also requires to make an initial guess on the anomalous precession period $T_a \sim 4.365\,\mu s$. For each of the four sub-groups, a histogram is built and filled with the detected times of decay positrons. The first two histograms are labelled $v_{1,2}(t)$ and leave the positron times unchanged, so that the positron time distribution is $N(t)$. The other two are labelled $u_{\pm}(t)$, where the subscript means that the positron times are shifted by $\mp T_a/2$: this is equivalent to say that the time distribution of positron hits for these histograms are $N(t \pm T_a/2)$. This random procedure is called "Quartering" and it depends on an input random seed. Two histograms are then built, $U(t) \equiv u_+(t) + u_-(t)$ and $V(t) \equiv v_1(t) + v_2(t)$, and the ratio histogram is defined as $R(t) \equiv (V(t) - U(t))/(V(t) + U(t))$. Assuming that the time distribution $N(t)$ of positrons is given by a simple 5-parameter function:

$$N(t) = N_0 e^{-t/\gamma\tau} \left[1 + A\cos\left(\omega_a t + \phi\right)\right] \tag{B.1}$$

and choosing $\phi = 0$ without loss of generality, then $R(t)$ is equal to:

$$\begin{aligned} R(t) &= \frac{2N(t) - N(t + T_a/2) - N(t - T_a/2)}{2N(t) + N(t + T_a/2) + N(t - T_a/2)} = \\ &= \frac{e^{-t/\gamma\tau}\left\{\frac{1}{2}\left[1 + A\cos\left(\omega_a t\right)\right] - \frac{1}{4}e^{-T_a/2\gamma\tau}\left[1 + A\cos\left(\alpha\right)\right] - \frac{1}{4}e^{T_a/2\gamma\tau}\left[1 + A\cos\left(\alpha'\right)\right]\right\}}{e^{-t/\gamma\tau}\left\{\frac{1}{2}\left[1 + A\cos\left(\omega_a t\right)\right] + \frac{1}{4}e^{-T_a/2\gamma\tau}\left[1 + A\cos\left(\alpha\right)\right] + \frac{1}{4}e^{T_a/2\gamma\tau}\left[1 + A\cos\left(\alpha'\right)\right]\right\}} \end{aligned} \tag{B.2}$$

where:

$$\begin{aligned} \cos\left(\alpha\right) &\equiv \cos\left(\omega_a t + \frac{2\pi}{T_a} T_a/2\right) = \cos\left(\omega_a t + \pi\right) = -\cos\left(\omega_a t\right) \\ \cos\left(\alpha'\right) &\equiv \cos\left(\omega_a t - \frac{2\pi}{T_a} T_a/2\right) = \cos\left(\omega_a t - \pi\right) = -\cos\left(\omega_a t\right) \end{aligned} \tag{B.3}$$

Equation (B.2) can be simplified and rearranged into:

$$R(t) = \frac{2\left[1 + A\cos\left(\omega_a t\right)\right] - \left[e^{-T_a/2\gamma\tau} + e^{T_a/2\gamma\tau}\right]\left[1 - A\cos\left(\omega_a t\right)\right]}{2\left[1 + A\cos\left(\omega_a t\right)\right] + \left[e^{-T_a/2\gamma\tau} + e^{T_a/2\gamma\tau}\right]\left[1 - A\cos\left(\omega_a t\right)\right]} \tag{B.4}$$

We will now exploit the fact that $T_a/2\gamma\tau \approx 0.034 \ll 1$, to replace the exponentials with their Taylor expansions at second order: $e^{\pm T_a/2\gamma\tau} \approx 1 \pm T_a/2\gamma\tau + \frac{1}{2}\left(T_a/2\gamma\tau\right)^2$. The sum of the

two exponentials becomes $2 + (T_a/2\gamma\tau)^2$ both at the numerator and at the denominator. By defining $\mathcal{C} \equiv \frac{1}{16}\left(T_a/\gamma\tau\right)^2$, the ratio becomes:

$$R(t) \approx \frac{4A\cos\left(\omega_a t\right) - \left(T_a/2\gamma\tau\right)^2\left[1 - A\cos\left(\omega_a t\right)\right]}{4 + \left(T_a/2\gamma\tau\right)^2\left[1 - A\cos\left(\omega_a t\right)\right]} = \frac{A\cos\left(\omega_a t\right) - \mathcal{C}\left[1 - A\cos\left(\omega_a t\right)\right]}{1 + \mathcal{C}\left[1 - A\cos\left(\omega_a t\right)\right]} \tag{B.5}$$

Finally, we can use that:

$$\begin{aligned} \frac{1}{1+x} &\approx 1 - x \qquad\qquad \text{if } |x| \ll 1 \\ \left|\mathcal{C}\left[1 - A\cos\left(\omega_a t\right)\right]\right| &\leq \mathcal{C}(1+A) \leq 2\mathcal{C} \approx 2.9 \cdot 10^{-4} \ll 1 \end{aligned} \tag{B.6}$$

so that Equation (B.5) becomes:

$$\begin{aligned} R(t) &\approx \left\{A\cos\left(\omega_a t\right) - \mathcal{C}\left[1 - A\cos\left(\omega_a t\right)\right]\right\}\left\{1 - \mathcal{C}\left[1 - A\cos\left(\omega_a t\right)\right]\right\} \\ &\approx A\cos\omega_a t + \mathcal{C}A^2\cos^2\omega_a t - \mathcal{C} + \mathcal{O}(\mathcal{C}^2) \end{aligned} \tag{B.7}$$

Since in the R/RA-Methods wiggle plots $A \sim 0.3 \div 0.4$, the term proportional to $\mathcal{C}A^2$ is an order of magnitude smaller than $\mathcal{C}$. Thus, we can approximate the expression in Equation (B.7) with a 4-parameter function (bringing back ϕ):

$$R(t) \approx A\cos\left(\omega_a t + \phi\right) - \mathcal{C} \tag{B.8}$$

where the normalization parameter N_0 and the boosted muon lifetime $\gamma\tau$ from Equation (B.1) are not present anymore: the former was divided out exactly in the ratio, the latter was absorbed by the constant $\mathcal{C}$.

In the R/RA-Methods ω_aEuropa analysis, the wiggle plots were not fitted with the function in Equation (B.8), but with a more complicated one that reproduces the Ratio formula $R(t) = (V(t) - U(t))/(V(t) + U(t))$ and explicitly includes the exponential both at the numerator and at the denominator. This procedure avoids the need to approximate the exponentials with their Taylor expansions, thus eliminating all orders of $\mathcal{C}$.

Appendix C

Run-2/3 representative fit results and correlation matrices

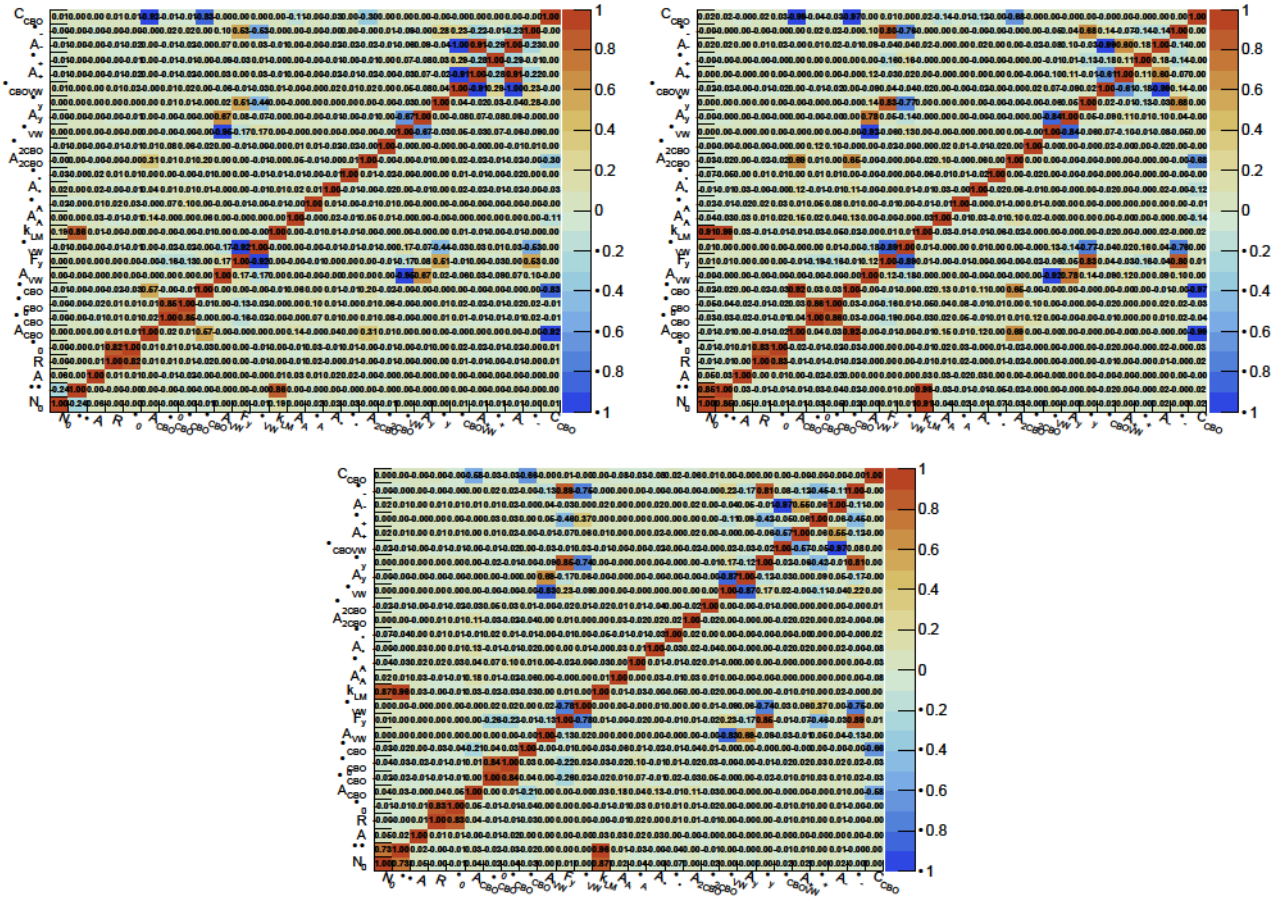

Figure C.1: A-Method correlation matrix between each pair of the 28 free parameters of the ω_aEuropa nominal fits, for Run-2 (top left), Run-3a (top right) and Run-3b (bottom).

Parameter [Unit]	Run-2	Run-3a	Run-3b
$\langle\chi^2/\text{n.d.o.f.}\rangle$	1.01794	1.00498	0.98441
$\langle R\rangle$ [ppm]	-80.571	-71.664	-70.241
σ_R [ppb]	30	30	46
χ^2/n.d.o.f.	4130.03/4127	4139.62/4127	3955.87/4127
p-value	0.48378	0.44192	0.97148
N_0	41953068 ± 717	55740312 ± 1342	22085561 ± 1042
$\gamma\tau$ [µs]	64.430 ± 0.001	64.417 ± 0.003	64.395 ± 0.003
A	0.37598 ± 0.00001	0.378741 ± 0.000011	0.374577 ± 0.000017
R [ppm]	-80.571 ± 0.377	-71.664 ± 0.323	-70.242 ± 0.520
ϕ_0 [rad]	4.11726 ± 0.00006	4.12033 ± 0.00005	4.10754 ± 0.00009
A_{CBO}	0.0035 ± 0.0004	0.0029 ± 0.0002	0.0014 ± 0.0001
ω^0_{CBO} [rad/µs]	2.34119 ± 0.00012	2.32926 ± 0.00013	2.3319 ± 0.0003
ϕ_{CBO} [rad]	6.017 ± 0.010	6.145 ± 0.011	6.08 ± 0.03
τ_{CBO} [µs]	238 ± 51	234 ± 36	93 ± 21
C_{CBO}	0.05 ± 0.13	0.02 ± 0.09	0.45 ± 0.09
A_{VW}	0.0013 ± 0.0003	0.00063 ± 0.00012	0.00047 ± 0.00017
F_y	1.0128 ± 0.0003	1.0121 ± 0.0003	1.0124 ± 0.0007
ϕ_{VW} [rad]	1.09 ± 0.18	0.83 ± 0.17	0.8 ± 0.4
k_{LM}	0.00109 ± 0.00008	-0.0005 ± 0.0004	-0.0006 ± 0.0004
A_A	0.00016 ± 0.00006	0.00009 ± 0.00006	0.00016 ± 0.00007
ϕ_A [rad]	5.6 ± 0.4	4.0 ± 0.7	4.8 ± 0.4
A_ϕ	0.00008 ± 0.00007	0.00008 ± 0.00006	0.00021 ± 0.00008
ϕ_ϕ [rad]	4.0 ± 0.9	4.3 ± 0.7	3.8 ± 0.4
A_{2CBO}	0.00018 ± 0.00005	0.00015 ± 0.00003	0.00003 ± 0.00002
ϕ_{2CBO} [rad]	3.28 ± 0.12	3.44 ± 0.14	1.4 ± 0.6
τ_{VW} [µs]	33.9 ± 4.7	42.2 ± 6.1	34.0 ± 8.2
A_y	0.00033 ± 0.00005	0.00045 ± 0.00005	0.00057 ± 0.00011
ϕ_y [rad]	0.82 ± 0.14	0.83 ± 0.12	0.6 ± 0.3
τ_{CBOVW} [µs]	8.5 ± 2.8	13.4 ± 2.6	22.8 ± 5.4
A_+	0.002 ± 0.003	0.0009 ± 0.0006	0.0003 ± 0.0002
ϕ_+ [rad]	3.6 ± 1.1	0.3 ± 0.4	1.2 ± 0.7
A_-	0.012 ± 0.015	0.004 ± 0.002	0.0016 ± 0.0007
ϕ_- [rad]	4.2 ± 0.2	4.30 ± 0.15	5.5 ± 0.4

Table C.1: T-Method fit results.

Parameter [Unit]	Run-2	Run-3a	Run-3b
$\langle\chi^2/\text{n.d.o.f.}\rangle$	1.02664	0.997004	0.999528
$\langle R\rangle$ [ppm]	-80.626	-71.390	-70.396
σ_R [ppb]	35	26	48
χ^2/n.d.o.f.	4225.91/4127	3981.24/4127	4154.14/4127
p-value	0.13842	0.94699	0.38003
N_0	20140739 ± 299	27021394 ± 562	10487162 ± 431
$\gamma\tau$ [µs]	64.430 ± 0.001	64.415 ± 0.003	64.392 ± 0.003
A	0.36064 ± 0.00001	0.36252 ± 0.00001	0.361262 ± 0.000015
R [ppm]	-80.628 ± 0.337	-71.393 ± 0.291	-70.397 ± 0.468
ϕ_0 [rad]	4.11775 ± 0.00006	4.12089 ± 0.00005	4.10803 ± 0.00008
A_{CBO}	0.0037 ± 0.0002	0.00294 ± 0.00016	0.00136 ± 0.00008
ω^0_{CBO} [rad/µs]	2.34122 ± 0.00010	2.32920 ± 0.00010	2.3318 ± 0.0003
ϕ_{CBO} [rad]	6.027 ± 0.008	6.143 ± 0.009	6.10 ± 0.02
τ_{CBO} [µs]	242 ± 27	213 ± 24	88 ± 18
C_{CBO}	0.04 ± 0.07	0.09 ± 0.07	0.47 ± 0.08
A_{VW}	0.0014 ± 0.0002	0.00075 ± 0.00012	0.00041 ± 0.00015
F_y	1.0127 ± 0.0003	1.0123 ± 0.0002	1.0112 ± 0.0005
ϕ_{VW} [rad]	1.10 ± 0.15	0.88 ± 0.15	1.8 ± 0.3
k_{LM}	0.00106 ± 0.00007	-0.0009 ± 0.0003	-0.0009 ± 0.0003
A_A	0.00037 ± 0.00006	0.00013 ± 0.00004	0.00015 ± 0.00007
ϕ_A [rad]	6.11 ± 0.15	0.41 ± 0.36	5.5 ± 0.4
A_ϕ	0.00010 ± 0.00006	0.00011 ± 0.00005	0.00012 ± 0.00007
ϕ_ϕ [rad]	4.1 ± 0.6	4.3 ± 0.4	4.3 ± 0.5
A_{2CBO}	0.00016 ± 0.00003	0.00013 ± 0.00002	0.000023 ± 0.000019
ϕ_{2CBO} [rad]	3.25 ± 0.12	3.60 ± 0.12	2.3 ± 0.8
τ_{VW} [µs]	32.4 ± 3.9	38.0 ± 4.6	34.7 ± 7.9
A_y	0.00029 ± 0.00005	0.00045 ± 0.00004	0.00045 ± 0.00008
ϕ_y [rad]	0.89 ± 0.13	0.78 ± 0.11	0.06 ± 0.20
τ_{CBOVW} [µs]	7.7 ± 2.5	14.6 ± 2.7	31.0 ± 8.1
A_+	0.002 ± 0.004	0.0003 ± 0.0003	0.00018 ± 0.00011
ϕ_+ [rad]	3.3 ± 1.3	0.1 ± 0.8	3.4 ± 0.6
A_-	0.012 ± 0.016	0.0032 ± 0.0015	0.0009 ± 0.0003
ϕ_- [rad]	4.2 ± 0.2	4.43 ± 0.14	4.9 ± 0.3

Table C.2: A-Method fit results.

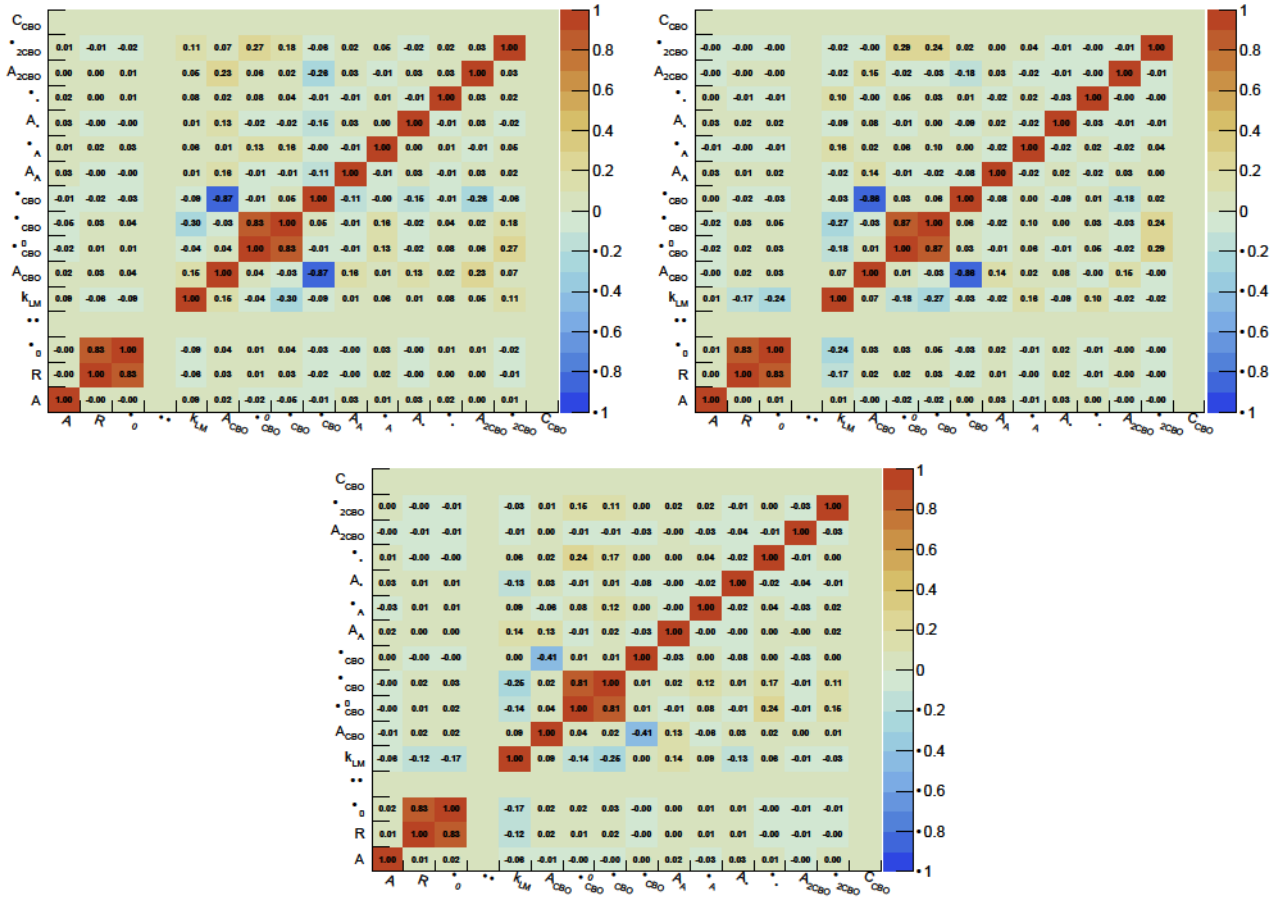

Figure C.2: RA-Method correlation matrix between each pair of the 14 free parameters of the ω_aEuropa nominal fits, for Run-2 (top left), Run-3a (top right) and Run-3b (bottom). The $\gamma\tau$ and C_{CBO} parameters are fixed in our fits, thus there is no entry in the correlation matrices

Parameter [Unit]	Run-2	Run-3a	Run-3b
$\langle\chi^2/\text{n.d.o.f.}\rangle$	0.996037	1.00563	1.0003
$\langle R\rangle$ [ppm]	-80.562	-71.667	-70.253
σ_R [ppb]	86	76	121
χ^2/n.d.o.f.	4118.38/4141	4119.15/4141	4132.35/4141
p-value	0.59549	0.59219	0.53498
$\gamma\tau$ [µs]	64.430 (fixed)	64.417 (fixed)	64.395 (fixed)
A	0.36971 ± 0.00001	0.37242 ± 0.00001	0.368331 ± 0.000017
R [ppm]	-80.563 ± 0.383	-71.667 ± 0.334	-70.255 ± 0.533
ϕ_0 [rad]	4.11763 ± 0.00006	4.12069 ± 0.00006	4.10790 ± 0.00009
A_{CBO}	0.00343 ± 0.00013	0.00280 ± 0.00010	0.00108 ± 0.00012
ω^0_{CBO} [rad/µs]	2.3414 ± 0.0004	2.32920 ± 0.00010	2.3310 ± 0.0010
ϕ_{CBO} [rad]	5.97 ± 0.04	6.180 ± 0.038	6.03 ± 0.09
τ_{CBO} [µs]	210 ± 21	234 ± 25	236 ± 118
C_{CBO}	0.05 (fixed)	0.02 (fixed)	0.45 (fixed)
k_{LM}	0.005 ± 0.023	-0.001 ± 0.013	0.014 ± 0.016
A_A	0.00018 ± 0.00010	0.00021 ± 0.00008	0.00008 ± 0.00009
ϕ_A [rad]	5.2 ± 0.5	3.6 ± 0.4	4.92 ± 1.00
A_ϕ	0.0003 ± 0.0001	0.00026 ± 0.00009	0.00011 ± 0.00009
ϕ_ϕ [rad]	4.6 ± 0.3	4.2 ± 0.3	3.39 ± 0.99
A_{2CBO}	0.00015 ± 0.00003	0.00011 ± 0.00003	0.000017 ± 0.000016
ϕ_{2CBO} [rad]	3.36 ± 0.19	3.7 ± 0.2	3.39 ± 0.99

Table C.3: R-Method fit results.

Parameter [Unit]	Run-2	Run-3a	Run-3b
$\langle\chi^2/\text{n.d.o.f.}\rangle$	0.999067	1.00046	0.997689
$\langle R\rangle$ [ppm]	-80.583	-71.435	-70.368
σ_R [ppb]	85	62	123
χ^2/n.d.o.f.	4191.42/4141	4184.78/4141	4106.18/4141
p-value	0.28804	0.31323	0.64668
$\gamma\tau$ [µs]	64.430 (fixed)	64.415 (fixed)	64.392 (fixed)
A	0.35479 ± 0.00001	0.35641 ± 0.00001	0.355156 ± 0.000015
R [ppm]	-80.583 ± 0.345	-71.435 ± 0.301	-70.369 ± 0.480
ϕ_0 [rad]	4.11815 ± 0.00006	4.12125 ± 0.00005	4.10840 ± 0.00008
A_{CBO}	0.00362 ± 0.00011	0.00272 ± 0.00008	0.0016 ± 0.0002
ω^0_{CBO} [rad/µs]	2.3415 ± 0.0003	2.3292 ± 0.0004	2.3322 ± 0.0009
ϕ_{CBO} [rad]	6.05 ± 0.03	6.17 ± 0.03	6.14 ± 0.08
τ_{CBO} [µs]	228 ± 19	222 ± 21	56 ± 18
C_{CBO}	0.04 (fixed)	0.09 (fixed)	0.47 (fixed)
k_{LM}	0.013 ± 0.019	-0.008 ± 0.011	-0.007 ± 0.014
A_A	0.00033 ± 0.00008	0.00016 ± 0.00007	0.00015 ± 0.00012
ϕ_A [rad]	6.1 ± 0.3	6.1 ± 0.4	0.51 ± 0.77
A_ϕ	0.00042 ± 0.00009	0.00025 ± 0.00007	0.00043 ± 0.00014
ϕ_ϕ [rad]	4.3 ± 0.2	4.3 ± 0.3	3.86 ± 0.28
A_{2CBO}	0.00016 ± 0.00002	0.000103 ± 0.000018	0.000016 ± 0.000030
ϕ_{2CBO} [rad]	3.05 ± 0.15	3.5 ± 0.2	3.2 ± 1.8

Table C.4: RA-Method fit results.

Acknowledgements

My deepest gratitude goes to my supervisor, Professor Graziano Venanzoni, who has been mentoring me since I joined the Muon $g-2$ experiment in 2020 as an undergraduate student. He has followed my work very closely during all these years, and he has always encouraged me to pursue personal growth in my scientific activities. I have learnt much and I still have a lot to learn from his teachings and his example, and for this I really have to thank him.
I would also like to thank Professor Giovanni Batignani, who first inspired me during his lectures when I was a Bachelor's student, and who has followed my PhD work with interest and constant encouragements in the past three years.

There are many, many other people that I encountered during my PhD journey and who have helped me so much in my research. First of all, the Italian Muon $g-2$ group, where Professors Marco Incagli and Alberto Lusiani have coordinated many aspects of the analysis and service work that I have performed in the experiment. My fellow PhD colleagues in Italy have been a great source of support throughout these years: it wouldn't have been such a fantastic experience without Elia Bottalico, Paolo Girotti, Riccardo Nunzio Pilato and Matteo Sorbara. I have also encountered many people at Fermilab who have cheered me up during the most challenging times, so I would like to thank (in no particular order) Stella Critelli, Martina Zanzi, Esra and Mete Yucel, Sudeshna Ganguly and Meghna Bhattacharya (my beloved "mother" and "sister" at Fermilab) and Micol, and everyone I have spent a great time with in Chicago. There are people who have helped me greatly during specific roles that I took up in the experiment, such as the Run-5/6 OPS managers when I was a Run Coordinator, the offline team when I signed up for DQC expert shifts, and my fellow early-career representatives since I was elected as one.

I have to dedicate a special "thank you" section to Dr Anna Driutti, I cannot thank her enough for all that she has done to help me. She has been the best office mate I could ever hope for; she constantly encourages me, she dedicates so much time to tutor me and, thanks to her great experience as a former OPS manager, analyzer, offline expert and - more in general - a passionate particle physics researcher, her help has been invaluable to me.

I want to thank my family, in Italy and in Australia, and all of my friends, the drama classes groups I joined and the high school mates whom I have kept in touch with, for always supporting me in everything. I am glad that, during the PhD years, I have kept in touch with my University colleagues (the "Fisici bestiali" group); in particular Francesco Garosi, whose passion and dedication to theoretical physics have very often supported me in my research. I have made many friends during the PhD school as well, especially Namitha Chithirasreemadam, Giuseppe Di Somma and Emma Hess, and in general all the "Contralini" group.
And last, but not least, I want to thank my beloved Alessio who's a truly wonderful person to be with. It was a blessing to meet you and fill my heart with so much love.

This work was supported in part by the US DOE, Fermilab, the Istituto Nazionale di Fisica Nucleare (Italy) and the European Union Horizon 2020 research and innovation programme under the Marie Skłodowska-Curie grant agreements No. 101006726, No. 734303.

Bibliography

[1] B. Abi *et al.* (Muon $g-2$ Collaboration), Measurement of the Positive Muon Anomalous Magnetic Moment to 0.46 ppm, Phys. Rev. Lett. **126**, 141801 (2021).

[2] G. W. Bennett *et al.* (Muon $g-2$ Collaboration), Final Report of the Muon E821 Anomalous Magnetic Moment Measurement at BNL, Phys. Rev. D **73**, 072003 (2006).

[3] D. P. Aguillard *et al.* (Muon $g-2$ Collaboration), Measurement of the Positive Muon Anomalous Magnetic Moment to 0.20 ppm, Phys. Rev. Lett. **131**, 161802 (2023).

[4] J. Grange *et al.* (Muon $g-2$ Collaboration), Muon $g-2$ Technical Design Report, arXiv:1501.06858 [physics.ins-det] (2015).

[5] T. Aoyama *et al.*, The anomalous magnetic moment of the muon in the Standard Model, Phys. Rep. **887**, 1 (2020).

[6] Sz. Borsanyi *et al.*, Leading hadronic contribution to the muon magnetic moment from lattice QCD, Nature **593**, 51 (2021).

[7] F. V. Ignatov *et al.*, Measurement of the $e^+e^- \to \pi^+\pi^-$ cross section from threshold to 1.2 GeV with the CMD-3 detector, arxiv:2302.08834 [hep-ex] (2023).

[8] W. Gerlach and O. Stern, Das magnetische Moment des Silberatoms, Zeitschrift für Physik **9**, 353 (1922).

[9] T. E. Phipps and J. B. Taylor, The Magnetic Moment of the Hydrogen Atom, Phys. Rev. **29**, 309 (1927).

[10] P. A. M. Dirac, The Quantum Theory of the Electron, Proceedings of the Royal Society A, **117**, 610 (1928).

[11] P. Zeeman, The Effect of Magnetisation on the Nature of Light Emitted by a Substance, Nature **55**, 347 (1897).

[12] A. A. Michelson and E. W. Morley, On a method of making the wave-length of sodium light the actual and practical standard of length, The London, Edinburgh, and Dublin Philosophical Magazine and Journal of Science, **24**, 463 (1928).

[13] W. E. Lamb and R. C. Retherford, Fine Structure of the Hydrogen Atom by a Microwave Method, Phys. Rev. **72**, 241 (1947).

[14] P. Kusch and H. M. Foley, Precision Measurement of the Ratio of the Atomic 'g Values' in the $^2P_{3/2}$ and $^2P_{1/2}$ States of Gallium, Phys. Rev. **72**, 1256 (1947).

[15] J. E. Nafe, E. B. Nelson and I. I. Rabi, The Hyperfine Structure of Atomic Hydrogen and Deuterium, Phys. Rev. **71**, 914 (1947).

[16] D. E. Nagle, R. S. Julian and J. R. Zacharias, The Hyperfine Structure of Atomic Hydrogen and Deuterium, Phys. Rev. **72**, 971 (1947).

[17] G. Breit, Does the Electron Have an Intrinsic Magnetic Moment?, Phys. Rev. **72**, 984 (1947) and erratum.

[18] J. S. Schwinger, On Quantum-Electrodynamics and the Magnetic Moment of the Electron, Phys. Rev. **73**, 416 (1948).

[19] R. L. Workman *et al.* (Particle Data Group), Prog. Theor. Exp. Phys. **2022**, 083C01 (2022) and 2023 update.

[20] X. Fan, T. G. Myers, B. A. D. Sukra and G. Gabrielse, Measurement of the Electron Magnetic Moment, Phys. Rev. Lett. **130**, 071801 (2023).

[21] J. Abdallah *et al.* (DELPHI Collaboration), Study of tau-pair production in photon-photon collisions at LEP and limits on the anomalous electromagnetic moments of the tau lepton, Eur. Phys. J. C **35**, 159 (2004).

[22] J. Fu *et al*, Novel Method for the Direct Measurement of the τ Lepton Dipole Moments, Phys. Rev. Lett. **123**, 011801 (2019).

[23] P. Bühler, N. Burmasov, R. Lavička and E. Kryshen, Feasibility study of tau-lepton anomalous magnetic moment measurements with ultra-peripheral collisions at the LHC, EPJ Web of Conferences **262**, 01021 (2022).

[24] L. J. Thomas, The Motion of the Spinning Electron, Nature **117**, 514 (1926).
L. J. Thomas, The kinematics of an electron with an axis, Philos. Mag. **3**, 1 (1927).

[25] V. Bargmann, L. Michel and V. L. Telegdi, Precession of the Polarization of Particles Moving in a Homogeneous Electromagnetic Field, Phys. Rev. Lett. **2**, 435 (1959).
J. D. Jackson, Classical Electrodynamics, 3$^{\text{rd}}$ edition, Wiley, New York (1999).

[26] G. W. Bennett *et al.*, Statistical equations and methods applied to the precision muon $(g-2)$ experiment at BNL, Nucl. Instrum. Meth. A **579**, 1096 (2007).

[27] F. Jegerlehner and A. Nyffeler, The muon $g-2$, Phys. Rep. **477**, 1 (2009).

[28] S. Laporta and E. Remiddi, The analytical value of the electron $(g-2)$ at order α^3 in QED, Phys. Lett. B **379**, 283 (1996).

[29] T. Kinoshita and W. B. Lindquist, Eighth-Order Anomalous Magnetic Moment of the Electron, Phys. Rev. Lett. **47**, 1573 (1981).
T. Kinoshita, B. Nižić and Y. Okamoto, Improved Theory of the Muon Anomalous Magnetic Moment, Phys. Rev. Lett. **52**, 717 (1984).
T. Aoyama, M. Hayakawa, T. Kinoshita and M. Nio, Complete Tenth-Order QED Contribution to the Muon $g-2$, Phys. Rev. Lett. **109**, 111808 (2012).

[30] L. Morel, Z. Yao, P. Cladé and S. Guellati-Khélifa, Determination of the fine-structure constant with an accuracy of 81 parts per trillion, Nature **588**, 61 (2020).

[31] R. H. Parker *et al.*, Measurement of the fine-structure constant as a test of the Standard Model, Science **360**, 191 (2018).

[32] A. Keshavarzi, K. S. Khaw and T. Yoshioka, Measurement of the fine-structure constant as a test of the Standard Model, Nucl. Phys. B **975**, 115675 (2022).

[33] R. Jackiw and S. Weinberg, Weak-Interaction Corrections to the Muon Magnetic Moment and to Muonic-Atom Energy Levels, Phys. Rev. D **5**, 2396 (1972).
W. A. Bardeen, R. Gastmans and B. Lautrup, Static quantities in Weinberg's model of weak and electromagnetic interactions, Nucl. Phys. B **46**, 319 (1972).
I. Bars and M. Yoshimura, Muon Magnetic Moment in a Finite Theory of Weak and Electromagnetic Interactions, Phys. Rev. D **6**, 374 (1972).
G. Altarelli, N. Cabibbo and L. Maiani, The Drell-Hearn sum rule and the lepton magnetic moment in the Weinberg model of weak and electromagnetic interactions, Phys. Lett. B **40**, 415 (1972).
K. Fujikawa, B. W. Lee and A. I. Sanda, Generalized Renormalizable Gauge Formulation of Spontaneously Broken Gauge Theories, Phys. Rev. D **6**, 2923 (1972).

[34] T. Ishikawa, N. Nakazawa and Y. Yasui, Numerical calculation of the full two-loop electroweak corrections to muon $(g-2)$, Phys. Rev. D **99**, 073004 (2019).

[35] F. Jegerlehner, The Anomalous Magnetic Moment of the Muon, Springer Tracts in Modern Physics **274** (2017).

[36] C. Bouchiat and L. Michel, La résonance dans la diffusion méson π- méson π et le moment magnétique anormal du méson π, J. Phys. Radium **22**, 121 (1961).
M. Gourdin and E. de Rafael, Hadronic contributions to the muon g-factor, Nucl. Phys. B **10**, 667 (1969).

[37] N. N. Achasov and A. V. Kiselev, Contribution to muon $g-2$ from $\pi^0\gamma$ to and $\eta\gamma$ intermediate states in the vacuum polarization, Phys. Rev. D **65**, 097302 (2002).

[38] A. Keshavarzi, D. Nomura, and T. Teubner, Muon $g-2$ and $\alpha(M_Z^2)$: A new data-based analysis, Phys. Rev. D **97**, 114025 (2018).

[39] M. Davier, A. Höcker, B. Malaescu and Z. Zhang, A new evaluation of the hadronic vacuum polarisation contributions to the muon anomalous magnetic moment and to $\alpha(m_Z^2)$, Eur. Phys. J. C **80**, 241 (2020).

[40] A. Keshavarzi, D. Nomura, and T. Teubner, $g-2$ of charged leptons, $\alpha(M_Z^2)$, and the hyperfine splitting of muonium, Phys. Rev. D **101**, 014029 (2020).

[41] R. N. Pilato, Feasibility study of the MUonE experiment, PhD Thesis, University of Pisa, 2022.

[42] B. E. Lautrup, A. Peterman and E. de Rafael, Recent developments in the comparison between theory and experiments in quantum electrodynamics, Phys. Rep. **3**, 193 (1972).

[43] T. Blum, Lattice Calculation of the Lowest-Order Hadronic Contribution to the Muon Anomalous Magnetic Moment, Phys. Rev. Lett. **91**, 052001 (2003).

[44] D. Bernecker and H. B. Meyer, Vector correlators in lattice QCD: Methods and applications, Eur. Phys. J. A **47**, 148 (2011).

[45] M. Della Morte *et al.*, The hadronic vacuum polarization contribution to the muon $g-2$ from lattice QCD, JHEP10, 020 (2017).

[46] T. Blum *et al.*, Calculation of the Hadronic Vacuum Polarization Contribution to the Muon Anomalous Magnetic Moment, Phys. Rev. Lett. **121**, 022003 (2018).

[47] G Colangelo *et al.*, Prospects for precise predictions of a_μ in the Standard Model, arXiv:2203.15810v1 [hep-ph] (2022).

[48] G. Colangelo, Hadronic contributions to $(g-2)_\mu$, Contribution to NePSi 2023, Pisa (Italy).

[49] M. Cè, The hadronic running of the electroweak couplings from lattice QCD and the connection with $(g-2)_\mu$, Contribution to ICHEP 2022, Bologna (Italy).

[50] P. Athron *et al.*, New physics explanations of a_μ in light of the FNAL muon $g-2$ measurement, JHEP09, 080 (2021).

[51] CDF collaboration *et al.*, High-precision measurement of the W boson mass with the CDF II detector, Science **376**, 170 (2022).

[52] P. Athron *et al.*, Hadronic uncertainties versus new physics for the W boson mass and Muon $g-2$ anomalies, Nature Communications **14**:659 (2023).

[53] B. Quinn (on behalf of the Muon $g-2$ collaboration), CPT- and Lorentz-Violation Tests with Muon $g-2$, Proceedings of CPT'19, 2019.

[54] B. Yu (on behalf of the Muon $g-2$ collaboration), Dark Matter Search in the Muon $g-2$ experiment at Fermilab, New Perspectives Conference at Fermilab, 2023.

[55] M. Pospelov, Secluded U(1) below the weak scale, Phys. Rev. D **80**, 095002 (2009).

[56] A. J. Krasznahorkay *et al.*, Observation of Anomalous Internal Pair Creation in ^{8}Be: A Possible Indication of a Light, Neutral Boson, Phys. Rev. Lett. **116**, 042501 (2016).

[57] B. Wojtsekhowski *et al.*, Searching for a dark photon: project of the experiment at VEPP-3, JINST **13**, P02021 (2018).

[58] M. Fabbrichesi, E. Gabrielli, and G. Lanfranchi, The Physics of the Dark Photon: A Primer, Springer Cham (2021).

[59] D. Banerjee *et al.* (NA64 Collaboration), Dark Matter Search in Missing Energy Events with NA64, Phys. Rev. Lett. **123**, 121801 (2019).

[60] G. Mohlabeng, Revisiting the dark photon explanation of the muon anomalous magnetic moment, Phys. Rev. D **99**, 115001 (2019).
A. M. Abdullahi, M. Hostert, D. Massaro and S. Pascoli, Semivisible dark photon phenomenology at the GeV scale, Phys. Rev. D **108**, 015032 (2023).

[61] G. W. Bennett *et al.* (Muon $g-2$ Collaboration), Improved limit on the muon electric dipole moment, Phys. Rev. D **80**, 052008 (2009).

[62] J. L. Feng, K. T. Matchev and Y. Shadmi, Theoretical expectations for the muon's electric dipole moment, Nucl. Phys. B **613**, 366 (2001).

[63] G. F. Giudice, P. Paradisi and M. Passera, Testing new physics with the electron $g-2$, JHEP11, 113 (2012).
A. Crivellin, M. Hoferichter and P. Schmidt-Wellenburg, Combined explanations of $(g-2)_{\mu,e}$ and implications for a large muon EDM, Phys. Rev. D **98**, 113002 (2018).

[64] R. Chislett (on behalf of the Muon $g-2$ collaboration), The muon EDM in the $g-2$ experiment at Fermilab, EPJ Web of Conferences **118**, 01005 (2016).

[65] Y. K. Semertzidis *et al.*, Sensitive Search for a Permanent Muon Electric Dipole Moment, Proceedings of HIMUS99, 1999.
F. J. M. Farley *et al.*, New Method of Measuring Electric Dipole Moments in Storage Rings, Phys. Rev. Lett. **93**, 052001 (2004).

[66] M. Abe *et al.*, A new approach for measuring the muon anomalous magnetic moment and electric dipole moment, Progress of Theoretical and Experimental Physics **2019**, 053C02 (2019).

[67] A. Adelmann *et al.*, Search for a muon EDM using the frozen-spin technique, arXiv:2102.08838 [hep-ex] (2021).

[68] L. Di Luzio, A. Masiero, P. Paradisi and M. Passera, New physics behind the new muon $g-2$ puzzle?, Phys. Lett. B **829**, 137037 (2022).

[69] G. Abbiendi *et al.*, Measuring the leading hadronic contribution to the muon $g-2$ via μe scattering, Eur. Phys. J. C **77**, 139 (2017).

[70] C. M. Carloni Calame, M. Passera, L. Trentadue and G. Venanzoni, A new approach to evaluate the leading hadronic corrections to the muon $g-2$, Phys. Lett. B **746**, 325 (2015).

[71] R. N. Pilato, The MUonE experiment: μ-e elastic scattering as a key to understand the muon $g-2$ puzzle, PoS (EPS-HEP2023) **449**, 305 (2024).

[72] T. D. Lee and C. N. Yang, Question of Parity Conservation in Weak Interactions, Phys. Rev. **104**, 254 (1956) and erratum.

[73] C. S. Wu *et al.*, Experimental Test of Parity Conservation in Beta Decay, Phys. Rev. **105**, 1413 (1957).

[74] R. L. Garwin, L. M. Lederman and M. Weinrich, Observations of the Failure of Conservation of Parity and Charge Conjugation in Meson Decays: the Magnetic Moment of the Free Muon, Phys. Rev. **105**, 1415 (1957).

[75] J. M. Cassels *et al.*, Experiments with a Polarized Muon Beam, Proceedings of the Physical Society A, **70**, 543 (1957).

[76] B. L. Roberts, The history of the muon $(g-2)$ experiments, SciPost Physics Proceedings, **1**, 032 (2018).

[77] R. L. Garwin, D. P. Hutchinson, S. Penman and G. Shapiro, Accurate Determination of the μ^+ Magnetic Moment, Phys. Rev. **118**, 271 (1960).

[78] D. P. Hutchinson, J. Menes, G. Shapiro and A. M. Patlach, Magnetic Moment of the Positive Muon, Phys. Rev. **131**, 1351 (1963).

[79] A. A. Schupp, R. W. Pidd and H. R. Crane, Measurement of the g Factor of Free, High-Energy Electrons, Phys. Rev. **121**, 1 (1961).

[80] G. Charpak *et al.*, Measurement of the Anomalous Magnetic Moment of the Muon, Phys. Rev. Lett. **6**, 128 (1961).

[81] G. Charpak *et al.*, A new measurement of the anomalous magnetic moment of the muon, Phys. Lett. **1**, 16 (1962).

[82] J. Bailey *et al.*, Precise measurement of the anomalous magnetic moment of the muon, Il Nuovo Cimento A **9**, 369 (1972).

[83] J. Bailey *et al.*, Precision measurement of the anomalous magnetic moment of the muon, Phys. Lett. B **28**, 287 (1968).

[84] J. Aldins, T. Kinoshita, S. J. Brodsky and A. J. Dufner, Photon-Photon Scattering Contribution to the Sixth-Order Magnetic Moment of the Muon, Phys. Rev. Lett. **23**, 441 (1969).
J. Aldins, S. J. Brodsky, A. J. Dufner and T. Kinoshita, Photon-Photon Scattering Contribution to the Sixth-Order Magnetic Moments of the Muon and Electron, Phys. Rev. D **1**, 2378 (1970).

[85] J. Bailey *et al.* (CERN Muon Storage Ring Collaboration), New measurement of (g-2) of the Muon, Phys. Lett. B **55**, 420 (1975).
J. Bailey *et al.* (CERN-Mainz-Daresbury Collaboration), Final report on the CERN muon storage ring including the anomalous magnetic moment and the electric dipole moment of the muon, and a direct test of relativistic time dilation, Nucl. Phys. B **150**, 1 (1979).

[86] D. H. Brown *et al.*, A New Precision Measurement of the Muon $g-2$ Value at the level of 0.35 ppm, Design Report BNL AGS E821, 3$^{\text{rd}}$ edition, 1995.

[87] J. M. Paley, Measurement of the anomalous magnetic moment of the negative muon to 0.7 parts per million, PhD Thesis, Boston University, 2004.

[88] H. N. Brown *et al.* (Muon $g-2$ Collaboration), Precise Measurement of the Positive Muon Anomalous Magnetic Moment, Phys. Rev. Lett. **86**, 2227 (2001).

[89] R. M. Carey *et al.* (New $g-2$ Collaboration), The New $(g-2)$ Experiment: A Proposal to Measure the Muon Anomalous Magnetic Moment to ± 0.14 ppm Precision, FERMILAB-PROPOSAL-0989 (2009).

[90] G. Venanzoni (on behalf of the Fermilab E989 collaboration), The New Muon $g-2$ experiment at Fermilab, Nuclear and Particle Physics Proceedings **273-275**, 584 (2016).
News on the Muon g-2 website, 2019.

[91] T. Mibe, Status of the experiment, Contribution to the 26$^{\text{th}}$ muon $g-2$/EDM collaboration meeting (J-PARC).

[92] M. Otani, First muon acceleration and muon linear accelerator for measuring the muon anomalous magnetic moment and electric dipole moment, Progress of Theoretical and Experimental Physics **2022**, 052C01 (2022).

[93] E. Preosti and D. Stratakis, Negative muon count for the Fermilab Muon Campus accelerator, Nucl. Instrum. Meth. A **1040**, 167082 (2022).

[94] N. S. Froemming *et al.* (on behalf of the Fermilab E989 collaboration), Commissioning the Superconducting Magnetic Inflector System for the Muon $g-2$ Experiment, Proceedings of IPAC2018, 2018.

[95] A. P. Schreckenberger *et al.*, The fast non-ferric kicker system for the Muon $g-2$ Experiment at Fermilab, Nucl. Instrum. Meth. A **1011**, 165597 (2021).

[96] T. Albahri *et al.* (Muon $g-2$ Collaboration), Beam dynamics corrections to the Run-1 measurement of the muon anomalous magnetic moment at Fermilab, Phys. Rev. Accel. Beams **24**, 044002 (2021).

[97] T. Albahri *et al.* (Muon $g-2$ Collaboration), Magnetic-field measurement and analysis for the Muon $g-2$ Experiment at Fermilab, Phys. Rev. A **103**, 042208 (2021).

[98] A. T. Fienberg *et al.*, Studies of an array of PbF_2 Cherenkov crystals with large-area SiPM readout, Nucl. Instrum. Meth. A **783**, 12 (2015).

[99] W. Gohn (on behalf of the Fermilab E989 collaboration), Data Acquisition for the New Muon $g-2$ Experiment at Fermilab, J. Phys. Conf. Ser. **664**, 082014 (2015).
J. Kaspar *et al.*, Design and performance of SiPM-based readout of PbF_2 crystals for high-rate, precision timing applications, JINST **12**, P01009 (2017).

[100] K. S. Khaw *et al.*, Performance of the Muon $g-2$ calorimeter and readout systems measured with test beam data, Nucl. Instrum. Meth. A **945**, 162558 (2019).

[101] A. Anastasi *et al.*, The laser-based gain monitoring system of the calorimeters in the Muon $g-2$ experiment at Fermilab, JINST **14**, P11025 (2019).
A. Anastasi *et al.*, An approach to light distribution for the calibration of high energy physics calorimeters, JINST **15**, P09014 (2020).

[102] B. T. King *et al.*, The straw tracking detector for the Fermilab Muon $g-2$ Experiment, JINST **17**, P02035 (2022).

[103] W. D. Phillips, W. E. Cooke and D. Kleppner, Magnetic Moment of the Proton in H_2O in Bohr Magnetons, Metrologia **13**, 179 (1977).

[104] S. G. Karshenboim and V. G. Ivanov, The g factor of the proton, Phys. Lett. B **566**, 27 (2003).
E. Tiesinga, P. J. Mohr, D. B. Newell and B. N. Taylor, CODATA recommended values of the fundamental physical constants: 2018, Rev. Mod. Phys. **93**, 025010 (2021).

[105] W. Liu *et al.*, High Precision Measurements of the Ground State Hyperfine Structure Interval of Muonium and of the Muon Magnetic Moment, Phys. Rev. Lett. **82**, 711 (1999).
E. Tiesinga, P. J. Mohr, D. B. Newell and B. N. Taylor, The 2018 CODATA Recommended Values of the Fundamental Physical Constants (Web Version 8.1).

[106] P. Strasser *et al.*, New muonium HFS measurements at J-PARC/MUSE, Hyperfine Interact. **237**, 234 (2016).

[107] P. Crivelli, The Mu-MASS (muonium laser spectroscopy) experiment, Hyperfine Interact. **239**, 49 (2018).

[108] T. Albahri *et al.* (Muon $g-2$ Collaboration), Measurement of the anomalous precession frequency of the muon in the Fermilab Muon $g-2$ Experiment, Phys. Rev. D **103**, 072002 (2021).

[109] L. Kelton, An Energy-Integrated Analysis for Measuring the Anomalous Precession Frequency for the Muon $g-2$ Experiment at Fermilab, PhD Thesis, University of Kentucky, 2022.

[110] R. Chakraborty, Energy Integrated Ratio Analysis of the Anomalous Precession Frequency in the Fermilab Muon $g-2$ Experiment, PhD Thesis, University of Kentucky, 2022.

[111] O. Kim *et al.*, Reduction of coherent betatron oscillations in a muon $g-2$ storage ring experiment using RF fields, New J. Phys. **22**, 063002 (2020).

[112] E. Bottalico, Beam Dynamics corrections in the measurement of the anomalous precession frequency at the Muon $g-2$ experiment at Fermilab, PhD Thesis, University of Pisa, 2022.

[113] N. S. Froemming, Optimization of Muon Injection and Storage in the Fermilab $g-2$ Experiment: From Simulation to Reality, PhD Thesis, University of Washington, 2018.

[114] D. A. Tarazona, Beam Dynamics Characterization and Uncertainties in the Muon $g-2$ Experiment at Fermilab, PhD Thesis, Michigan State University, 2021.

[115] Y. Orlov, C. S. Ozben and Y. K. Semertzidis, Muon revolution frequency distribution from a partial-time Fourier transform of the g-2 signal in the muon g-2 experiment, Nucl. Instrum. Meth. A **482**, 767 (2002).

[116] F. J. M. Farley, Pitch correction in $(g-2)$ experiments, Phys. Lett. B **42**, 66 (1972).

[117] M. W. Smith, Developing the Precision Magnetic Field for the E989 Muon $g-2$ Experiment, PhD Thesis, University of Washington, 2017.

[118] P. Girotti, Measurement of the muon anomalous precession frequency at the Muon $g-2$ Experiment at Fermilab, PhD Thesis, University of Pisa, 2022.

[119] H. Binney, Precession frequency analysis for Run-2 and Run-3 of the Muon $g-2$ experiment, PhD Thesis, University of Washington, 2022.

[120] J. Hempstead, Measuring the anomalous precession frequency ω_a for the Muon $g-2$ experiment, PhD Thesis, University of Washington, 2021.

[121] S. Di Falco, A. Driutti, A. Gioiosa and M. Sorbara, Lost Muons Correction, E989 Internal Doc. 16402, 2019.

[122] M. Sorbara, Measurement of the anomalous precession frequency in the Muon $g-2$ (E989) experiment at Fermilab, PhD Thesis, Università degli Studi di Roma Tor Vergata, 2022.

[123] L. Lönnblad, CLHEP - a project for designing a C++ class library for high energy physics, Comp. Phys. Comm. **84**, 307 (1994).

[124] J. M. Kindem, The Anomalous Magnetic Moment of the Positive Muon, PhD Thesis, University of Minnesota, 1998.

[125] L. H. Duong, A Precise Measurement of the Anomalous Magnetic Moment of the Positive Muon (preview, compressed PostScript file), PhD Thesis, University of Minnesota, 2001.

[126] N. B. Kinnaird, Muon spin precession frequency extraction and decay positron track fitting in Run 1 of the Fermilab Muon $g-2$ experiment, PhD Thesis, Boston University, 2020.

[127] S. B. Foster, Measurement of the Muon Anomalous Precession Frequency in Runs 2 & 3 of the Muon $g-2$ Experiment at Fermilab, PhD Thesis, Boston University, 2023.

[128] A. Edmonds, Kernel for BU Ratio Method Analysis, E989 Internal Doc. 26149, 2021.

[129] A. A. Goldstein and J. F. Price, On Descent from Local Minima, Math. Comp. **25**, 569 (1971).

[130] D. A. Sweigart, A Measurement of the Anomalous Precession Frequency of the Positive Muon, PhD Thesis, Boston University, 2020.

[131] T. Barrett, The Fast Rotation Fourier Method, E989 Internal Doc. 26033, 2021.